NORTHWESTERN UNIVERSITY

ROTATIONAL STRUCTURE IN INTERSYSTEMS CROSSING

A DISSERTATION

SUBMITTED TO THE GRADUATE SCHOOL

IN PARTIAL FULFILLMENT OF THE REQUIREMENTS

for the degree

DOCTOR OF PHILOSOPHY

Field of Physical Chemistry

By

WILLIS EDGAR HOWARD, III

Evanston, Illinois

June 1978

ACKNOWLEDGEMENTS

The author wishes to thank Prof. E. W. Schlag whose guidance and inspiration were essential for this work.

The author also thanks Dean Baker of the Graduate School and Prof. Basolo of the Chemistry Department for making it possible for him to complete his doctoral work at the Technical University of Munich, Germany.

The assistance of Herr Uli Bösl and Dr. Heinrich Selzle at various stages of experimental construction is also acknowledged. Thanks are also due to the members of the electronics and mechanics shops, especially to Herr Stoiber who built the fluorescence and absorption cells used in this work.

The author thanks Dr. F. Metz for many helpful discussions concerning the theoretical aspects of this work.

TABLE OF CONTENTS

I. Introduction 1

II. Historical Background: Quantum Yield and Lifetime Techniques 5

III. Experimental

A. Introduction: experimental setup 11

B. Quantum yield determination 13

C. Lifetime determination 17

D. The flashlamp pumped dye laser 21

E. The fluorescence cell 24

F. Fluorescence collection geometry 27

G. The absorption cell 35

H. Photomultiplier characteristics

1. Introduction 37

2. Photocathode spectral response 38

3. Surface sensitivity 39

4. Voltage dividers 39

5. Photomultiplier linearity 41

6. PM gain stability 46

7. PM relative gain 49

I. Electronics 51

J. Appendix 1. Quantum yield interface to the PDP 11/45 54

K. Appendix 2. WP2221 interface to the PDP 11/45 58

IV. Historical: Structure in Non-radiative Processes 62

V. Experimental results

A. Introduction 70

B. Measured data 71

VI. Absorption Transition Probabilities

A. Introduction 99

B. The ground state ensemble 100

C. One photon transition intensity 102

D. Two photon transition probability 104

E. The asymmetric rotor 105

F. Transition selection rules 110

G. Rotational contour program 113

H. The excited state ensemble 125

I. Appendix 1. The Wigner 3-J symbols 133

VII. Characteristics of the Excited Ensemble

A. Introduction 137

B. Isolated molecule conditions 137

C. Intramolecular energy transfer 139

VIII. Excited State Relaxation

A. Decay of a single level 146

B. Decay of an ensemble 146

IX. The Radiative Rate Constant 153

X. The Mechanism of Non-radiative Decay

A. The zero order Hamiltonian 159

B. Coupling schemes in ISC 163

C. ISC coupling in naphthalene 166

XI. Models of Non-radiative Decay

A. The general equation for the rate 170

B. Density of states models 173

C. Time representation models 176

D. Higher approximations 183

XII. Rotational Dependence in Non-radiative Transitions 192

XIII. Vibronic Coupling in ISC

A. Determination of the vibrational parameters 203

B. Density of states 207

C. Franck-Condon factors 214

D. The promoting mode 218

XIV. Numerical Results

A. Computational procedure 225

B. ISC from the $^{3}(b_{1g})_{o}^{1}$ band 227

C. ISC from the 0-0 band 253

XV. Conclusion 272

LIST OF FIGURES

Figure		Page
1.	Experimental setup	12
2.	Measured absorption spectrum of the $8(b_{1g})^1_o$ band of naphthalene, h_8	15
3.	Measured excitation spectrum of the $8(b_{1g})^1_o$ band of naphthalene, h_8	16
4.	Typical lifetime decay curve	20
5.	Flashlamp pumped dye laser	22
6.	Fluorescence cell	26
7.	Absorption region in the fluorescence cell	28
8.	Fluorescence cell emission geometry	31
9.	Fluorescence area viewed by the PM	33
10.	Absorption cell	36
11.	56 DUVP voltage divider modifications	40
12.	1P28 voltage divider	42
13.	Setup for PM linearity calibration	45
14.	1P28 linearity curve at 1100 volts	48
15.	Collection geometry for the 1P28	50
16.	Current integrator schematic	52
17.	Quantum yield interface to the PDP 11/45	55
18a.	Measured quantum yield spectrum of the 0-0 band of naphthalene, h_8	73
18b.	Lifetime spectrum of the 0-0 band	75
19.	High pressure quantum yield spectrum of the $8(b_{1g})^1_o$ band of naphthalene, h_8	76

20. Low pressure quantum yield spectrum of the $8(b_{1g})^1_o$ band 77

21. Quantum yield spectrum of the $8(b_{1g})^1_o\ 4(b_{1u})^1_1$ 79

22. Quantum yield spectrum of the $8(b_{1g})^1_o\ 3(b_{2g})^1_1$ 81

23. Quantum yield spectrum of the $8(b_{1g})^1_o\ 4(b_{1u})^1_1\ 3(b_{2g})^1_1$ band 82

24. Quantum yield spectrum of the $7(b_{1g})^1_o$ 84

25. Quantum yield spectrum of the $7(b_{1g})^1_o\ 3(b_{2g})^1_1$ 85

26. Quantum yield spectrum of the $9(a_g)^1_o$ 87

27. Quantum yield spectrum of the $9(a_g)^1_o\ 3(b_{2g})^1_1$ 88

28. Quantum yield spectrum of the $8(a_g)^1_o$ 89

29. Quantum yield spectrum of the $8(a_g)^1_o\ 3(b_{2g})^1_1$ 90

30. Quantum yield spectrum of the $8(b_{1g})^1_o\ 8(a_g)^1_o$ 92

31. Quantum yield spectrum of the $8(b_{1g})^1_o\ 8(a_g)^1_o\ 3(b_{2g})^1_1$ 93

32. Quantum yield spectrum of the $4(a_g)^1_o$ 94

33. Quantum yield spectrum of the $4(a_g)^1_o\ 3(b_{2g})^1_1$ 95

34. Quantum yield spectrum of the $3(a_g)^1_o$ 97

35. The rotational distribution in the ground state of naphthalene, h_8 101

36. Rotational program flowchart 115

37. Calculated contour of the 0-0 transition of naphthalene, h_8 117

38. Calculated contour of the $8(b_{1g})^1_o$ band of naphthalene, h_8 118

39. Calculated 2 photon contour of an a_g transition with $x^2/y^2 = 9$ for

a) two linearly polarized photons 119

b) two circularly polarized photons 120

40. Calculated 2 photon a_g contour with $x^2/y^2 = 3$ for a) two linearly polarized photons 121

b) two circularly polarized photons 122

41. Calculated 2 photon a_g contour with $x^2/y^2=1$ for a) two linearly polarized photons 123

b) two circularly polarized photons 124

42. Calculated 2 photon b_{1g} contour 126

43. The rotational distribution in the excited state of naphthalene,h_8 at the band origin 127

44. Rotational distribution at + 1.5 cm^{-1} 128

45. Rotational distribution at + 2.5 cm^{-1} 129

46. Rotational distribution at + 3.5 cm^{-1} 130

47. Rotational distribution at + 4.23 cm^{-1} 131

48. Turnover point for ß-naphthylamine 142

49. Turnover point for naphthalene,h_8 143

50. Measured radiative rate constant spectrum of the 0-0 band of naphthalene,h_8 154

51. Measured radiative rate constant spectrum of the $8(b_{1g})^1_o$ band 155

52. Coupling schemes for ISC in naphthalene,h_8 167

53. Computed naphthalene,h_8 phosphorescence spectrum 208

54. Density of states in T_1 of naphthalene,h_8 as a function of the relative energy gap 215

55. Franck-Condon weighted density of states for naphthalene,h_8 with a final state linewidth of 25 cm^{-1} 219

56. Franck-Condon weighted density of states with a final state linewidth of 2.5 cm^{-1} 220

57. Computed k_{nr}^{a} spectrum for the $8(b_{1g})_{o}^{1}$ band with B axis spin population and ω_p=422 cm^{-1} 229

58. Computed k_{r}^{e} spectrum 230

59. Computed ϕ^{e} spectrum 231

60. Computed k_{nr}^{a} spectrum with in-plane spin polarization 233

61. Computed k_{r}^{e} spectrum 234

62. Computed ϕ^{e} spectrum 235

63. Computed k_{nr}^{a} spectrum with A axis spin population 236

64. Computed k_{r}^{e} spectrum 237

65. Computed ϕ^{e} spectrum 238

66. Computed k_{nr}^{a} spectrum with a constant rotational factor 240

67. Computed k_{nr}^{a} spectrum with a constant vibrational factor 242

68. Computed k_{nr}^{a} spectrum including all factors for the $\Delta N = -1$ component 243

69. Computed k_{nr}^{a} spectrum for $\Delta N = 0$ 244

70. Computed k_{nr}^{a} spectrum for $\Delta N = +1$ 245

71. Computed k_{nr}^{a} spectrum with a constant rotational factor for the $\Delta N = -1$ component 247

72. Computed k_{nr}^{a} spectrum for $\Delta N = 0$ 248

73. Computed k_{nr}^{a} spectrum for $\Delta N = +1$ 249

74. Computed k_{nr}^{a} spectrum with a constant vibrational factor for $\Delta N = -1$ 250

75. Computed k_{nr}^{a} spectrum for $\Delta N = 0$ 251

76. Computed k_{nr}^{a} spectrum for $\Delta N = +1$ 252

77. Computed k_{nr}^{a} spectrum for the 0-0 band of naphthalene, h_8 for B axis spin population and $\omega_p = 422\ cm^{-1}$ 255

78. Computed k_{r}^{e} spectrum 256

79. Computed ϕ^{e} spectrum 257

80. Computed k_{nr}^{a} spectrum for A axis population 258

81. Computed k_{r}^{e} spectrum 259

82. Computed ϕ^{e} spectrum 260

83. Computed k_{nr}^{a} spectrum for B axis spin population and $\omega_p = 522\ cm^{-1}$ 261

84. Computed k_{r}^{e} spectrum 262

85. Computed ϕ^{e} spectrum 263

86. Computed k_{nr}^{a} spectrum for B axis spin population and $\omega_p = 622\ cm^{-1}$ 265

87. Computed k_{r}^{e} spectrum 266

88. Computed ϕ^{e} spectrum 267

89. Computed k_{nr}^{a} spectrum for A axis spin population and $\omega_p = 722\ cm^{-1}$ 268

90. Computed k_{r}^{e} spectrum 269

91. Computed ϕ^{e} spectrum 270

VITA

The author was born on March 20, 1948 in Oklahoma City, Oklahoma. He moved to Huntsville, Alabama where he attended Rison Grade School and Lee High School.

He attended Samford University from 1966 to 1970. He received his B.S. in Chemistry with Honors in June, 1970.

In September, 1970 he became a graduate student at Northwestern University. In 1972, he moved to Munich, Germany to complete his doctoral work.

The author married Gabriele Christ on December 28, 1976 in Munich, Germany.

Chapter I
Introduction

Molecules which are electronically excited through optical excitation are only quasistationary and have two mechanisms of decay: radiative and non-radiative. Experimentally, the measurable properties of excited molecules are related to their radiative properties of absorption and emission. In the gas phase, the absorption coefficient, quantum yield and lifetime can be measured. In certain experiments, polarization information can also be obtained. In Chapters II and III the experimental procedures are discussed in detail.

The radiative properties of excited molecules are well understood and the measured quantities are thus used to probe the dynamics of the non-radiative processes. In contrast to the radiative process, there exists a large variety of non-radiative processes. If the final state of the transition has a different spin from the initial state, the process is called intersystems crossing (ISC). If the spin of the two states is the same, the process is called internal conversion (IC). However, if there are large geometry changes, the process is also one of isomerization. It is also possible for the molecule to break up via predissociation or unimolecular reaction. At very high energies, electrons can be emitted via auto- or direct ionization.

ISC and IC are the most common non-radiative processes in large, isolated molecules. For diatomic molecules, predissociation is dominant. For non-isolated molecules, energy transfer and chemical reaction also occur. The non-radiative process depends on the nature of the electronic, vibrational and rotational states which are excited. The experimental evidence relating to this is discussed in Chapters IV and V.

The ground state rotational levels form a Boltzmann distribution. This can not be assumed for the excited states unless a very large bandwidth or high pressures are used. The initial rotational distribution in the excited state is discussed in Chapter VI and the factors which can alter the distribution, in Chapter VII.

Unless single ro-vibronic states are excited, the observed molecular properties are related to the prepared ensemble of states. For an ensemble, the standard formulas

$$k_r = \phi / \tau$$

and

$$k_{nr} = (1 - \phi) / \tau$$

are not generally applicable. An excited state ensemble must be described by a Master Equation. The Master Equation valid for pulsed excitation is discussed in Chapter VIII. The final solutions are somewhat simplified by the assumption of a constant microscopic radiative rate constant as discussed in Chapter IX.

The microscopic non-radiative rate constants are, in general, different for each excited molecular state. The rate constants depend on the interaction matrix elements connecting the initial and final states. The electronic and vibrational coupling terms and the zero-order Hamiltonian for the molecular states are discessed in Chapter X.

Non-radiative processes are subject to two very important conservation laws. The first is conservation of total angular momentum. No process in the isolated molecule is allowed to change J, the total angular momentum including spin, or P, its projection on the molecular z axis. Thus, the selection rules $\Delta J = 0$ and $\Delta P = 0$ apply. The second is conservation on energy. The final state of the transition must have the same energy as the initial state. This is somewhat relaxed via the Heisenberg uncertainty principle which only requires energy matching to within initial and final state natural linewidths.

The requirement of isoenergetic initial and final states in a non-radiative process is paralleled in the radiative process with the requirement that the energy difference of initial and final states equals the photon energy. The full implications of this have not, in general, been recognized in the various theories of non-radiative processes. The most important theories are reviewed in Chapter XI.

In absorption, it is well known that various rotational transitions of a single vibronic band do not occur at the same transition energy. This is also true for transitions obeying the selection rules $\Delta J = 0$ and $\Delta K = 0$. One reason for this is the different inertial constants of the two electronic states. Likewise, in a non-radiative process the energy difference of the initial and final rotational states can not be considered constant. The rotational energy difference, which is accounted for by a change in photon energy in a radiative process, must be made up by a change in the vibrational energy in a non-radiative process. This represents a change in the effective energy gap due to rotational excitation.

In Chapter XII, the rotational dependence in non-radiative processes is discussed. Both the effects of the rotational energy difference and the consequences of the selection rules $\Delta J = 0$ and $\Delta P = 0$ are analyzed in detail. Model calculations for $T_1 \leftarrow S_1$ ISC in naphthalene, h_8 employing the full Master equation solutions and rotational dependence in the non-radiative rate constant are presented in Chapter XIV.

Chapter II

Historical Background: Quantum Yield and Lifetime Techniques

Quantum yields in the solid and liquid phases have a long history and good reviews are available.[1] The first direct measurement of absolute gas phase quantum yields was made by Noyes, et al.[2] on benzene at 10 torr. This measurement has been taken as the reference standard for most other gas phase work[3-10] and thus deserves special consideration.

Noyes' experimental setup consisted of a long cell with extended entrance and exit windows which allowed the simultaneous determination of emission and absorption spectra. The fraction of absorbed radiation, f, was measured with an RCA 935 and given by the equation $f = (i_4 - i_5)/i_4$ where i_4 was the phototube current with vacuum in the cell and i_5 the current with the sample. The fluorescence was measured with an RCA 1P28. The signal, i_f, was corrected for both scattered light and PM dark current. The photocathode was restricted to an area of constant sensitivity allowing fluorescence to be observed with a collection efficiency of 0.00263. The relative gain of the tube was corrected for the spectral shift in emission with sodium salicylate thin films. An additional value, r_4, accounted for the absorption within the cell. The combined factors

allowed the quantum yield to be written as

$$\phi = 190\ i_f\ i_5 / (i_4 - i_5) r_4 .$$

The error in this experiment was given as 20% and is thus the minimum error of all experiments using the reported value of 0.18 as the reference standard.

In addition to the work of Noyes, the only other absolute determination of a gas phase quantum yield without a reference standard was that of v. Weyssenhoff et al.[11,12] on aniline and substituted anilines. In his experiment a single, movable detector was used to monitor fluorescence and transmitted light intensity. The detector consisted of an RCA C31000E photomultiplier used in conjunction with an aqueous fluorescein quantum converter. Transmitted intensity was reduced with neutral density filters. Hence the calibration was transfered from one of measuring relative PM gain to one of measuring reflections and transmissions of filters. Circular apertures were used to carefully define the emission collection geometry.

Quantum yield measurements were extended to single vibronic levels by Parmenter and Schuyler.[13] They first measured benzene excited to the 6^1 and $6^1 1^1$ levels of S_1 using integrated SVL fluorescence spectra and the high pressure quantum yields of Noyes. The quantum yields were given by the equation

$$\phi = 0.18\ I^{SVL} / I^{Bolz} .$$

Methods similar to this, using the above equation, have been employed to measure SVL quantum yields of naphthalene[7,14] and substituted benzenes.[4,5] Note that this method often assumes a constant photomultiplier response, a condition which is generally provided only by quantum converters.

A variant of this method employs single photon counting.[6-8] Intensities in this case correspond to the accumulated count from the fluorescence PM. However, extreme care must be taken in such experiments since the photon counting electronics samples only a restricted region of the entire Poisson distribution. This distribution depends on the entire detection electronics and especially the discriminator settings which must be kept constant during all calibrations and measurements.

The measurement of lifetimes requires that the decay of the sample be timed relative to a time signal impressed on the excitation source. The excitation may be either pulsed or continuous. In the latter case the intensity must be modulated and the signal will be in the form of a phase shift relative to the source. This method was introduced by Gavolia in 1926.[15]

The phase shift signal is related to the lifetime by the equation

$$\tan \theta = \tau \omega$$

where θ is the phase angle and ω the modulation

frequency. Detection may be analog[16,17] or via single photon correlation.[18] The first measurement of gas phase fluorescence lifetimes using this method was made by Schlag and von Weyssenhoff.[17]

In the case of pulsed excitation, it is also possible to have either analog or single photon signals. In either case, the fluorescence is monitored directly in real time, in contrast to the phase shift technique which performes the measurement in Fourier space. The first measurement of fluorescence decay in the nanosecond region was made by Phillips and Swank in 1953[19] using X-rays. Accurate lifetime measurements in the visible using a pulsed excitation source were made by Brody[20] in 1957.

The single photon counting lifetime technique has been widely discussed in the literature[21,22] and the apparatus can be constructed entirely from commercial components. However, to function properly the technique demands a low excitation source intensity. This, in turn, often demands very long data collection times.

The use of pulsed laser excitation often produces enough excited molecules to allow the collection of a decay curve with a single shot. In the case of very low quantum yields, a good curve can be collected by summing over multiple laser shots. With the advent of the tunable, pulsed dye laser, this method is replacing all previous methods.

References to Chapter II

1. J. N. Demas and G. A. Crosby, J. Phys. Chem. 75, 991 (1971).
2. W. A. Noyes, et al., J. Chem. Phys. 44, 2100 (1966).
3. C. S. Parmenter and M. D. Schuh, Chem. Phys. Lett. 13, 120 (1972).
4. M. G. Rockley and D. Phillips, Chem. Phys. Lett. 21, 181 (1973).
5. M. G. Rockley and D. Phillips, J. Phys. Chem., 78, 7 (1974).
6. K. Spears and S. A. Rice, J. Chem. Phys. 55, 5561 (1971).
7. A. Abramson, K. Spears and S. A. Rice, J. Chem. Phys. 56, 2309 (1972).
8. R. Scheps, D. Florida and S. A. Rice, J. Chem. Phys. 61, 1730 (1974).
9. S. F. Fischer, A. L. Stanford and E. C. Lim, J. Chem. Phys. 61, 582 (1974).
10. E. C. Lim and J. O. Uy, J. Chem. Phys. 56, 3374 (1972).
11. H. v. Weyssenhoff and F. Kraus, J. Chem. Phys. 51, 2508 (1969).
12. F. Kraus, E. Gregorek and H. v. Weyssenhoff, Z. F. Phys. Chem. N. F. 82, 139 (1972).
13. C. S. Parmenter and M. W. Schuyler, Chem. Phys. Lett. 6, 339 (1970).
14. M. Stockburger, H. Gettermann and W. Klusmann, J. Chem. Phys. 63, 4529 (1975).
15. E. Gaviola, Z. Phys. 35, 748 (1926).
16. J. B. Birks and I. H. Munro, Prog. Reaction Kinetics 4, 239 (1967).
17. E. W. Schlag and H. v. Weyssenhoff, J. Chem. Phys. 51, 2508 (1969).
18. E. W. Schlag, et al., Rev. Sci. Inst. 45, 364 (1974).

19. H. B. Phillips and R. K. Swank,
Rev. Sci. Inst. 24, 661 (1953).
20. S. S. Brody, Rev. Sci. Inst. 28, 1021 (1957).
21. W. R. Ware, Creation and Detection of the Excited State, ed. A. A. Lamola, Vol. 1A,
(Marcel Dekker, New York, 1971).
22. S. Cova, M. Bertolacini and C. Bussolati,
IEEE Trans. on Nuc. Sci., 19, 18 (1972).

Chapter III

Experimental

Introduction: Experimental setup

The experiment was constructed so that absolute quantum yields and lifetimes could be simultaneously measured. The experimental setup is shown on Fig. 1. The excitation source was a flashlamp pumped dye laser operated with Rhodamine 6G. The laser had a resolution of 120000 in the UV after frequency doubling with a KDP crystal. An external Pockel cell chopped the laser pulse to 50 nsec with 2 nsec rise and fall times.

The cell consisted of a well baffled fluorescence cell ahead of a multiple path absorption cell with adjustable path length (up to 10 meters). The two cells were connected to each other via O-rings and stainless steel flanges. Thus they contained the same gas at the same pressure at all times. The absorption path length was adjusted so that the laser light would be approximately half absorbed within the entire cell.

The initial laser intensity and cell transmission were monitored with RCA 1P28's and the fluorescence with an Amperex 56 DUVP. The anode signal of each PM was electronically integrated to give a signal proportional to the total pulse intensity. The integrated signals were digitized and transferred to a PDP 11/45 for on-line analysis of absorption and quantum yield. The time

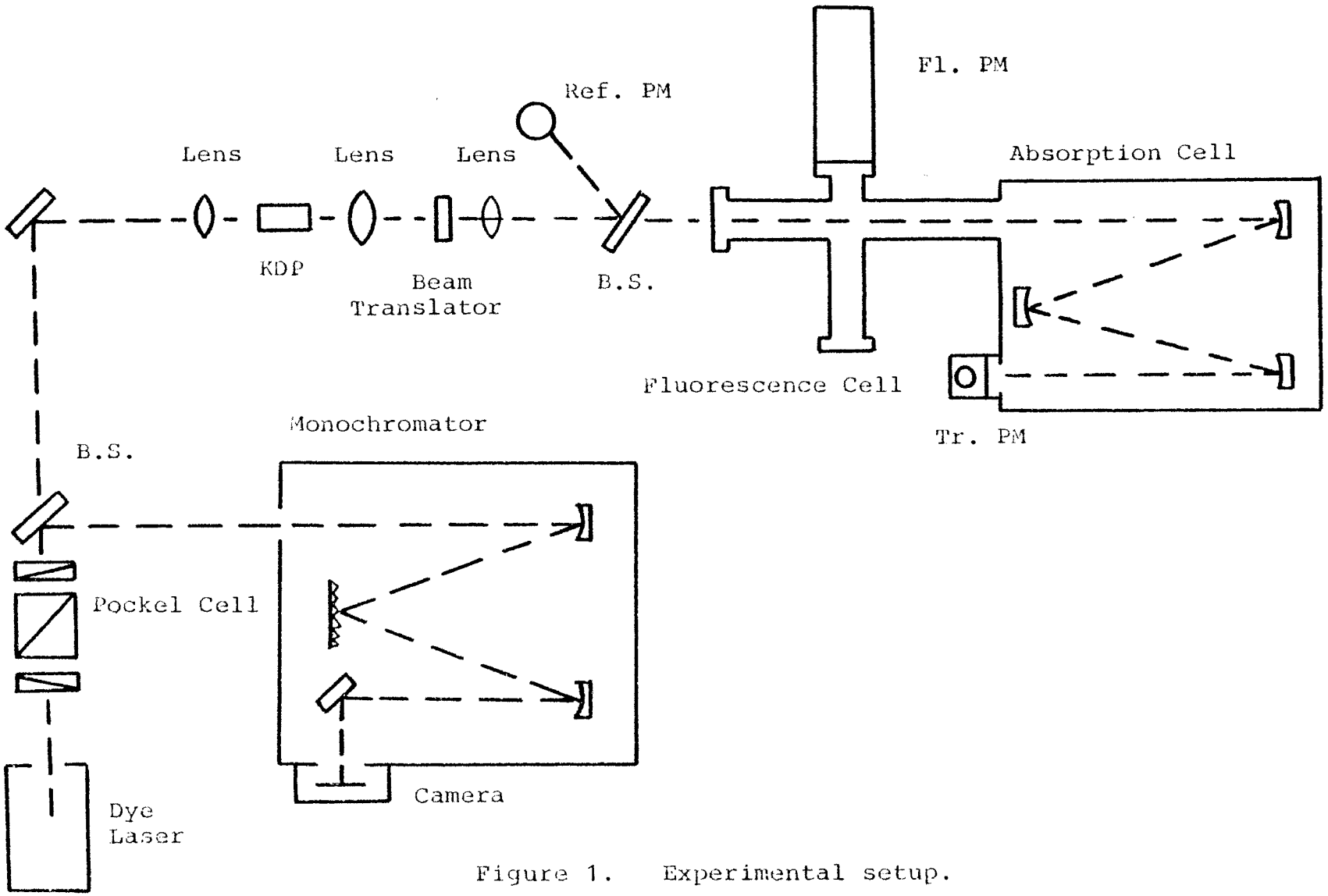

Figure 1. Experimental setup.

response of the fluorescence was monitored via the last dynode of the 56 DUVP. The time response curve was digitized on a Tektronix WP2221 transient digitizer and transferred to the PDP 11/45 for lifetime calculation.

Quantum yield determination

The equations for the integrated signal observed at each photomultiplier (PM) are as follow:

PM (ref.): $I_{ref} = I_o \; r \; D_{ref}$

PM (tr.): $I_{tr} = I_o \exp (-\varepsilon Cd) \; r \; D_{ref} \; T(\lambda)$

PM (fl.): $I_{fl} = I_o \; t \; D_{fl} \exp(-\varepsilon Cc) \; C \; \bar{x} \varepsilon \phi \alpha$

These equations can be solved for the quantum yield and absorption coefficient. The solutions are

(1) $\phi = \exp(\varepsilon cC) \; (C\bar{x}\varepsilon)^{-1} \; (1/\alpha) \; (r/t) \; (I_{fl}/I_{ref}) \; (D_{ref}/D_{fl})$

(2) $\varepsilon = (Cd)^{-1} \ln(T(\lambda) \; (I_{ref}/I_{tr}))$

where

ϕ = quantum yield,

$T(\lambda)$ = transmission factor for the laser beam through the entire apparatus with an empty cell relative to the reference PM,

c = preabsorption path length,

ε = absorption coefficient,

$\bar{x}$ = active fluorescence length,

C = concentration,

α = fluorescence PM collection efficiency,

t = transmission of all windows and the beam splitter in the laser/fluorescence path,

r = reflectance of the beam splitter,

D = PM relative gain times spectral sensitivity,

d = total absorption path length.

In order to measure absolute quantum yields, each term in Eqs. 1 and 2 must be known. The integrated signals constitute the actual measurement and all other factors must be previously calculated or measured.

An example of optical density measurements is shown on Fig. 2. In this measurement of naphthalene, h_8 the rotational contour of the $8(b_{1g})^1_o$ band is shown. Error bars indicating one standard deviation are given when the error is larger than the symbol size. Since the error is almost always less than 1%, error limits will not be displayed on any other absorption diagrams.

The quantum yield equation contains the equation for the relative excitation spectrum intensity. This is given by

$$I_{ex} = \exp(\epsilon c C)\ (I_{fl}/I_{ref}) .$$

The excitation spectrum is the integrated fluorescence intensity as a function of excitation wavelength. An example of a measured excitation spectrum is shown on Fig. 3. Again, error bars are only shown when the error is larger than the symbol size.

The small error limits of the last two figures show that the precision of the data used to calculate

Figure 2. Measured absorption spectrum of the $8(b_{1g})_o^1$ band of naphthalene, h_8. Error bars indicating one standard deviation are shown if larger than the symbol size.

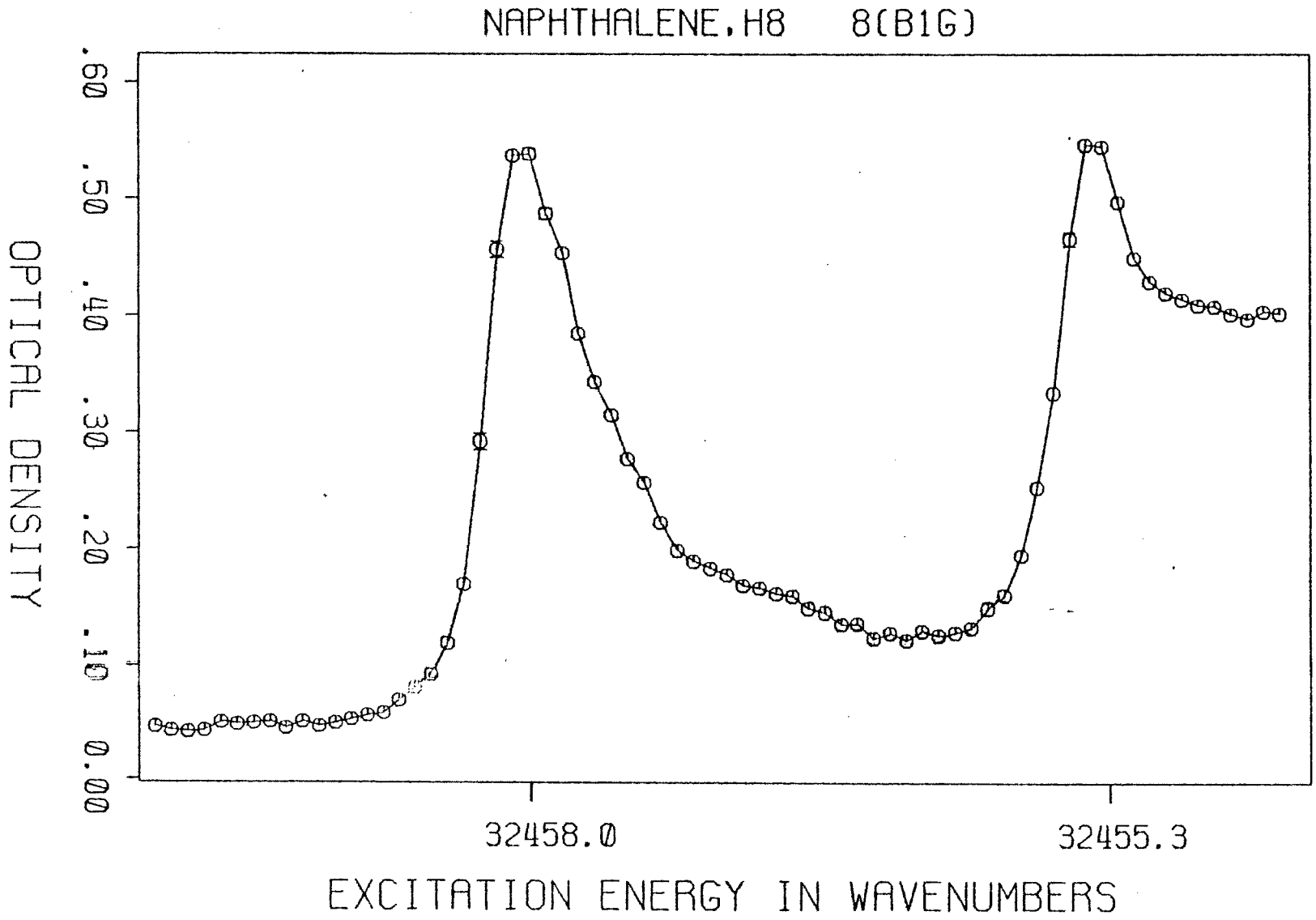
NAPHTHALENE,H8 8(B1G)
OPTICAL DENSITY
.00
.10
.20
.30
.40
.50
.60
32458.0
32455.3
EXCITATION ENERGY IN WAVENUMBERS

Figure 3. Measured excitation spectrum of the $8(b_{1g})_o^1$ band of naphthalene, h_8. Error bars are shown if the standard deviation is larger than the symbol size.

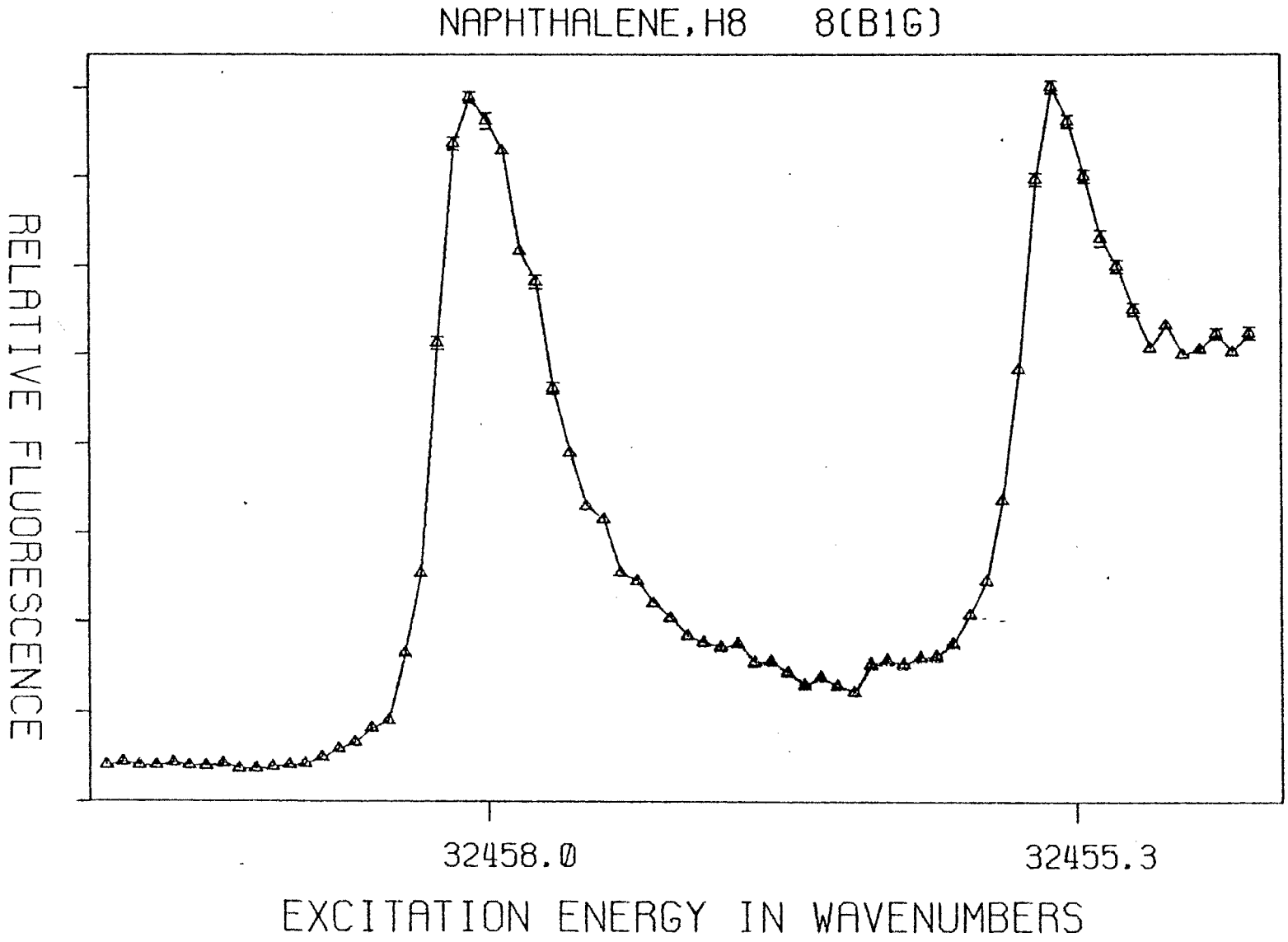
NAPHTHALENE, H8 8(B1G)
RELATIVE FLUORESCENCE
32458.0
32455.3
EXCITATION ENERGY IN WAVENUMBERS

the quantum yields is very high. In general, the standard deviation in the quantum yield measurements was 1-2% and never exceeded 3%.

The standard deviation could be kept low due to the fact that the quantum yield and absorption coefficient were calculated on-line with a PDP 11/45 computer. The computer could thus dynamically calculate the standard deviation and collect enough points to bring it down to a preset level. All data points were the result of at least 5 laser shots and at most 16 laser shots. A detailed description of the computer interface for quantum yield collection is given in Appendix 1.

Lifetime determination

Lifetime decay curves were obtained from the last dynode of a 56 DUVP with a specially modified EG&G voltage divider and digitized on a Tektronix WP2221. For the lifetimes in this work, it is assumed that the short fall time of the excitation pulse required no deconvolution of the excitation pulse shape from the observed decay curve.

For multilevel excitation, one has no guarantee that the observed decay curve, D(t), will be exponential. The only meaningful time constant for non-exponential decay is the mean first passage time (MFPT) which is defined by the equation

$$\tau_{mfp} = \int_0^\infty P(t)\, t\, dt$$

where the probability function for decay is defined as

$$P(t) = D(t) \Big/ \int_0^\infty D(t')\, dt' ,$$

If the curve is also exponential, t_{mfp} is also equal to the lifetime described by the equation

$$D(t) = x \exp(-t/t_{mfp}) .$$

However, integrating to obtain the MFPT requires the entire decay curve until D(t) goes to zero and is very sensitive to noise in the tail. With the assumption of exponential decay, the observed points can be fit via a non-linear least squares technique.

The function to be fit is of the form $D(t)= x \exp(-kt)$. This function is first expanded around $(\bar{x},\bar{k})$, the initial approximations for the curve height at t=0 and the rate constant, in a Taylor series terminated with second order terms. Thus,

$$D(t,x,k) = D(t,\bar{x},\bar{k}) + \partial D/\partial x \Big|_{x=\bar{x}} (x-\bar{x}) + \partial D/\partial k \Big|_{k=\bar{k}} (k-\bar{k})$$

and defining $(x-\bar{x})= \xi$ and $(k-\bar{k})= \mu$ yields

$$D(t,x,k) = \bar{x} \exp(-\bar{k}t) + \xi \exp(-kt) - \mu\, t\bar{x} \exp(-kt).$$

Equating D(t,x,k) with D_i, the observed curve height at time t_i allows this equation to be rewritten as

$$n_i = (D_i \exp(\bar{k}t_i) - \bar{x})$$

$$= \xi - \mu\, t_i\, \bar{x} .$$

The least squares conditions are given by

$$\sum_i a_i n_i = \sum_i a_i a_i \xi + \sum_i a_i b_i \mu$$

$$\sum_i b_i n_i = \sum_i b_i a_i \xi + \sum_i b_i b_i \mu$$

where $a_i=1$ and $b_i=-t_i\bar{x}$ with the resulting ξ and μ being used to correct the approximate $(\bar{x},\bar{k})$. New values are obtained by iteration until the correction values are virtually zero. Solving the above equations gives

$$\mu = 6 \sum_i (D_i \exp(t_i\bar{k}) (1-2/s) i)/(\bar{x}t_{del}(1+s)(2+s))$$

$$\xi = 6 \sum_i (D_i \exp(t_i\bar{k}) ((2s+1)/3-i)/((s+1)(s+2))) - \bar{x}$$

where $t_i = it_{del}$, t_{del} = time per channel and s-1 is the point count.

These equations were programmed on a PDP 11/45 which performed on-line lifetime evaluation for each curve collected on the WP2221. Data transfer between the two computers was accomplished via a pseudo-paper tape reader/punch connection. A detailed description of the interface is given in Appendix 2. An example of computed and observed decay curves is shown on Fig. 4. The standard deviation as estimated from the least squares best fit was generally around 2-3%. Worst case fit was around 6% but not typical.

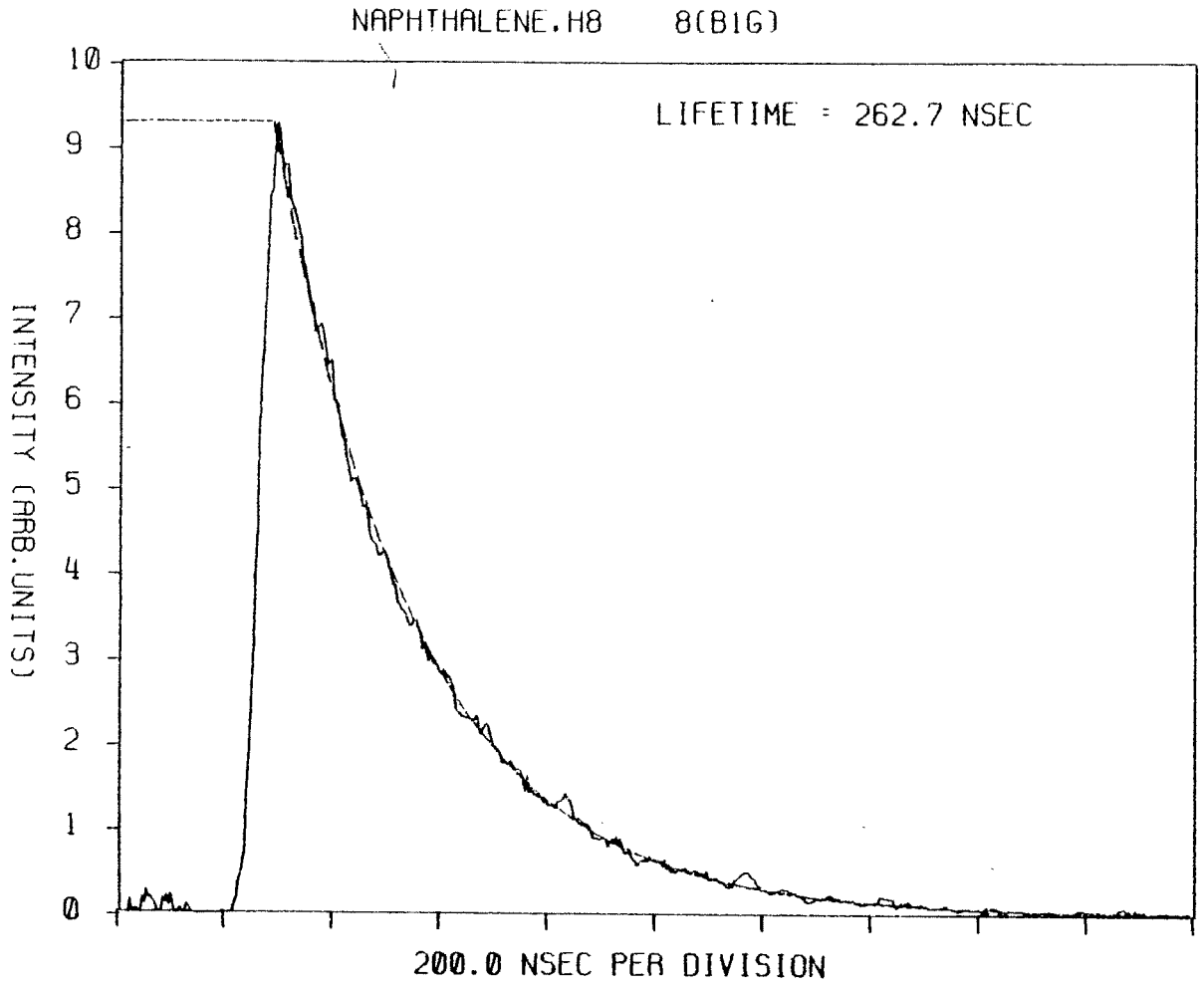

Figure 4. Typical lifetime decay curve.

The flashlamp pumped dye laser

The laser used in these experiments was a tunable flashlamp pumped dye laser with intracavity interference filter and Fabry-Perot etalon.[1] The pulse was shortened outside the cavity with a Pockel cell and frequency doubled into the UV by a KDP crystal. This provided a 50 nsec pulse with less than 2 nsec rise and fall times, tunable from 3100 to 2850 Å with a resolution of 120000. A 5×10^{-4} molar Rhodamine 6G solution in methanol was used as the active medium.

A diagram of the laser cavity is shown on Fig. 5. The front mirror, M1, had a reflectivity of 60% and the end mirror, M2, of 99.8%. The cavity length was 35 cm. The flashlamp (Novatron 599AR) and dye curvette (3mm inner diameter tube with Brewster angle windows) were obtained from Zeiss as an assembled unit. The flashlamp and curvette were situated on the focal axes of a 4" elliptical, cylindrical mirror within the unit.

The flashlamp was fired for 400 nsec by the discharge of a 0.1 μF capacitor at 15-18 kV. The resulting laser pulse was approximately 200 nsec long. The trigger unit was constructed so that the laser could be fired manually or under computer control.

In order to obtain the stated wavelength resolution of the laser, two frequency selective elements were placed inside the cavity. The Fabry-Perot etalon

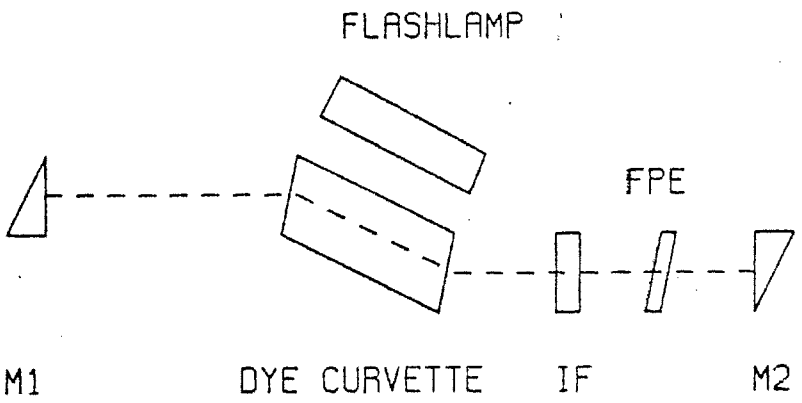

Figure 5. Block diagram of the flashlamp pumped dye laser with intracavity interference filter and Fabry-Perot.

(0.15 mm plate spacing) had a transmission of 83% at 5800 Å and a free spectral range of 7 Å at 6000 Å. With only the etalon in the cavity, the frequency spectrum of the laser consisted of a series of lines spaced by 7 Å. The interference filter had a transmission of 60% at 6140 Å and a halfwidth of 10 Å. With only this element in the cavity, the laser frequency spectrum was virtually the transmission spectrum of the filter. With both elements in the cavity, laser action was only at those frequencies where the etalon and interference filter overlapped. The resulting pulse had a resolution of 120000 but was not continuous over the frequency range, a result of the multimode structure of the laser. Higher resolution measurements[2] showed that the light to dark ratio in the energy spectrum was 1/5.

Frequency tuning could be achieved with either the etalon or the filter. The tuning was continuous, however, only with the etalon and over about a 5 cm^{-1} region. The interference filter then had to be adjusted to insure that the laser was running on a single etalon mode. Tuning was discontinuous when the etalon had to be adjusted to the next mode.

In order to perform lifetime measurements, the laser pulse was shortened to 50 nsec with less than 2 nsec rise and fall times with a Pockel cell placed outside the cavity. The crystal from Electro Optic Developments was driven with a 3000 volt pulse from

a Laser Optronics unit.

The visible pulse was frequency doubled into the UV with a 38 mm KDP (KH_2PO_4) crystal from Kuhl and Spitshom. The laser beam was focused on the middle of the crystal with a 30 cm focal length lens and since conversion was only about 10%, the non-converted visible light was eliminated with a filter of 10^{-6} transmission in the visible and 50% in the UV.

The long fluorescence cell placed in front of the absorption cell made very critical demands on the laser beam path. After allignment, it was not allowed to deviate by more than 0.5 mm at the absorption cell entrance, more than 1 meter from the KDP. The KDP, on the other hand, had the very inconvenient characteristic of vertically shifting the laser beam since it was tuned to the phase match angle by a rotation about an axis perpendicular to the laser beam. This was overcome by placing a 1 cm thick Spectrosil quartz plate behind the KDP which was antirotated to compensate for beam displacement. Another lens was placed behind the beam translator to focus the laser beam on the absorption cell entrance.

The fluorescence cell

The fluorescence cell was constructed with two points in mind. First, scattered light from all sources must be virtually eliminated. Second, the cell and

fluorescence collection geometry must be such that one can accurately calculate the fluorescence collection efficiency, α , and the average absorption length, $\bar{x}$, from which fluorescence is observed. These last two values are the only ones not amenable to direct measurement and care must be taken to insure that the calculations are valid.

The scattered light originates from two sources: primary beam scattering and reflected fluorescence. By extending the entrance window 20 cm in front of the fluorescence region via a well baffled tube, the primary scattered light to primary beam intensity was reduced below 10^{-12}. Reflected fluorescence was removed by two means. First, light can be reflected from the wall opposite the fluorescence detector. The wall was eliminated and replaced with a hole, i.e. a baffled tube 20 cm long. Second, light can be reflected off the wall between the laser beam and the fluorescence detector. To reduce scattering from this source, a series of baffles were placed within the tube and the interior of the cell was molded to minimize reflections in the direction of the fluorescence detector. A diagram of the fluorescence cell is shown on Fig. 6. Dimensions are in mm and the extended tubes, all 20 cm long, are not shown.

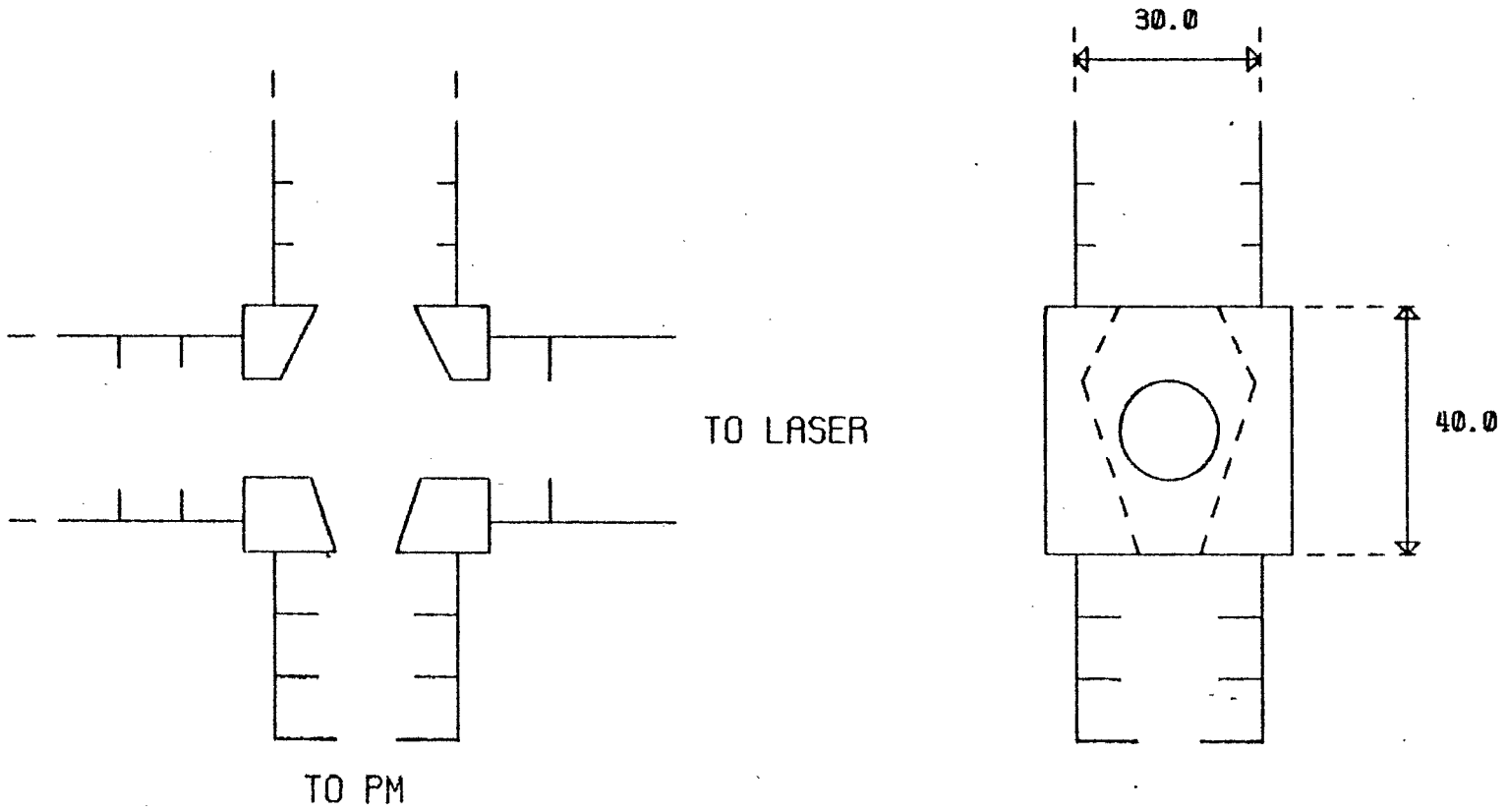

FLUORESCENCE CELL

Figure 6.

Fluorescence collection geometry

From the equation for the quantum yield (Eq. 1) it is found that only the product of the average absorption length, $\bar{x}$, and the collection efficiency, α, is required for the calculation. This is fortuitous because the product is a better defined term than $\bar{x}$ or α. However, each term will be characterized individually first and then the simplified product will be considered.

The quantity $\bar{x}$ is determined by both the laser dimensions and the fluorescence geometry. For purposes of this discussion, the laser beam will be treated as an infinite sheet of height h and no depth. The photomultiplier views emission from a fluorescence region shaped like a long, thin rectangle but with circular ends. This is illustrated on Fig. 7. The radius beyond which no fluorescence is observed is denoted as r_m. The area of the shaded portion of Fig. 7 is given by the equation

$$(3) \quad A(r_m) = 4 \left(\left(h/4 \right) r_m \sin\left(\cos^{-1}\left(h/2r_m \right) \right) + r_m^2 \left(\left(\left(\pi/2 \right) - \cos^{-1}\left(h/2r_m \right) \right) /2 \right) \right).$$

To get the average absorption length, the shaded portion of the figure is approximated by a rectangle of the same area and height. Thus,

$$(4) \quad \bar{x} = A(r_m) / h .$$

In general, the collection efficiency varies over the

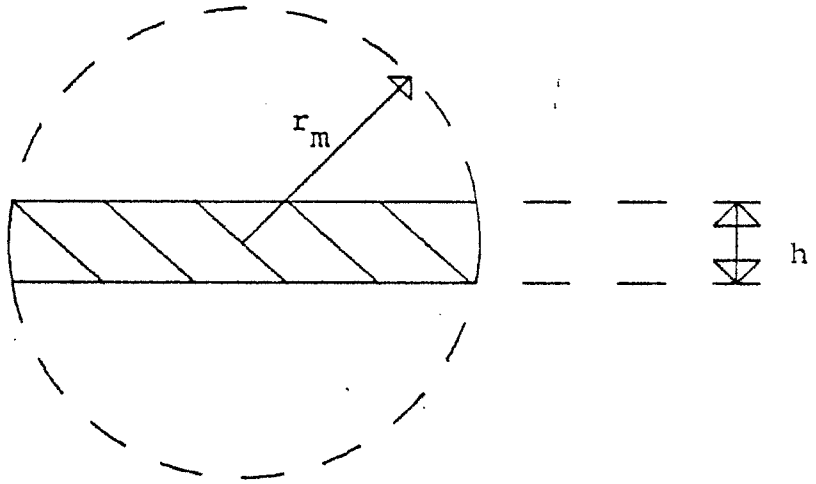

Figure 7. Active absorption region within the fluorescence cell. No fluorescence is observed beyond radius r_m and the laser has a height h.

shaded portion of the last figure. The average is given by integrating α over the entire surface and dividing by the total area. Thus,

(5) $$\alpha = A^{-1}(r_m) \int_S \alpha(s)\, ds .$$

However, for any radius r_k the collection efficiency is the same due to the cylindrical symmetry of the collection geometry. Thus, the surface integral can be changed to a line integral if a weighting factor W(r) is included to give the total arc length of the overlap of the circumference of the circle with the laser sheet. This gives

(6) $$\alpha = A^{-1}(r_m) \int_0^{r_m} W(r)\, \alpha(r)\, dr.$$

Combining Eqs. 4 and 6 yields

(7) $$\alpha \bar{x} = h^{-1} \int_0^{r_m} W(r)\, \alpha(r)\, dr .$$

This simple product formula represents the collection efficiency weighted absorption length. The only thing required is to develop equations for W(r) and $\alpha(r)$ and integrate.

There are two distinct cases in the calculation of the weighting factors:

Case 1: r less than h/2,

Case 2: r greater than h/2.

For case 1, the weighting factor is simply the entire

circumference of the circle with radius r since it lies entirely within the laser sheet. Thus, $W_1(r)=2\pi r$. For case 2, this must be reduced by the fraction of arc length overlapped with the laser sheet. This fraction is simply $(2/\pi)\sin^{-1}(h/2r)$ from which $W_2(r) = 4\ r\ \sin^{-1}(h/2r)$.

A simplified diagram of the collection geometry is shown on Fig. 8. Evaluation of $\alpha(r)$ is divided into two parts. First, the region from r = 0 to r_t is the region from which emission from point r causes no shadow from the first baffle to be cast on the last baffle aperture. The second region is the region of shadow effects, reaching to r_m beyond which point no emission is observed.

In region 1, the collection efficiency is approximated as the ratio of the last baffle aperture surface area to the surface of the entire sphere containing the last baffle with the origin at r. Thus,

$$\alpha_1 = \left(\frac{m}{2}\right)^2 \left[(d+\ell)^2 + r^2\right]^{-1}$$

where

$$r_t = (n\ell - dn - dm)/\ell$$

and n and m are the radii of the first and last baffles, resp.

For region 2, $\alpha(r)$ is approximated as the ratio of the surface area of overlap of the last baffle

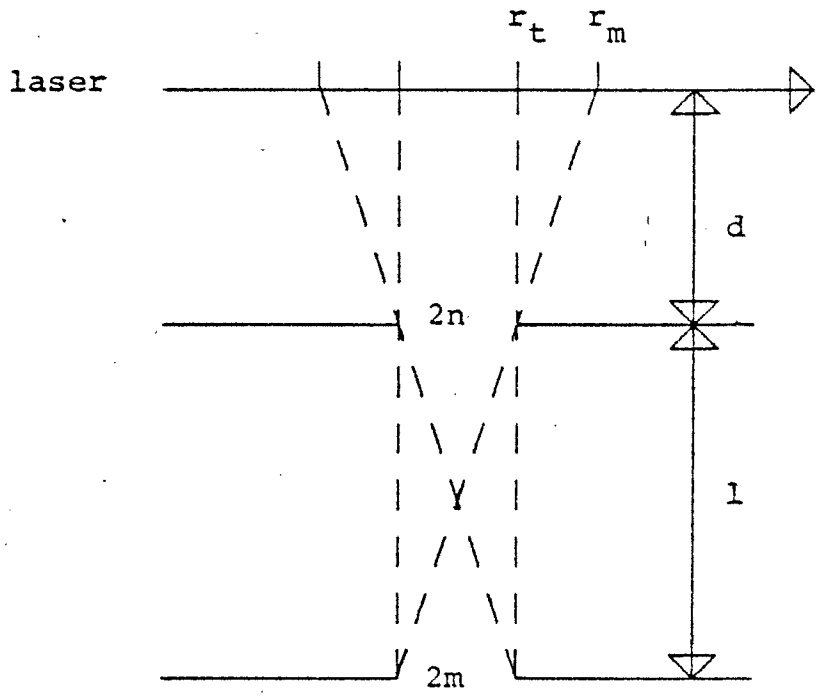

Figure 8. Fluorescence cell emission geometry. The initial aperture has a radius n and the final, m.

aperture and the projection of the first baffle aperture on the last to the surface of the entire sphere containing the overlapped region with the origin at r. Fig. 9 shows the overlapped region at the last baffle schematically. The circle projected from the first baffle has a radius given by $r_y=n(d+1)/d$ and an origin given by $y_o=r(1/d)$. Using half the length of the overlapped area, t, as a parameter defined by

$$t = (m^2 - ((r_y^2 - m^2 - y_o^2)/(-2y_o))^2)^{1/2}$$

the overlapped area is given by

$$a(r) = r_y^2 \sin^{-1}(t/r_y) + m^2 \sin^{-1}(t/m) - y_o t .$$

The collection efficiency in region 2 is then

$$\alpha_2 = \frac{a(r)}{4\pi ((d+1)^2 + (r+r_c)^2)}$$

where

$$r_c = m (1 - (t/m)^2)^{1/2} .$$

Using these equations, the product $\alpha \bar{x}$ was determined by numerical integration. A list of calculated values is given on Table I. Although not amenable to direct measurements, the values can be tested for self-consistency by use of the condition that $I_{fl}/I_{ref}(\bar{x}\alpha)^{-1}$ remain constant, independent of baffle size. Baffles of 7, 8, and 9 $\pm$ 0.01 mm diameter were used and the last equation varied by less than 2%. This reflected the accuracy of the calculation and of the electronics.

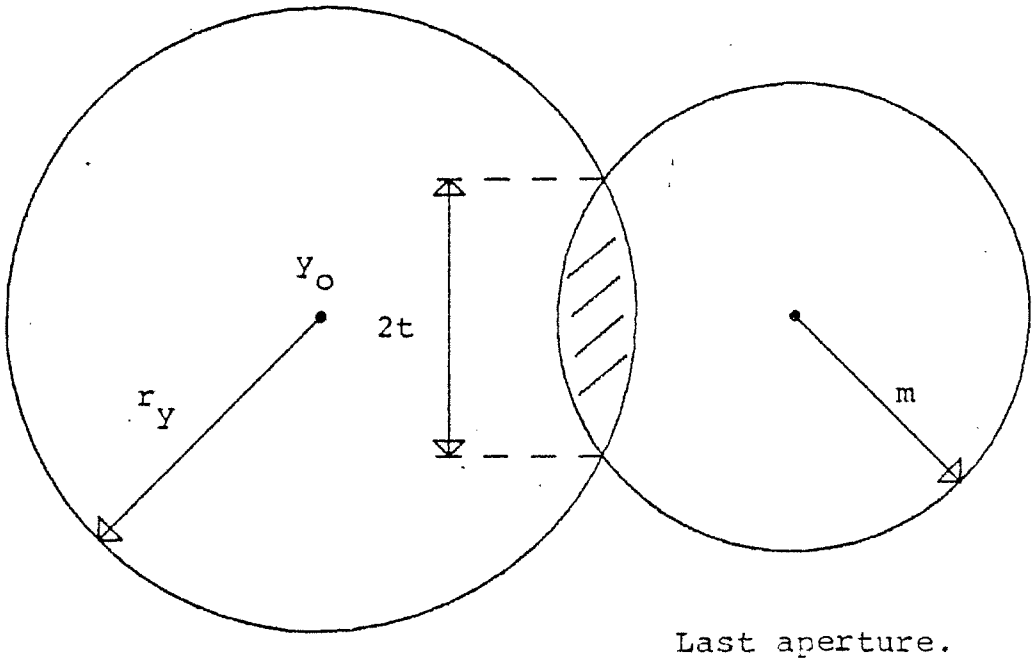

Figure 9. Fluorescence area viewed by the photomultiplier.

Table I

Calculated collection efficiency weighted absorption length of the fluorescence cell

h	m	$(\alpha \bar{x})^{-1}$
2	8	75.43
2	7	98.30
2	6	133.47
2	5	191.84
3	8	75.82
3	7	98.77
3	6	134.21
3	5	192.87
4	8	76.39
4	7	99.54
4	6	135.15
4	5	194.17

(d=20.0 , l=42.5 , n=9 mm)

The absorption cell

From the equation for the quantum yield, it is found that one requires the absolute absorption coefficient. For many molecules, including naphthalene, the absorption coefficient is very small. An accurate determination of ϵ in the low pressure gas phase requires long path lengths. Hence, a multiple path absorption cell was used.

The optical system employed a Perkin-Elmer 10 meter gas cell mirror assembly. The mirrors were coated for optimal transmission in the UV. The cell and mirror mounts were constructed in house from stainless steel. The cell was sealed with grease-free O-rings and could be evacuated to pressures of ca. 10^{-6} torr. The leak rate (virtual plus real) was 1 mtorr per day.

The absorption cell path length could be varied according to the equation

$$d = 1267 + (n - 1) 1240 \text{ mm}$$

where n was the pass number which assumed values from 1 to 10. When used in conjunction with the fluorescence cell, the total path length was increased by 448 mm.

A drawing of the absorption cell is shown on Fig. 10. Mirror A had a fixed focal point at A′ and mirror B, a movable focal point at B′. The condition that light which enters the cell at the entrance will leave

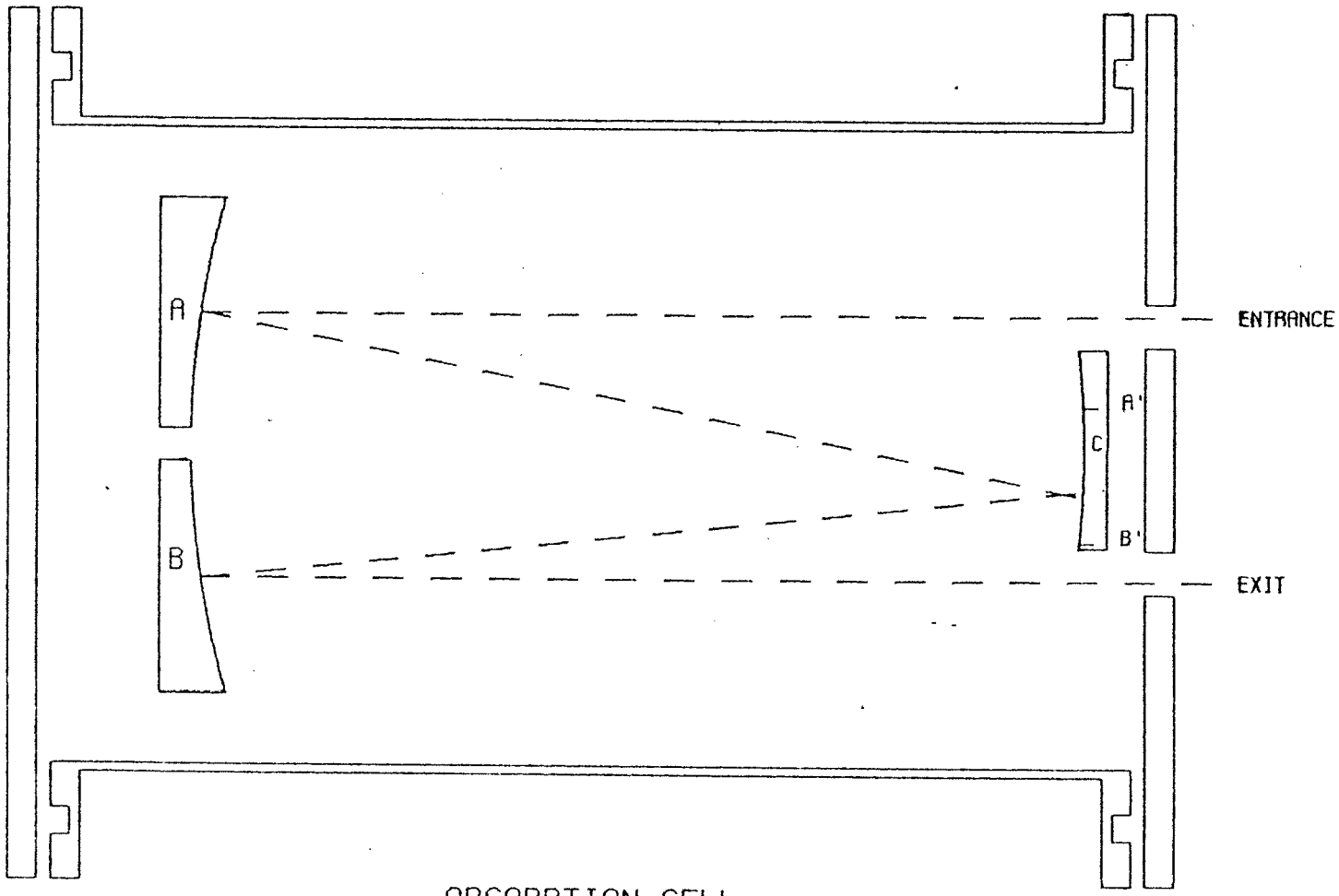

ABSORPTION CELL

Figure 10.

the cell at the exit is fulfilled when the following equation is satisfied:

$$B' - A' = X / 2n$$

where n is an integral pass number and X is the length between the entrance and exit. The focal points shown on Fig. 10 are for n=1. Values of n=3 or 4 were used in the experiments. Mirror B could be adjusted from outside the cell via a welded bellows feedthrough.

The vacuum system employed only Nupro stainless steel welded bellows valves, stainless steel Swagelok fittings and tubing. A Balzers type ECM 68/4 vacuum pump was used and pressure measured with an MKS Baratron type 144 differential pressure guage employing a type 77 pressure head.

Photomultiplier characteristics

Introduction

The photomultipliers and their voltage dividers were necessarily the most important components of the quantum yield and lifetime experiments. Thus, they were subjected to many tests for linearity, gain stability and time response. As a result, several tubes and dividers were rejected. In the following sections, the tests and their results, as well as several other factors relating to the photomultipliers, are discussed in detail.

Photocathode spectral response

The spectral shift in fluorescence relative to excitation wavelength can cause systematic errors in the measurement of quantum yields. This comes from the fact that photocathode sensitivity changes with the wavelength of the detected light. An Amperex 56 DUVP was employed as the fluorescence detector. In the UV the spectral response of this tube sharply increases with wavelength. The spectral shift thus gives rise to quantum yields which are too high.

In order to eliminate the effect of the spectral shift, quantum converters were used. Sodium salicylate was chosen because of its high quantum yield of 53% and constant response in the UV from 2500 to 3500 Å.[3] A thin film of about 1 mg/cm^2 was deposited on a Schott edge filter from a spray containing sodium salicylate in a methanol solution. The edge filter passed only the emission of the quantum converter and absorbed any UV passing through the film. Since the converters emit into a solid angle of 4π , the photocathodes of all tubes were always fully illuminated.

No quantum yield experiment should employ the direct spectral response of the PM without allowing for the fact that the emission is usually red shifted relative to absorption wavelength. Quantum yields were measured with and without converters. In each case the

yield without converters was about 10% too high. For example, the effective high pressure quantum yield of naphthalene was 18% with and 22% without the converters.

The finite lifetime of the converter emission could, in principle, alter the observed molecular decay curve. However, measurements with and without converters gave the same lifetime down to 150 nsec, the fastest decay measured in these experiments.

Surface sensitivity

Small surface sensitivity variations along the quantum converters could be measured. For the 1P28's the laser was always directed toward an area of constant sensitivity. For the 56 DUVP, a mask allowed only the center of the converter (17 mm diameter) to view the fluorescence. The sensitivity of this area showed variations of 5% which were reproducable and could thus be averaged.

Voltage dividers

The Amperex 56 DUVP employed a modified EG&G positive high voltage divider (B56 AVP - 1R). In order to measure the fluorescence decay curve and simultaneously obtain the integrated current, the divider was modified as shown on Fig. 11.

The anode signal was input to the integrator and the dynode signal, to the WP2221 for acquisition of the decay curves. A series of tests using variable length pulses showed that the anode and the dynode gave the

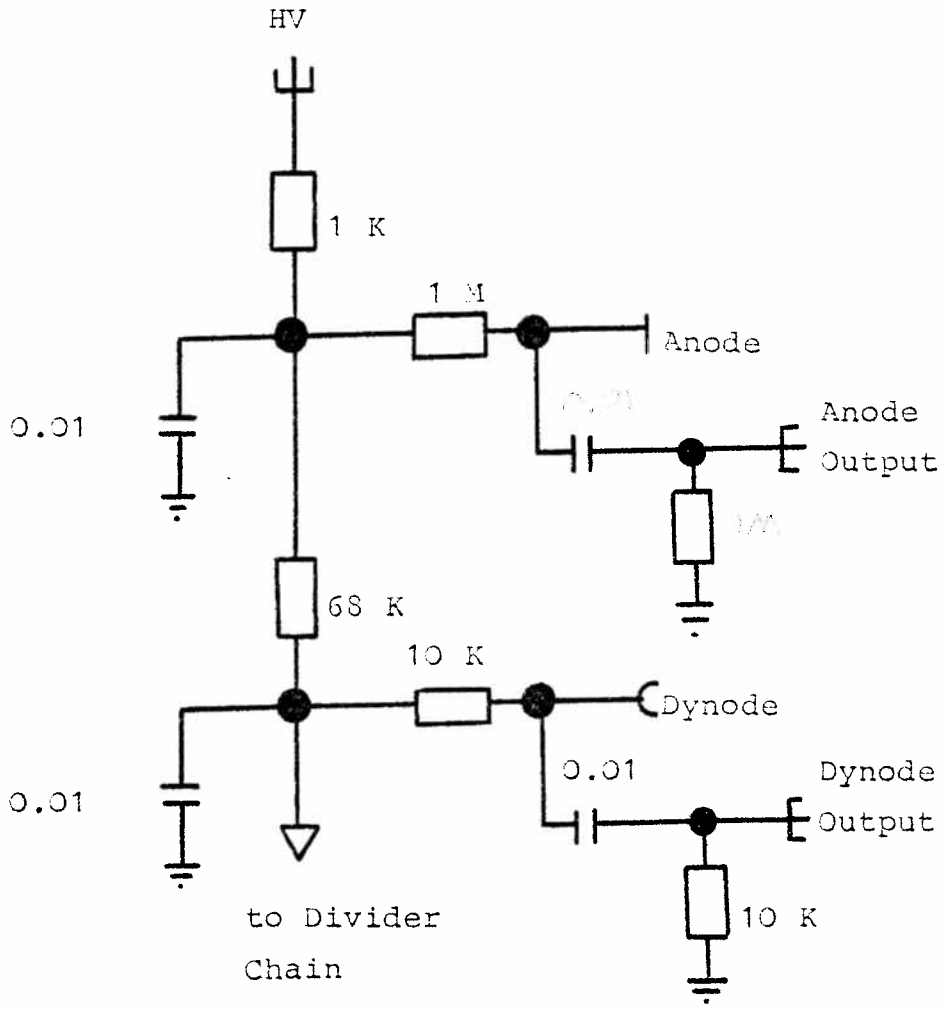

Figure 11. Modified section of 56 DUVP voltage divider.

same time response curves. Only the curve height and pulse polarity were different.

The complete voltage divider of the 1P28 is shown on Fig. 12. The 1P28's were used only for measuring integrated currents and the time response was not tested except as explained in the next section on linearity.

Photomultiplier linearity

Direct measurement of the time and intensity characteristics of laser induced emission requires detectors which are linear to large currents. Even weakly absorbing molecules can produce intense emission. For example, excitation of the S_1 state of naphthalene in the gas phase can give rise to 10^6 photons per laser pulse striking the photocathode. If the photomultiplier has a gain of 10^6, a decay signal of 1 volt (20 ma in 50 ohms) can be directly viewed on the oscilloscope. Linearity is rarely guaranteed to currents of this magnitude and one is required to measure it in the laboratory.

The most common technique of linearity calibration is that of neutral density filters (NDF). Insertion of an NDF between a light source and the PM causes a reduction in current output. As long as the decrease is proportional to the optical density of the NDF, the tube is linear. Thus, deviations from proportionality directly measure non-linearity. It has the drawback that small deviations from and thus the onset of non-

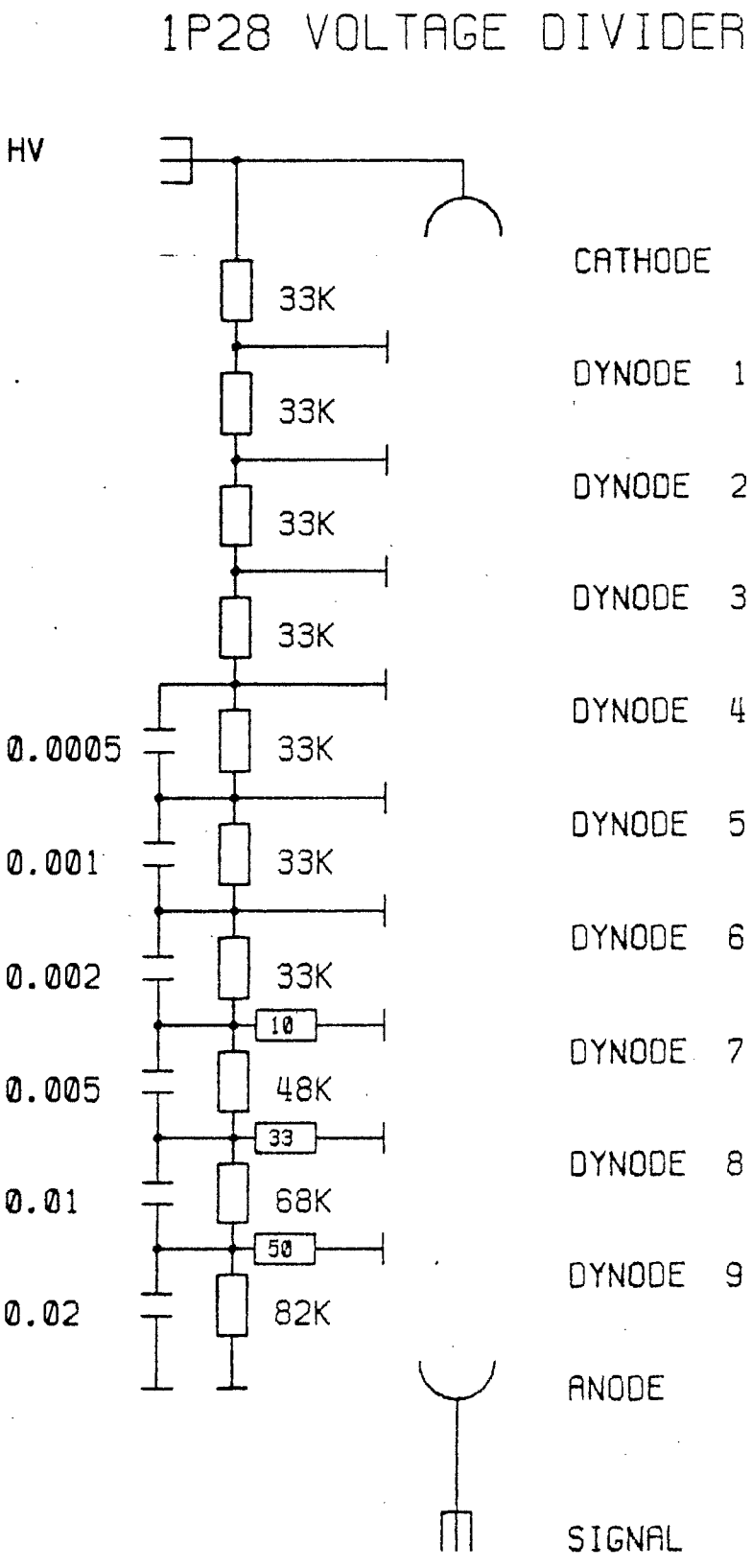
1P28 VOLTAGE DIVIDER
HV
CATHODE
33K
DYNODE 1
33K
DYNODE 2
33K
DYNODE 3
33K
DYNODE 4
0.0005
33K
DYNODE 5
0.001
33K
DYNODE 6
0.002
33K
10
DYNODE 7
0.005
48K
33
DYNODE 8
0.01
68K
50
DYNODE 9
0.02
82K
ANODE
SIGNAL

Figure 12.

linearity are difficult to determine. Because of this, several new techniques have been developed.

The concept involved in the next two techniques is the same. A short light pulse of constant intensity was superimposed on a longer pulse of variable intensity. A change in the amplitude of the short pulse as the long pulse intensity was varied measured the linearity. Hunt, et al.[4] superimposed a 2-50 nsec pulse from a PEK barium titanate lamp on a shuttered 20-100 msec pulse from a tungsten iodide lamp. Fenster, et al.[5] superimposed a 50 microsecond pulse (rotating mirror) on a 30 msec pulse, the same tungsten lamp being used as the light source. The intensity of the long pulse was varied with NDF's. The primary drawback of this technique is the length of the shortest pulse obtainable from convential shutters. For PM's operated at high gain, a pulse of 20 msec could easily damage or fatigue the tube. In addition, if one is observing signals shorter than a microsecond, the onset of non-linearity may be different from that measured at a millisecond.

These objections also apply to the method of Ellison and Wilkenson[6] who used a pulsed Xenon lamp to give a 5 msec pulse with a spike. NDF's were used to vary the total intensity and variations in the spike to base pulse height ratio were taken as a measure of the non-linearity.

A block diagram of the setup of our technique is shown on Fig. 13. Two pulse generators (HP 214 A) each drove a light emitting diode (LED). The LED was connected in series with a 47 ohm resistor and parallel to a 200 ohm resistor to approximately correct for the non-linear resistance of the LED and to properly terminate the pulse generator. The LED's were placed as close to each other as possible (about 3 mm between centers) and directed toward the photocathode of the PM under test. Pulses to the LED's were delayed in time from each other by means of the internal delay of the pulse generators. By observing the two pulses on an oscilloscope, the pulse heights and widths were adjusted to be equal. This usually required a different voltage for each LED due to differences in manufacture. The pulse height was recorded and the delay then adjusted so that the LED's fired simultaneously. At this point, only one pulse was observable on the oscilloscope and if the PM was linear, the pulse height was exactly two times that of the consecutively fired pulses. In general, deviations as small as 1-2% were observable with sensitivity limited only by the linewidth shown on the oscilloscope.

The LED's used were Monsanto MV-52's which emitted in the green. They were chosen over red LED's since the PM's used in the experiments displayed maximum

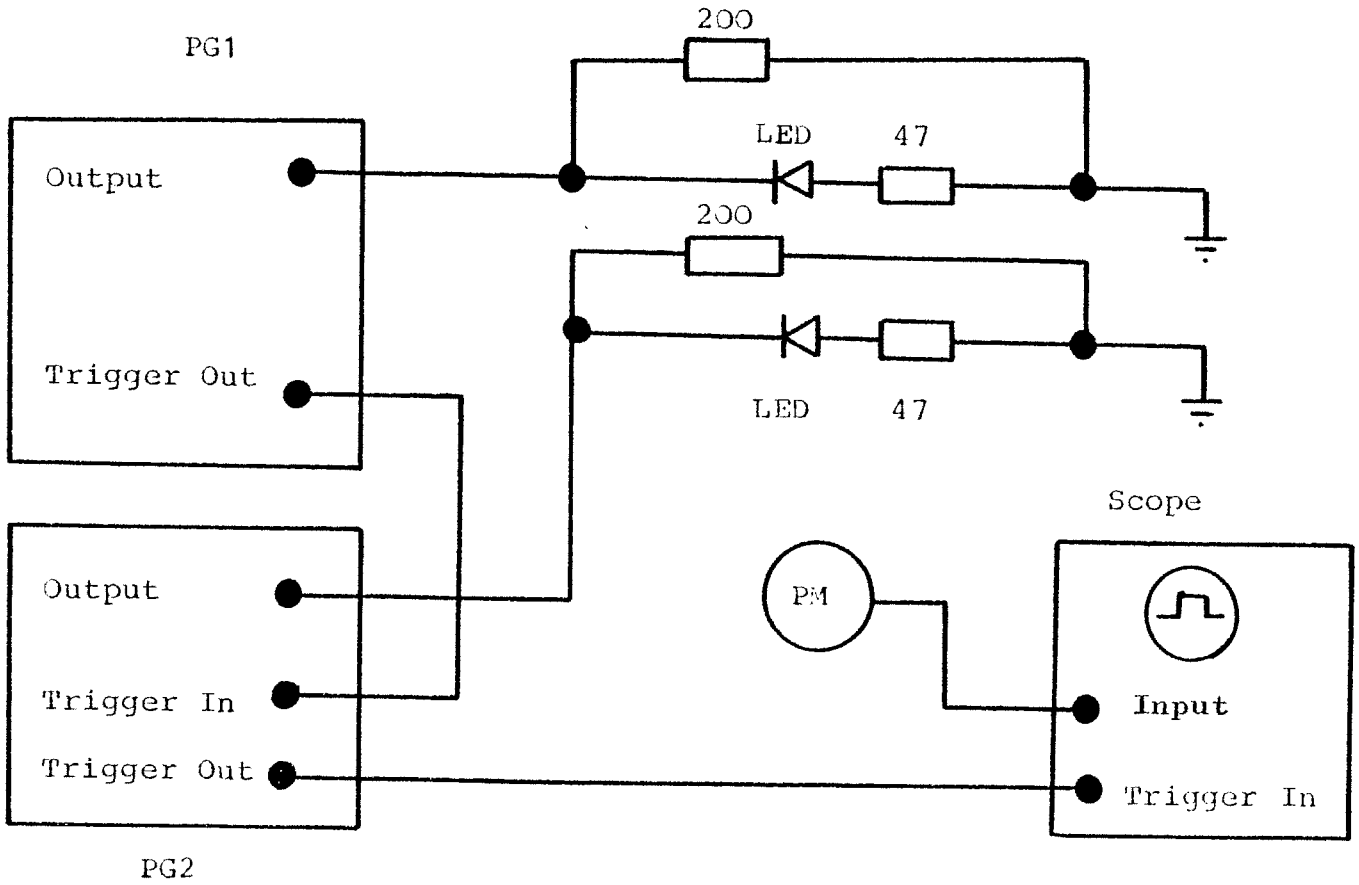

Figure 13. Setup for PM linearity calibration.

sensitivity in the green and thus required lower currents through the LED's to obtain the same response.

In the linearity calibration of tubes with a gain of less than 10^5 it was found that the HP pulse generators were unable to produce enough current through the LED's to drive the PM's into the non-linear region. One of the LED's was then replaced with three driven in series by a Velonix model 350 pulse generator. Using this method, any PM could be driven into the non-linear region. The 2000 volt (10 A in 200 ohm) pulses of 1 microsecond produced no deterioration or breakdown of the LED's at the normal pulse rate of 40 Hz.

For the experiments reported here, two different PM's were employed. The 56 DUVP was linear to 100 ma for the high voltage range from 1500 to 2100 volts. The 1P28's were linear to at least 30 ma in the range from 750 to 1150 volts. The exact results for all tubes are given on Table II. The linearity curve at 1100 volts for the 1P28 is shown on Fig. 14. During all experiments the signal was kept within the linear region of all PM's.

PM gain stability

The gain stability of each tube was tested with a setup similar to that shown on Fig. 13 but with only one LED and pulse generator. The response of the PM's to a fixed light level was monitored for a period of

Table II

Linearity of Photomultipliers

Reference 1P28		Transmission 1P28		Fluorescence 56 DUVP	
-HV	V_1	-HV	V_1	HV	V_1
750	1.75	750	1.7	1500	5.0
850	2.5	850	2.5	1600	5.5
950	1.5	950	1.5	1700	6.0
1050	1.5	1050	1.5	1800	6.0
1150	2.0	1150	1.8	1900	6.5

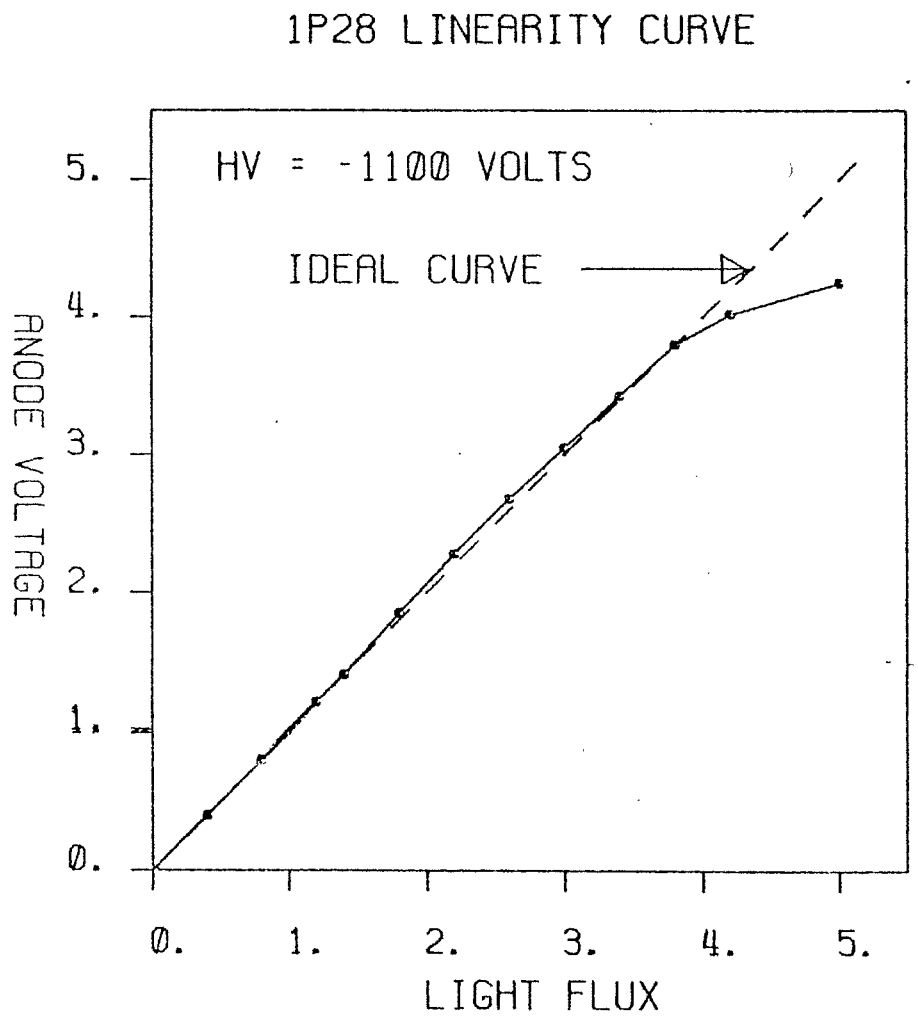
1P28 LINEARITY CURVE
HV = -1100 VOLTS
IDEAL CURVE
ANODE VOLTAGE
5.
4.
3.
2.
1.
0.
0.
1.
2.
3.
4.
5.
LIGHT FLUX

Figure 14.

about a day. During this time the high voltage was changed or turned off and on. Only those tubes which repeatedly gave the same signal at the same high voltage setting were retained.

The 1P28's, however, were always unstable above 1200 volts. This came from overheating of the voltage divider which changed the resistance of the divider chain. From 750 to 1150 volts the tubes showed a stable gain.

PM relative gain.

The relative gain of the reference and fluorescence photomultipliers (D_{ref}/D_{fl} in Eq. 1) was the most critical parameter measured. The laser intensity was sufficient to produce a 1 volt signal from a photodiode placed in the reference position. However, attempts to compare absolutely the response of a photodiode with a photomultiplier of gain 10^6 resulted in values with very large error limits.

It was thus decided to replace the photodiode with a photomultiplier. The collection geometry of the 1P28 is shown on Fig. 15. The actual gain of the tube was 10^6 but the effective gain was about unity. This was achieved by placing the quantum converter far from the photocathode, thus reducing the solid angle for collection of converter emission. In addition, visible filters were placed behind the converter.

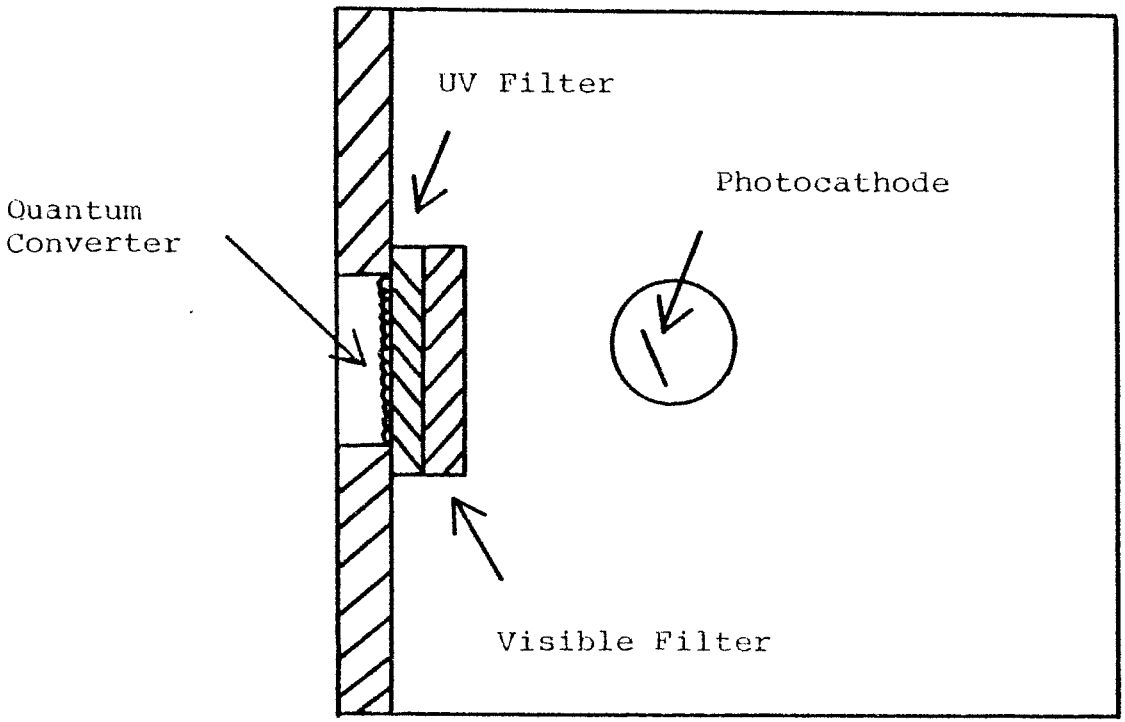

Figure 15. Collection geometry for the 1P28.

The filters were calibrated absolutely using the emission of the sodium salicylate film to an accuracy of 1%.

The relative gain of the tubes could then be measured with converters in place and filters removed. The integrated signal from each tube was measured relative to the same photodiode. From these measurements the relative gain could be easily determined and then adjusted for filter transmission. The final value had a standard deviation of 3%.

Electronics

The determination of quantum yields required the integrated current of each PM. Since the anode of a photomultiplier is a nearly ideal current source, the current could be integrated on a capacitor to give a voltage according to the equation

$$V = C^{-1} \int i(t)\, dt.$$

Normally, capacitors of 10 nF were used and the voltage followed with an FET operational amplifier. Including associated circuit components, the input impedance was 10^6 ohms. This gave a time constant of 10 msec. The output of the follower was given to a 20 dB amplifying sample and hold (S/H) with a time window of 20 microseconds. A schematic excluding trigger circuitry is shown on Fig. 16.

The same trigger circuitry was used to drive 3

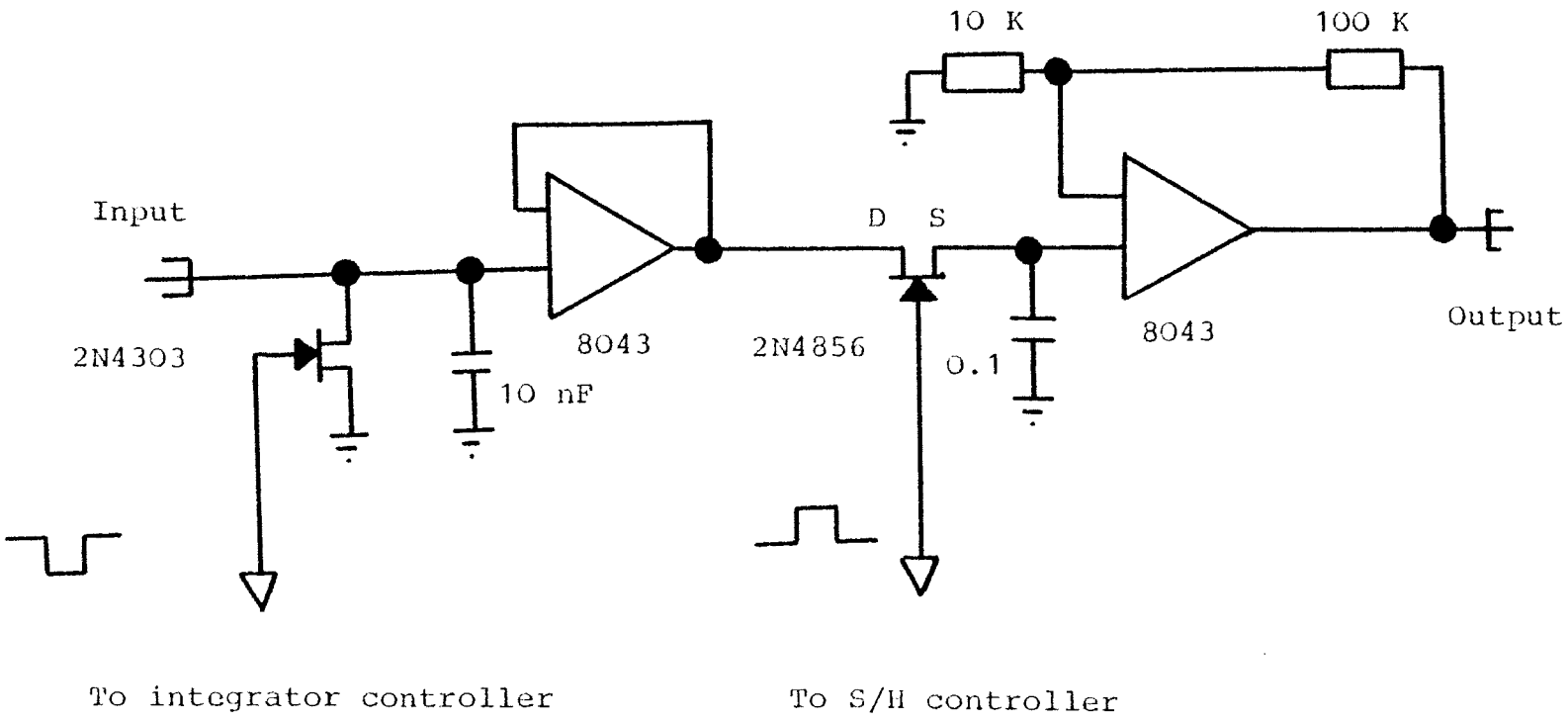

Figure 16. Current integrator schematic.

integrator and S/H circuits, one for each PM shown on Fig. 1. The S/H circuits had time constants of 100 sec. The outputs were multiplexed and converted to digital form for transfer to the PDP 11/45 for on-line calculation. A description of the interface is given in Appendix 1.

Appendix 1

Quantum Yield Interface to the PDP 11/45

The quantum yield experiment was connected to the PDP 11/45 via the DR11-C interface card. The three registers of the card were used as follow:

Output word:	Low byte	LED register
	High byte	Multiplexer address
Input word:	Bits 0-11	ADC output
	Bits 12-15	Switch register
Status word:	CSR0	Start ADC conversion
	Int. B	End of conversion
	CSR1	Computer trigger command
	Int. A	Trigger from experiment
	Data trans.	Clear all interupts

A block diagram of the interface electronics at the experiment is shown on Fig. 17. The integrated signals were input to a 5 channel multiplexer. The channel to be output was selected via the address given in the low byte of the DR11-C output word. The output of the multiplexer was converted to digital form by the ADC which was edge triggered with the CSR0 signal. End of conversion resulted in the setting of the interupt B bit of the status word. The interupt was automatically cleared with the data transmitted signal which implied that the input word had been read by the

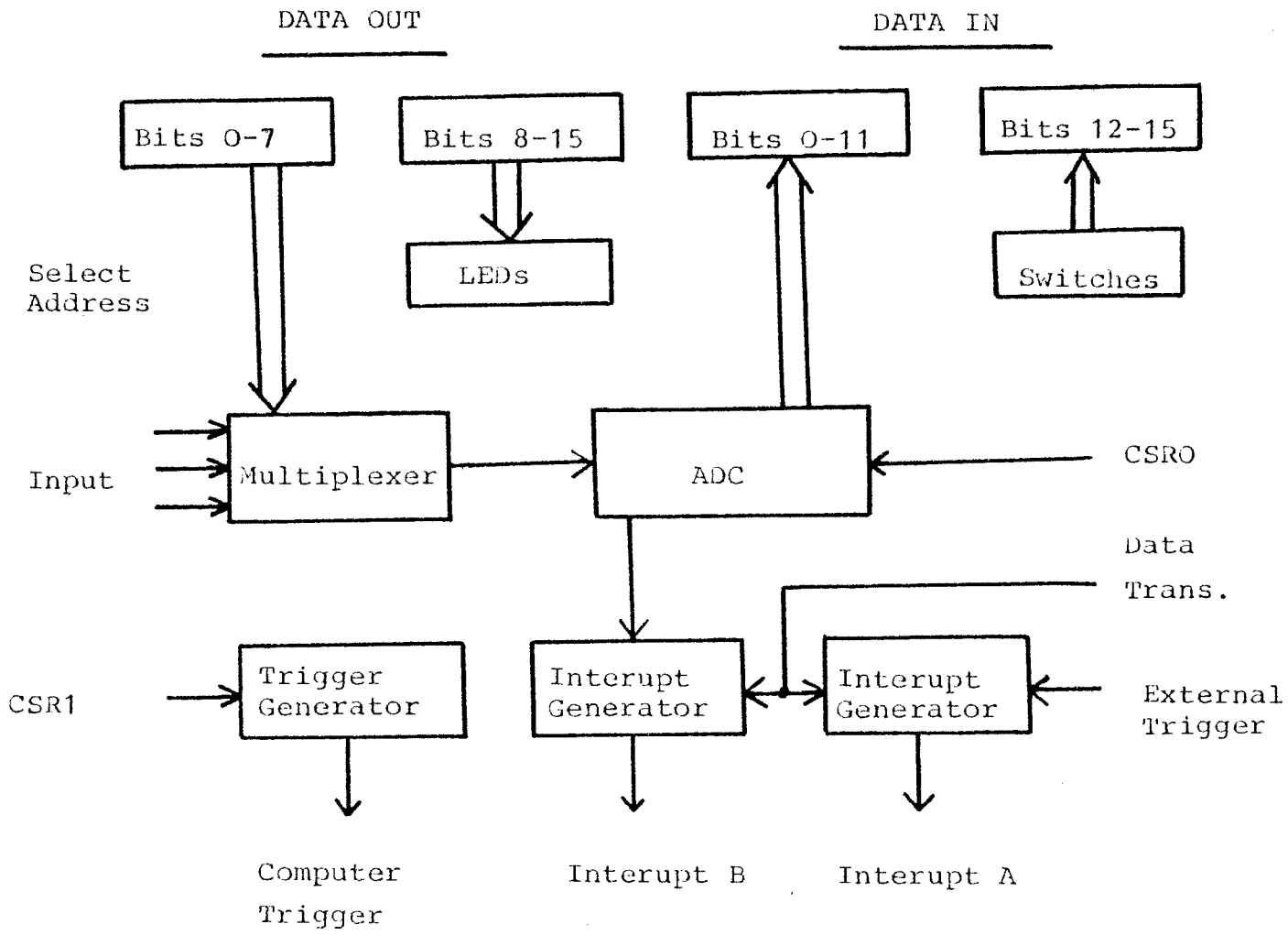

Figure 17. Quantum yield interface to PDP 11/45.

computer. At this point, a new multiplexer address was selected and the cycle repeated until all channels were read.

Reading and writing on the DR11-C card was controlled by the DRC device handler. Access by Fortran programs was allowed through the following subroutines:

SETLED: set a bit pattern in the LED's,

SWITCH: read the switch register,

MULTPX: multiplex through n channels and read the output of the ADC and the switches,

ROTATE: set the handler idle condition.

When in the idle condition, the quantum yield monitor program could be requested by setting octal code 17 in the switch register and generating interupt A. The monitor, DRM1, was used to request that a program be run via a directive to the RSX 11-D executive. The program name was of the form "DR1MXX" where the XX value was acquired via a read switch request to the DRM handler. XX could range from 1 to 16, octal. The code of 0 resulted in monitor exit and the code of 17 was ignored. A list of the programs used follows:

DR1M04: Collect transmission data of empty cell.

DR1M05: Collect relative integrator gains.

DR1M06: Collect excitation and absorption spectra.

DR1M07: List calibration files.

DR1M10: Monitor single shots.

DR1M11: Average multiple shots.

DR1M13: Collect relative PM gains.

DR1M15: Initialize calibration data.

DR1M16: Collect quantum yield and absorption spectra.

Appendix 2

WP2221 interface to the PDP 11/45

The PDP 11/45 was connected to the WP2221 via a pseudo-PP/PR interface. Both computers contained the PC11 paper tape reader/punch interface cards which were connected as shown in the following diagram.

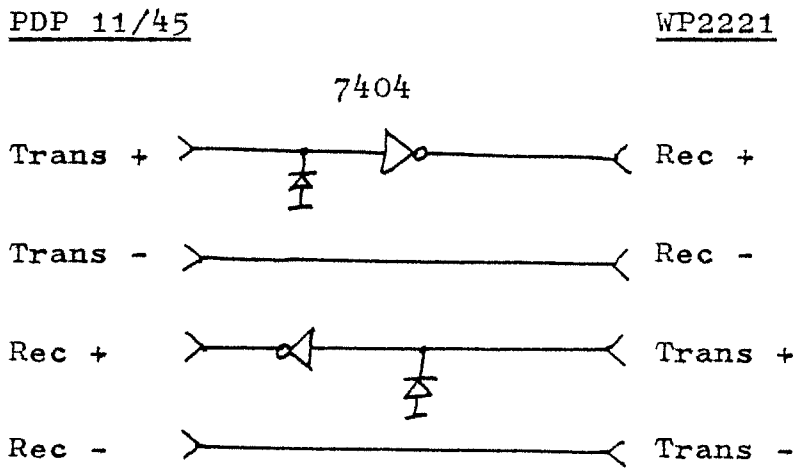

Thus, each computer interpreted the other as the paper tape device.

The WP2221 system used a modified BASIC programming language. The input/output device was specified by the variable "OD" which was zero for the teletype and unity for the paper tape. Data transfer was thus limited to data in ASCII. Data from the PDP 11/45 could be read by the WP2221 by issuing commands of the form:

```
LET OD=1 : INPUT X : LET OD=0 .
```

Data could be written to the PDP 11/45 by issuing commands of the form:

```
LET OD=1 : PRINT Y : LET OD=0 .
```

Data transfer in and out of the PDP 11/45 was achieved via the following special programs:

OLD: This program read and stored on disk the program transfered by issuing the "SAVE" command on the WP2221.

WPS: When the "OLD" command was issued on the WP2221, this program would transfer a BASIC program out of the PDP 11/45.

PRN: This was the device handler which coordinated all input/output with the PC11 interface card of the PDP 11/45.

The handler could be accessed via 3 Fortran subroutines:

WPWRIT: output a number,

GETARR: input a number or array,

GETMSG: input an ASCII string.

Data was read as fast as it was written by the WP2221. However, data was written at a rate of 50 ASCII characters per second.

When the PRN handler received a control-X from the WP2221 a monitor program, WPM, was loaded in the PDP 11/45 which would issue a read command to the handler and wait for input from the WP2221. The ASCII string input would then be scanned and action taken based on the following criteria:

1) If the command was of the form " RUN XXXXXX", the monitor would attempt to load the requested program

from the disk into core and run it.

2) If the command was "EXIT", the monitor would exit.

3) Any other command was treated as a remark and spooled to the console log.

This feature allowed the user to dynamically run any program from the WP2221 console under the BASIC operating system. The program of most importance was LT2221 which calculated the lifetime of the decay curve collected on the WP2221.

References to Chapter III

1. U. Bösl, H. Neusser and E. W. Schlag, Chem. Phys. Lett. 31, 1 (1975).
2. U. Bösl, private communication.
3. H. G. Küttner, H. L. Selzle and E. W. Schlag, Z. Naturforsh., 29a, 224 (1974).
4. J. W. Hunt, et al., Int. J. Rad. Phys. Chem. 4, 87 (1972).
5. A. Fenster, et al.,Rev. Sci. Inst.,44, 689 (1973).
6. D. H. Ellison and F. Wilkinson, Int. J. Rad. Phys. Chem., 4, 389 (1972).

Chapter IV

Historical: Structure in Non-radiative Processes

For many years, the nature of radiative processes has been well understood. Structure in optical absorption or emission spectra has been explained in terms of the electronic, vibrational and rotational states of the molecule which are coupled via the dipole operator.[1] The case of radiative transitions between singlets and triplets requires consideration of the spin states.[2]

The role of the various quantum states in non-radiative processes has, however, not been so well understood. This is primarily a result of the difficulty in measuring the effects which give insight to the internal processes of an excited molecule.

The first lifetime spectrum of a molecular system in the gas phase was make by Schlag and v. Weyssenhoff in 1969 on ß-naphthylamine.[3] The measured spectrum showed that the lifetime monotonically decreased with increasing excitation energy through S_1 and S_2. Previous to this experiment, only the work of Kistiakowsky and Parmenter[4] on the low pressure quantum yield of benzene existed as positive evidence that intersystems crossing was a true intramolecular process. The lifetime spectrum of ß-naphthlyamine demonstrated not only this but also that the rate constant was dependent on the excitation energy.

Quantum yield measurements were made on naphthalene in the gas phase by Uy and Lim in 1970[5]. With a resolution of 10 Å, the quantum yield was observed to vary over the entire $S_1 \leftarrow S_o$ absorption region with a tendency to decrease toward higher excitation energies. A subsequent measurement by Lim and Uy[6] with a resolution of 50 Å indicated that the non-radiative rate increased monotonically with excitation energy. Measurements by v. Weyssenhoff and Kraus[7] on aniline, however, showed a very structured quantum yield spectrum.

An interpretation of the results is more straightforward if the measurements of quantum yields and/or lifetimes are related to the energy of the excited state instead of the excitation energy. This requires, as a minimum, excitation of single vibronic levels (SVL) with the results given as a function of excess energy above the origin of the excited electronic state.

The first comprehensive study of the quantum yields and lifetimes for single vibronic levels of benzene was made by Spears and Rice[8] although Parmenter and Schuyler[9] were the first to measure SVL yields and Selinger and Ware[10], to measure SVL lifetimes. The final results of Spears and Rice gave non-radiative lifetimes as a function of excess energy. The lifetimes linearly decreased with energy in modes $\nu_1(a_{1g})$ and $\nu_6(e_{2g})$ and showed a much sharper falloff for levels

containing $\nu_{16}(e_{2u})$, $\nu_{10}(e_{1g})$, $\nu_{11}(a_{2u})$ or $\nu_{5}(b_{2g})$. Two photon measurements by Wunch, Neusser and Schlag[11] showed that progressions of the $\nu_{14}(b_{2u})$ have non-radiative lifetimes which parallel the ν_1 and ν_6 values but are generally 20 nsec longer while progressions of the $\nu_{18}(e_{1u})$ also parallel ν_1 and ν_6 but are about 20 nsec shorter.

The first SVL lifetime data on naphthalene by Schlag, Schneider and Chandler[12] showed an overall decrease in lifetime with increasing excess energy. The observation of significant fluctuations of the lifetime spectrum was of a similar nature to the results on benzene[8] but in direct contrast to the work of Hsieh, Laor and Ludwig[13] on naphthalene. The latter found a smooth decrease in lifetime with excess energy. However, their use of an excitation bandpass of 100 cm^{-1} precluded the excitation of single vibronic levels.

High accuracy lifetime measurements on naphthalene by Knight, Selinger and Ross[14] with a bandpass of 6-10 cm^{-1} showed marked fluctuations as a function of excess energy. Lifetime measurements with a resolution of 0.5 cm^{-1} by Boesl, Neusser and Schlag[15] and quantum yield measurements by Stockburger, Gattermann and Klusmann[16] substantiated the reality of the fluctuations. These experiments demonstrate that the nature of the excited vibrational state plays an important role in

ISC and not just the energy of the state as indicated by earlier experiments.

The influence of rotational state selection on intramolecular processes was investigated by Parmenter and Schuh in 1972[17]. Fluorescence quantum yields were measured at various positions along the rotational contours of 4 different vibrational levels of benzene. To within the stated accuracy of 10%, no dependence of the yield on the rotational distribution was found.

In contrast to these results, measurements by Boesl, Neusser and Schlag[15] along the rotational contour of the 0-0 band in naphthalene, h_8 revealed strong structure in the lifetime spectrum. The maximum lifetime of 310 nsec was observed to coincide with the maximum of the absorption spectrum. This was the first observation of a rotational effect on the non-radiative process of ISC in a large molecule.

Formaldehyde is an interesting example because it has observable triplet states and many pure ro-vibronic levels can be seen in the $S_1 \leftarrow S_o$ absorption spectrum. Unfortunately, lifetimes for this molecule have only been measured with low resolution, revealing only single vibronic levels.[18,19] However, rotational structure has been seen via S-T perturbations in the Zeeman spectrum. Energy displacements and line broadening of dispersed absorption lines have been explained via spin-

rotation coupling in the $2^1 4^1$ vibrational state of $^1A_2$ with the final triplet[20,21].

Recent measurements on formaldehyde by Tang, Fairchild and Lee[22] have achieved excitation of single rotational levels of the $2^3 4^1$ vibrational state of S_1. The results indicate a very strong variation in the fluorescence quantum yield as a function of rotational excitation. The variations of over a factor of 4 have been attributed to variations in $S_1 - S_o$ coupling. The results display no apparent correlation with J or K and point to a very specific energy dependent coupling scheme.

Lifetimes of diatomics have been measured and variations of the lifetimes have been attributed to the onset of predissociative processes. For example, OH, OD and CH have been excited to single ro-vibronic levels. CH excited to the $C^2\Sigma^+$ level showed a smooth increase in the lifetime with J (5.6 μsec at J=2 to 9.0 μsec at J=23)[23]. OH showed irregular but reproducable lifetime structure at low J and sharply decreased at high J[24,25]. Rotational and vibrational effects have also been observed for Br_2[26,27] and ICl[28].

The results of the measurements on diatomics show that a rotational dependence exists for the non-radiative process of predissociation. The results on formaldehyde indicate rotational structure in IC.

The results on naphthalene point to a dependence in ISC. Thus, the experimental evidence supports the view that, as in the case of optical excitation, non-radiative processes depend upon the nature of the states which are excited: electronic, vibrational and rotational. More data will be brought to bear on this point in the next chapter.

References to Chapter IV

1. G. Herzberg, Electronic Spectra and Electronic Structure of Polyatomic Molecules, (Van Nostrand, Princeton, N.J., 1966).
2. F. Creutzberg and J. T. Hougen, J. Mol. Spec., 38, 257 (1971).
3. E. W. Schlag and H. v. Weyssenhoff, J. Chem. Phys., 51, 2508 (1969).
4. G. B. Kistiakowsky and C. S. Parmenter, J. Chem. Phys., 42, 2942 (1965).
5. J. O. Uy and E. C. Lim, Chem. Phys. Lett., 7, 306 (1970).
6. E. C. Lim and J. O. Uy, J. Chem. Phys., 56, 3374 (1972).
7. H. v. Weyssenhoff and F. Kraus, J. Chem. Phys., 51, 2508 (1969).
8. K. Spears and S. A. Rice, J. Chem. Phys., 55, 5561 (1971).
9. C. S. Parmenter and M. W. Schuyler, Chem. Phys. Lett., 6, 339 (1970).
10. B. K. Selinger and W. R. Ware, J. Chem. Phys., 52, 5482 (1970).
11. L. Wunch, H. J. Neusser and E. W. Schlag, Chem. Phys. Lett., 32, 210 (1975).
12. E. W. Schlag, S. Schneider and D. W. Chandler, Chem. Phys. Lett., 11, 474 (1971).
13. J. C. Hsieh, U. Laor and P. K. Ludwig, Chem. Phys. Lett., 10, 412 (1971).
14. A. E. W. Knight, B. K. Selinger and I. G. Ross, Aust. J. Chem., 26, 1159 (1973).
15. U. Boesl, H. J. Neusser and E. W. Schlag, Chem. Phys. Lett., 31, 1 (1975).
16. M. Stockburger, H. Gattermann and W. Klusmann, J. Chem. Phys., 63, 4529 (1975).

17. C. S. Parmenter and M. D. Schuh,
Chem. Phys. Lett., 13, 120 (1972).
18. E. S. Yeung and C. B. Moore,
J. Chem. Phys., 58, 3988 (1973).
19. R. O. Miller and E. K. C. Lee, preprint.
20. J. C. D. Brand and C. G. Stevens,
J. Chem. Phys., 58, 3331 (1973).
21. J. C. D. Brand and D. S. Liv,
J. Phys. Chem., 78, 2270 (1974).
22. K. Y. Tang, P. W. Fairchild and E. K. C. Lee,
J. Chem. Phys., 66, 3303 (1977).
23. N. Elander and W. H. Smith,
Astrophys. Journal, 184, 663 (1973).
24. E. G. Elmergreen and W. H. Smith,
Astrophys. Journal, 178, 557 (1972).
25. W. H. Smith, B. G. Elmergreen and N. H. Brooks,
J. Chem. Phys., preprint.
26. K. B. McAfee, Jr. and R. S. Hazack,
J. Chem. Phys., 64, 2491 (1976).
27. F. Zaraga, N. S. Noger and C. B. Moore,
J. Mol. Spec., 63, 564 (1976).
28. C. D. Olson and K. K. Innes,
J. Chem. Phys., 64, 2405 (1976).

Chapter V
Experimental Results

Introduction

Using the apparatus described above, the fluorescence quantum yields of naphthalene, h_8 have been measured along the rotational contours of several vibrational bands. In general, the results show extensive structure, rivaling variations between different vibronic origins.

The absorption spectrum of naphthalene in the gas phase has been measured and analyzed in detail[1-4]. The 0-0 transition occurs at 32020.2 cm^{-1} and is polarized along the long in-plane axis (x or b_{3u} in representation III^r). A-type bands also arise from excitation of the totally symmetric vibrations $9(a_g)$ and $8(a_g)$. Both of these modes involve a C-C in-plane stretch. The analysis of Lather and Drewitz[5] shows that they are of the following form:

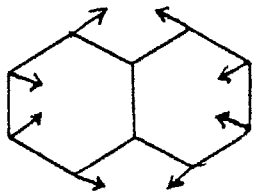

$9(a_g)$

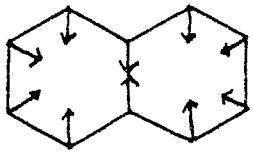

$8(a_g)$

Although the 0-0 transition is allowed, naphthalene is one of few molecules for which vibronic induction results in a stronger absorption strength than the 0-0 transition. The vibronically induced bands come from modes of b_{1g} symmetry which couple with S_2 and give rise to B-type rotational contours. The two b_{1g} modes

measured in these experiments also involve an in-plane C-C stretch. The normal modes have the following form:

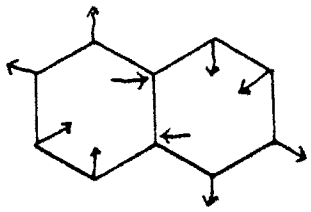

$8(b_{1g})$

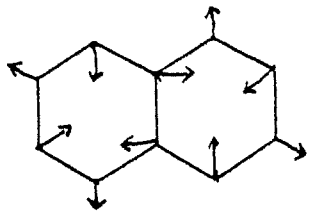

$7(b_{1g})$

Apart from the four modes which are the progression origins of the observed spectra, two vibrations give rise to sequences in the spectrum. The $3(b_{2g})$ forms 55 cm^{-1} sequences and the $4(b_{1u})$, 10 cm^{-1} sequences. These C-C out-of-plane vibrations have the following form:

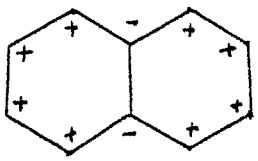

$4(b_{1u})$

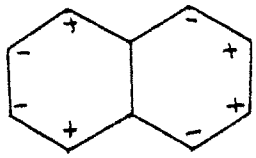

$3(b_{2g})$

In the sections which follow, the results for each vibronic band are discussed. On all figures, quantum yields are absolute and absorption is in arbitrary units. The absorption, however, is linear in optical density. A summary of all measured bands is given in Table III.

Measured data

Origin

The measured absorption and quantum yield spectra of the origin in the vicinity of 32020 cm^{-1} is shown on Fig. 18a. The quantum yield has a maximum of 0.154 at the absorption maximum. The quantum yields tend to

Table III

Measured Vibrational Bands of Naphthalene, h_8

Transition	Excitation and Excess Energy	
0-0 (origin)	32020.2	0.
$8(b_{1g})^1_o$	32457.9	437.7
$8(b_{1g})^1_o\ 4(b_{1u})^1_1$	32448.0	604.
$8(b_{1g})^1_o\ 3(b_{2g})^1_1$	32401.4	578.
$8(b_{1g})^1_o\ 4(b_{1u})^1_1\ 3(b_{2g})^1_1$	32391.3	744.
$7(b_{1g})^1_o$	32931.2	911.
$7(b_{1g})^1_o\ 3(b_{2g})^1_1$	32875.9	1051.
$9(a_g)^1_o$	32520.9	500.7
$9(a_g)^1_o\ 3(b_{2g})^1_1$	32465.	643.
$8(a_g)^1_o$	32722.2	702.
$8(a_g)^1_o\ 3(b_{2g})^1_1$	32667.7	842.
$8(b_{1g})^1_o\ 8(a_g)^1_o$	33158.5	1138.3
$8(b_{1g})^1_o\ 8(a_g)^1_o\ 3(b_{2g})^1_1$	33104.2	1278.
$4(a_g)^1_o$	33409.7	1389.5
$4(a_g)^1_o\ 3(b_{2g})^1_1$	33354.4	1530.
$3(a_g)^1_o$	33454.9	1434.7

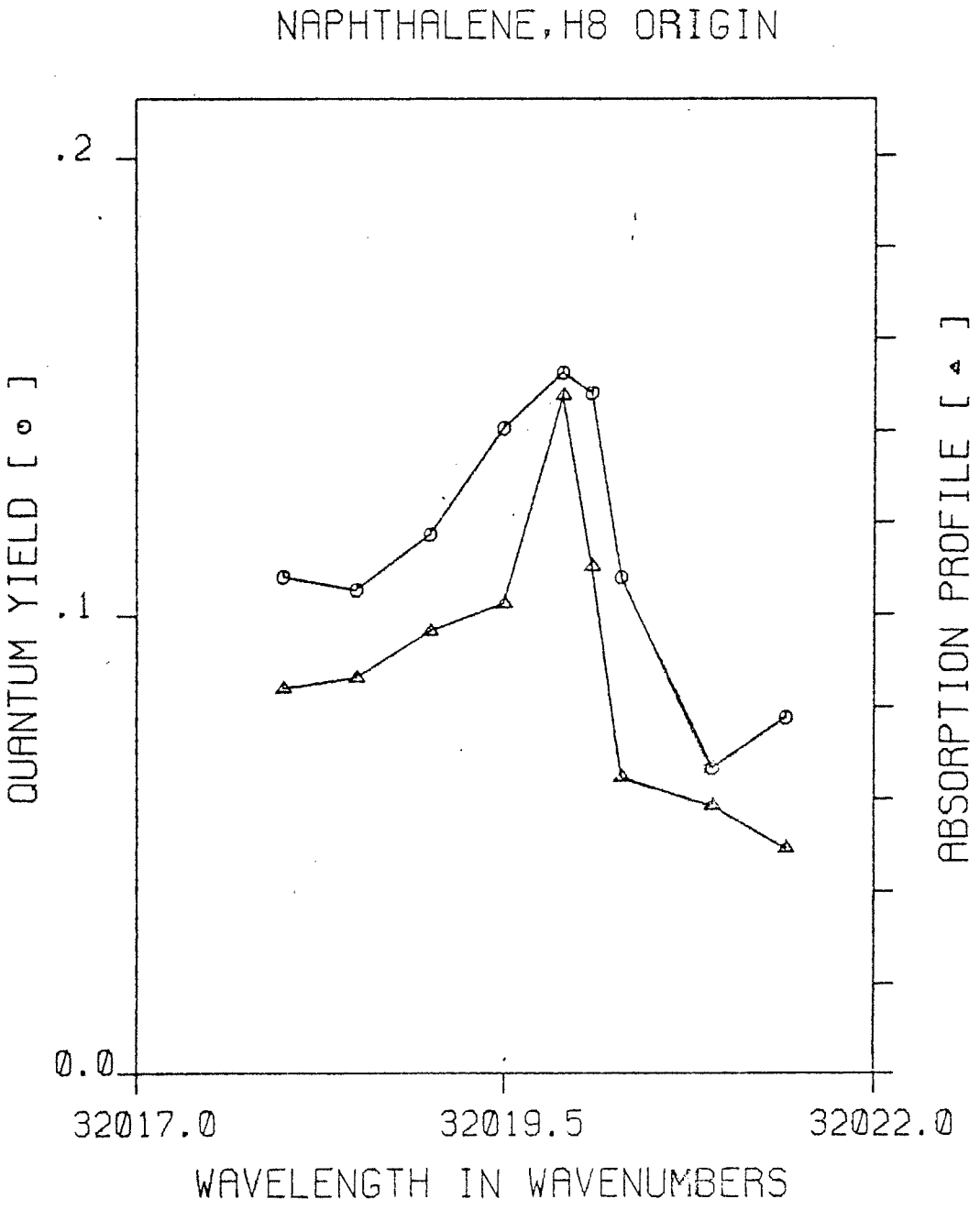

Figure 18a. Quantum yield spectrum of the 0-0 band of naphthalene, h_8.

follow the optical density but are not proportional to it. The same type of structure is observable in the lifetime spectrum as shown on Fig. 18b. The maximum lifetime is 310 nsec.

$8(b_{1g})^1$

A most dramatic manifestation of the rotational effect on quantum yields may be seen by examining Figs. 19 and 20. Fig. 19 shows the high pressure quantum yields of naphthalene, h_8 excited to the $8(b_{1g})$ in the vicinity of the blue absorption peak. The constant quantum yield over strong changes in absorption is exactly what was expected since, at 760 torr of added gas, the electronic state should be completely vibrationally and rotationally equilibrated.

In Fig. 20, the same vibronic band is excited, now at 70 mtorr. At this pressure, the quantum yield can be seen to vary from 0.18 to 0.38 - over a factor of 2. Such strong variations raise the important question of which quantum yield is to be used as the quantum yield of the single vibronic level. Strong rotational averaging in medium resolution experiments must be explicitly taken into account for a valid comparison with theory.

The effect of excitation of ro-vibronic levels other than those belonging to the vibrational state of interest can not be ignored. In naphthalene, this

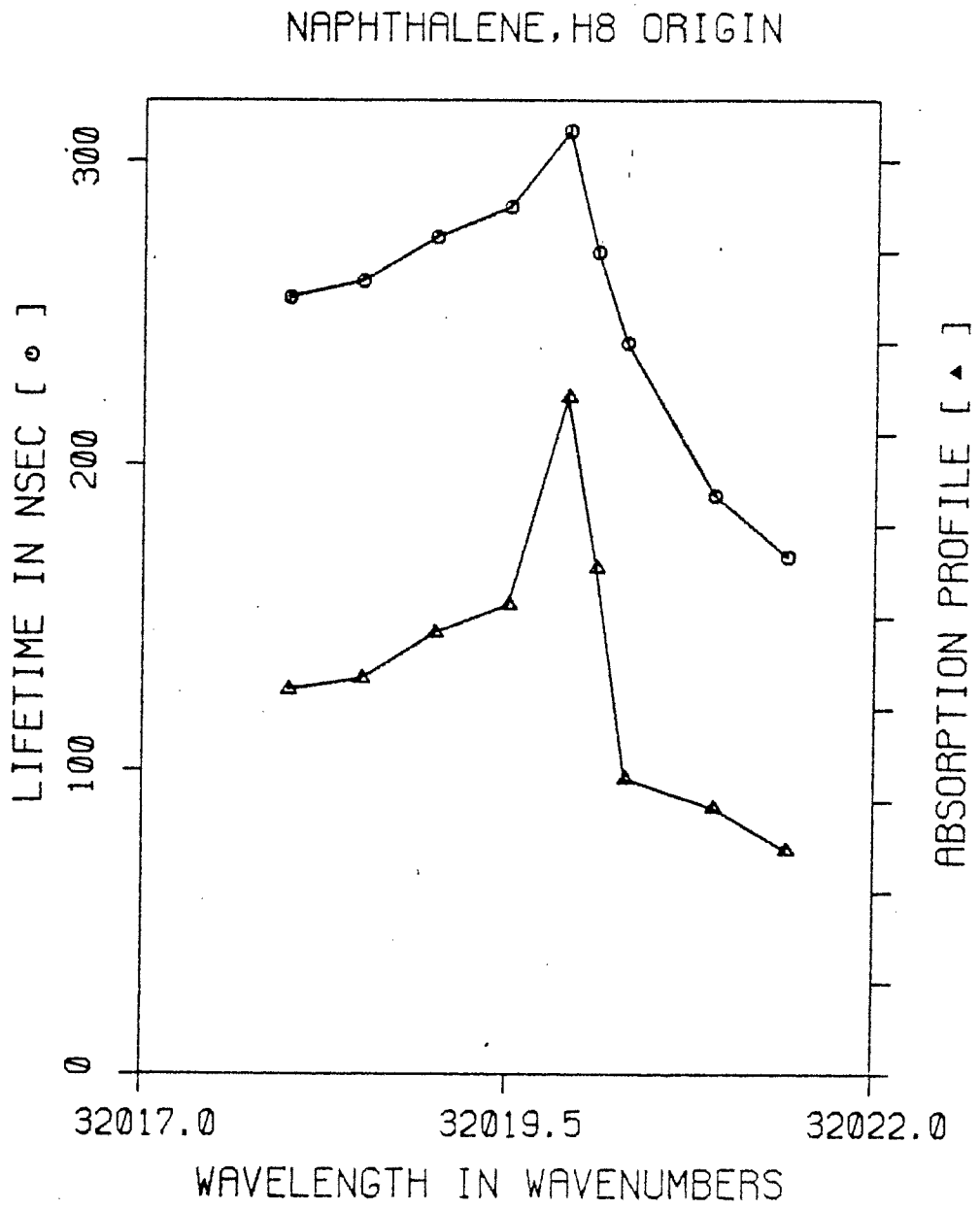

Figure 18b. Lifetime spectrum of the 0-0 band of naphthalene, h_8.

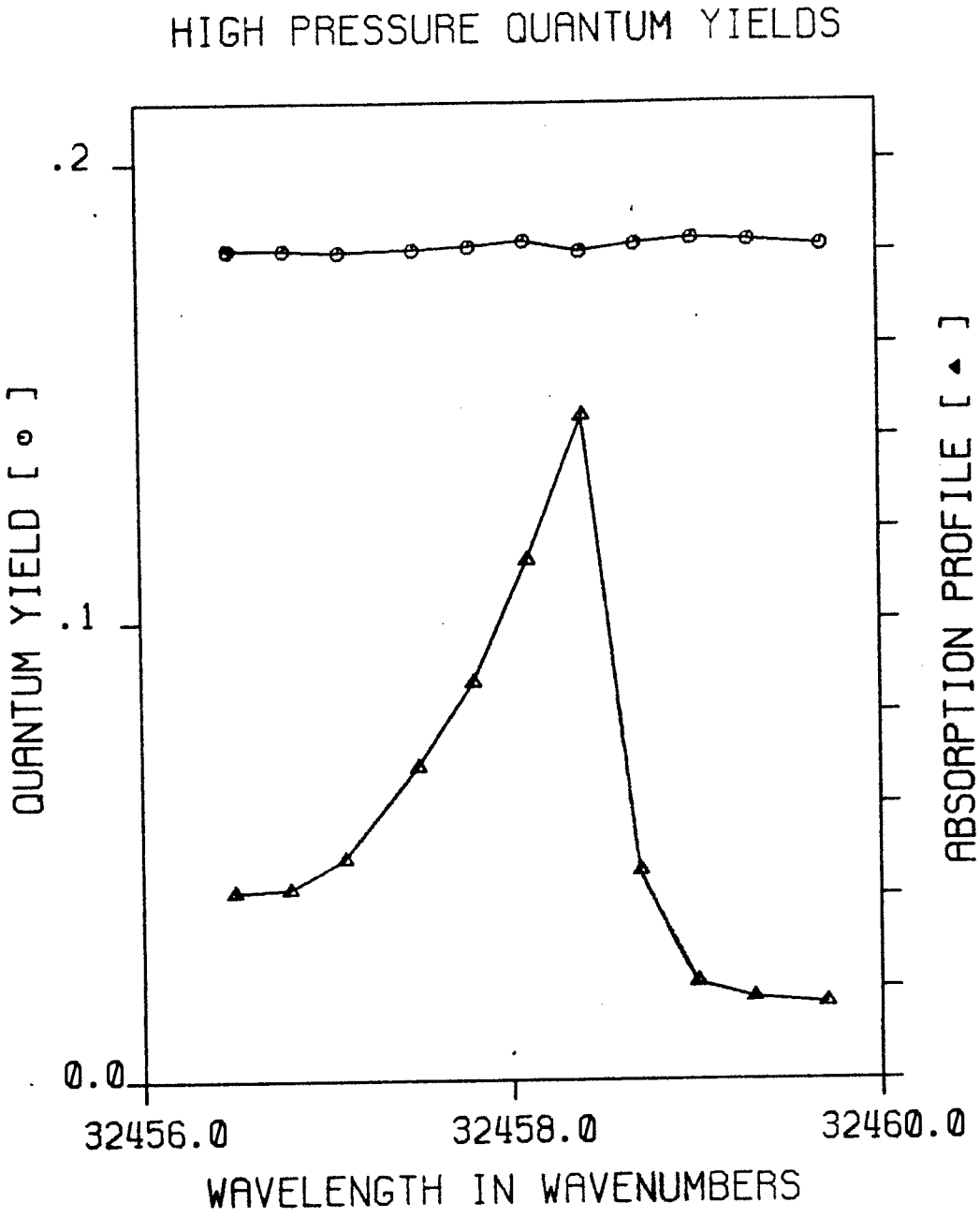

Figure 19. High pressure quantum yield spectrum of the blue peak of the $8(b_{1g})^1_o$ band of naphthalene, h_8.

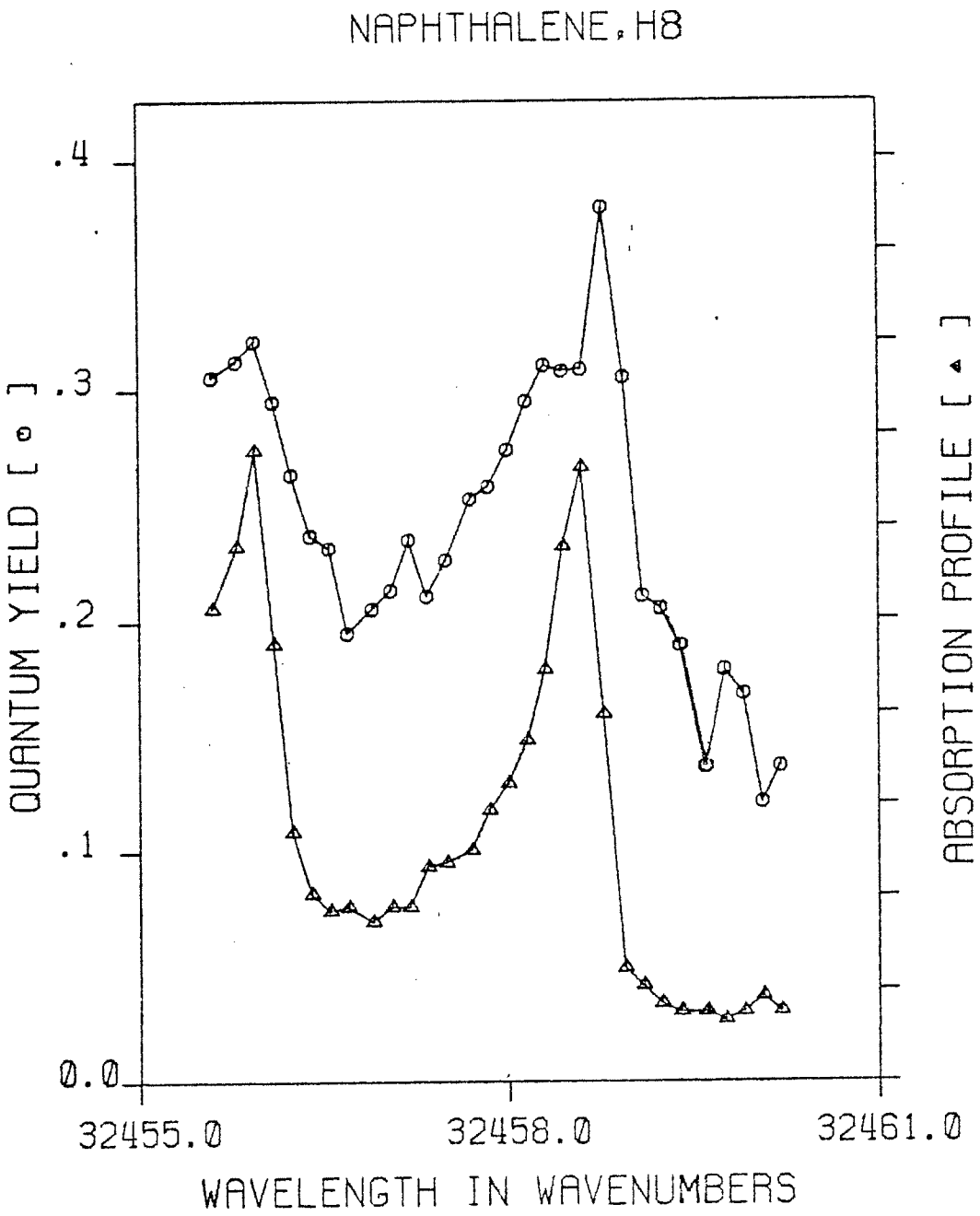

Figure 20. Low pressure quantum yield spectrum of the $8(b_{1g})^1_o$ band of naphthalene, h_8.

is a known problem, particularly with regard to the sequence bands. Thus, many of the measurements reported here are of progression origins. By extrapolating the background due to the previous peak, it was found that the major contribution to the $8(b_{1g})$ comes in the valley, between the peaks. If the background were to result in no emission, the worst case background, it is estimated that the quantum yield in the valley must be increased by about 15%. This change is much less than the observed change of over 50%. In addition, worst case background does not exist since it is observed to have a finite (ca. 15%) quantum yield in this region of excess energy.

The lifetime of the absorption peak to the blue is 270 nsec. This is in good agreement with that observed by Boesl, et al.[6] and Knight, et al.[7]. The quantum yield at this peak is 0.356, in good agreement with the value of Stockburger.[8]

$\underline{8(b_{1g})^1\ 4(b_{1u})^1}$

The quantum yield spectrum of the first 10 cm^{-1} sequence of the $8(b_{1g})$ band is shown on Fig. 21. The peak to the blue has a lifetime of 260 nsec and the highest quantum yield (0.42) of any band measured. The quantum yield structure is inverted relative to the $8(b_{1g})$ in that the quantum yield increases in going from the blue peak to the red.

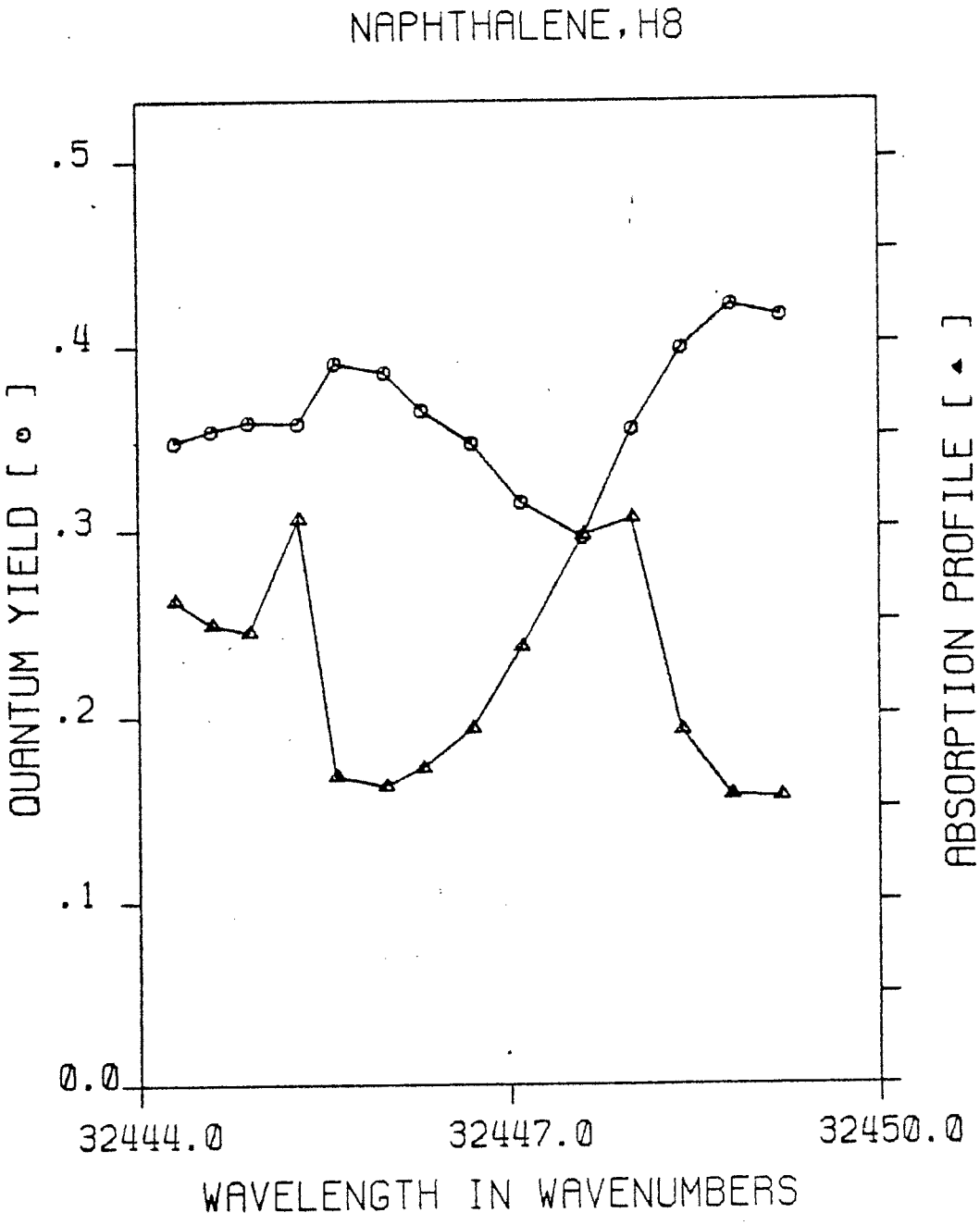

Figure 21. Quantum yield spectrum of the $8(b_{1g})_0^1\ 4(b_{1u})_1^1$ band.

Interpretation of the quantum yield structure of this band is difficult since it is located on top of the P branch of the $8(b_{1g})$. However, the large quantum yield to the blue of the band comes from the $8(b_{1g})$. The dips around the absorption peaks indicate that the overall quantum yields originating from the $8(b_{1g})\ 4(b_{1u})$ are smaller than those of the $8(b_{1g})$, perhaps by a factor of 2.

$8(b_{1g})^1\ 3(b_{2g})^1$

The first 55 cm^{-1} sequence of the $8(b_{1g})$ is shown on Fig. 22. This vibronic level has an excess energy of 578 cm^{-1} and a lifetime at the blue absorption peak of 250 nsec. The rotational structure is similar to that of the $8(b_{1g})$. The background of about 15% at the absorption peaks is due to the red rotational structure of the $8(b_{1g})$ and its first five 10 cm^{-1} sequences.

$8(b_{1g})^1\ 4(b_{1u})^1\ 3(b_{2g})^1$

The quantum yield spectrum of the combination 10 cm^{-1} and 55 cm^{-1} sequences of the $8(b_{1g})$ is shown on Fig. 23. This vibrational band, at an excess energy of 744 cm^{-1}, is the most impure level measured. The background is formed by at least 9 identifiable vibrations. In spite of the background and structured absorption, a virtually constant quantum yield is

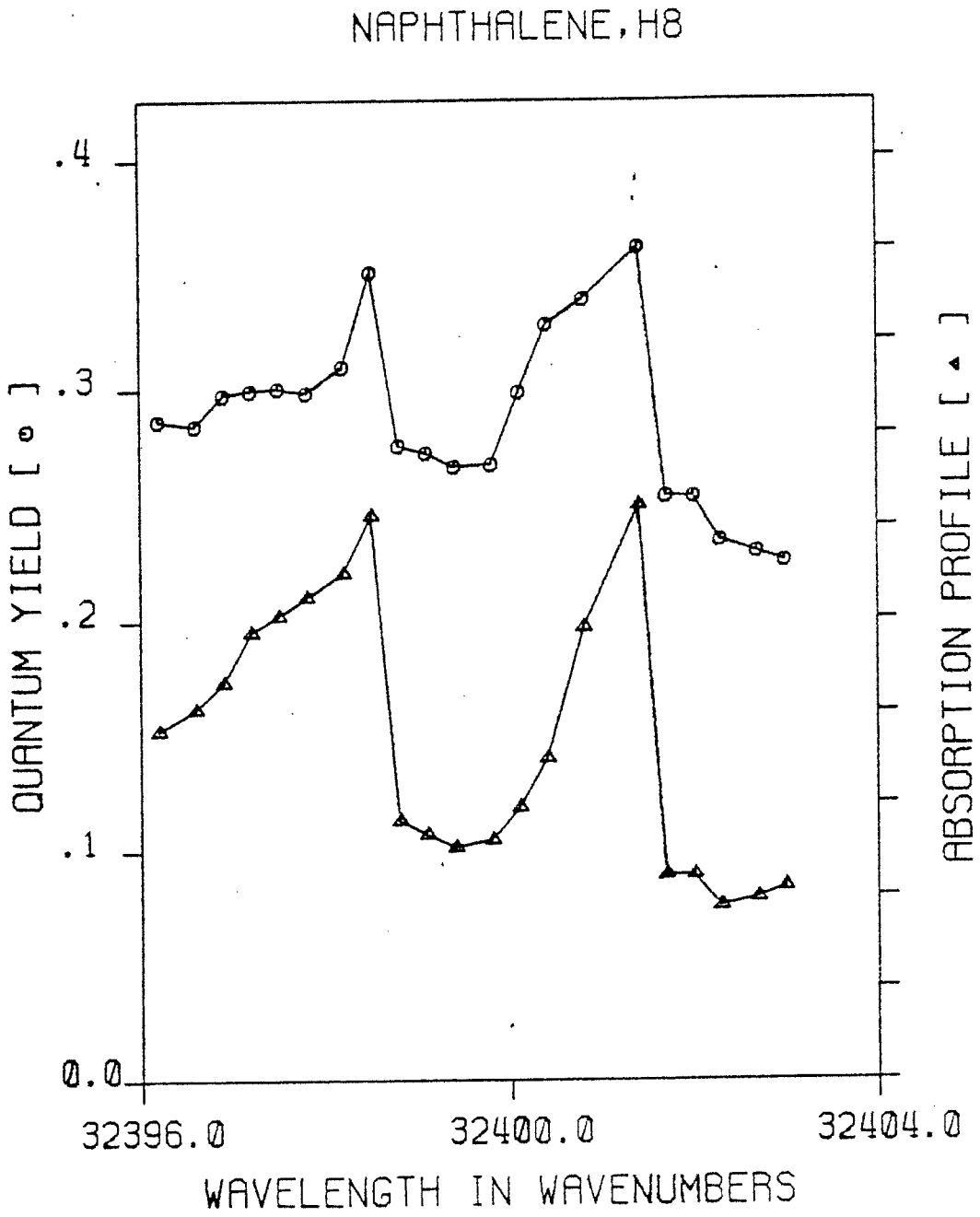

Figure 22. Quantum yield spectrum of the $8(b_{1g})_0^1\ 3(b_{2g})_1^1$ band.

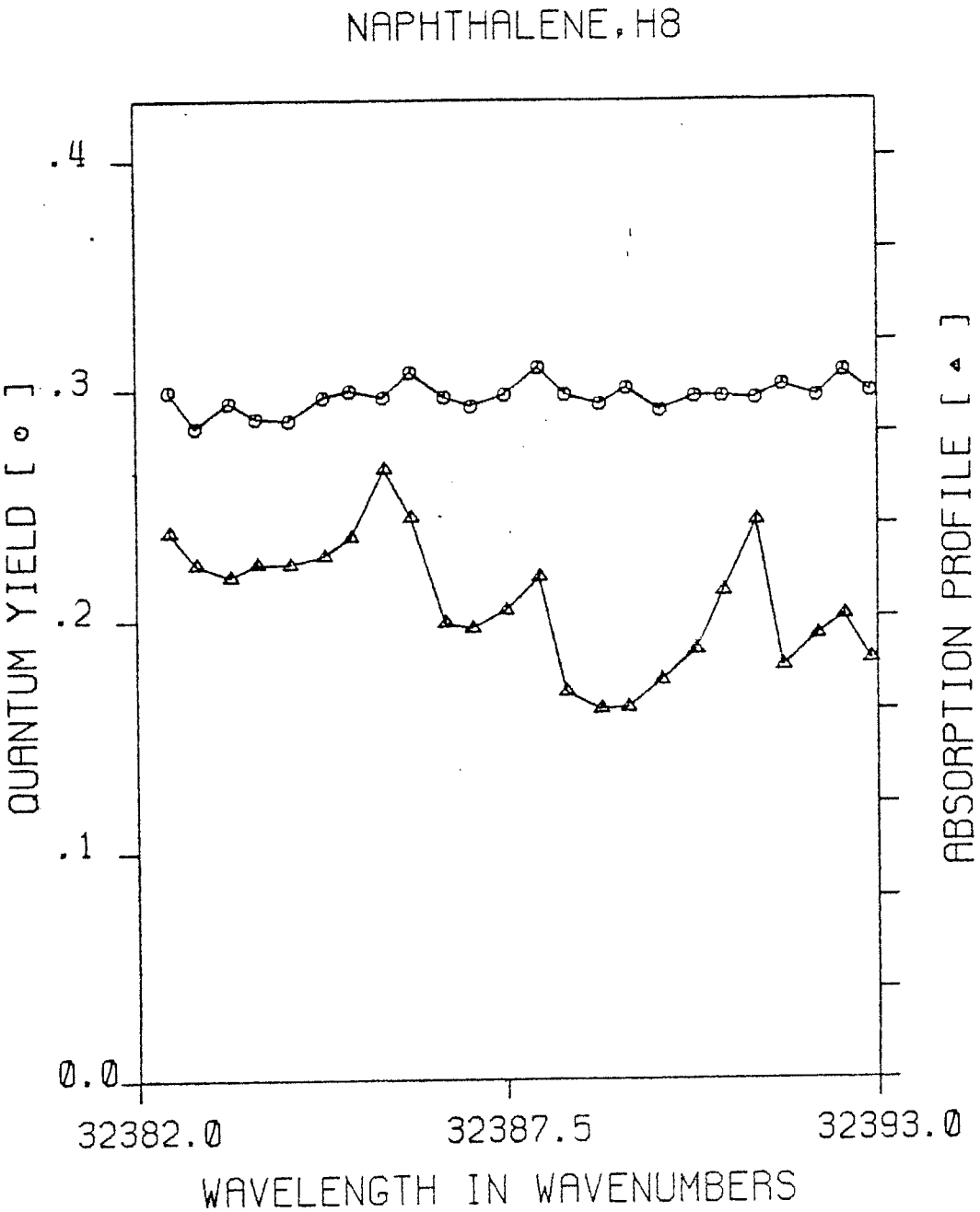

Figure 23. Quantum yield spectrum of the $8(b_{1g})_0^1\ 4(b_{1u})_1^1\ 3(b_{2g})_1^1$ band.

observed in this region. This plot demonstrates that the measured quantum yields are not just artifacts which mirror the absorption spectrum.

$7(b_{1g})^1$

Excitation of the $7(b_{1g})$ mode produces a quantum yield spectrum similar to that of the $8(b_{1g})$, as shown on Fig. 24. The absorption peak to the blue has a maximum quantum yield of 0.195 and a lifetime of 238 nsec. Interesting in this plot is the dip in the quantum yield around 32928 cm^{-1}. A dip in this region was also found for the $8(b_{1g})$ $8(a_g)$ but not for the $8(b_{1g})$ in spite of a detailed quantum yield scan. The dip occurs in the region of the rotational origin or at the Q branch of the transition. Thus, this is a region in which many states of low J are populated. The influence of J on excited state decay processes will be discussed later.

$7(b_{1g})^1$ $3(b_{2g})^1$

As shown on Fig. 25, the 55 cm^{-1} sequence of the $7(b_{1g})$ has quantum yields somewhat lower that the $7(b_{1g})$. The lifetime of the blue absorption peak is 237 nsec, almost the same as that of the $7(b_{1g})$. The large background precludes any meaningful analysis.

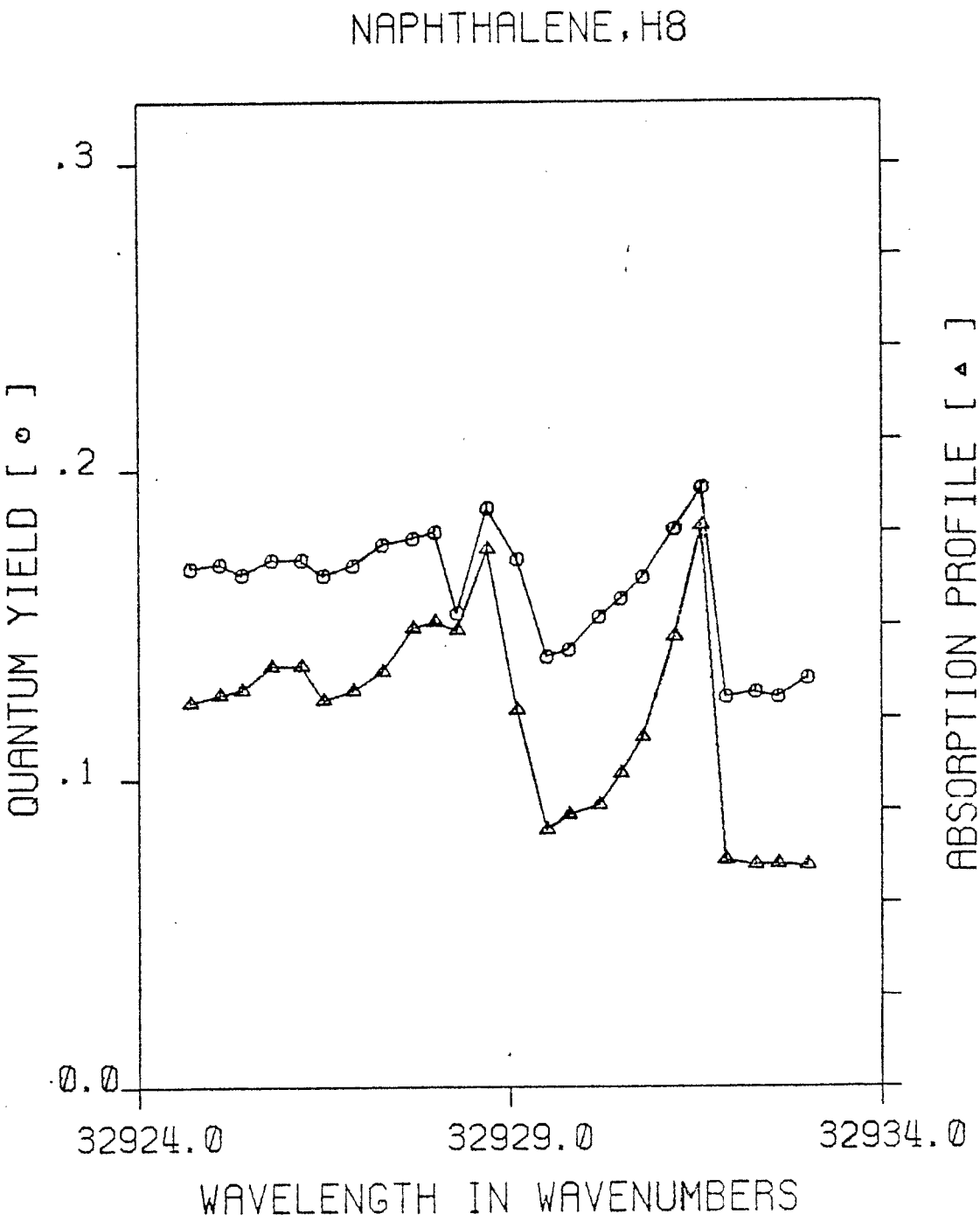

Figure 24. Quantum yield spectrum of the $7(b_{1g})^1_o$ band.

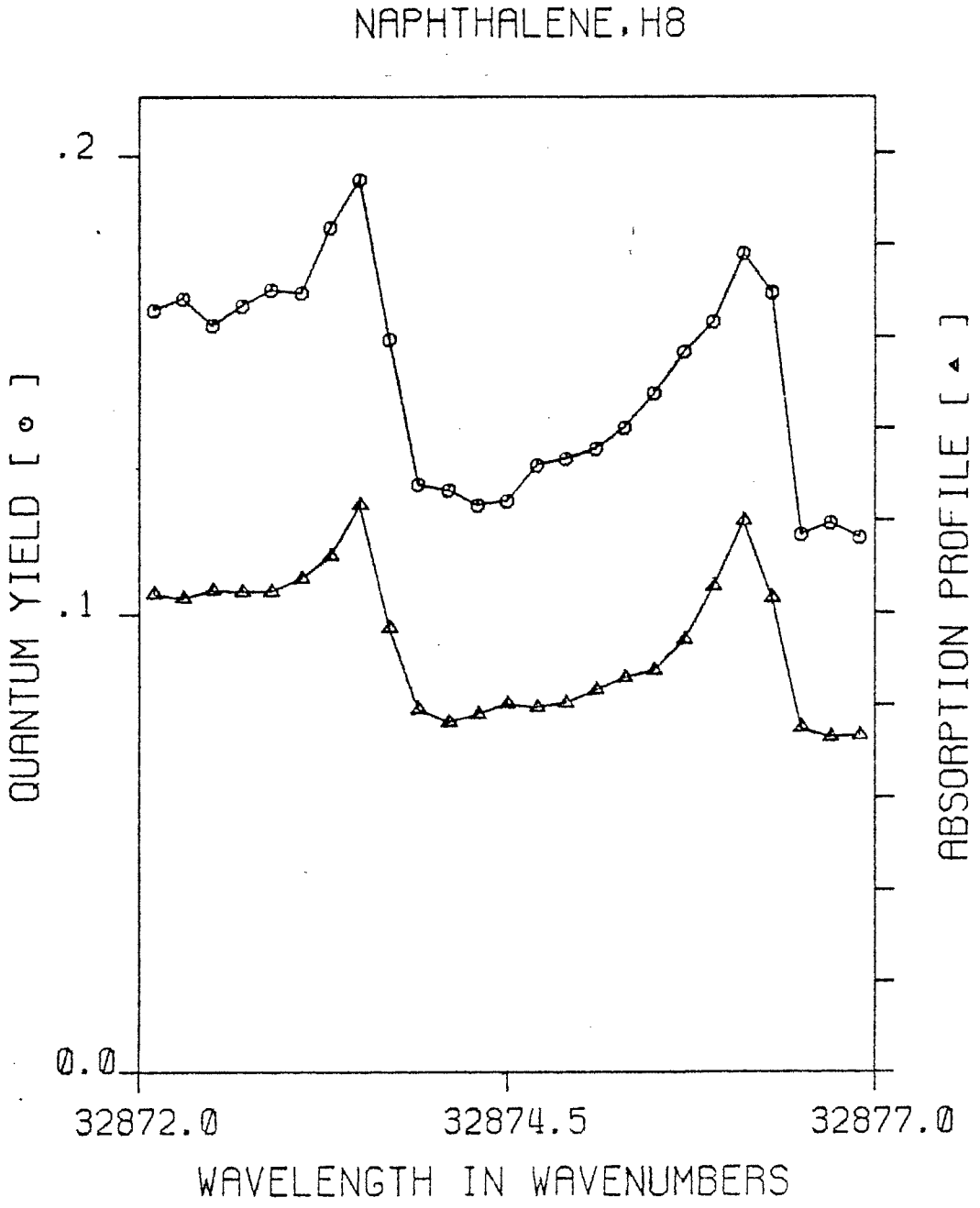

Figure 25. Quantum yield spectrum of the $7(b_{1g})^1_0\ 3(b_{2g})^1_1$ band.

$9(a_g)^1$ and $9(a_g)^1\ 3(b_{2g})^1$

The quantum yield spectrum of the $9(a_g)$ mode is shown on Fig. 26. With 500.7 cm^{-1} of excess energy, this totally symmetric mode shows a maximum quantum yield of 0.20. The maximum optical density is 5 times greater than the background which indicates that primarily one vibronic level is excited. Virtually no rotational structure is seen.

This is not the case, however, for the 55 cm^{-1} sequence of the $9(a_g)$ mode as shown on Fig. 27. The quantum yield varies slowly through the main absorption peak with structure first appearing 3 cm^{-1} to the red of the absorption maximum.

$8(a_g)^1$ and $8(a_g)^1\ 3(b_{2g})^1$

Unlike the $9(a_g)$ but like the origin, the $8(a_g)$ has a quantum yield spectrum which tends to follow the absorption spectrum as shown on Fig. 28. The absorption maximum has a quantum yield of 0.17 and a lifetime of 234 nsec. These values differ only slightly from the $8(a_g)\ 3(b_{2g})$ mode as shown of Fig. 29. For the latter mode, the maximum quantum yield is 0.18 and the lifetime, 230 nsec.

$8(b_{1g})^1\ 8(a_g)^1$

This state, as stated above, has a quantum yield structure similar to the $8(b_{1g})$ but with a dip near the

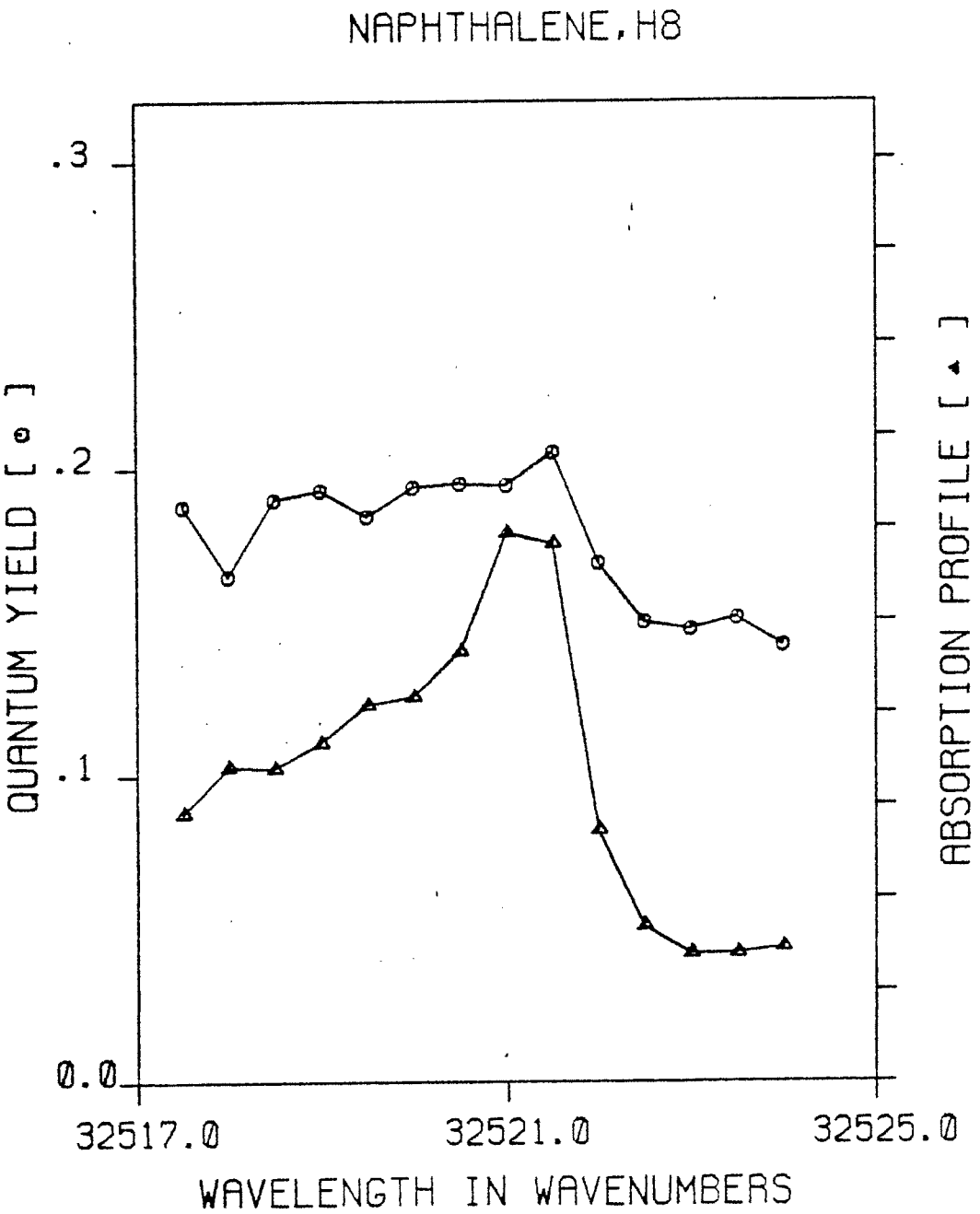

Figure 26. Quantum yield spectrum of the $9(a_g)^1_o$ band.

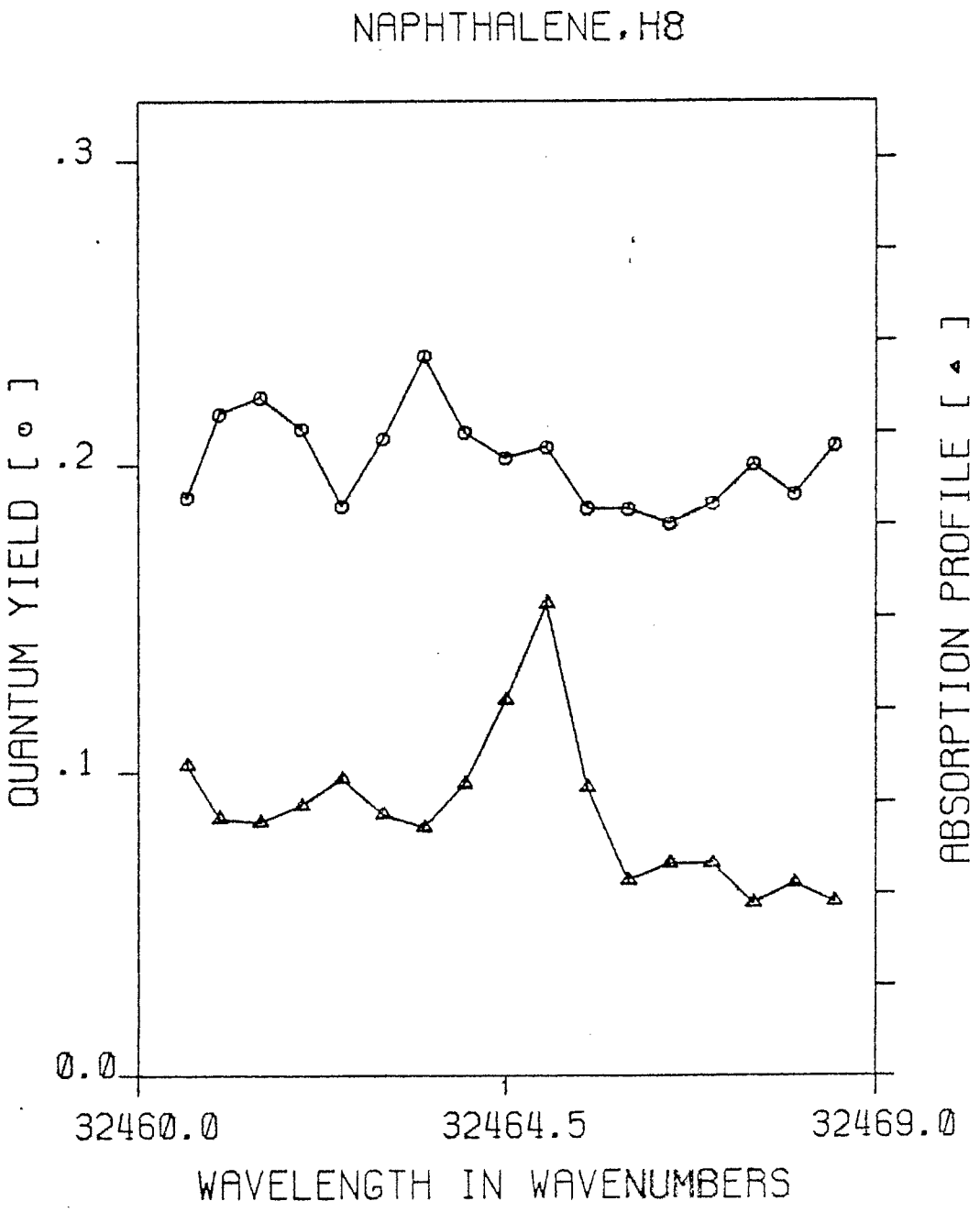

Figure 27. Quantum yield spectrum of the $9(a_g)_o^1\ 3(b_{2g})_1^1$ band.

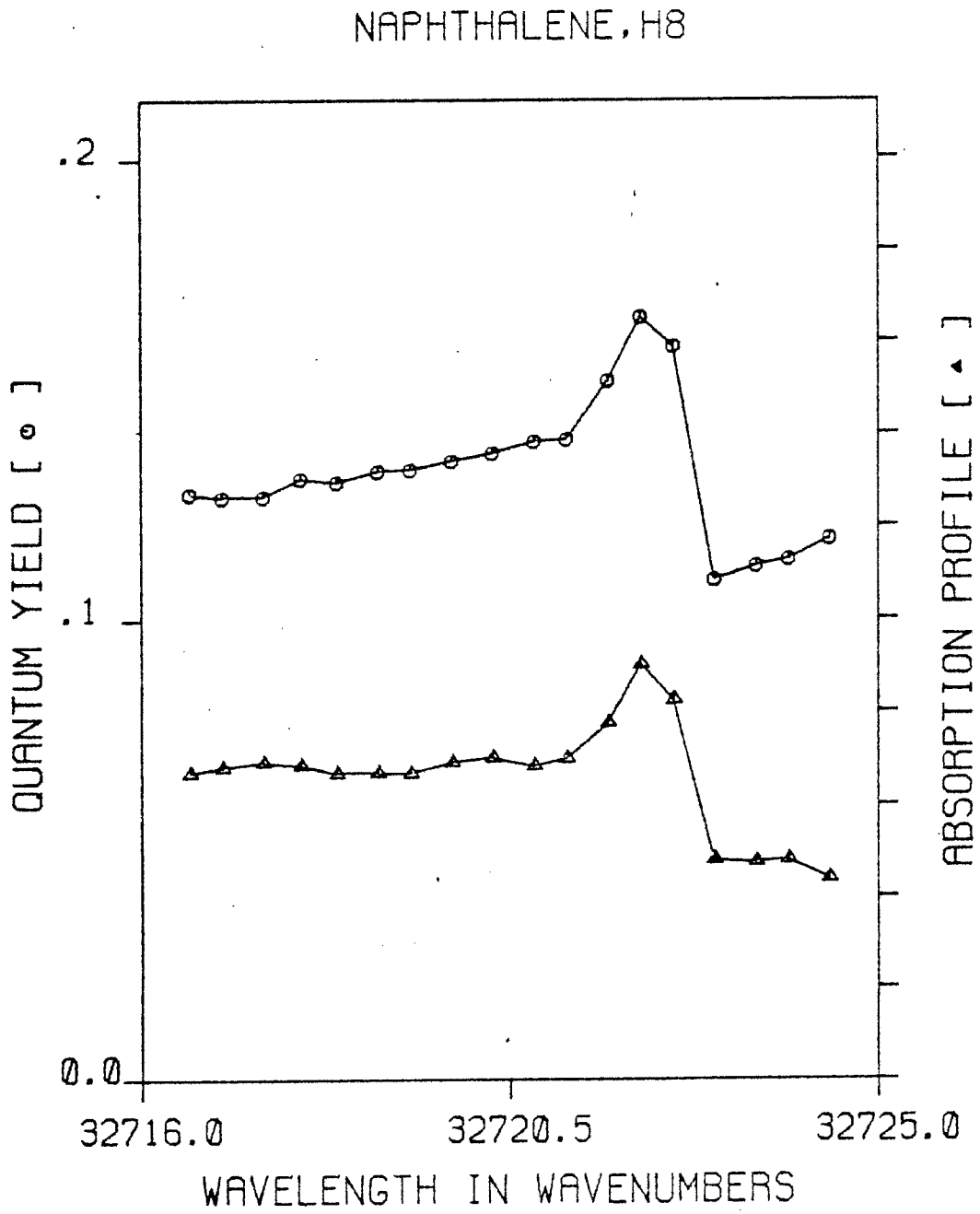

Figure 28. Quantum yield spectrum of the $8(a_g)^1_o$ band.

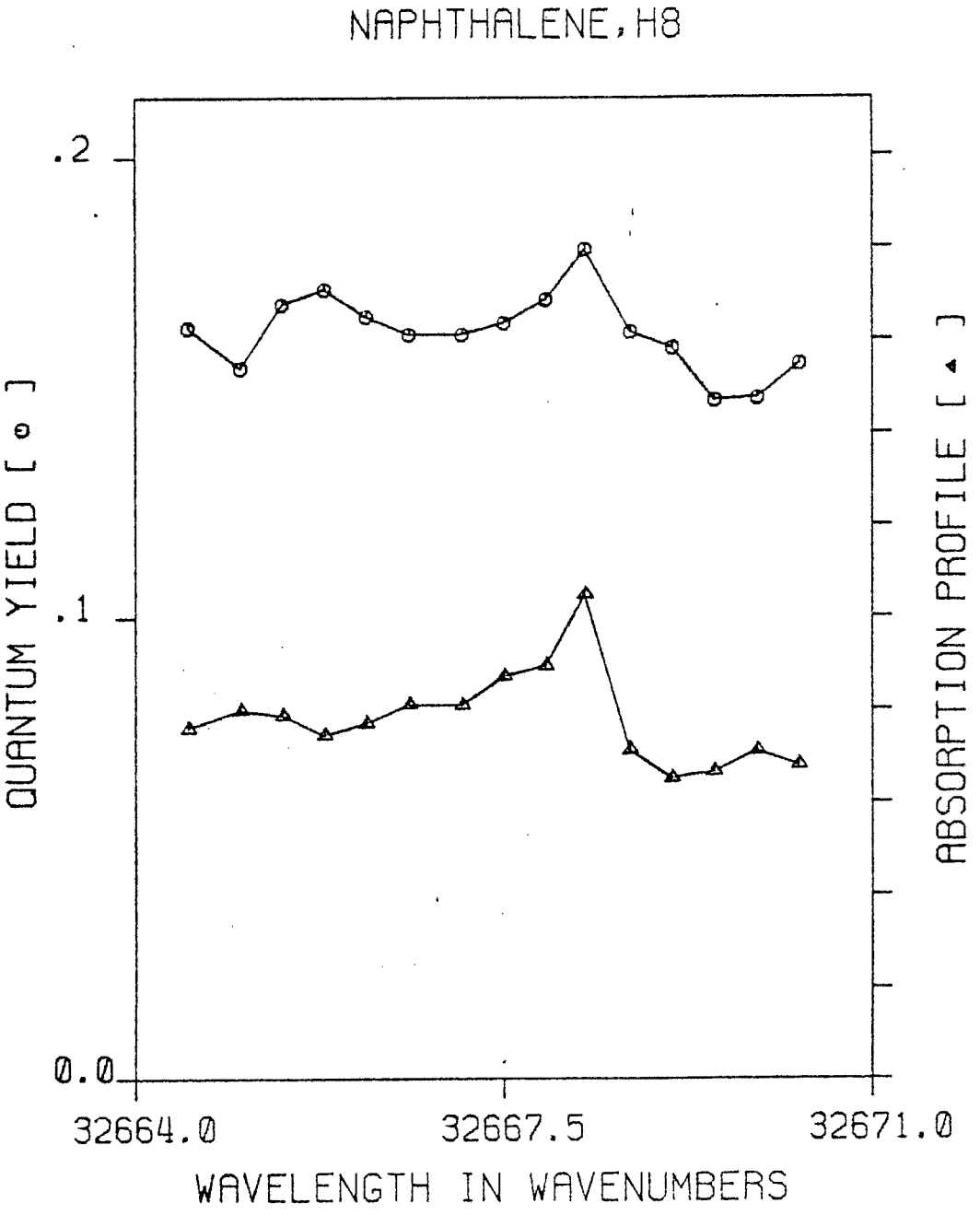

Figure 29. Quantum yield spectrum of the $8(a_g)_0^1\ 3(b_{2g})_1^1$ band.

Q branch. The quantum yield spectrum is shown on Fig. 30. The points of these spectra come from two different measurements, the even points at a path length of 4.2 meters and the odd points at 5.4 meters. The fact that all points form smooth quantum yield and absorption spectra demonstrates that the measured data is invariant to path length.

$8(b_{1g})^1\ 8(a_g)^1\ 3(b_{2g})^1$

The 55 cm^{-1} sequence of the $8(b_{1g})\ 8(a_g)$ band has a quantum yield spectrum as shown on Fig. 31. The lifetime of the blue peak is 180 nsec and the same as that of the $8(b_{1g})\ 8(a_g)$. Very little structure is to be seen and this is probably due to the very strong background.

$4(a_g)^1$ and $4(a_g)^1\ 3(b_{2g})^1$

The quantum yield spectra of the $4(a_g)$ and $4(a_g)\ 3(b_{2g})$ modes are shown on Figs. 32 and 33, respectively. The spectra are virtually flat, with a very slight decrease near the absorption maxima. This indicates that the quantum yields of these two modes are only slightly below the background quantum yield (0.10) at excitation energies around 33400 cm^{-1}.

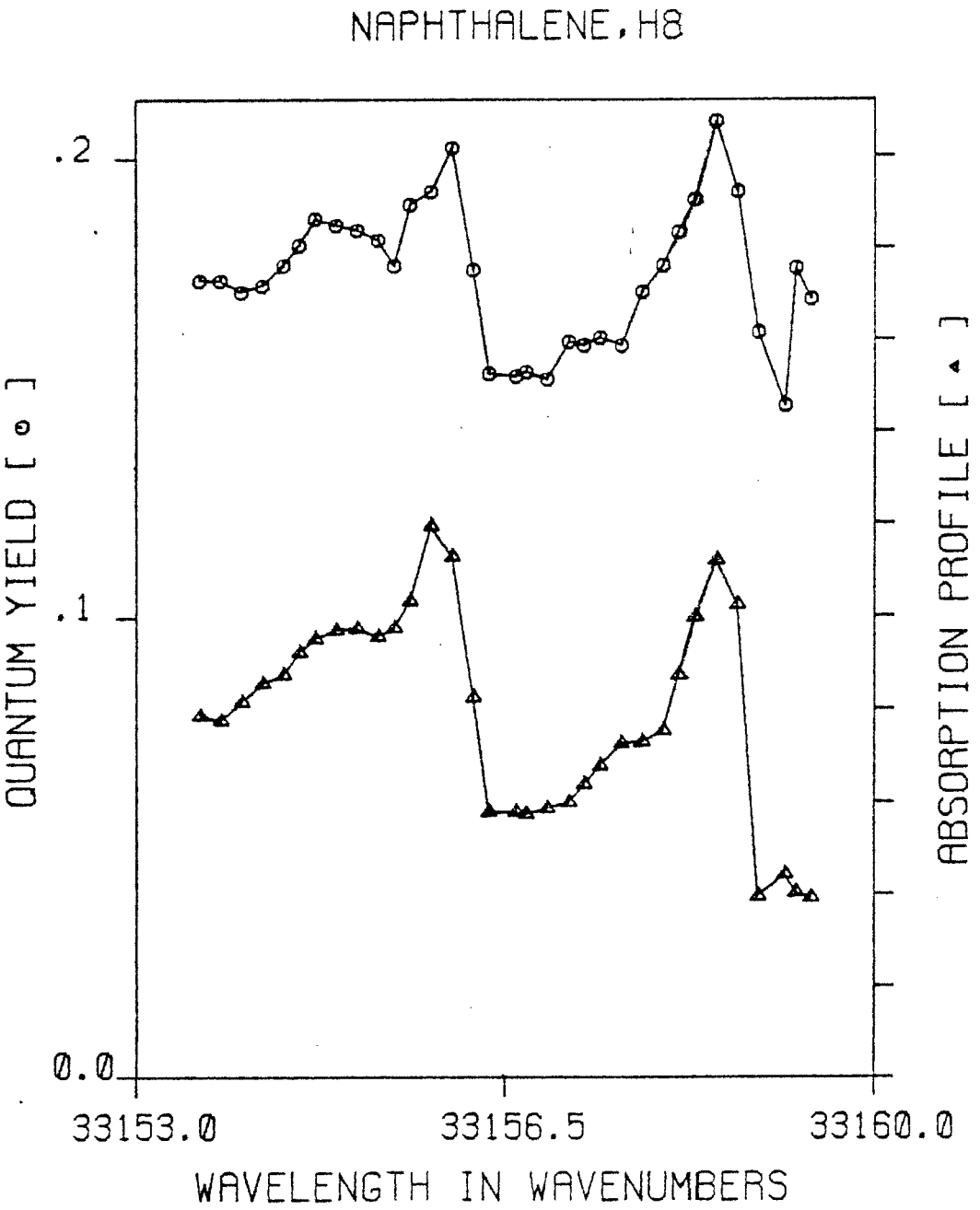

Figure 30. Quantum yield spectrum of the $8(b_{1g})^1_o$ $8(a_g)^1_o$ band.

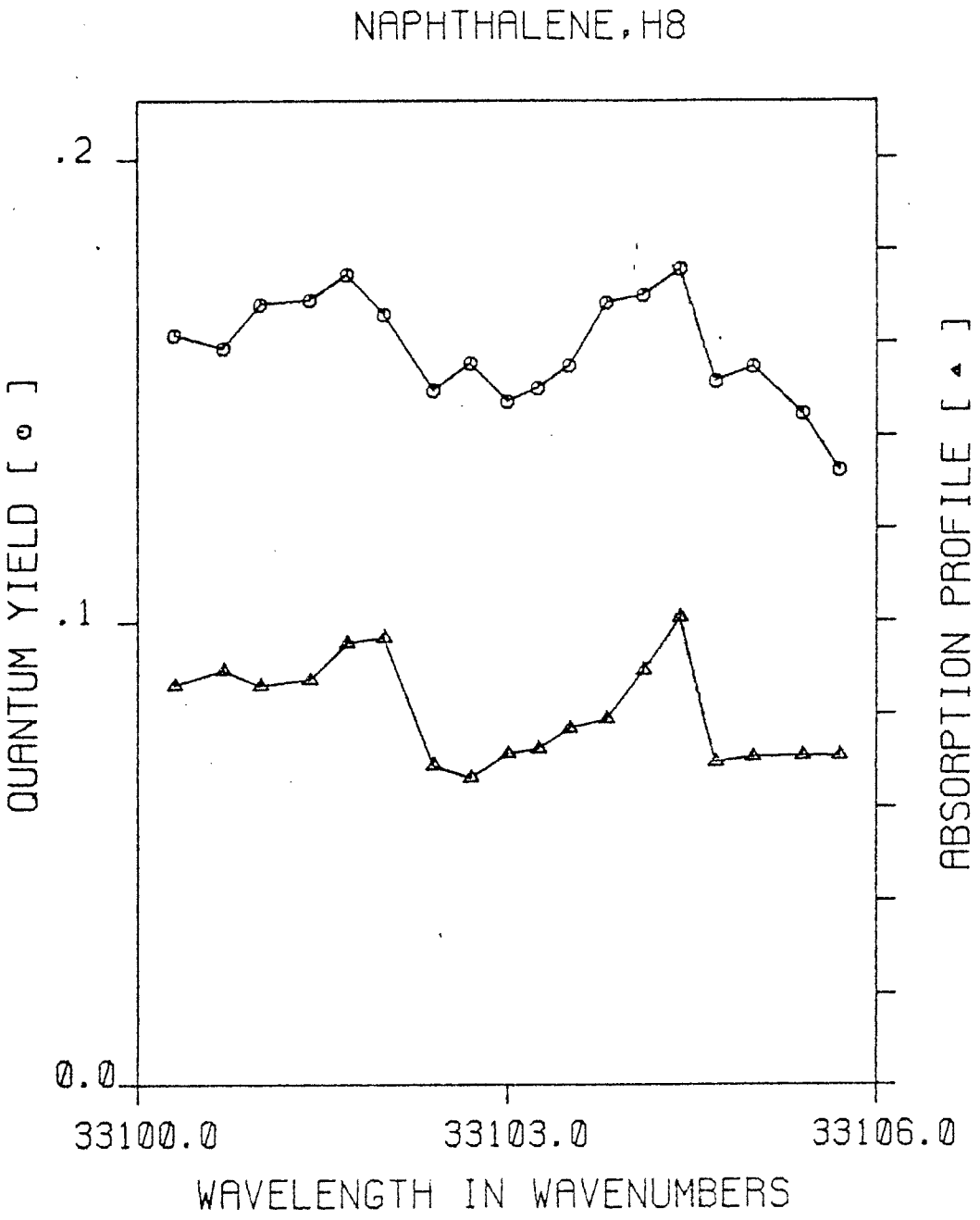

Figure 31. Quantum yield spectrum of the $8(b_{1g})_0^1\ 8(a_g)_0^1\ 3(b_{2g})_1^1$ band.

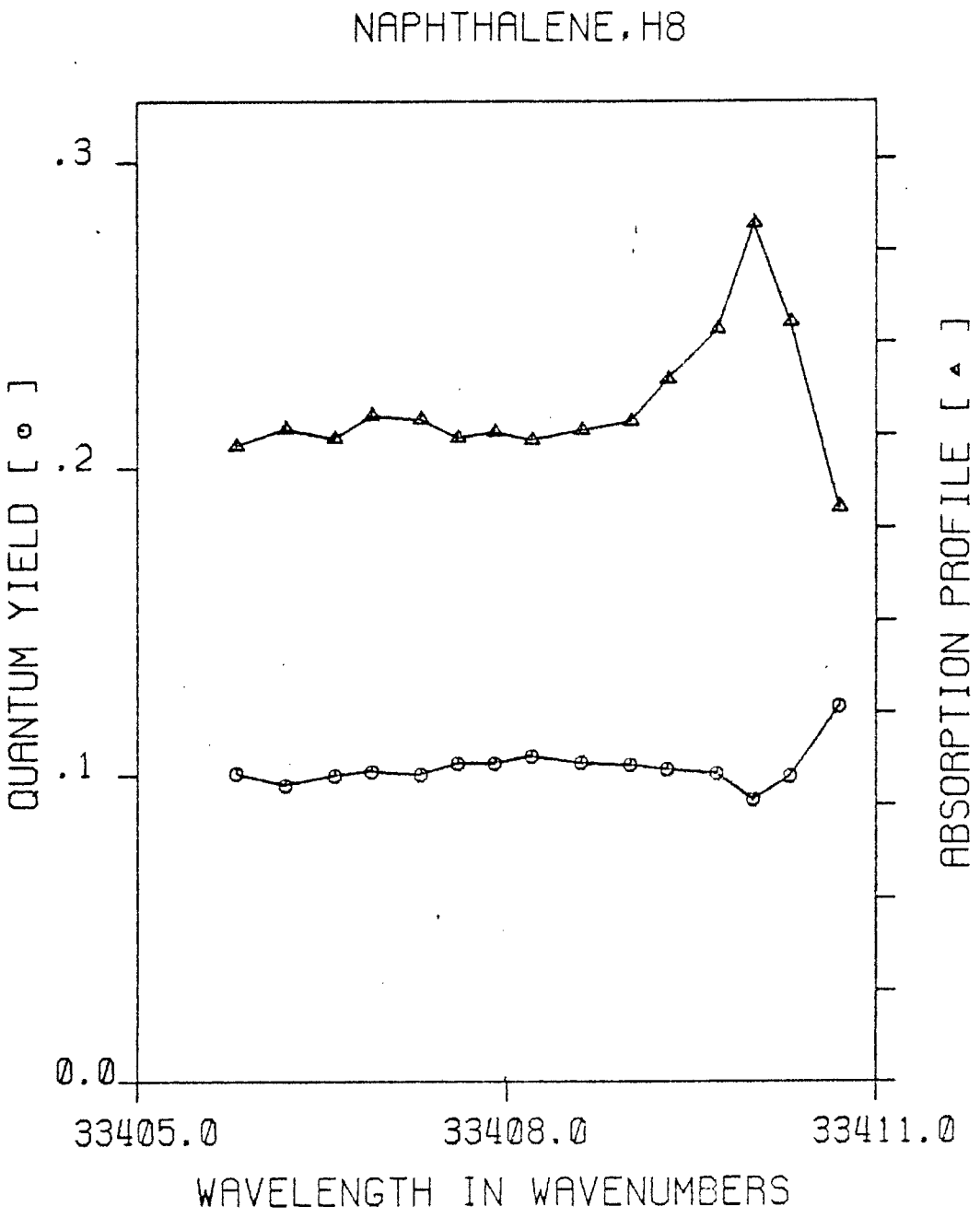

Figure 32. Quantum yield spectrum of the $4(a_g)^1_o$ band.

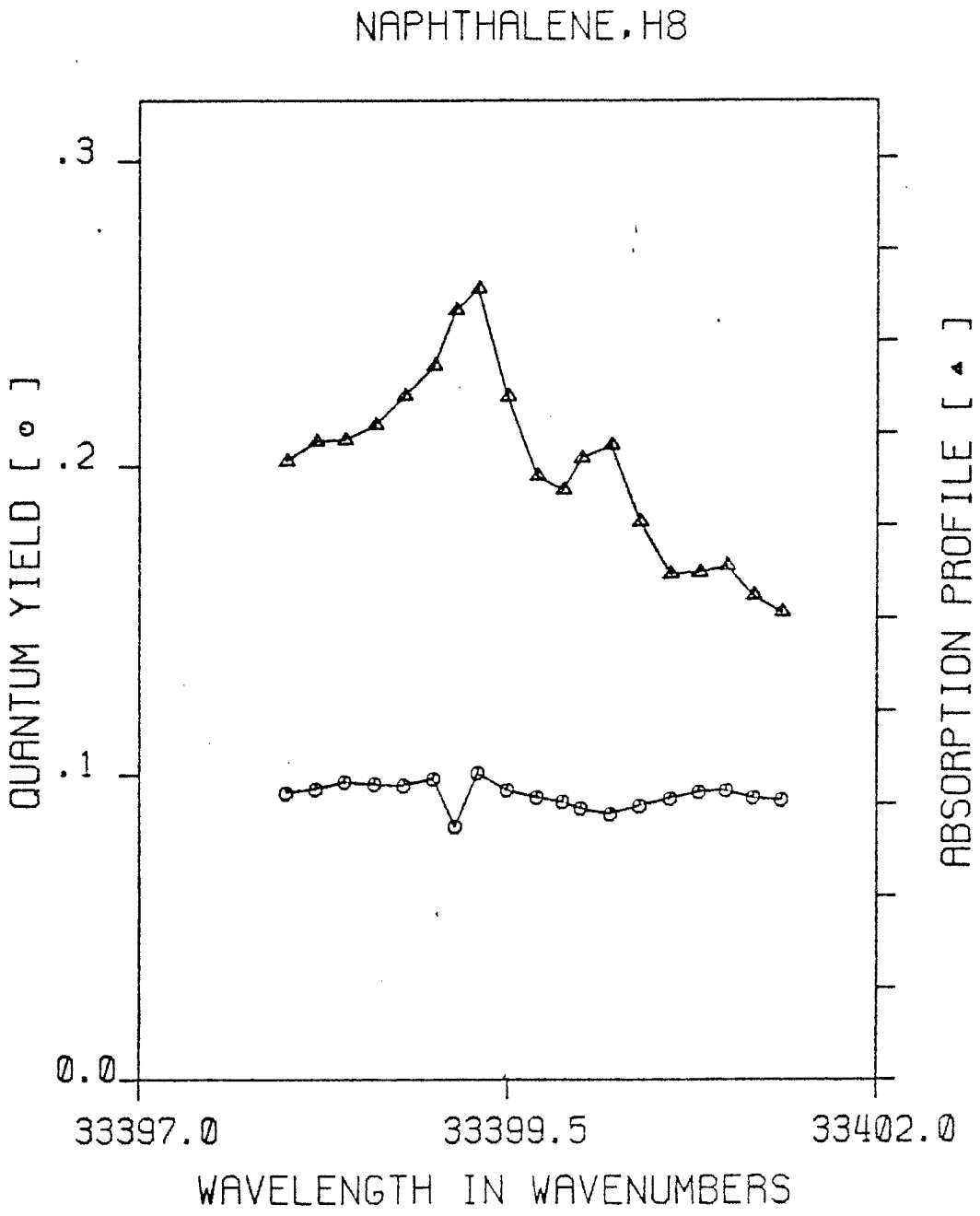

Figure 33. Quantum yield spectrum of the $4(a_g)_o^1\ 3(b_{2g})_1^1$ band.

$3(a_g)^1$

The quantum yield spectrum of the $3(a_g)$ mode is shown on Fig. 34. The quantum yields of this mode are only slightly above background and only a small peak can be observed in the vacinity of the strong absorption maximum.

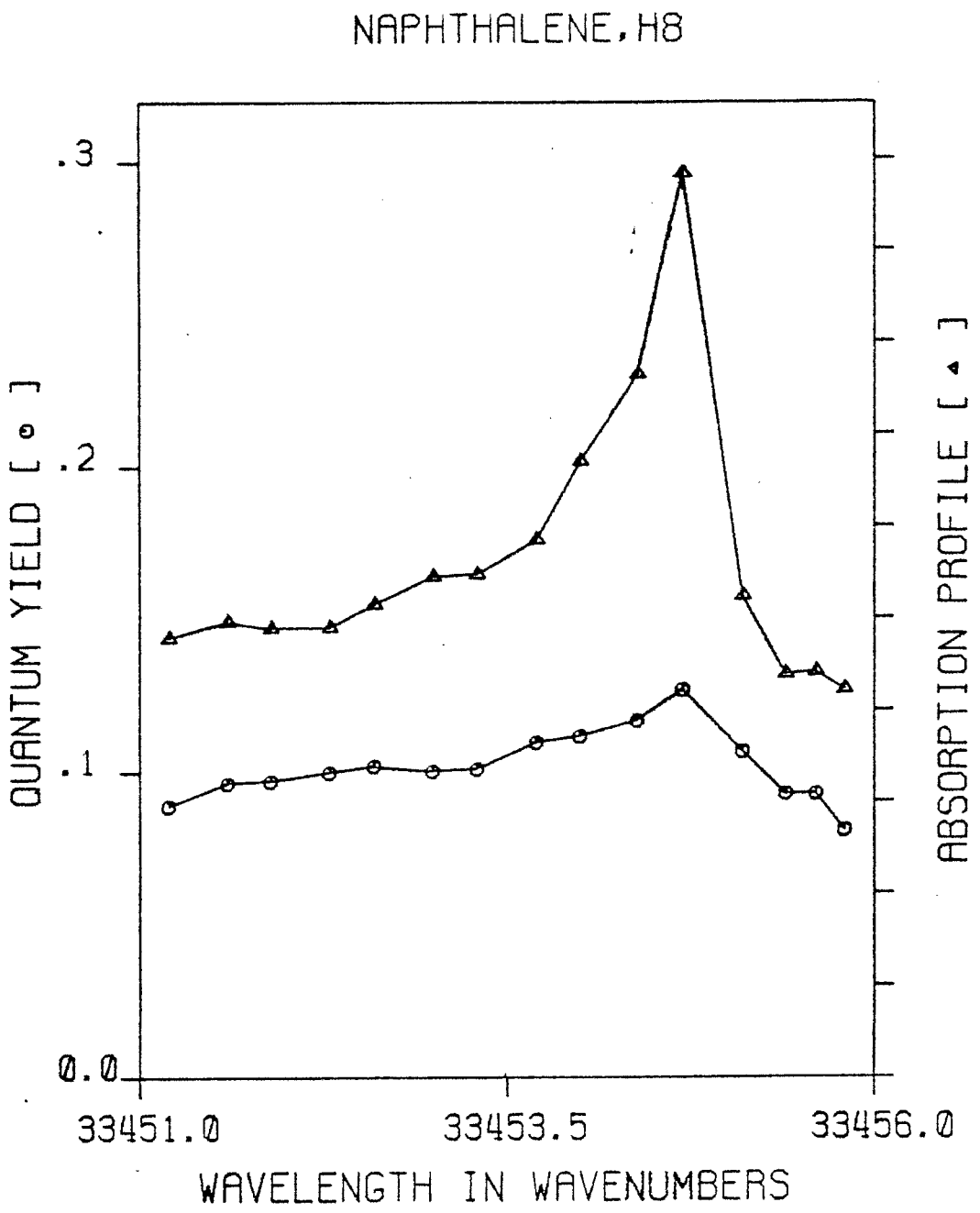

Figure 34. Quantum yield spectrum of the $3(a_g)^1_o$ band.

References to Chapter V

1. K. K. Innes, et al., J. Mol. Spec., 16, 404 (1965).
2. J. M. Hollas and S. N. Thakur, Mol. Phys., 22, 203 (1971).
3. J. M. Hollas, J. Mol. Spec., 9, 138 (1962).
4. D. P. Craig, et al., Phil. Trans. Roy. Soc., A253, 543 (1961).
5. H. Lather and H. J. Drewitz, Zeit. f. Electrochemie Ber. d. Bun. f. phsy. Chemie, 66, 548 (1962).
6. U. Boesl, H. J. Neusser and E. W. Schlag, Chem. Phys. Lett., 31, 1 (1975).
7. A. E. W. Knight, B. K. Selinger and I. G. Ross, Aust. J. Chem., 26, 1159 (1973).
8. M. Stockburger, H. Gattermann and W. Klusmann, J. Chem. Phys., 63, 4519 (1975).

Chapter VI

Absorption Transition Probabilities

Introduction

Before a molecule can undergo a radiationless transition, it must be prepared in a state which can decay. In the majority of cases, such excitation is achieved through optical absorption. The nature of the excited state plays an important role in ISC. In addition, if multiple states are excited, the observed decay properties of the excited ensemble will be different from those of single level excitation. Thus, the first step in an analysis of excited state decay processes is to characterize the excited state ensemble. In this chapter, the emphasis will be on transition probabilities and in the next, on problems involving the interactions of the individual excited states.

Optical transition probabilities have, in general, been evaluated through the methods of band contour analysis. It was first applied to IR bands of diatomics in 1913[1] and later to symmetric rotors in 1933[2]. Both band contour analysis[3] and rotational theory[4,5] have been well reviewed. Virtually all calculated spectra have been based on one photon theory. No two photon band contours of an asymmetric rotor have been reported in the literature although calculations for the Raman spectra of ethylene[6], butadiene[7] and trans-dichloro-

ethylene[8] exist.

In the following sections, the equations and procedures for calculation of one and two photon transition probabilities for the symmetric and asymmetric rotor will be discussed. Then the calculations of rotational contours and excited state ensembles will be presented.

The ground state ensemble

The molecules which are to be excited initially form a canonical ensemble. The various rotational states are populated according to the rotational M degeneracy, nuclear statistical weights and the energy dependent Boltzmann factor. This is described by the equation

(6) $N = (2J+1) g_N \exp (- E (J, \tau)/ kT)$.

For naphthalene, h_8 the nuclear statistical weights are 136 for states of Wang symmetry E^+ and E^- and 120 for O^+ and O^-. On the basis of the last equation and using a program to calculate asymmetric rotor energies, the ground state rotational distribution as a function of rotational energy has been calculated. The results are shown on Fig. 35. An expanded scale would show only discrete peaks for each rotational state with a mean separation of 0.04 cm^{-1}.

The ground state ensemble will be selectively excited as a function of excitation energy, resolution and the transition probabilities. The contour intensity

Figure 35. The rotational distribution in the ground state of naphthalene, h_8.

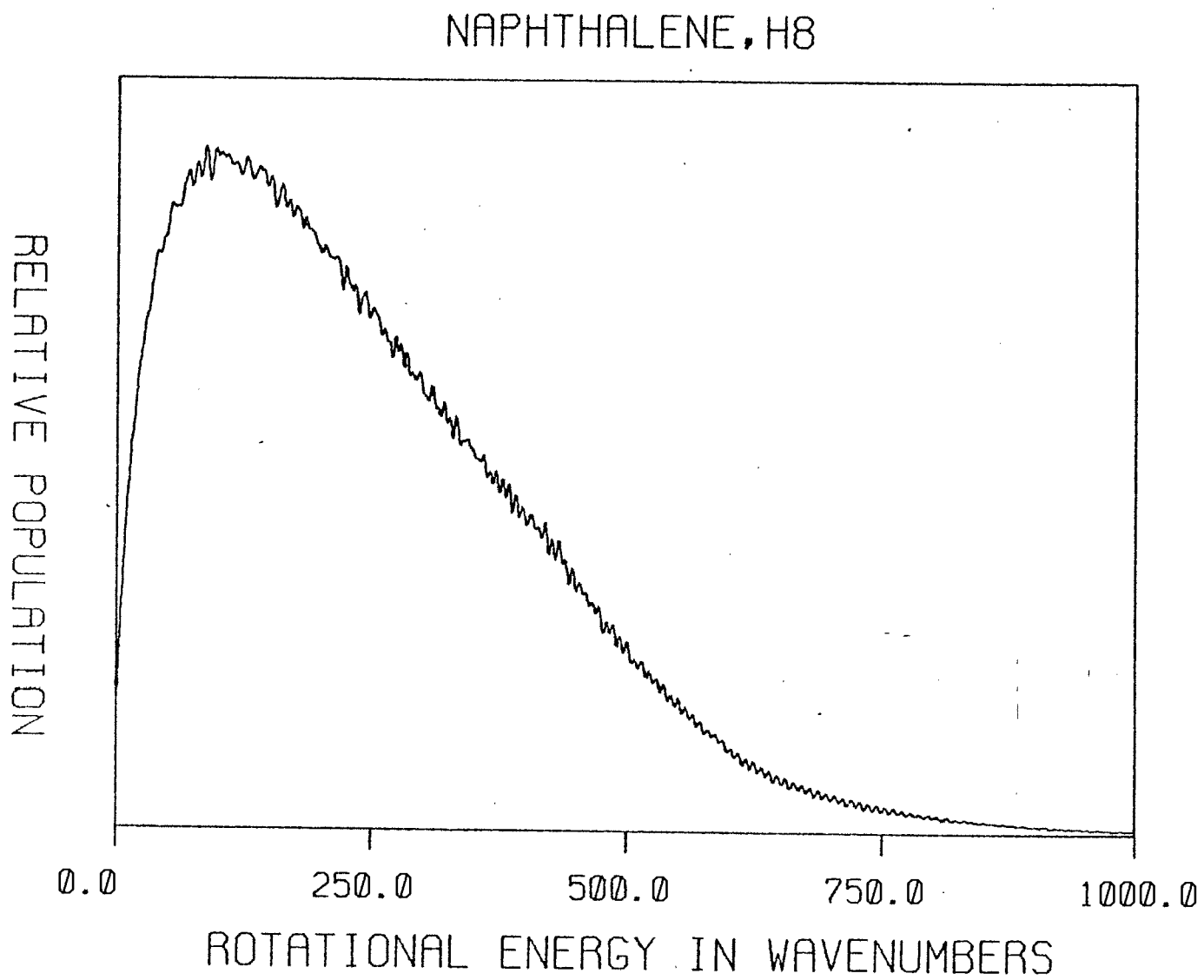
NAPHTHALENE, H8
RELATIVE POPULATION
0.0
250.0
500.0
750.0
1000.0
ROTATIONAL ENERGY IN WAVENUMBERS

C(E) is given by

$$C(E) = \sum_{i,f} \left(\frac{N_i}{2J_i+1} \right) I_{if} \, \Delta(E - \Delta E_{if})$$

where I_{if} is the line strength of the transition and $\Delta (E - \Delta E_{if})$ is the resolution function.

One photon transition intensity

The rotational wavefunctions of a symmetric rotor may be written as[9]

$$(7) \quad |JKM\rangle = (-1)^{M-K} \left(\frac{2J+1}{8\pi^2} \right)^{1/2} D^J_{KM}(\Omega)$$

where the symbols are defined as follow:

J: total rotational angular momentum,

K: molecular z axis projection of J,

M: space fixed z axis projection of J,

$D^J_{MK}(\Omega)$: matrix elements of the finite rotation operator or D-functions.

The use of the D-functions implies a III^r representation for which a, b and c axes of the molecule are correlated with x, y and z, resp.

The line strength of a one photon transition is defined as

$$(8) \quad I_1 = \sum_{M_1, M_2} |\langle J'K'M' | M^s | JKM \rangle|^2$$

where M^s is the $s^{\underline{th}}$ component of the matrix element of the electric moment in space fixed Cartesian coordinates.

It is defined as

(9) $$M^s = \langle \phi' \chi' | r_s | \phi \chi \rangle$$

where r_s is the s $\underline{\text{th}}$ component of the dipole operator. In general, this quantity is very difficult to calculate. However, for rotational transitions it usually suffices to know its symmetry.

The problem is most easily solved by transforming to spherical tensor coordinates. These are defined by the following equations:

(10)

$$r_0 = z \quad , \quad r_\pm = \mp 2^{-1/2} (x \pm iy).$$

Transforming the dipole operator gives

$$r_\mu = \sum_s C_{\mu s} r_s$$

in space fixed spherical coordinates. These may be transformed to molecular fixed spherical coordinates to give

$$r_{\mu'} = \sum_\mu D'_{\mu\mu'}(\Omega) r_\mu$$

Thus, the electric moment is given by

$$M^s = \sum_{\mu,\mu'} C_{s\mu} D'_{\mu'\mu}(\Omega) M_{\mu'}$$

The matrix element is thus

(11)

$$\langle J'K'M' | M^s | JKM \rangle = (2J+1)^{1/2} (2J'+1)^{1/2} (8\pi^2)^{-1}$$

$$\cdot \int D^{J'}_{K'M'}(\Omega) \left(\sum_{\substack{\mu \\ \mu'}} D'_{\mu'\mu}(\Omega) C_{s\mu} M_{\mu'} \right) D^J_{KM}(\Omega) \, d\Omega$$

$$= (2J+1)^{1/2}(2J'+1)^{1/2}\left(\sum_{M} C_{SM}\begin{pmatrix} J & J' & 1 \\ M & -M' & M \end{pmatrix}\right)$$
$$\cdot\left(\sum_{M'} M_{M'}\begin{pmatrix} J & J' & 1 \\ K & -K' & M' \end{pmatrix}\right)$$

where terms of the type $\begin{pmatrix} J_1 & J_1' & 1 \\ M & -M' & M \end{pmatrix}$ are Wigner 3-J symbols. A brief description of the 3-J symbols is given in Appendix 1. Evaluating the equation for the one photon line strength yields

(12) $$I_1 = (2J+1)(2J'+1)\left(\tfrac{1}{3}\right)\left| M_{\Delta K}\begin{pmatrix} J & J' & 1 \\ K & -K' & \Delta K \end{pmatrix}\right|^2$$

which is the final formula for the symmetric rotor.

Two photon transition intensity

The line strength for a two photon transition is defined as

(13) $$I_2 = \sum_{M_1, M_2} |\langle J'K'M'|M^{rs}|JKM\rangle|^2.$$

The transition matrix element M^{rs}, as in the one photon case, is integrated over vibronic and electronic coordinates. The operator is different, however, since two photons are involved. The two photon operator is $r_s r_r$, the product of the projections of the dipole operator on the direction of the polarization vectors e_s and e_r of the respective photons.

As in the one photon case, the transition matrix element is transformed from space fixed Cartesian coordinates to molecular fixed spherical tensor coordinates. Metz[10] has shown that this transformation

yields

$$(14)\quad M^{rs} = \sum_{\bar{J}=0}^{2} \sum_{\lambda,\lambda'} C_{\lambda}^{\bar{J}} M_{\lambda'}^{\bar{J}} D_{\lambda\lambda'}^{\bar{J}}(\Omega)$$

where

$$C_{\lambda}^{\bar{J}} = (2\bar{J}+1)^{1/2} \sum_{\mu,\nu} \begin{pmatrix} 1 & 1 & \bar{J} \\ -\mu & -\nu & -\lambda \end{pmatrix} C_{\mu r}^{*} C_{\nu s}^{*}$$

and

$$M_{\lambda'}^{\bar{J}} = (2\bar{J}+1)^{1/2} \sum_{\mu'\nu'} \begin{pmatrix} 1 & 1 & \bar{J} \\ -\mu' & -\nu' & -\lambda' \end{pmatrix} M_{\mu'\nu'} .$$

Using some well known integral solutions[9] and some algebra, the rotational matrix element becomes[10]

$$(15)\quad \langle J'K'M'|M^{rs}|JKM\rangle = (-1)^{M-K} (2J+1)^{1/2} (2J'+1)^{1/2} \sum_{\bar{J},\lambda,\lambda'} C_{\lambda}^{\bar{J}} M_{\lambda'}^{\bar{J}} \begin{pmatrix} J & J' & \bar{J} \\ K & -K' & \lambda' \end{pmatrix} \begin{pmatrix} J & J' & \bar{J} \\ M & -M' & \lambda \end{pmatrix}.$$

This may be used to directly obtain the two photon line strength. The final solution is

$$(16)\quad I_2 = (2J+1)(2J'+1) \sum_{\bar{J}=0}^{2} C_{\bar{J}} \left| M_{\Delta K}^{\bar{J}} \begin{pmatrix} J & J' & \bar{J} \\ K & -K' & \Delta K \end{pmatrix} \right|^2$$

where

$$C_{\bar{J}} = (2\bar{J}+1)^{-1} \sum_{\lambda} |C_{\lambda}^{\bar{J}}|^2 .$$

The asymmetric rotor

Transition amplitudes for the asymmetric rotor can not be written in closed form as they were for the symmetric rotor in the previous two sections. Quantum number K is no longer good and is replaced by an index τ which simply orders the 2J+1 energy levels. The

index τ is defined by the equation $\tau = K_- - K_+$ where K_- is the quantum number in the prolate limit (A > B=C) and K_+, in the oblate limit (A=B > C). Quantum numbers J and M remain good.

The asymmetric rotor wavefunctions can be expanded in terms of the symmetric rotor wavefunctions since they form a complete basis set. This is given by

$$(17) \quad |J\tau M\rangle = \sum_K a^J_{K\tau} |JKM\rangle.$$

The expansion coefficients and asymmetric rotor energies must be found by matrix diagonalization techniques. Determination of asymmetric rotor energies is well documented in the literature but will be briefly reviewed here, primarily for the sake of nomenclature.

By diagonalizing the expression for the energy of the asymmetric rotor about the b axis, the energy formula can be written as

$$(18) \quad E_{J,\tau} = \frac{A+C}{2} J(J+1) + \frac{A-C}{2} E_\tau(\kappa)$$

In this formula, κ is the Ray[11] asymmetry parameter which is defined as

$$(19) \quad \kappa = \frac{2B - A - C}{A - C}$$

$E_\tau(\kappa)$ are the eigenvalues of a matrix $\underset{\sim}{E}$ having non-zero elements given by[4]

$$E_{K,K} = F\ J(J+1) + (\ G-F\ )K^2$$

and

$$E_{K,K+2} = H\, f_K\, f_{K+1}$$

where

$$f_K = \left(J(J+1) - K(K+1) \right)^{1/2} .$$

F, G, and H are functions of the asymmetry parameter and the representation correlating a, b and c with x, y and z. The coefficients for the two representations of interest here are listed below[4].

	I^l (a=z, b=y, c=x)	III^r (a=x, b=y, c=z)
F	$(\kappa - 1)/2$	$(\kappa + 1)/2$
G	1	-1
H	$(\kappa + 1)/2$	$(\kappa - 1)/2$

Diagonalization of the $\underset{\sim}{E}$ matrix yields not only the energy eigenvalues for use with Eq. 18 but also the transformation coefficients for use with Eq. 17.

However, the actual calculation is greatly simplified by the use of the Wang basis set. The rotational wavefunctions are written as symmetric and antisymmetric linear combinations of symmetric rotor wavefunctions differing only in the sign of K. This is given by

(20) $$|J\,|K|\,M\,\gamma\rangle = 2^{-1/2}\left(|JKM\rangle + (-1)^{\gamma}\,|J\,-K\,M\rangle\right)$$

and $|J\,0\,M\,0\rangle = |J\,0\,M\rangle$.

The Wang transformation[12] factors the initial $\underset{\sim}{E}$ matrix of order 2J+1 into 4 submatrices of order $\sim J/2$. The submatrices are labeled E^+, O^+, O^- and E^- with

(E,O) denoting even or odd K values and (+,-) denoting symmetric or antisymmetric linear combinations. The matrix elements are described in the literature[4] and have the elements

$$O^{\pm} = \begin{pmatrix} E_{1,1} \pm E_{-1,1} & E_{1,3} & 0 \\ E_{1,3} & E_{3,3} & E_{3,5} \\ 0 & E_{3,5} & E_{5,5} \end{pmatrix}$$

$$E^{+} = \begin{pmatrix} E_{0,0} & \sqrt{2}\, E_{0,2} & 0 \\ \sqrt{2}\, E_{0,2} & E_{2,2} & E_{2,4} \\ 0 & E_{2,4} & E_{4,4} \end{pmatrix}$$

and E^{-} the same as E^{+} but with the first row and column removed. Diagonalization of these 4 submatrices yields energies $E_{\gamma}(\mathcal{K})$ and coefficients $a^{J}_{K\gamma}$. The symmetry properties of the submatrices facilitate determination of the selection rules.

The form of Eq. 7 implies a III^{r} representation. This is the proper correlation for molecules best described in the oblate limit. However, most molecules are best described in the prolate limit. As far as the energies and transformation coefficients are concerned, the calculation is performed in the proper limiting case by selection of the proper values of F, G and H. The situation, however, is somewhat more complicated for

the transition amplitudes which must be described in the same limit as the transformation coefficients.

For a one photon transition, the only part of I_1 which must be transformed is

(21) $$B_1(K,K') = M_{\Delta K} \begin{pmatrix} J & J' & 1 \\ K & -K' & \Delta K \end{pmatrix} .$$

For a two photon transition, the part of I_2 which must be transformed is

(22) $$B_2^{\bar{J}}(K,K') = M_{\Delta K}^{\bar{J}} \begin{pmatrix} J & J' & \bar{J} \\ K & -K' & \Delta K \end{pmatrix} .$$

In either case, a matrix $\underset{\sim}{X}^{sym}$ is filled with the elements of B such that rows are labeled by initial state and columns by final state quantum numbers. The elements are

(23) $$x_{ij} = B_n(2(i-1) + K_s , 2(j-1) + K_s')$$

where K_s is the starting K value of the submatrix. The K_s values are as follow:

K_s	Submatrix
0	E^+
1	O^+, O^-
2	E^-

In addition, in the Wang basis set the B element must be multiplied by the square root of two if one of the arguments is zero and the other unity.

The transition to asymmetric rotor amplitudes is given by the equation

(24) $$\underset{\sim}{X}^{asym} = \underset{\sim}{A}_1^{-1} \; \underset{\sim}{X}^{sym} \; \underset{\sim}{A}_2$$

where $\underset{\sim}{A}_1$ and $\underset{\sim}{A}_2$ are the transformation matrices for the lower and upper states, resp. As stated above, the B elements are valid only for representation III^r. The $\underset{\sim}{X}^{sym}$ matrix as previously defined can be transformed to representation I^l via the canonical transformation

$$\underset{\sim}{Y}^{sym} = \underset{\sim}{T}^{-1} \; \underset{\sim}{X}^{sym} \; \underset{\sim}{T}$$

where $\underset{\sim}{T}$ is a diagonal matrix with elements given by

(25) $$t_{ij} = \delta_{ij} \cdot (-1)^{i+1} .$$

Thus, the elements of $\underset{\sim}{Y}^{sym}$ are

(26) $$y_{ij} = x_{ij} \cdot (-1)^{i+j} .$$

Transition selection rules

The internal rotation group of the asymmetric rotor is the group V which defines four species of wavefunctions. This group is characterized by the following group table.

	E	C_c	C_b	C_a
A	1	1	1	1
B_c	1	1	-1	-1
B_b	1	-1	1	-1
B_a	1	-1	-1	1

Each of the four species A, B_a, B_b and B_c may be characterized by the double indices ee, eo, oo and oe, resp., in which the first symbol gives the parity in the prolate limit and the second, in the oblate limit. The parity is e for even K and o for odd K.

The Wang basis functions which give rise to wavefunctions of the type E^+, O^+, O^-, E^- are constructed relative to an arbitrary axis system and not to a, b and c. Thus, they are characterized by the representations A, B_x, B_y and B_z. The following correlation exists.[4]

	J_{even}	J_{odd}
E^+	A	B_z
O^+	B_y	B_x
O^-	B_x	B_y
E^-	B_z	A

This table may be used to map the Wang type functions into the molecule fixed functions. Given any particular representation which identifies x, y and z with a, b and c, the correlation is always one to one. Symmetry considerations allow, at most, four different transition types. In the following table, all possible transition types are listed. The symmetry index refers to the symmetry of the product of the representations of the intial and final states.

Type	Symmetry	I^l	III^r	Transitions
1	A	A	A	ee ⇜⇝ ee
				oo ⇜⇝ oo
				oe ⇜⇝ oe
				eo ⇜⇝ eo
2(A)	B_a	B_z	B_x	ee ⇜⇝ eo
				oo ⇜⇝ oe
3(B)	B_b	B_y	B_y	ee ⇜⇝ oo
				eo ⇜⇝ oe
4(C)	B_c	B_x	B_z	ee ⇜⇝ oe
				oo ⇜⇝ eo

The allowed transitions may be identified by noting that the product of the symmetry representations of operator and wavefunctions in the matrix element $\langle \Psi_2 | H' | \Psi_1 \rangle$ must contain the totally symmetric representation.

For one photon absorption, the dipole operator is responsible for the observed transitions. Its components have the symmetry B_x, B_y and B_z. Thus, the totally symmetric type 1 transitions never occur. For a change in electric moment parallel to the a, b or c axis, a transition of type 2(A), 3(B) or 4(C), resp., is allowed.

The case of two photon absorption is only slightly more complicated. McClain[13] has shown that the two photon tensor of the D_{2h} symmetry group, which contains

all asymmetric rotor groups as subgroups, can be partitioned as follows:

$$A = \begin{pmatrix} x^2 & 0 & 0 \\ 0 & y^2 & 0 \\ 0 & 0 & z^2 \end{pmatrix} \qquad B_1 = \begin{pmatrix} 0 & xy & 0 \\ yx & 0 & 0 \\ 0 & 0 & 0 \end{pmatrix}$$

$$B_2 = \begin{pmatrix} 0 & 0 & xz \\ 0 & 0 & 0 \\ zx & 0 & 0 \end{pmatrix} \qquad B_3 = \begin{pmatrix} 0 & 0 & 0 \\ 0 & 0 & yz \\ 0 & zy & 0 \end{pmatrix}$$

By knowing which subtensor is non-zero, the allowed transition type can be obtained from the following table.

Non-zero tensor	Type (I^l)	Type (III^r)
A (x^2, y^2, z^2)	1	1
B_1 (xy, yx)	2	4
B_2 (xz, zx)	3	3
B_3 (yz, zy)	4	2

In addition, the one photon operator transforms as a translation and thus connects states of differing (u, g) symmetry. The two photon operator, which transforms as a rotation, connects states of the same (u, g) symmetry.

Rotational contour program

A rotational band contour analysis program for asymmetric rotors was developed for one and two photon absorption. A very brief flowchart of the program is

shown on Fig. 36. The initialization section read in such data as inertial constants, temperature, transition symmetry and photon count. The program would then cycle through all ground state J values with a maximum of 120 for 1 photon and 119 for 2 photon absorption. For each J value, a scan of all possible one or two photon transitions was made until an allowed transition was found.

The excited state eigenvalues and eigenvectors were then calculated and stored. The ground state eigenvalues and vectors were calculated only if the ground state J and/or Wang symmetry differed from those of the last allowed transition. Otherwise, the previous values were used. Diagonalization of the Wang submatrices utilized the Fortran subroutine SQL2 which employed the QR transformation technique.

Symmetric rotor amplitudes were then calculated and transformed by the ground and excited state eigenvectors. From the final matrix, the total transition probability was calculated and summed in a matrix to give the contour. For 2 photon absorption, the last step was repeated for $\overline{J}$ = 0, 1 and 2, each having a seperate contour matrix. This allowed the plot program to dynamically fill in the photon polarization coefficients, $C_{\overline{J}}$. At the end of the calculation, all data was stored on disk and could be plotted later.

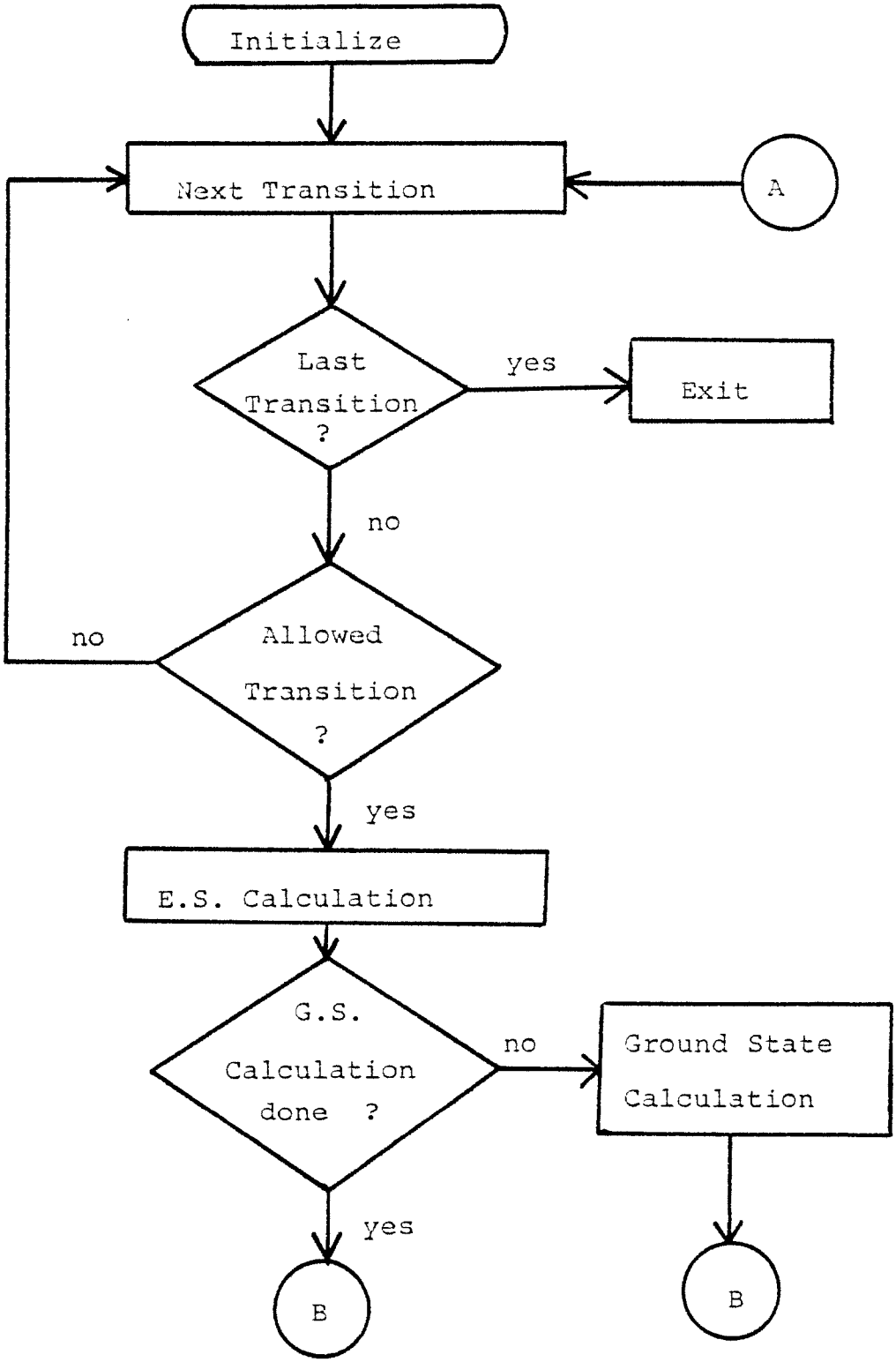

Figure 36. Rotational program flowchart.

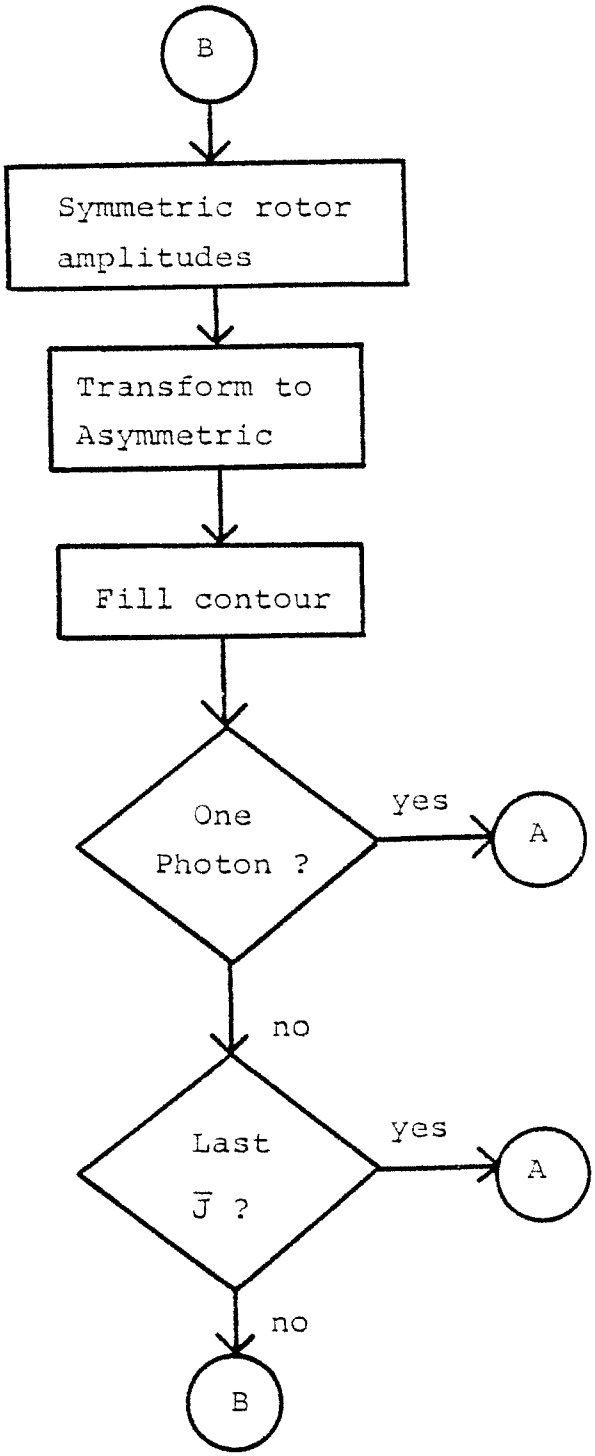

Figure 36. (cont.)

One photon band contour calculations were made for naphthalene,h_8. Transitions involving vibrations of a_g symmetry and the origin exhibit type A contours. The calculation shown on Fig. 37 may be compared with the measured spectra on Figs. 18, 26 and 34. Transitions involving b_{1g} vibrations exhibit type B contours. The calculated contour on Fig. 38 may be compared with measured spectra on Figs. 20, 24 and 30. In each case, calculated and measured absorption spectra are very well correlated.

Two photon calculations were also made for naphthalene,h_8. Boesl, et al.[14] have measured transitions of a_g and b_{1g} symmetry. A difficulty in the calculation of two photon a_g transitions is that the two photon tensor contains the elements x^2, y^2 and z^2, all of which are, in general, different. The calculated contour, moreover, is very sensitive to the relative values of these elements.

The fact that no b_{2g} or b_{3g} transition was observed indicates that z^2 is very small. The observation of a b_{1g} transition indicates that both x^2 and y^2 are non-zero. Hence it is necessary to vary the ratio x^2/y^2 until a best fit with experiment is obtained. Calculations for $x^2/y^2 = 9$, 3 and 1 are shown on Figs. 39, 40 and 41, respectively. The contour showing the best fit is for $x^2/y^2 = 3$.

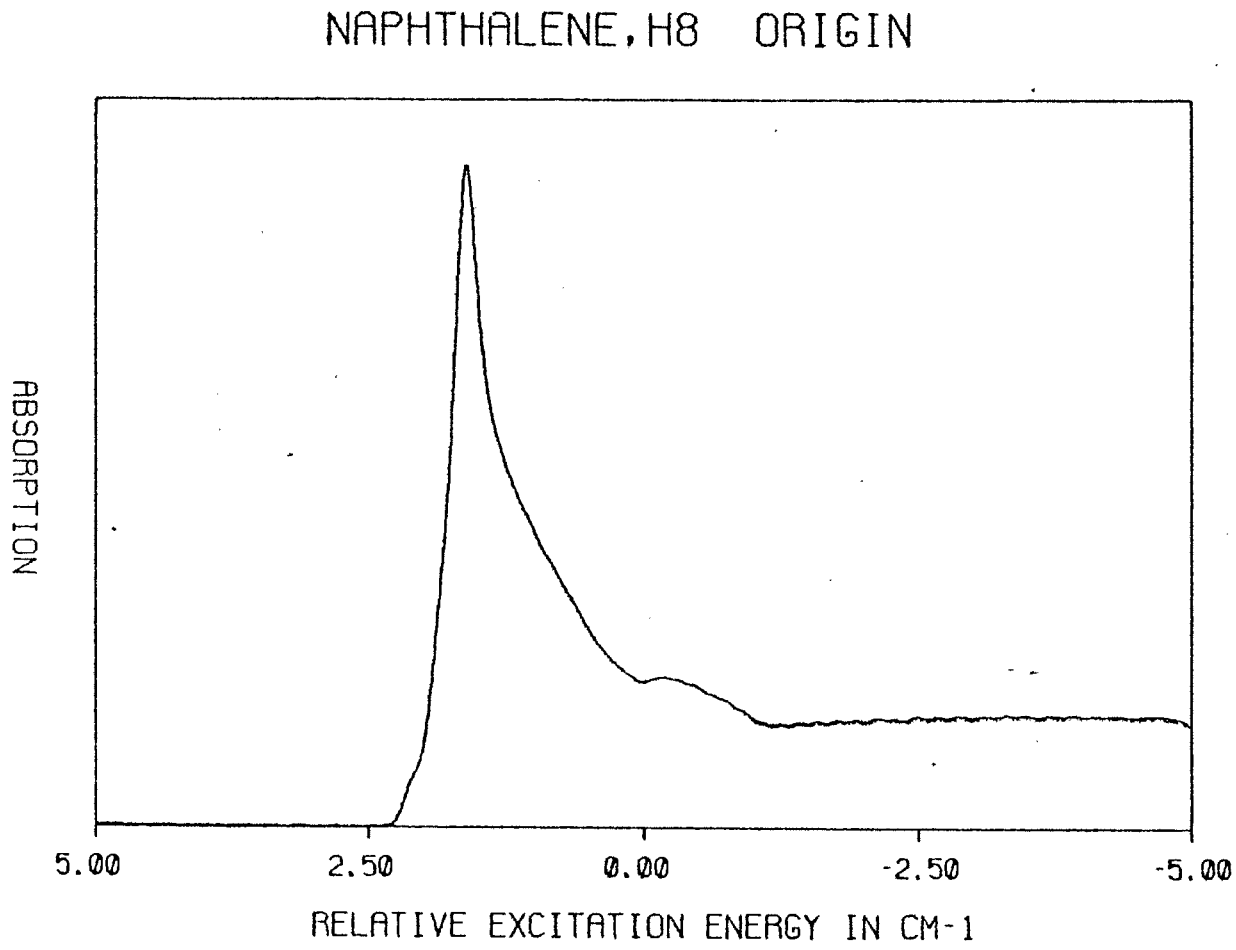

Figure 37. Calculated contour of the 0-0 transition.

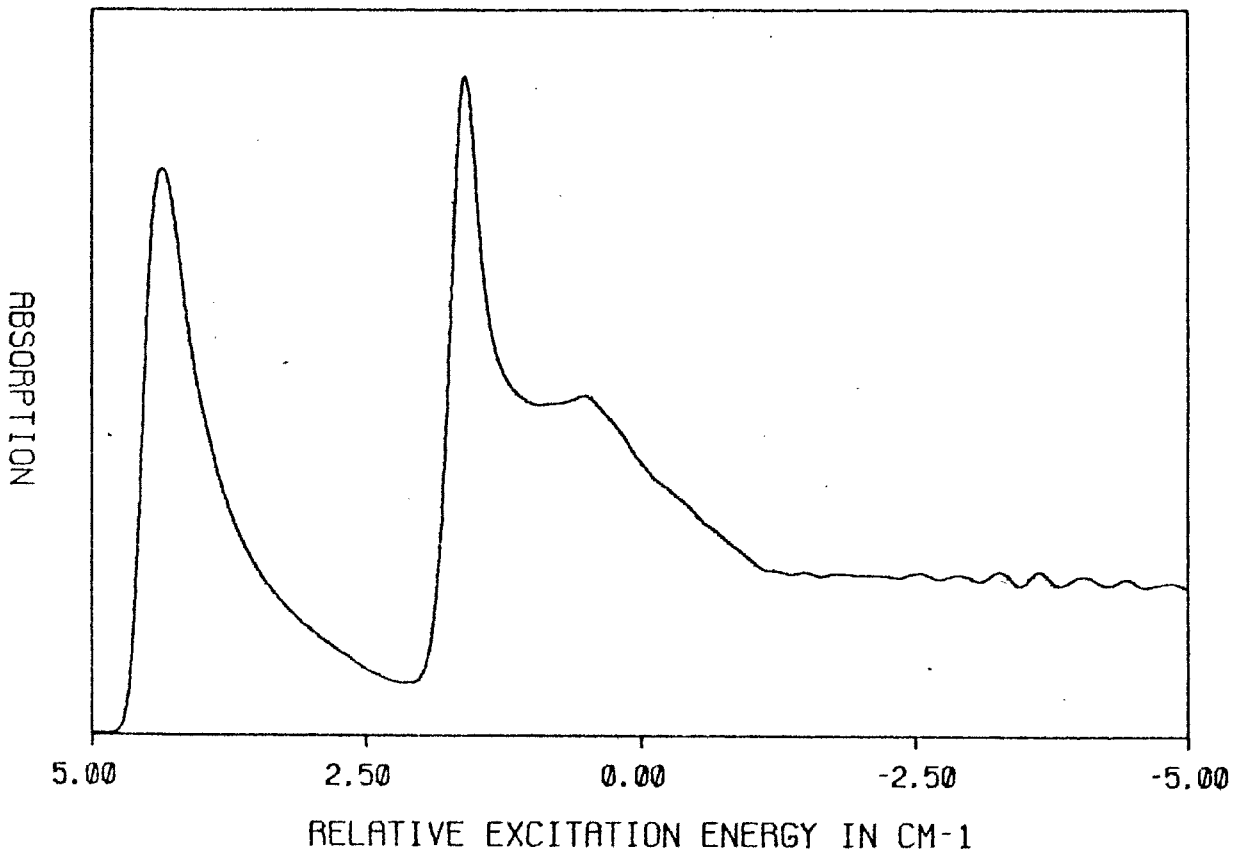

Figure 38. Calculated contour of the $8(b_{1g})_o^1$ band of naphthalene,h_8.

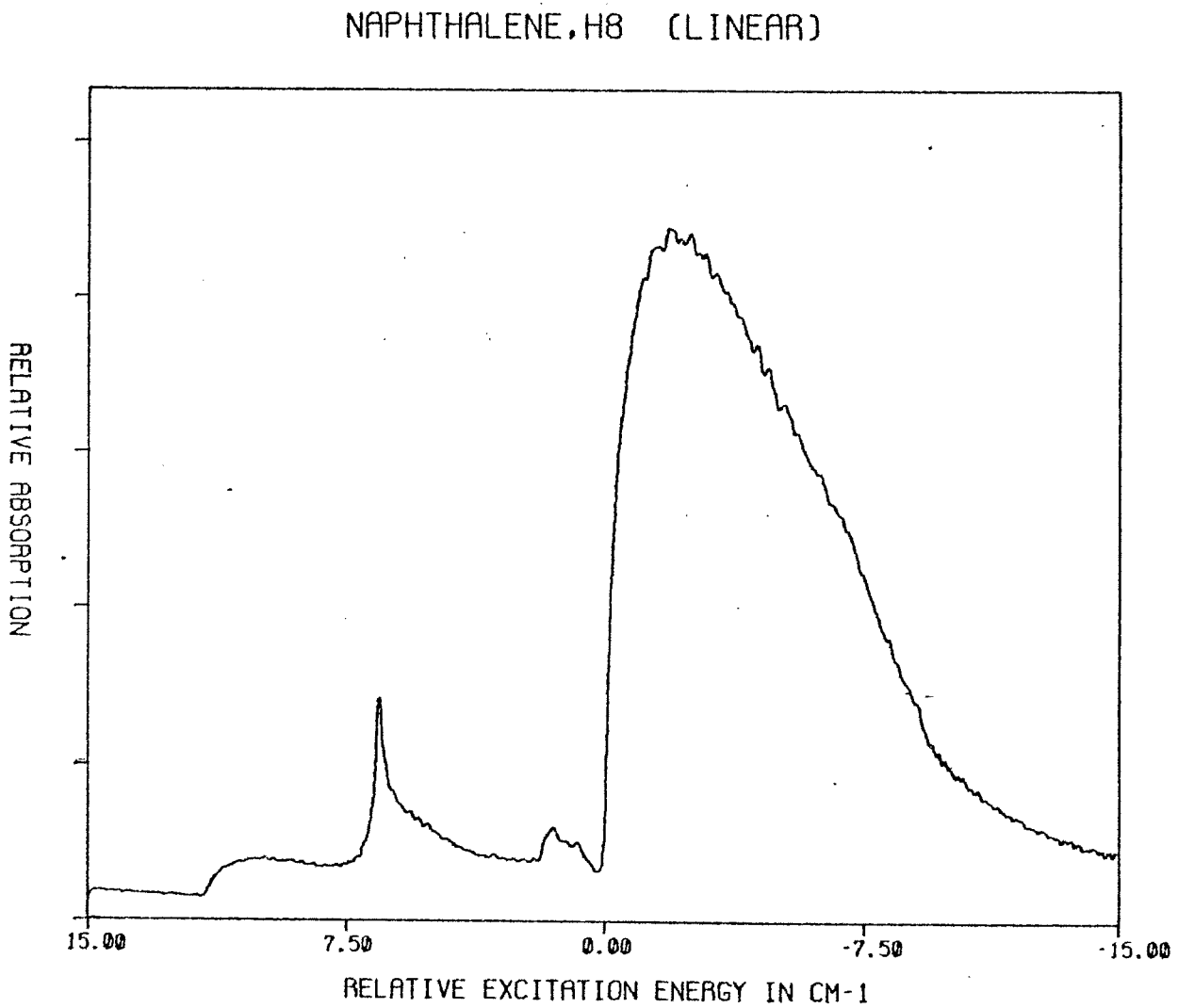

Figure 39a. Calculated 2 photon a_g contour with $x^2/y^2 = 9$ for naphthalene,h_8.

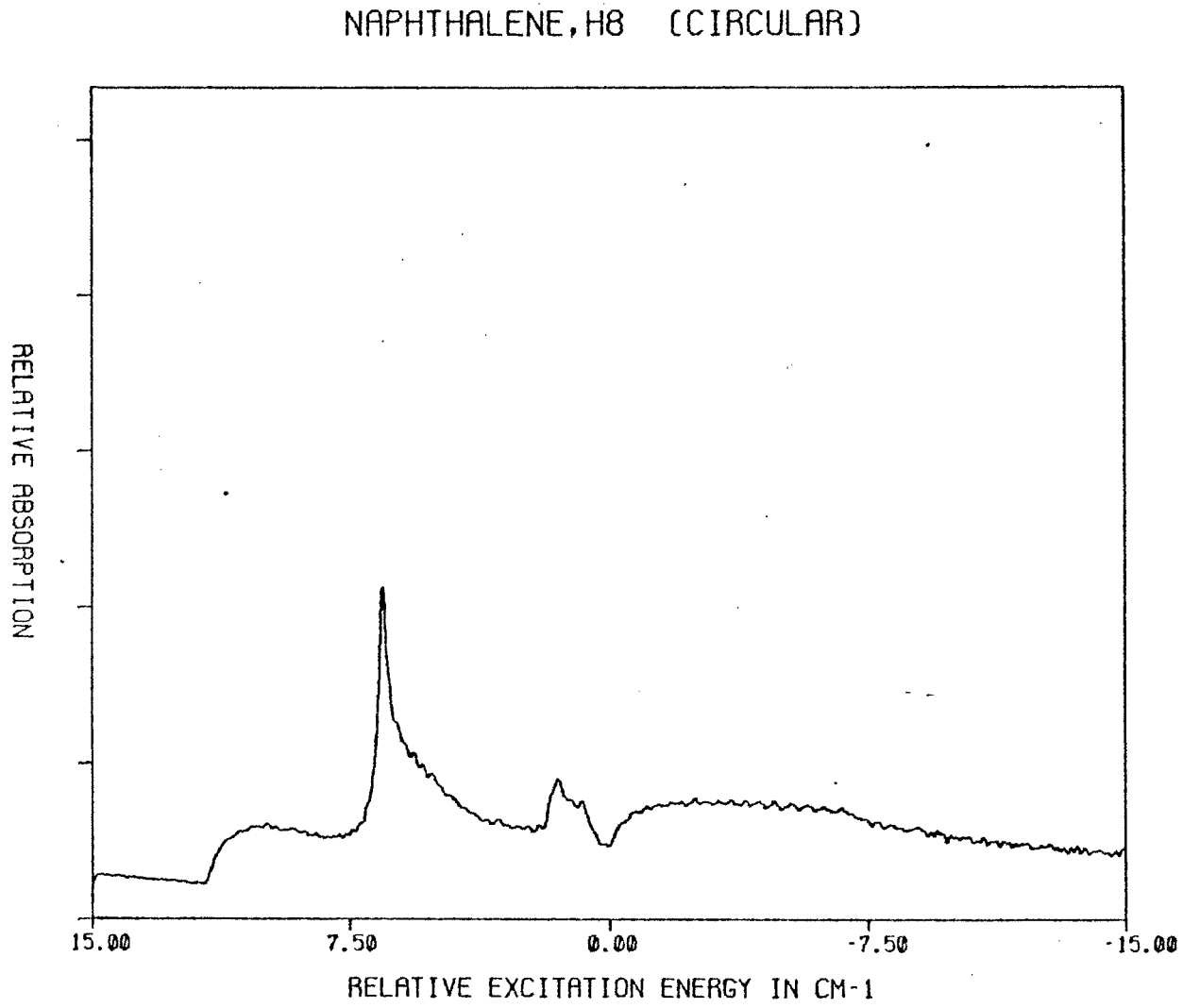

Figure 39b. Calculated 2 photon a_g contour with $x^2/y^2 = 9$.

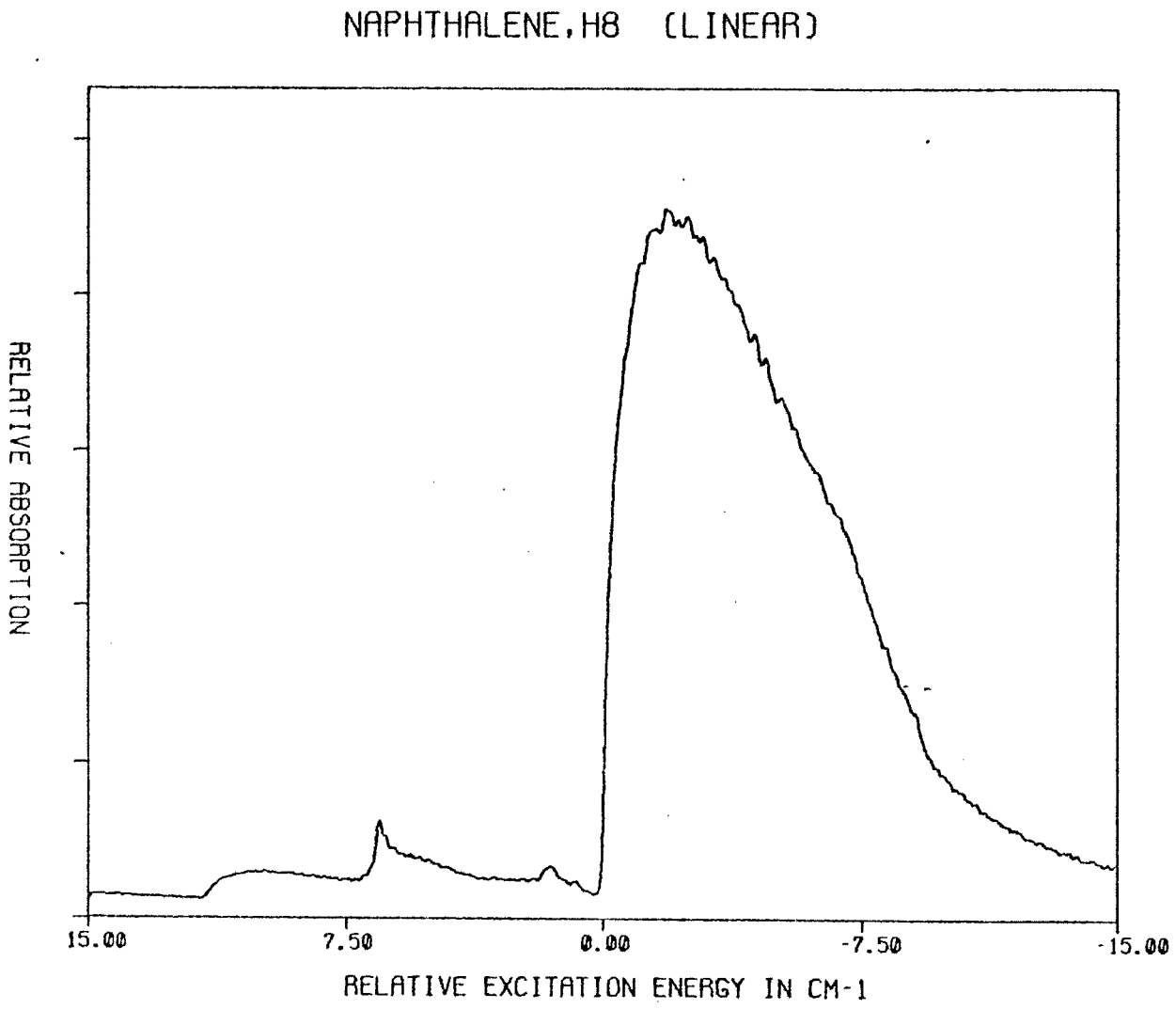

Figure 40a. Calculated 2 photon contour (a_g) with $x^2/y^2 = 3$.

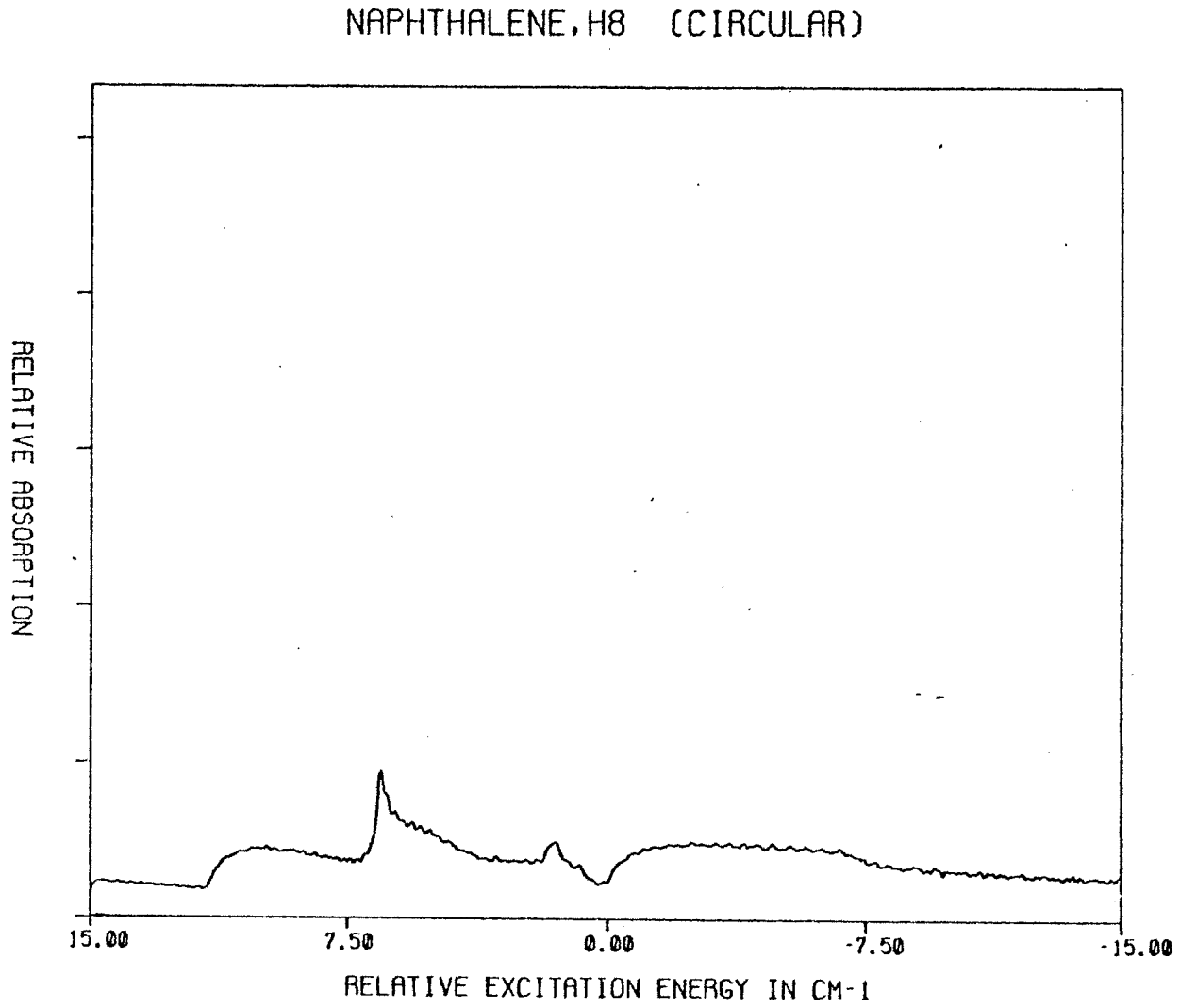

Figure 40b. Calculated 2 photon contour (a_g) with $x^2/y^2 = 3$.

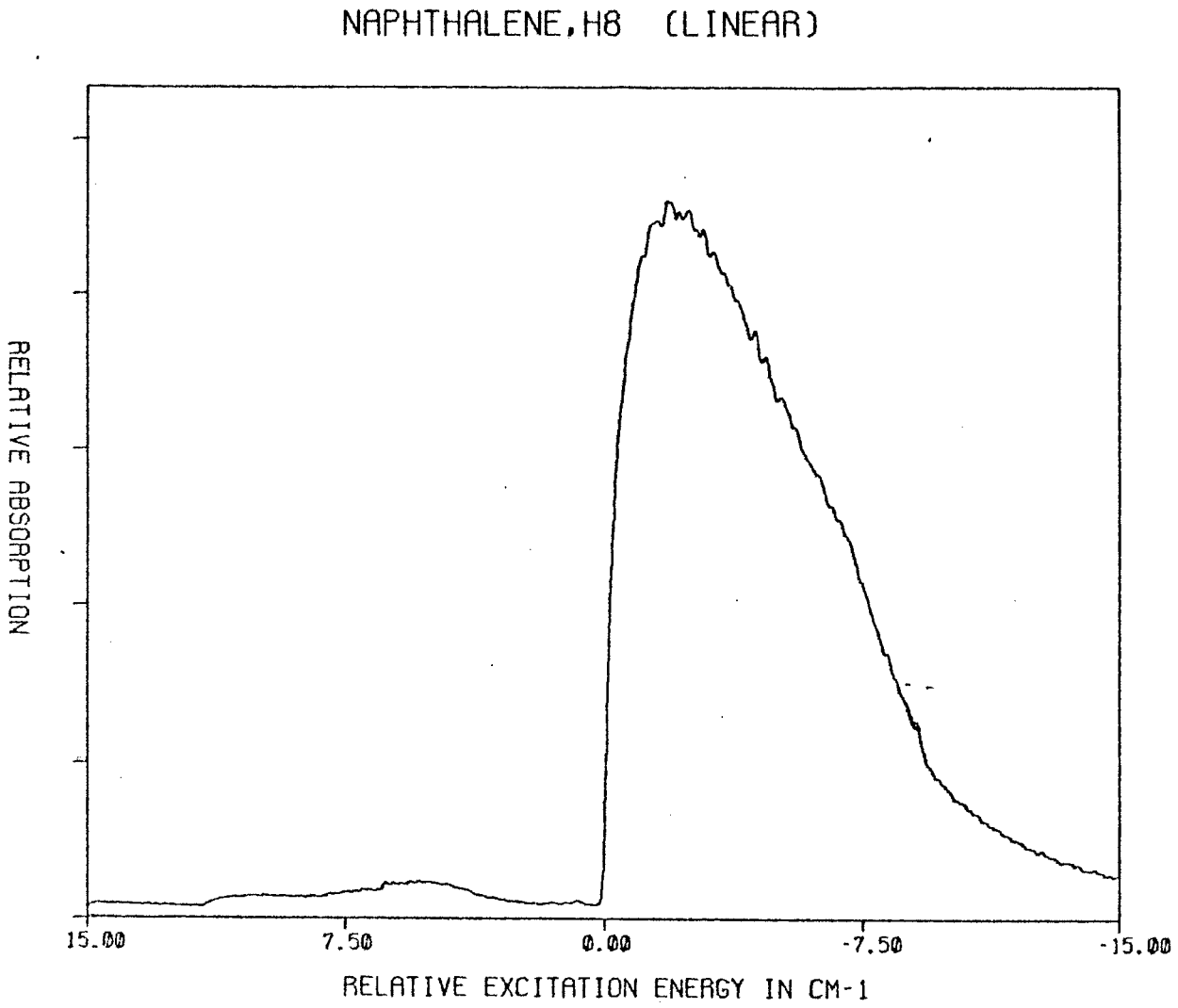

Figure 41a. Calculated 2 photon a_g contour with $x^2=y^2$.

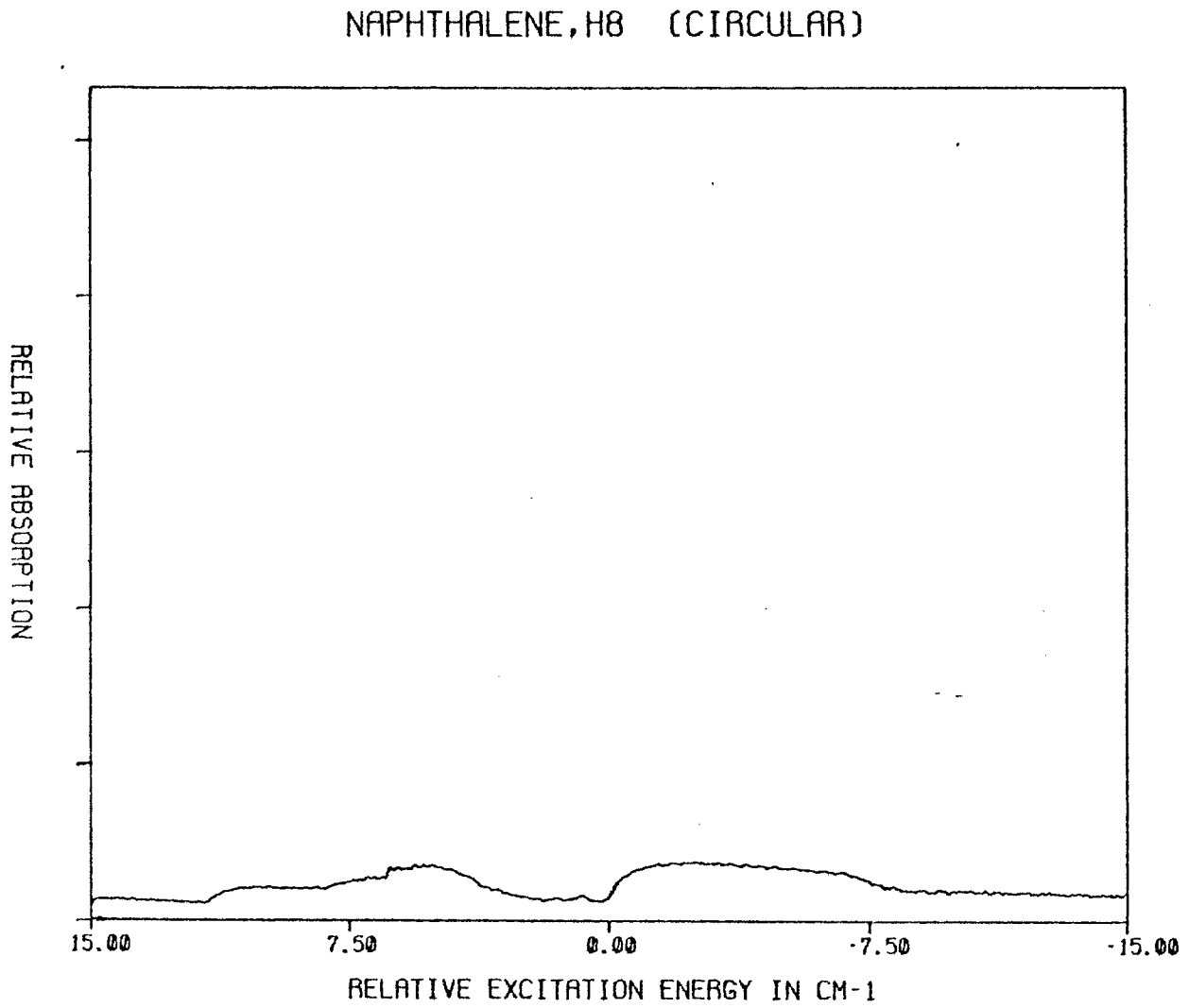

Figure 41b. Calculated 2 photon a_g contour with $x^2=y^2$.

On Fig. 42, the calculated b_{1g} contour is shown. For this calculation no parameters were adjusted since, for photons of the same energy, xy=yx. The poor experimental resolution makes a comparison very difficult for this band.

The excited state ensemble

As stated at the beginning of this chapter, the ground state ensemble has an important influence on the nature of the absorption spectrum. Likewise, the excited state ensemble has an important influence on the observed ISC rates. The exact nature of this influence will be discussed in Chapter VIII.

Using a modified version of the previously described contour program, the excited state rotational distribution was calculated as a function of excitation energy and resolution. For the results reported here, the resolution was fixed at 0.2 cm^{-1} which is almost the same as the resolution for the measured absorption and quantum yield spectra. The calculated excited state rotational distributions are all related to the $8(b_{1g})^1_o$ contour as shown on Fig. 38. Results for relative excitation energies of 0.0 cm^{-1}, 1.5 cm^{-1} (red peak), 2.5 cm^{-1}, 3.5 cm^{-1} and 4.23 cm^{-1} (blue peak) are shown on Figs. 43, 44, 45, 46 and 47, respectively.

The calculations show that the excited state rotational distributions vary strongly as a function

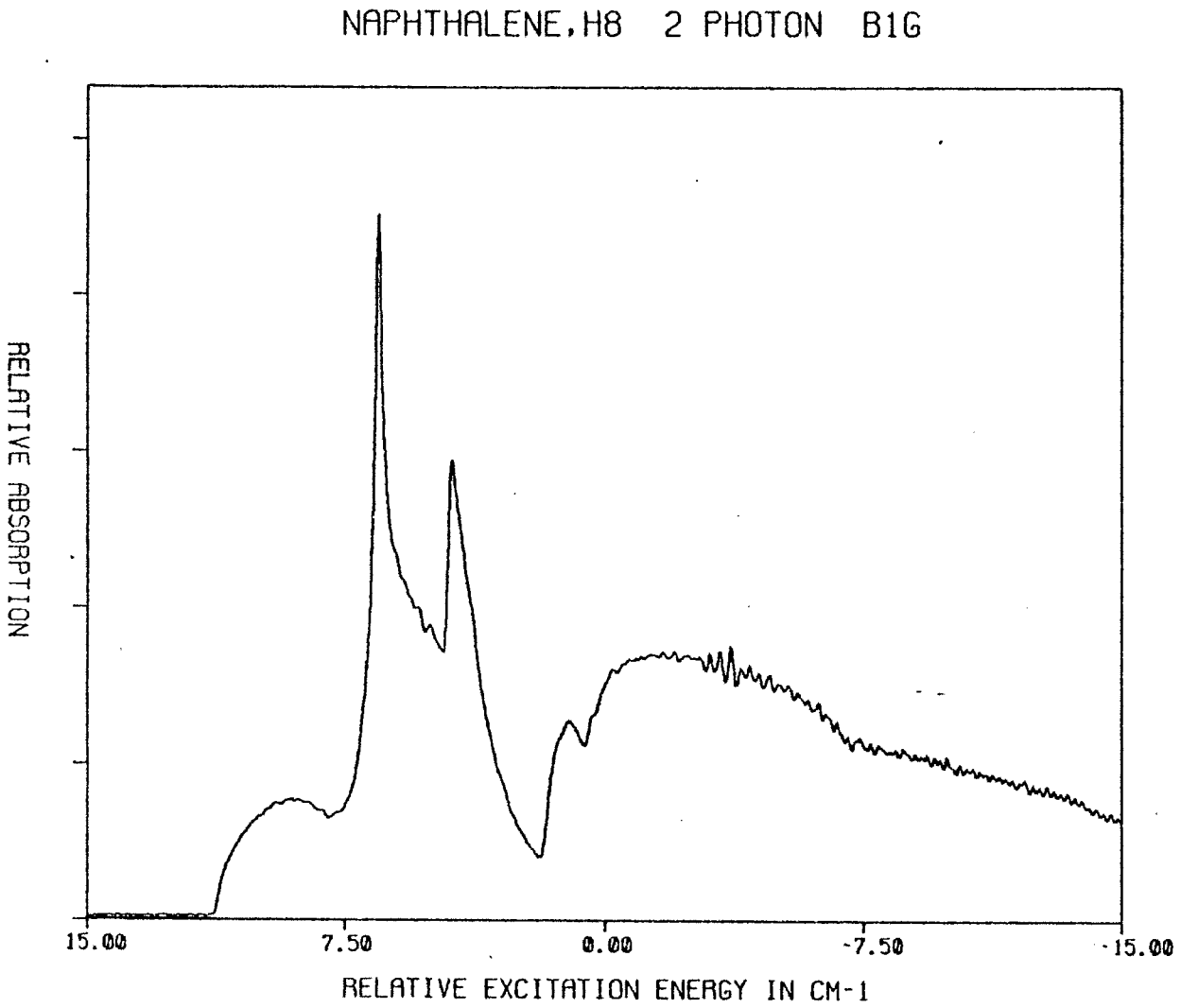

Figure 42. Calculated 2 photon contour (b_{1g}).

Figure 43. The rotational distribution in the excited state of naphthalene, h_8 at the band origin.

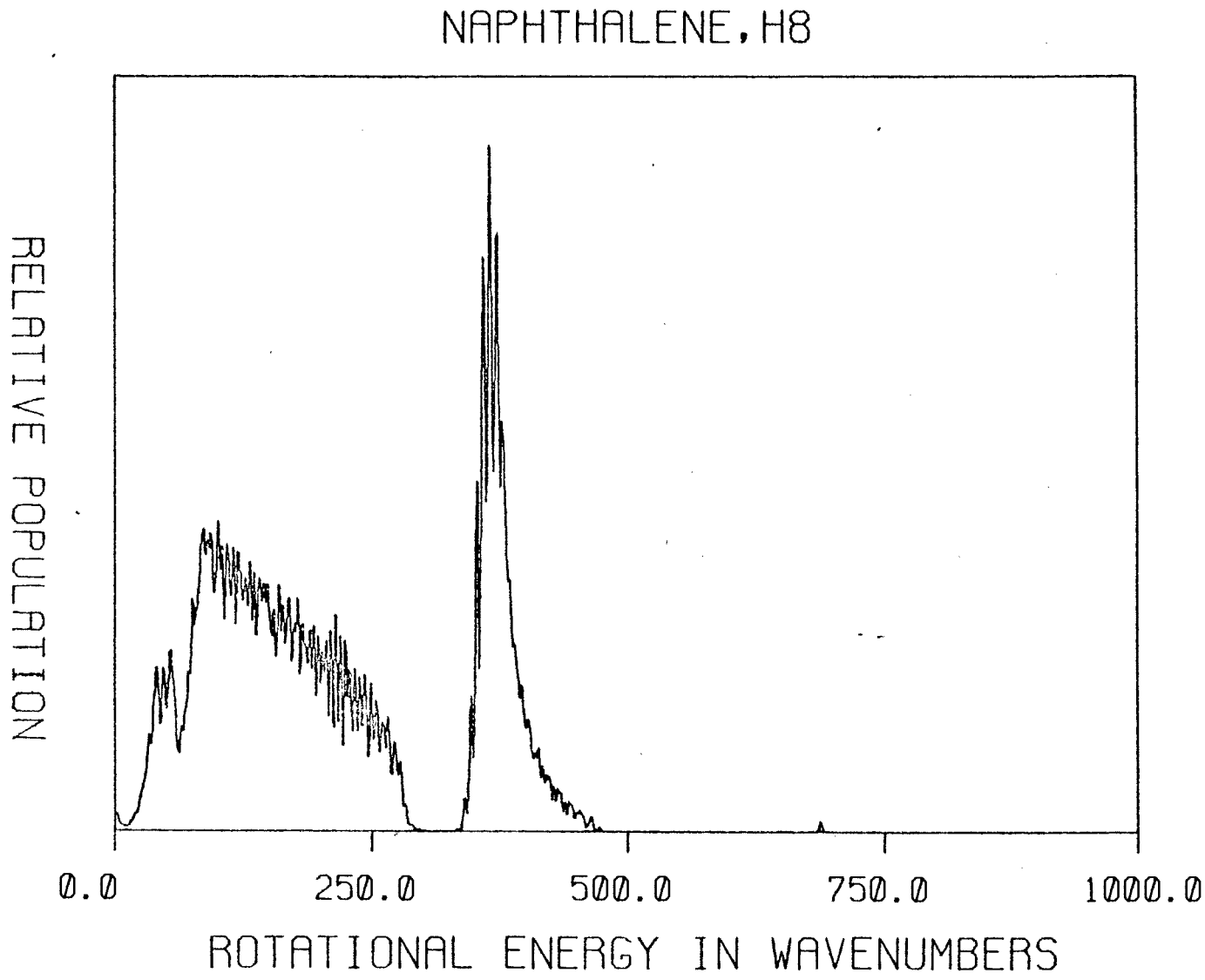
NAPHTHALENE, H8
RELATIVE POPULATION
0.0
250.0
500.0
750.0
1000.0
ROTATIONAL ENERGY IN WAVENUMBERS

Figure 44. The rotational distribution in the excited state of naphthalene, h_8 following optical excitation of 0.2 cm^{-1} bandwidth, 1.5 cm^{-1} to the blue of the band origin.

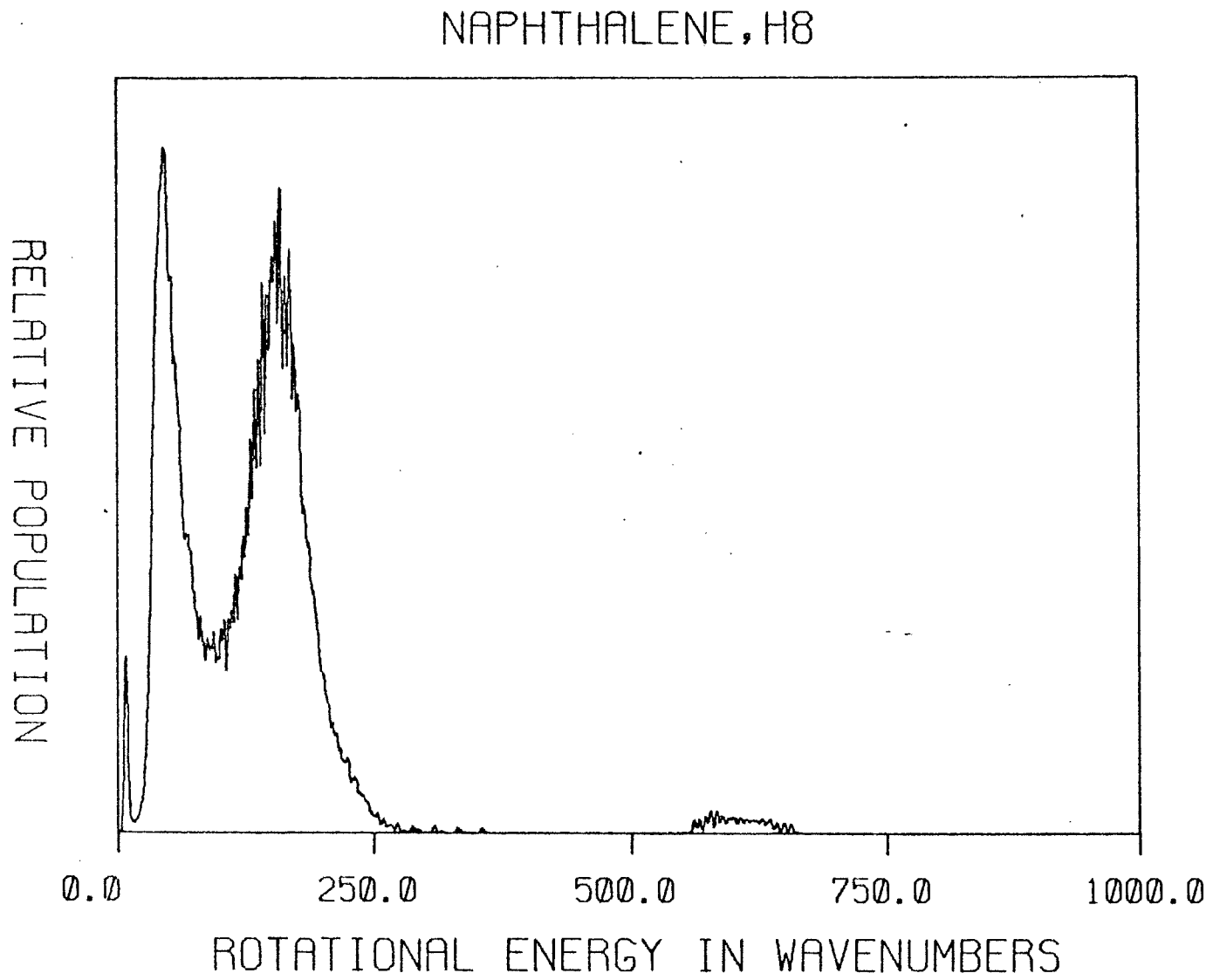
NAPHTHALENE, H8
RELATIVE POPULATION
0.0
250.0
500.0
750.0
1000.0
ROTATIONAL ENERGY IN WAVENUMBERS

Figure 45. The rotational distribution in the excited state of naphthalene, h_8 following optical excitation of 0.2 cm^{-1} bandwidth, 2.5 cm^{-1} to the blue of the band origin.

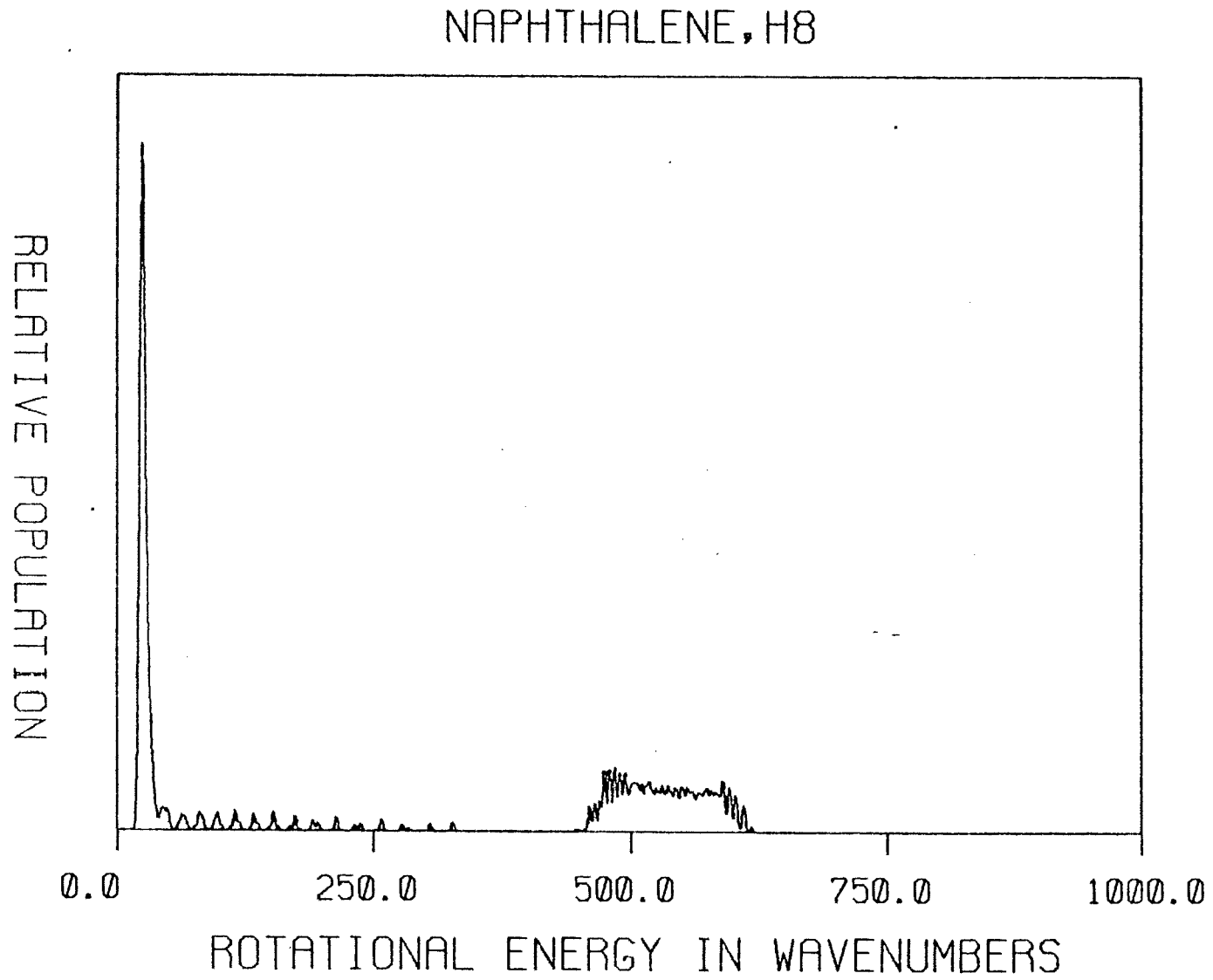
NAPHTHALENE, H8
RELATIVE POPULATION
0.0
250.0
500.0
750.0
1000.0
ROTATIONAL ENERGY IN WAVENUMBERS

Figure 46. The rotational distribution in the excited state of naphthalene, h_8 following optical excitation of 0.2 cm^{-1}, 3.5 cm^{-1} to the blue of the band origin.

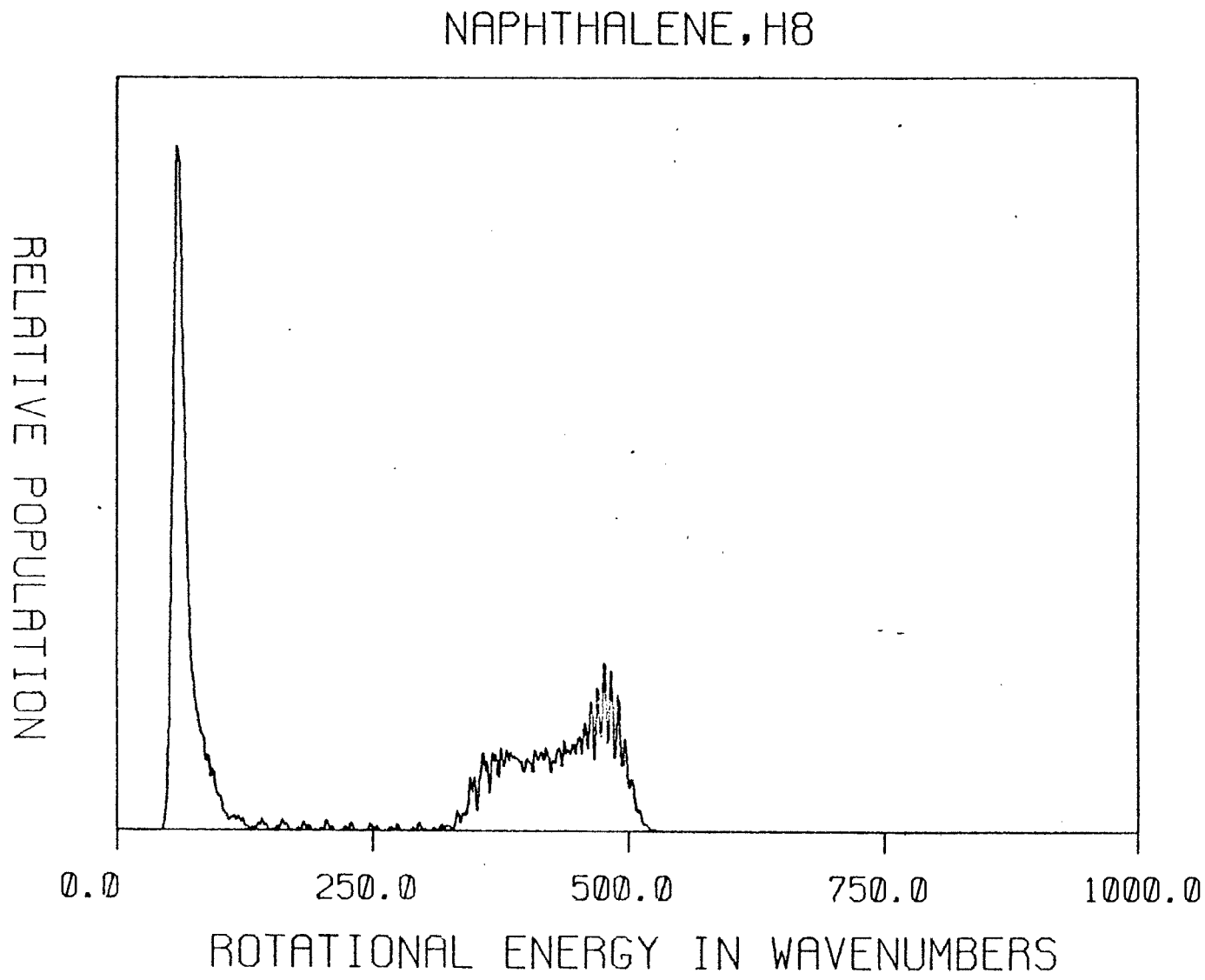
NAPHTHALENE, H8
RELATIVE POPULATION
0.0
250.0
500.0
750.0
1000.0
ROTATIONAL ENERGY IN WAVENUMBERS

Figure 47. The rotational distribution in the excited state of naphthalene, h_8 following optical excitation of 0.2 cm^{-1} bandwidth, 4.23 cm^{-1} to the blue of the band origin.

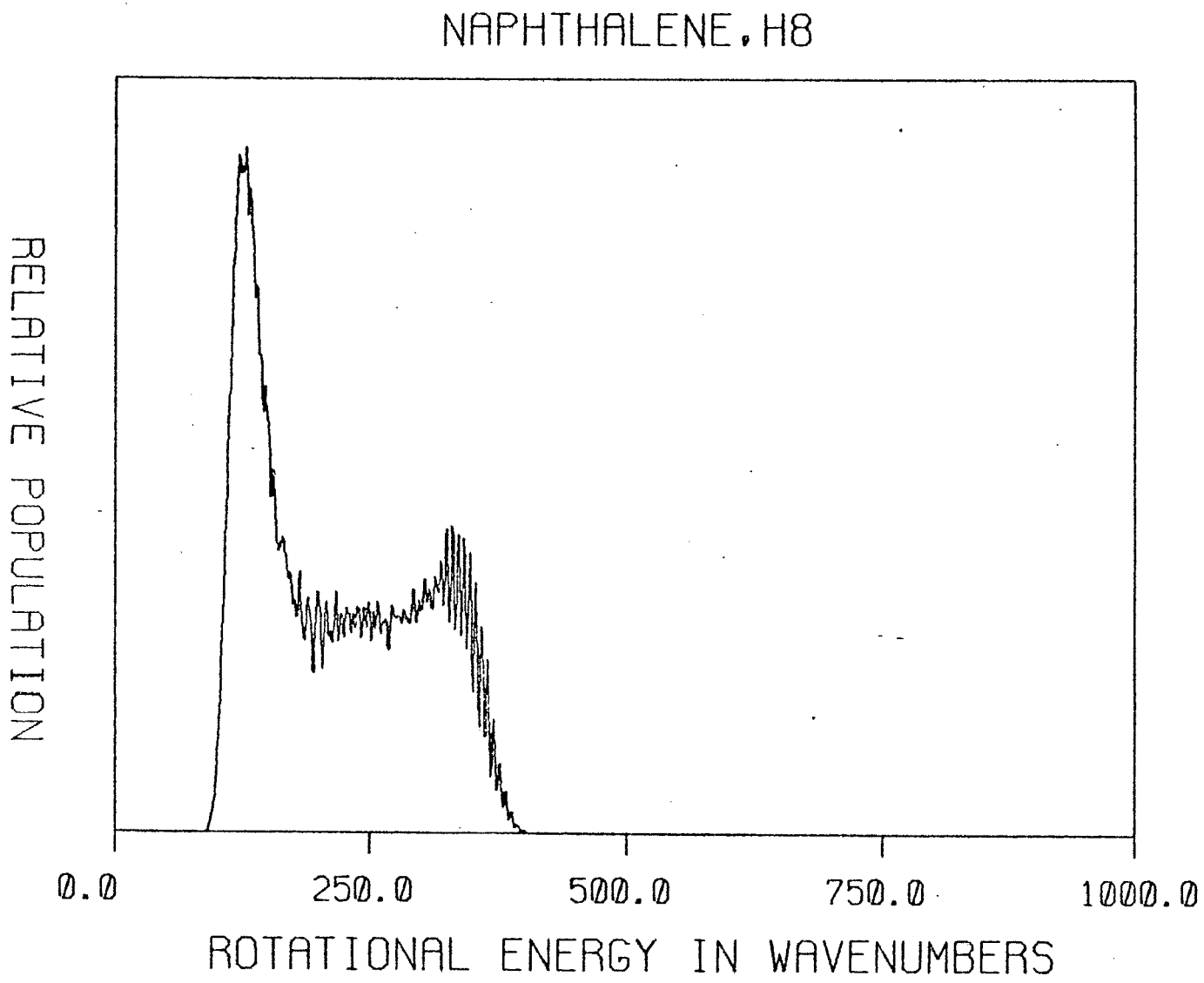
NAPHTHALENE, H8
RELATIVE POPULATION
0.0
250.0
500.0
750.0
1000.0
ROTATIONAL ENERGY IN WAVENUMBERS

of excitation energy. Variations of over 200-300 cm^{-1} seem to be typical. Indeed, the form of the distribution is markedly different from that of the ground state as shown on Fig. 35 and depends strongly on the excitation energy. A larger bandwidth tends to spread out the distribution and a smaller bandwidth tends to make it more linelike. In the limit of very large excitation bandwidths, the distribution would almost mirror the ground state distribution.

Appendix 1

The Wigner 3-J Symbols

Throughout this work, the Wigner 3-J symbols are used. In this appendix a brief explanation of their meaning is presented. A detained description can be found in the books of Edmonds[9] or Rose[15].

The Wigner 3-J symbols arise from a description of the coupling of two angular momenta. Coupling of more is generally described by the 6-J or 9-J symbols. For a system with two angular momenta which satisfy the commutation relation

$$\left[\tilde{J}_1 , \tilde{J}_2 \right] = 0 ,$$

there exist simultaneous eigenvectors which are given by $| J_1 \; M_1 \; J_2 \; M_2 \rangle$ where the M quantum number refers to the z axis projection of J. In this system, the angular momenta are seperately quantized. If $\tilde{J}_1$ adds to $\tilde{J}_2$ via the operator equation

$$\tilde{J} = \tilde{J}_1 + \tilde{J}_2 ,$$

the eigenvectors of the coupled system are given by $| J_1 \; J_2 \; J \; M \rangle$. The two sets of angular momentum eigenvectors are related via the unitary transformation

$$| J_1 \; J_2 \; J \; M \rangle = \sum_{M_1, M_2} |J_1 \; M_1 \; J_2 \; M_2\rangle \; (J_1 \; M_1 \; J_2 \; M_2 \, | \, J_1 \; J_2 \; J \; M)$$

The terms of the form $(\cdots | \cdots)$ are the vector-coupling or Clebsch-Gordon (CG) coefficients. The non-symmetric relations between the CG coefficients prompted the

introduction of the Wigner 3-J symbols. They are defined by the equation

$$\begin{pmatrix} J_1 & J_2 & J \\ M_1 & M_2 & M \end{pmatrix} = (-1)^{J_1 - J_2 - M} (2J+1)^{-1/2} \cdot \left(J_1 M_1 \; J_2 M_2 \mid J_1 J_2 \; J\text{-}M \right).$$

Thus, the two basis sets are related by the equation

$$\left| J_1 \; J_2 \; J \; M \right\rangle = \sum_{M_1, M_2} \left| J_1 M_1 \; J_2 M_2 \right\rangle (-1)^{J_2 - J_1 - M} (2J+1)^{1/2} \begin{pmatrix} J_1 & J_2 & J \\ M_1 & M_2 & -M \end{pmatrix}.$$

The value of the 3-J symbol is unchanged by an even permutation of the columns and must only be multiplied by $(-1)^{J_1 + J_2 + J}$ for an odd permutation or if all M values are negated.

Thus, the 3-J symbols simply represent coupling coefficients between different sets of angular momentum eigenfunctions. For example, in optical absorption terms of the form $\begin{pmatrix} J_1 & J_2 & 1 \\ M_1 & -M_2 & q \end{pmatrix}$ arise. The initial rotational state $\left| J_1 \; M_1 \right\rangle$ is coupled with a photon state $\left| 1 \; q \right\rangle$ where q is the polarization, ± 1 or 0, of the photon. Absorption produces a final state $\left| J_2 \; M_2 \right\rangle$ Non-zero 3-J symbols arise only on the condition that $J_1 + J_2 \geq 1 \geq |J_1 - J_2|$. This immediately gives rise to the selection rules $\Delta J = \pm 1, 0$ and $J_1 = 0 \not\leftrightarrow J_2 = 0$. Thus, the symmetry properties of the 3-J symbols can often be used to obtain the selection rules for the

process.

The equation $\tilde{J} = \tilde{J}_1 + \tilde{J}_2$ can be rearranged to give

$$\tilde{J}_1 = -\tilde{J}_2 + \tilde{J} \ .$$

In this equation, a partial angular momentum is given as the vector difference of the total and another partial angular momentum. Such a situation often arises with respect to molecular rotation and has been discussed in detail by Van Vleck[16]. The important point is that $-\tilde{J}_2$ is a time reversed angular momentum operator which has eigenfunctions that are time reversed relative to those of $\tilde{J}_2$. The operation of time reversal on the eigenvectors gives

$$\widetilde{|J_2\ M_2\rangle} = (-1)^{J_2 + M_2} \ |J_2\ -M_2\rangle \ .$$

The coupling in this case can also be described by the Wigner 3-J symbols.

References to Chapter VI

1. W. Burmeister, Ber. Deutsch. Phys. Ges., 15, 575 (1913).
2. S. L. Gerhard and D. M. Dennison, Phys. Rev., 43, 197 (1933).
3. J. C. D. Brand, MTP International Review of Science: Spectroscopy, ed. D. A. Ramsey, (Butterworth & Co., London, 1972).
4. A. C. Allen and P. C. Cross, Molecular Vib-Rotors, (J. Wiley & Sons, New York, 1963).
5. W. Gordey and R. L. Cook, Microwave Molecular Spectra, (Interscience, New York, 1970).
6. G. W. Hills and W. J. Jones, J. C. S. Faraday II, 71, 812 (1975).
7. G. W. Hills and W. J. Jones, J. C. S. Faraday II, 71, 827 (1975).
8. G. W. Hills amd W. J. Jones, J. C. S. Faraday II, 71, 835 (1975).
9. A. R. Edmonds, Angular Momentum in Quantum Mechanics, (Princeton Univ. Press, Princeton, 1959).
10. F. Metz, L. Wunch, H. J. Neusser, W. E. Howard and E. W. Schlag, preprint.
11. B. S. Ray, Z. Physik, 78, 74 (1932).
12. S. C. Wang, Phys. Rev., 34, 243 (1929).
13. W. M. McClain, J. Chem. Phys., 55, 2789 (1971).
14. U. Boesl, H. J. Neusser and E. W. Schlag, Chem. Phys., 15, 167 (1976).
15. M. E. Rose, Elementary Theory of Angular Momentum, (Wiley, New York, 1957).
16. J. H. Van Vleck, Rev. Mod. Phys., 23, 213 (1951).

Chapter VII

Characteristics of the Excited State Ensemble

Introduction

In the last chapter, the excited state ensemble of a single vibronic level was shown to vary as a function of excitation energy and resolution. In general, each of the ro-vibronic states in the ensemble can have a different lifetime and quantum yield. The consequences of this on the observed, experimental lifetimes and quantum yields will be discussed in the next chapter. However, the factors which could alter the initial state distribution will be discussed first. There are two that are important: collisions and intramolecular energy transfer.

Isolated molecule conditions

For a molecule to be isolated, the effect of the environment must be such that neither the energies of the molecular states are shifted on the relevant molecular energy scale nor transitions induced between states on the relevant experimental time scale. These two requirements describe the maximum perturbation which can come from the environment. However, only the latter can change the initial rotational distribution. In the gas phase, collisional effects arise from both the cell wall and other molecules.

Collisions with the wall generally destroy the excited molecular states. As a minimum, the ro-vibronic distribution is completely destroyed. In lifetime or quantum yield work, considerable error can be introduced. This is clearly seen, for example, in the work on SO_2 by Brus and McDonald[1] where longer lifetimes were observed than in any previous experiment. This was attributed to a much larger cell size which reduced the number of wall collisions. This problem has been analyzed in detail by Sackett[2] and is generally not important for molecules as large as naphthalene.

Collisions with other molecules present considerably more difficulties, however. At high pressures, any rotational distribution will assume the thermalized form shown on Fig. 35 on a timescale short relative to radiative decay.

Vibronic redistribution is generally the result of short range forces between the collision partners. However, a dipole-dipole interaction which produces electronic energy transfer at large distances can occur. This effect has been postulated as operative in NO[3] and glyoxal[4] but has not yet been observed for molecules the size of benzene, or larger.

Collisions which result in rotational redistribution ganerally have large cross sections. Thus, rotational scrambling of the initial rotational ensemble

formed by optical excitation can occur at pressures which do not disturb the vibrational purity of the excited state. Hence, the measurement of the properties of specific rotational ensembles requires much lower pressures than measurements involving only single vibronic levels.

Intramolecular energy redistribution

In the absence of collisions, there is still a possibility of energy redistribution within the excited electronic state. However, very strict rotational selection rules ($\Delta J = 0$ and $\Delta K = 0$) do not allow any change in the rotational ensemble. Thus, redistribution is limited to vibrational degrees of freedom.

The possibility of redistribution influences the selection of a model to describe the experimental data. In the limit of a large density of states and complete redistribution, the model of communicating states is applicable. In the limit of small density of states, models of discrete states must be used. The applicable coupling regime depends not only on the size of the molecule but also on the critical energy required to turn from one type of dynamic process to another. This is designated as the turnover point of the system and sets the criteria for discrete and communicating states.

A molecule which has been excited from S_o to S_1 by the absorption of a photon will, at low excess energies,

have vibronic states which are discrete. This means that the linewidth of the vibronic state - which is determined by all processes acting to depopulate the state - is much smaller than the energy seperation of adjacent states or $\Gamma_{total} < \Delta E_s \propto \rho^{-1}$ where ρ is the density of states. At very high excess energies, vibronic states are closely spaced and the linewidths tend to be broader since the total rate is faster. In the extreme case, one comes to overlapping states and hence, just by virtue of this alone, may have reached the communicating state limit. This limit will be reached for most polyatomic molecules at sufficiently high energies. This means that no amount of spectroscopic resolution will produce single vibronic structure beyond the turnover point. Experimentally, it is the point above which no pure vibronic state can be excited. Theoretically, one is required to turn from a model of discrete to communicating states. The intramanifold turnover point is defined as the excess energy at which the following equality is satisfied:

$$\Gamma_{total}(E_{xs}) = \Delta E_s (E_{xs}).$$

The linewidth Γ_{total} is determined by lifetime broadening and may be defined as

$$\Gamma_{total} = \hbar / \tau_{obs}.$$

The average initial state seperation, ΔE_s, is inversely

proportional to the density of states and may be defined as

(23) $\Delta E_s = h\nu = hc\bar{\nu} = hc/\rho$

where ρ is the density of states per cm^{-1}. From Eqs. 21, 22 and 23, the following equation is obtained as the criteria for the turnover point:

(24) $1/\tau_{obs} = 2\pi c/\rho(E_{xs})$.

A plot of the l.h.s. and the r.h.s. of Eq. 24 as a function of excess energy on the same graph allows the turnover point to be determined by the point of intersection.

This is illustrated for ß-naphthylamine on Fig. 48. Most of the measured data for this molecule lie above the turnover point of 5000 cm^{-1}. It is for this molecule that the communicating states model found its first successful application.[5] There has been some question about the experimental results for this molecule[6] where it has been contended that the resolution of the exciting light may have been insufficient to excite single vibronic levels. This may well be impossible for this system above 5000 cm^{-1}. Above the turnover point, the only experimentally meaningful quantity refers to mixed states, hence $k(E_{xs})$ and not k(SVL).

The results for naphthalene are shown on Fig. 49. The extrapolated turnover point occurs at 4500 cm^{-1}. Thus, intramolecular processes below this point should

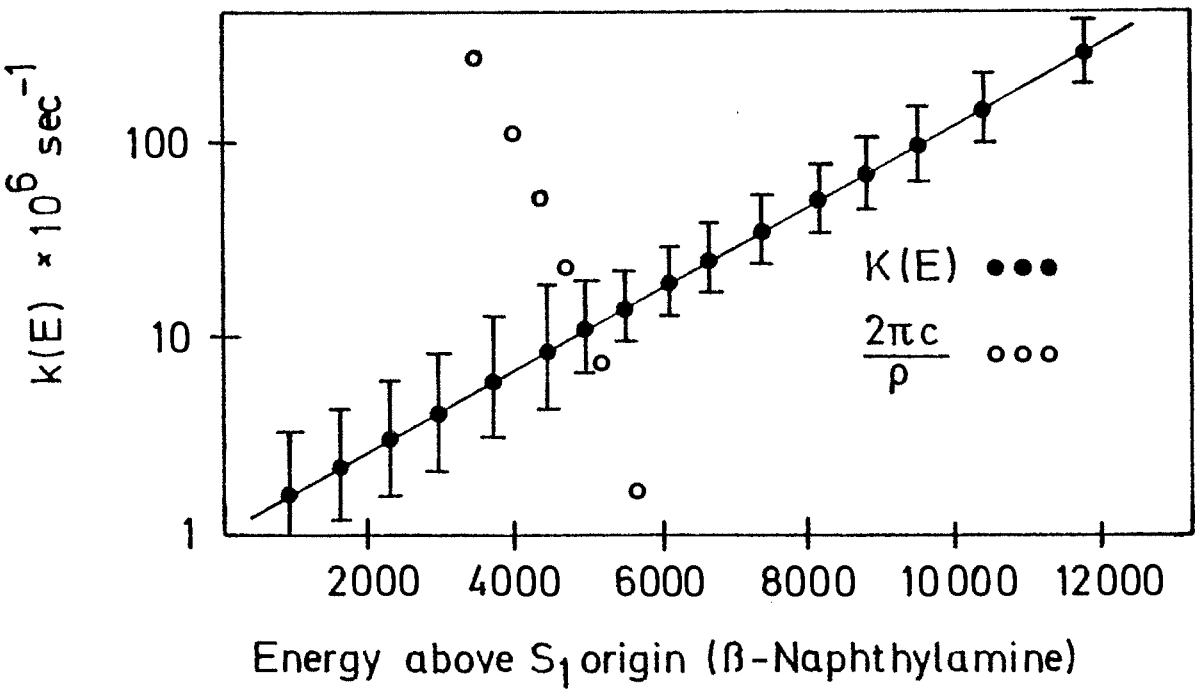

Figure 48. Turnover point for ß-naphthylamine.

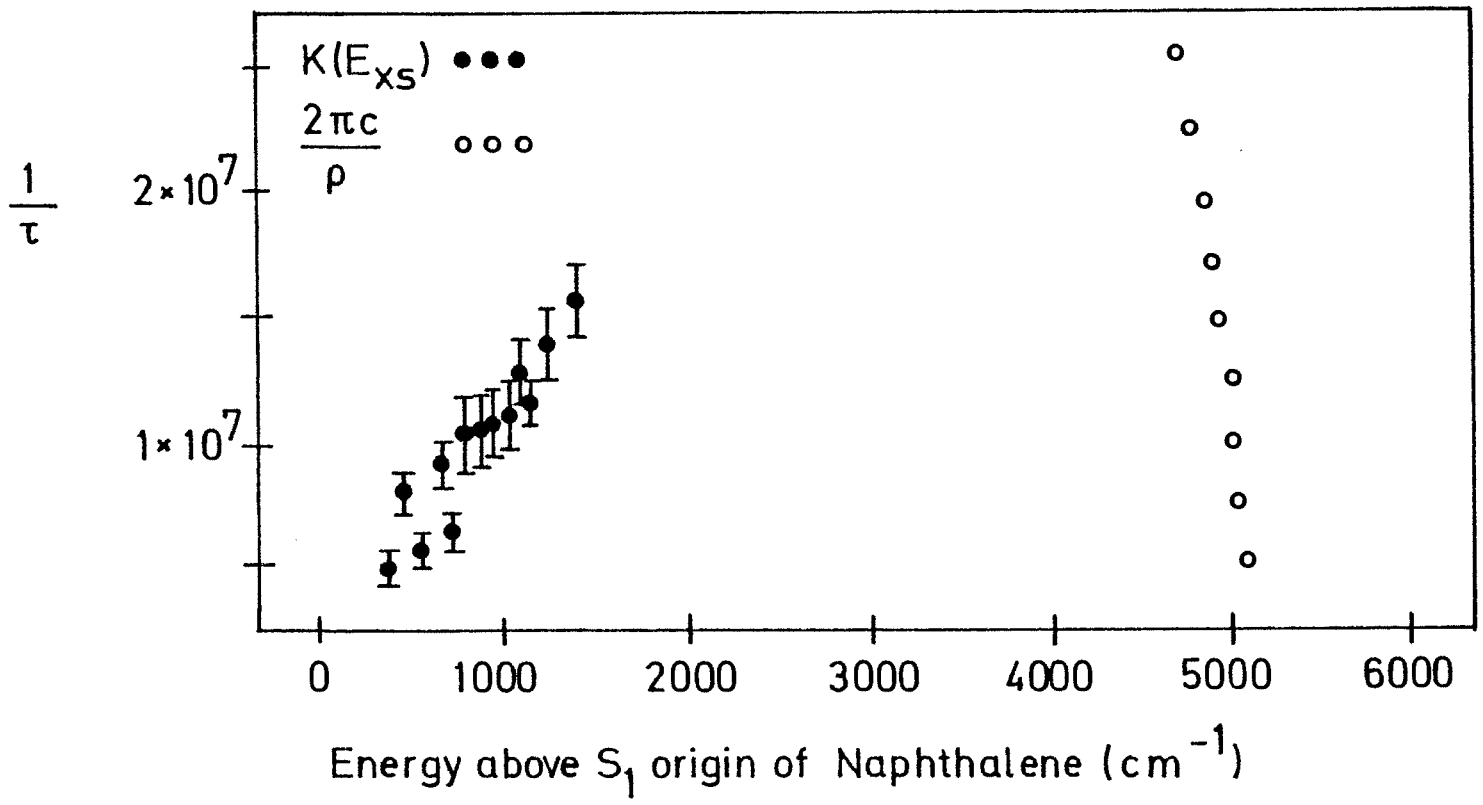

Figure 49. Turnover point for naphthalene, h_8.

be considered within the framework of discrete states. This supports the calculations of Fischer, Lim and Stanford[7] who showed that the communicating model gave very poor agreement with experiment. An early study of naphthalene[8] employed the communicating states model to explain the observed non-radiative rate constants. The use of a broadband excitation resulted in the excitation of many vibrational modes. However, the number of modes is of no importance if energy redistribution is excluded on a microscopic level for each mode. Below the turnover point, states can not communicate. The excitation of many modes does have importance, however, and will be discussed in the next chapter.

References to Chapter VII

1. L. E. Brus and J. R. McDonald,
   Chem. Phys. Lett., 21, 283 (1973).
2. P. B. Sackett, Applied Optics, 11, 2181 (1972).
3. L. A. Melton and W. Klemperer,
   J. Chem. Phys., 59, 1099 (1973).
4. L. G. Anderson, C. S. Parmenter and H. M. Poland,
   Chem. Phys., 1, 401 (1973).
5. S. Fischer and E. W. Schlag,
   Chem. Phys. Lett., 4, 393 (1969).
6. K. G. Spears and S. A. Rice,
   J. Chem. Phys., 55, 5561 (1971).
7. S. F. Fischer, E. C. Lim and L. A. Stanford,
   J. Chem. Phys., 61, 582 (1974).
8. E. C. Lim amd J. O. Uy,
   J. Chem. Phys., 56, 3374 (1972).

Chapter VIII

Excited State Relaxation

Decay of a single level

The measurement of the fluorescence quantum yield and lifetime of a single ro-vibronic level under isolated conditions yields information on the radiative channel (k_r) and the non-radiative channel (k_{nr}) of molecular decay. The following equations are almost universally applied to interpret the experimental observables:

(25) $$k_r = \phi / \tau$$

(26) $$k_{nr} = (1 - \phi) / \tau .$$

These equations do not apply to the relaxation of a multilevel system unless it can be shown that the individual levels of the system are all characterized by the same microscopic lifetime and quantum yield. This is often ignored in spite of such warnings as the variation in lifetime as a function of resolution of the exciting light or the detection bandwidth.

Decay of an ensemble

Multistate relaxation processes are of interest in many areas of physics, chemistry and biology. Reviews over the general theory of multistate relaxation[1], particular applications to chemistry[2], and molecular decay following sinusoidal excitation[3] exist. In this section a stochastic theory, starting with a Master

Equation, is presented for the case of molecular decay following pulsed excitation. Equations for the laboratory observables and rate constants are developed.

For each microscopic parameter, there exists an associated ensemble matrix, diagonal in the microscopic parameters with rows and columns labeled by all significant quantum numbers. For example, the population matrix contains, as diagonal elements, the initial concentrations of each quantum state of the ensemble. Off-diagonal terms are absent from the present discussion but in a more general theory would represent energy transfer or other coupling of states. A correlation of the ensemble to microscopic parameters is given in Table IV. The necessity of often taking the trace of the product of the population matrix times another matrix justifies the introduction of a special notation for this operation. This is denoted by

$$[\underset{\sim}{X}] = \mathrm{tr}\,(\underset{\sim}{N}\,\underset{\sim}{X}) \tag{27}$$

where $\underset{\sim}{X}$ is any matrix. The simplest example is the total excited state population given by

$$N_o = [\underset{\sim}{I}] = \mathrm{tr}\,(\underset{\sim}{N}\,\underset{\sim}{I}) = \mathrm{tr}\,(\underset{\sim}{N}) \tag{28}$$

where $\underset{\sim}{I}$ is the identity matrix.

The decay of the entire ensemble as a function of time is given by

$$-\dot{\underset{\sim}{N}}(t) = \underset{\sim}{K_f}\,\underset{\sim}{N}(t) \tag{29}$$

Table IV

Correlation Table

Parameter	Ensemble matrix	Microscopic
Population	$\underset{\sim}{N}$	$n(i)$
Radiative rate	$\underset{\sim}{K}_r$	$k_r(i)$
Non-radiative rate	$\underset{\sim}{K}_{nr}$	$k_{nr}(i)$
Total decay rate	$\underset{\sim}{K}_f$	$k_f(i)$
Lifetime	$\underset{\sim}{\gamma}$	$\gamma(i)$
Quantum yield	$\underset{\sim}{\phi}$	$\phi(i)$

which in integrated form is

(30) $\underset{\sim}{N}(t) = \exp\left(-\underset{\sim}{K}_f\, t\right)\underset{\sim}{N}(0)$.

Thus,

(31) $$-\dot{\underset{\sim}{N}}(t) = \underset{\sim}{K}_f \exp\left(-\underset{\sim}{K}_f\, t\right)\underset{\sim}{N}(0)$$
$$= \underset{\sim}{P}(t)\,\underset{\sim}{N}(0)$$

where $\underset{\sim}{P}(t)$ is the decay probability function. The signal matrix is defined as the product of the ensemble decay function and the ratio of emission probability to all other decay paths. Thus,

(32) $\underset{\sim}{S}(t) = \underset{\sim}{\phi}\,\underset{\sim}{P}(t)\,\underset{\sim}{N}(0)$

and since the observed signal is just the sum of the signals from all states, the signal function is given by

(33) $$S(t) = \mathrm{tr}\left(\underset{\sim}{\phi}\,\underset{\sim}{P}(t)\,\underset{\sim}{N}(0)\right)$$
$$= \left[\underset{\sim}{\phi}\,\underset{\sim}{P}(t)\right].$$

The signal S (t) contains all information about the ensemble. From this function all observables can be immediately obtained.

The observable quantum yield, ϕ_{obs}, is defined as the ratio of the number of photons emitted to the number absorbed. The number emitted is given as the integral of S (t) for all time and the number absorbed by the initial total population of the excited state. Thus,

(34) $$\phi_{obs} = \int_0^\infty S(t)\,dt \;/\; N_o$$
$$= \int_0^\infty \left[\underset{\sim}{\phi}\,\underset{\sim}{P}(t)\right] dt \;/\; N_o .$$

However, $\underset{\sim}{P}(t)$ is just a normalized probability function so that

(35) $$\phi_{obs} = [\underset{\sim}{\phi}] / N_o \ .$$

The only unambiguous way to characterize an ensemble lifetime is as the mean first passage time of the ensemble. Thus defined,

(36) $$\tau_{obs} = \int_o^\infty S(t)\, t\, dt \Big/ \int_o^\infty S(t)\, dt$$
$$= [\underset{\sim}{\tau}\,\underset{\sim}{\phi}] / [\underset{\sim}{\phi}] .$$

Using the last two equations for the ensemble quantum yield and lifetime, the ensemble rate constants are given by

(37) $$k_r^e = \phi_{obs} / \tau_{obs}$$
$$= [\underset{\sim}{\phi}]^2 / N_o [\underset{\sim}{\tau}\,\underset{\sim}{\phi}]$$

and

(38) $$k_{nr}^e = (1 - \phi_{obs}) / \tau_{obs}$$
$$= (N_o - [\underset{\sim}{\phi}])[\underset{\sim}{\phi}] / N_o [\underset{\sim}{\tau}\,\underset{\sim}{\phi}]$$

One special case is of importance. It asks what the observed ensemble radiative rate constant will be if the microscopic radiative rate constamt is constant for all levels. Substituting in Eq. 37 gives

$$k_r^e = k_r^m [\underset{\sim}{\tau}]^1 / N_o [\underset{\sim}{\tau}^1] .$$

By defining the average lifetime as

$$\langle \tau \rangle = [\underset{\sim}{\tau}] / N_o$$

and the average squared lifetime as

$$\langle \tau^1 \rangle = [\underset{\sim}{\tau} \cdot \underset{\sim}{\tau}] / N_o$$

the radiative rate constant of the ensemble is given by

(39) $k_r^e = k_r^m \langle \tau \rangle^2 / \langle \tau^2 \rangle$.

Thus, the measured radiative rate constant will be equal to the microscopic rate constant only if the average squared lifetime equals the average lifetime squared.

A most extreme example would be the excitation of two levels which were equally populated but with one having such a large non-radiative rate constant that no emission from the state could be observed. In this case,

$$\langle \tau \rangle^2 / \langle \tau^2 \rangle = 1/2 \quad .$$

The important point is that lifetime averaging can severely affect the observed rate constants. The above treatment is valid for any excited ensemble. However, in the chapters to come, emphasis will be placed on the rotational ensemble of a single vibronic level.

References to Chapter VIII

1. I. Oppenheim, et al., Advances in Molecular Relaxation Processes, 1, 13 (1967).
2. D. A. McQuarrie, Stoichastic Approach to Chemical Kinetics in Methuen's Monographs on Applied Probability and Statistics, ed. M. S. Bartlett, (Methuen & Co., London, 1967).
3. E. W. Schlag, S. J. Yao and H. v. Weyssenhoff, J. Chem. Phys., 50, 732 (1969).

Chapter IX

The Radiative Rate Constant

The dependence of the radiative rate constant on vibrational excitation has been widely discussed in the literature[1-4]. A vast amount of absorption and fluorescence spectral data exists with which these theories can be tested.

The simultaneous measurement of lifetimes and quantum yields along the rotational contours of the 0-0 and $8(b_{1g})^1_o$ bands of naphthalene allow the radiative rate constant to be calculated via the equation $k_r^e = \phi / \tau$. The radiative rate constant spectra of these two transitions are shown on Figs. 50 and 51. In both cases, maxima are observable in the region of the absorption maxima.

As shown in Chapter VIII, the observed radiative rate constant is subject to a somewhat complicated lifetime averaging scheme and structure in k_r^e may be seen while the microscopic radiative rate constant k_r^m remains constant. In general, rotational effects have not been included in any theoretical analysis of radiative rate constants. They have been considered constant for any single vibronic level.

The radiative rate constant for any particular $|\, JKM\rangle$ rotational state is given by

$$(40)\quad k_r^m \propto R(J,K,M) = \sum_{J',K',M',F} |\langle J'K'M'|M_F|\, J\ K\ M\rangle|^2$$

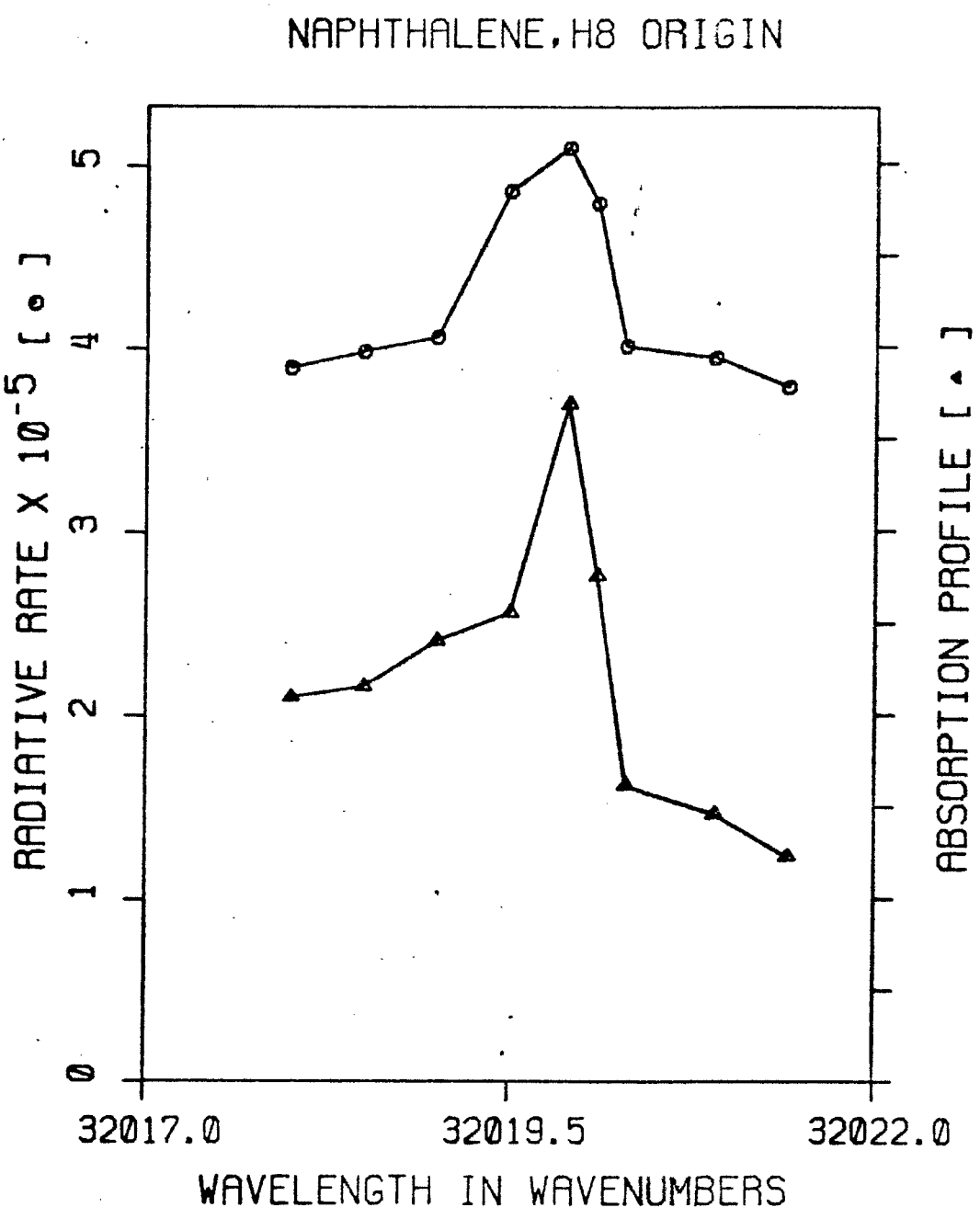

Figure 50. Radiative rate constant spectrum for the 0-0 band of naphthalene, h_8.

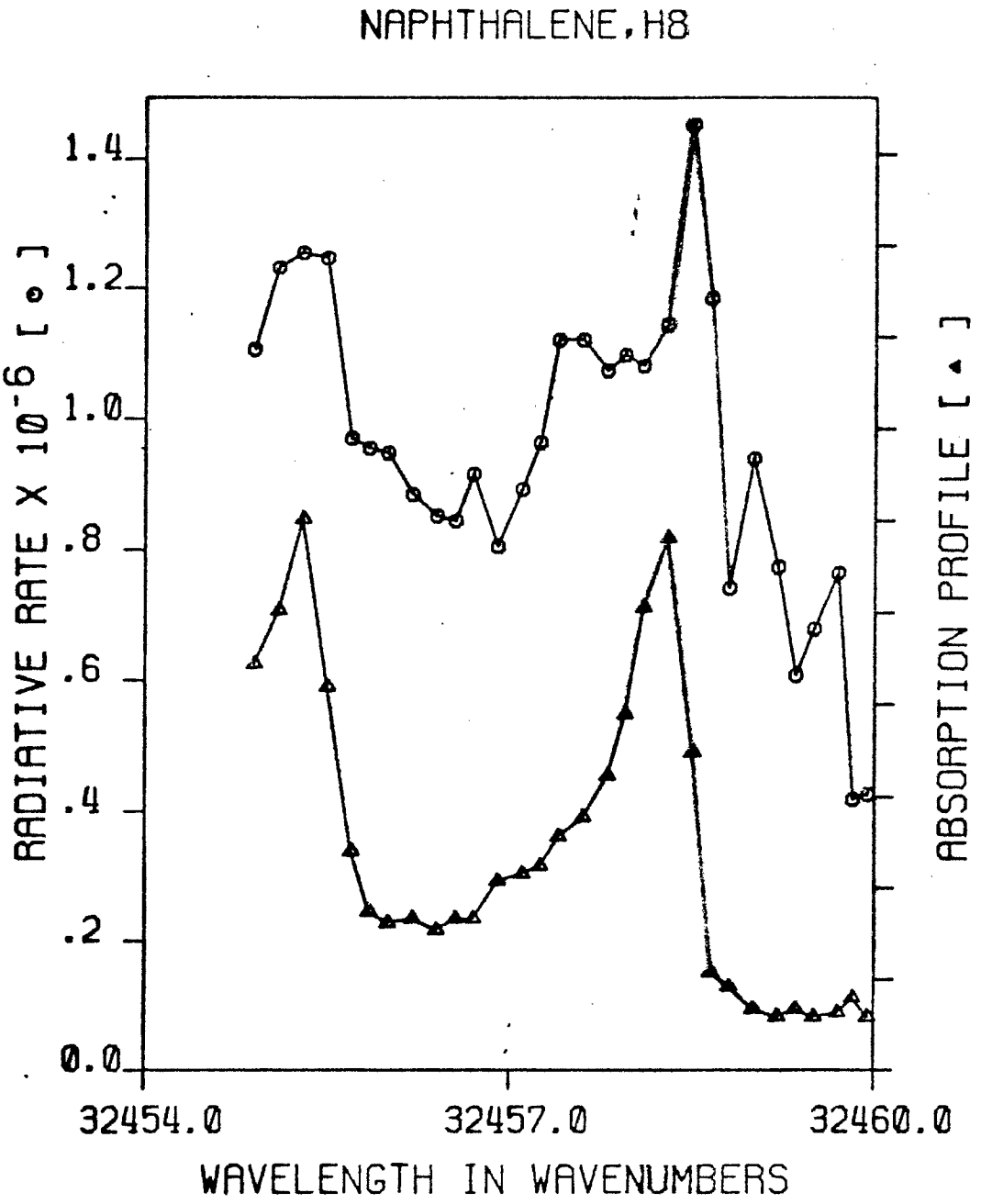

Figure 51. Radiative rate constant spectrum for the $8(b_{1g})$ band of naphthalene,h_8.

where M_F is the F $\underline{\text{th}}$ component of the electric moment which is integrated over the electronic and vibrational coordinates. The proportionality is an approximation since a factor including the frequency of the exciting light should also be included. However, for large energy gaps, variations among various rotational states should be small.

The expression for the microscopic radiative rate constant is most simply obtained by summing R(J,K,M) over all initial M states and dividing by the M state degeneragy. This is given by

$$(41) \quad k_r^m \propto \sum_M R(J,K,M) \; / \; (\; 2J+1 \;) .$$

From the well known sum rule[5]

$$(42) \quad \sum_{\substack{J',K',M', \\ M,\ F}} \left| \langle J \; K \; M | \phi_{Fg} M_g | J'K'M' \rangle \right|^2 = \left| M_g \right|^2 \; (2J+1)$$

where

$$M_F = \sum_g M_g \phi_{Fg}$$

it is easily shown that

$$(43) \quad k_r^m \propto \sum_g \left| M_g \right|^2$$

where the index g relates to the molecular coordinates and the index F relates to the laboratory coordinates. Thus, the radiative rate constant will be considered as constant for all rotational levels belonging to the same vibronic level.

It is important to emphasize that the observation of structure in the ensemble radiative rate constant as a function of rotational excitation in no way conflicts with a microscopic radiative rate constant which is independent of rotational quantum numbers. The observation of structure is due to a lifetime averaging effect which can easily arise from the non-radiative rate constants. However, lack of structure in the radiative part demands structure in the non-radiative rate constants for a consistent explanation of the experimental results.

References to Chapter IX

1. G. R. Fleming, et al., Chem. Phys. Lett., 21, 527 (1973).
2. G. Orlandi and W. Siebrand, J. Chem. Phys., 58, 4513 (1973).
3. G. Orr and G. J. Small, Chem. Phys., 2, 60 (1973).
4. P. A. Geldof, et al., Chem. Phys. Lett., 10, 549 (1971).
5. H. C. Allen and P. C. Cross, Molecular Vib-Rotors, (John Wiley, New York, 1963).

Chapter X

The Mechanism of Non-radiative Decay

The zero order Hamiltonian

A description of the non-radiative decay of an excited electronic state rests on a determination of the interaction of the prepared state with states which are not coupled, or at least very weakly coupled, to the radiation field. The interaction arises through terms in the full Hamiltonian which make the prepared state non-stationary. The factorization of the full Hamiltonian into zero order and interaction terms determines the basis set for the representation of the zero order states.

It has been pointed out that the final non-radiative rate constant given by the choice of any complete basis set will be the same if the calculation is carried out to a high enough order of perturbation theory.[1] However, it is advantagous to keep the order to a minimum. If the zero order states do not give a good representation of the prepared states, high order calculations may be necessary. Thus, the choice of the zero order basis set, and therefore the zero order Hamiltonian, should be determined by the nature of the states which are prepared and subsequently observed.

Thus, if the Hamiltonian is written as

$$(44) \qquad \tilde{H} = \tilde{H}_o + \tilde{H}'$$

it is desireable that the prepared states be eigenfunctions of $\tilde{H}_o$. Transitions between the zero order states will then be governed by $\tilde{H}'$.

It is, therefore, worthwile to consider the nature of the prepared states. Due to the fact that the electromagnetic field strongly discriminates against transitions which involve a change in spin quantum number, the states which are optically excited from a singlet ground state, and thus the states which are observed in emission, are primarily of singlet character. If the state acquires triplet character via a change in spin (ISC), it is no longer strongly coupled to the radiation field and is not observable via UV emission. This suggests that the zero order states should be described within a pure spin representation. The full Hamiltonian becomes $\tilde{H} = \tilde{H}_o + \tilde{H}_{so}$ where $\tilde{H}_{so}$ is the spin orbit operator which can induce S-T transitions.

The zero order Hamiltonian is given by

$$\tilde{H}_o = \tilde{T}(q) + \tilde{U}(qQ) + \tilde{T}_N(Q) \tag{45}$$

where the three terms to the right are the electronic kinetic energy operator, the electronic-nuclear interaction operator and the nuclear kinetic energy operator, respectively. These are functions of the electronic coordinates q and the nuclear coordinates Q.

An approximation found very useful in optical transitions is to separate $\tilde{T}_N(Q)$ out of the zero order

Hamiltonian and to also consider it as an interaction term. This is the Born-Oppenheimer (BO) approximation. It is assumed that the motion of the nuclei is so slow that the motion of the electrons instantaneously adjusts to any nuclear motion. Thus, the electronic energy can be calculated with the nuclei at various fixed positions. The energy hypersurface can then be obtained by a point to point calculation. Derivations of the BO theorem have been based on the relative mass of the electron to the nucleus[2,3] and their relative energies[4].

The Hamiltonian becomes

$$\tilde{H} = \tilde{H}_o + \tilde{T}_N(Q) + \tilde{H}_{so} \tag{46}$$

and the wavefunctions assume the product form

$$\psi_i = \phi_i \chi_i s_i$$

where ϕ , χ and s refer to the electronic, vibrational and spin wavefunctions, respectively. Although not considered in this chapter, rotational wavefunctions arise through a factorization which separates out translation and rotation of the entire molecule.

Within the BO approximation a large variety of coupling schemes have been developed[5]. However, only two have been widely discussed and used in the literature. These are the adiabatic BO (ABO) and crude BO (CBO) approximations.

For IC between two singlets, only the operator $\tilde{T}_N$ is important. However, for ISC between a singlet and a triplet or IC between two triplets, the full perturbation must be used.

Coupling schemes in ISC

Of the three types of radiationless processes just mentioned, the majority of calculations and measurements are related to ISC. The numerical results reported in this work also assume that ISC is the primary non-radiative decay channel of naphthalene excited to S_1. The interaction matrix element for ISC is given by Eq. 51. To first order in a perturbation expansion, the matrix element has the components

$$(52)\quad \langle {}^1\psi_i | \tilde{H}_{so} + \tilde{T}_N | {}^3\psi_f \rangle = \langle {}^1\psi_i | \tilde{H}_{so} | {}^3\psi_f \rangle + \sum_j (E_j - E_f)^{-1} \left[\langle {}^1\psi_i | \tilde{H}_{so} | {}^3\psi_j \rangle \cdot \langle {}^3\psi_j | \tilde{T}_N | {}^3\psi_f \rangle + \langle {}^1\psi_i | \tilde{T}_N | {}^1\psi_j \rangle \cdot \langle {}^1\psi_j | \tilde{H}_{so} | {}^3\psi_f \rangle \right].$$

Siebrand and coworkers[6] have shown that this equation can be divided into 5 distinct terms, each of which corresponds to a different mechanism for ISC. The first two are obtained by expanding the first matrix element on the r.h.s of Eq. 52 in a Taylor series terminated after the second term. The first mechanism, $H^{(1)}$, is that of direct spin orbit coupling. It arises from the evaluation of the first term in the Taylor

expansion at the equilibrium position and is given by

(53) $H^{(1)} = \langle {}^1\Psi_i(qQ_e) \mid H_{so} \mid {}^3\Psi_f(qQ_e) \rangle$.

For interactions involving $\sigma\pi^*$ or $\pi\sigma^*$ transitions, it is expected to dominate due to one-center integrals. However, for $\pi\pi^*$ transitions, only smaller three-center integrals are non-zero. In molecules with a center of symmetry, these are identically zero for S_o-T_1 transitions.

The second mechanism, $H^{(2)}$, is the second term in the Taylor expansion. Because it is vibronically induced SOC, it gives rise to promoting modes via terms of the type

(54) $\langle \phi_i | \partial/\partial Q_K | \phi_j \rangle \langle \chi_i | Q_K | \chi_j \rangle$.

$H^{(2)}$ becomes identically zero for out-of-plane vibrations within the one-center approximation for a $\pi\pi^*$ intermediate state. Thus, in-plane vibrations are considered to dominate[6]. However, there are no such symmetry restrictions on the promoting mode if two- or three-center integrals are important. Metz, Fredrich and Hohlneicher[7] have shown that this may be the case in calculations on T_1-S_o ISC in naphthalene.

The term $H^{(3)}$ is simply the second term on the r.h.s of Eq. 52. It corresponds to mixed vibronic and spin-orbit coupling. Terms given by Eq. 54 also appear in this case and out-of-plane modes which couple

to $\sigma\pi^*$ or $\pi\sigma^*$ intermediate states are expected to be the promoting modes since one-center integrals exist.

The last two terms, $H^{(4)}$ and $H^{(5)}$, appear only when the intermediate state of $H^{(2)}$ or $H^{(3)}$ is isoenergetic with the final state. These resonance terms are expected to be small for naphthalene ISC $T_1 \leftarrow S_1$ at low excess energies and will not be considered further.

As mentioned above, the existence of a promoting mode, k, implies terms of the form

$$\langle \Psi_i(qQ) | \partial/\partial Q_k | \Psi_j(qQ) \rangle = (E_i(Q) - E_j(Q))^{-1} \cdot \langle \Psi_i(qQ) | \partial U(qQ)/\partial Q_k | \Psi_j(qQ) \rangle .$$

The normal procedure has been to neglect the Q dependence of this equation. Orlandi and Siebrand[8] have introduced a correction factor p_k to approximately correct for this dependence. Model calculations indicate that it is on the order of 1-10. Nitzan and Jortner[9] have estimated the error in the numerator and denominator of the last equation and found that errors from the former are dominant and may be several orders of magnitude. Freed and Lin[10] have introduced a Q-centroid approximation scheme in which Eq. 53 is evaluated at a fixed nuclear position Q_o which does not correspond to the equilibrium position of either state. They indicate that the term $H^{(1)}$, if zero at Q_e, may be dominant at Q_o. This could make $H^{(1)}$ the

leading mechanism and obliviate the need for a promoting mode.

ISC coupling in naphthalene

At low excess energies, only T_1 cam be a final state of ISC from S_1 in naphthalene. Both of these states are characterized as $\pi\pi^*$. Direct spin orbit coupling, $H^{(1)}$, is expected to be small due to three-center integrals. Symmetry considerations[11,12] show that $H^{(1)}$ couples only with the spin component perpendicular to the molecular plane, σ_z. Measurements im the solid phase indicate that σ_z is the least populated of all spin components[11,13].

$H^{(2)}$ and $H^{(3)}$ with promoting modes of b_{2g} or b_{3g} can populate spin components σ_x or σ_y, respectively. The intermediate $\sigma\pi^*$ or $\pi\sigma^*$ states are of symmetry B_{1u} for σ_x and A_{1u} for σ_y. These mechanisms are summarized on Fig. 52.

The experimental evidence indicates that $H^{(2)}$ or $H^{(3)}$ is responsible for the observed ISC in naphthalene. However, it is far from conclusive. Low temperature solid phase measurements are not directly transferable to the gas phase. In addition, the observed population of the various spin levels at low temperature may not reflect just the electronic matrix elements.

For relative rate calculations, the exact mechanism need not be known as long as no more that one promoting

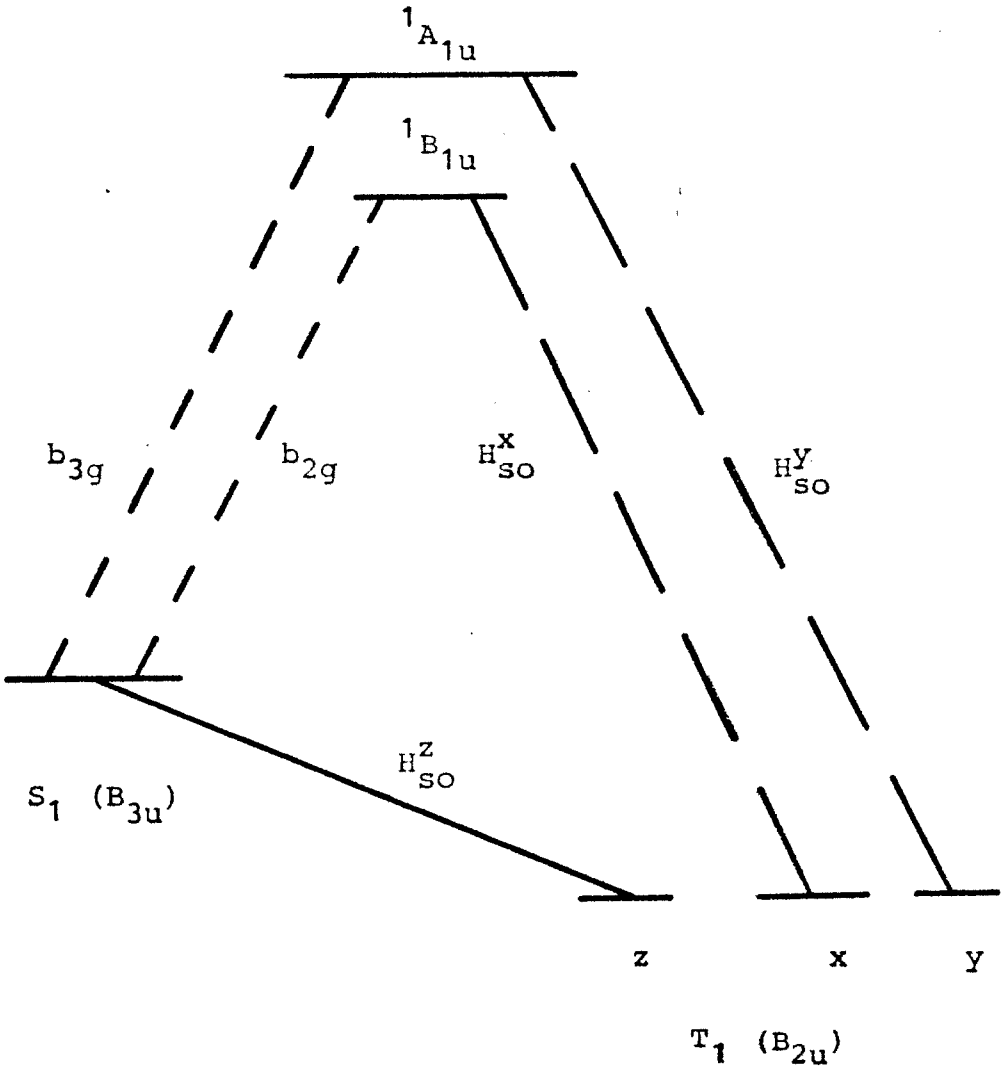

Figure 52. Coupling schemes for ISC in naphthalene-h_8.

mode is responsible for the non-radiative transition. In this case, the electronic factor cancels out of the ratio.

References to Chapter X

1. K. F. Freed and W. M. Gelbart, Chem. Phys. Lett., 10, 187 (1971).
2. M. Born and J. R. Oppenheimer, Ann. Physik, 84, 457 (1927).
3. M. Born, Festschrift. Goett. Nachr. Math. Phys., 1951, Kl. 1, p. 1.
4. H. A. Bethe and R. W. Jackiw, Intermediate Quantum Mechanics, 2nd edition, (W. A. Benjamin, New York, 1968).
5. E. W. Schlag, S. Schneider and S. F. Fischer, Ann. Rev. Phys. Chem., 22, 465 (1971).
6. a) W. Siebrand, Chem. Phys. Lett., 6, 192 (1970).
   b) B. R. Henry and W. Siebrand, J. Chem. Phys., 54, 1072 (1971).
   c) V. Lawetz, G. Orlandi and W. Siebrand, J. Chem. Phys., 56, 4058 (1972).
   d) B. R. Henry and W. Siebrand, Organic Molecular Photophysics, Vol. 1, ed. J. B. Birks, (Wiley, New York, 1973).
7. F. Metz, S. Friedrich and G. Hohlneicher, Chem. Phys. Lett., 16, 353 (1972).
8. G. Orlandi and W. Siebrand, Chem. Phys. Lett., 8, 473 (1971).
9. A. Nitzan and J. Jortner, J. Chem. Phys., 56, 3360 (1972).
10. K. F. Freed and S. H. Lin, Chem. Phys., 11, 409 (1975).
11. M. A. El-Sayed, W. R. Moomaw and J. B. Chodak, Chem. Phys. Lett., 20, 11 (1973).
12. S. McGlynn, P. Azumi and T. Kinoshita, Molecular Spectroscopy of the Triplet State, (Prentice Hall, Englewood Cliffs, New Jersey, 1969).
13. H. Sixl and M. Schwoerer, Chem. Phys. Lett.,6, 21 (1970).

Chapter XI

Models of Non-radiative Decay

The general equation for the rate

There have been many different models for the non-radiative decay of an excited electronic state. However, virtually all models have started with the same basic equation for the non-radiative rate constant. To derive this equation, it is easiest to start with a quantum mechanical treatment of time dependent states[1].

If a system is in state $|i\rangle$ at time t=0, it will develop according to the transformation

(55) $$|\Psi(t)\rangle = U(t,0)\ |i\rangle$$

with $U(0,0)=1$. The time evolution operator is fully determined by the Hamiltonian of the system and is also valid for the time dependent Schroedinger equation. Thus,

(56) $$i\,\partial U(t,0)/\partial t\ |i\rangle = \tilde{H}\,U(t,0)\ |i\rangle\ .$$

Solution of the last differential equation with the initial condition $U(0,0)=1$ gives rise to the equation

$$U(t,0) = 1 - i \int_0^t \tilde{H}(t')\,U(t',0)\,dt'$$

which is solved through iteration to give

(57) $$U(t,0) = \hat{T} \exp\left(-i \int_0^t \tilde{H}(t')\,dt' \right)$$

where the time ordering operator $\hat{T}$ stipulates that the earliest time is to the right and latest, left.

Writing the Hamiltonian as

$$\tilde{H}(t) = \tilde{H}_o(t) + \tilde{H}'(t)$$

where $\tilde{H}'(t)$ is the interaction operator, the time evolution operator assumes the form

(58) $\quad U(t,0) = U_0(t,0)\, U'(t,0)$

where $U_0(t,0)$ belongs to $\tilde{H}_0$. If $\tilde{H}_0$ is time independent, the following equation is valid

(59) $\quad U_0(t,0) = \exp(-i\tilde{H}_0 t)$

and the second term has the form

(60) $\quad U'(t,0) = \hat{T} \exp(-i \int_0^t U_0^*(t',0)\, \tilde{H}'(t')\, U_0(t',0) dt').$

To describe the decay of state $|\, i\rangle$ it is necessary to note that the probability that the system is in the final state $|\, f\rangle$ at time t is given by

(61) $\quad w_{if}(t) = |\langle f | \Psi(t)\rangle|^2$

which can be rewritten as

(62) $\quad w_{if}(t) = |\langle f |\, U(t,0)\, |\, i\rangle|^2$

$$= |\langle f | U_0(t,0) U'(t,0)\, |\, i\rangle|^2 .$$

Since $|\, i\rangle$ and $|\, f\rangle$ are eigenstates of $\tilde{H}_0$, the operation of $U_0(t,0)$ gives only a phase factor. Thus,

(63) $\quad w_{if}(t) = |\langle f | U'(t,0)\, |\, i\rangle|^2 .$

To first order, $U'(t,0)$ is approximated by

(64) $\quad U'(t,0) = 1 - i \int_0^t U_0^*(t',0)\, \tilde{H}'(t')\, U_0(t',0)\, dt'.$

Substituting Eq. 64 into Eq. 63 yields

(65) $\quad w_{if}(t) = \left| \int_0^t \exp(i \omega_{if} t') \langle f |\, \tilde{H}'(t')\, |\, i \rangle\, dt' \right|^2$

which may be simplified if the perturbation is time independent to give

$$(66) \quad w_{if}(t) = |\langle f \mid \tilde{H}' \mid i \rangle|^2 \quad (2-2\cos(\omega_{if}t))\,\omega_{if}^{-2}.$$

The non-radiative rate constant is defined as the time derivative of $w_{if}(t)$ summed over all final states. Thus,

$$(67) \quad k_{nr} = \sum_f \frac{dw_{if}(t)}{dt}$$

$$= 2\pi \sum_f |\langle f \mid \tilde{H}' \mid i \rangle|^2 \quad \frac{\sin(\omega_{if}t)}{\pi\omega_{if}}$$

$$= 2\pi \sum_f |\langle f \mid \tilde{H}' \mid i \rangle|^2 \quad \Delta_t(\omega_{if}) .$$

In the limit of $t \to \infty$, $\Delta_t(\omega)$ becomes a delta function in ω . Thus,

$$(68) \quad k_{nr}^1 = 2\pi \sum_f |\langle f \mid \tilde{H}' \mid i \rangle|^2 \quad \delta(\omega_{if}) .$$

Higher order solutions for the non-radiative rate constant can be obtained via Green's function methods or direct substitution of a higher approximation of $U'(t,0)$ in Eq. 63. Goldberger and Watson[1] have given a solution valid to all orders of perturbation theory. Their equation is

$$k_{nr} = 2\pi \sum_f |\langle f \mid \tilde{R}(E) \mid i \rangle|^2 \quad \delta(\omega_{if})$$

where $\tilde{R}(E)$ is the level shift operator. In general, the equation for the rate constant can be written as

$$(69) \quad k_{nr} = 2\pi \sum_f |V_{if}|^2 \quad \delta(E_i - E_f)$$

where V_{if} represents the coupling strength of the

initial to the final state and it is assumed that sufficient terms in the perturbation expansion have been included to properly describe the coupling.

Density of states models

A closed form solution for the non-radiative rate constant was first given by Bixon and Jortner[2] and Stepanov[3]. They assumed a constant coupling strength between initial and final states so that $V_{if}=V$. An additional assumption was that all final states were equally spaced with a spacing $\varepsilon = 1/\rho$ where ρ is the density of states. Their final solution can be obtained by changing the sum in Eq. 69 to an integral, yielding

$$(70) \quad k_{nr} = 2\pi \int_{-\infty}^{\infty} |V|^2 \rho \, \Delta_f(\omega) \, d\omega$$

$$= 2\pi |V|^2 \rho .$$

Thus, the rate constant is given by a coupling strength times the density of states.

In the Bixon-Jortner derivation, a zero order state of energy E_i which coupled to the radiative continuum was shown to be split into many lines by interaction with the quasi-continuum of secondary states. The probability of light absorption was found to be a Lorenzian envelope around the absorption lines centered at E_i. The halfwidth was given by

$$\Delta E = \pi |V|^2 \rho \quad .$$

They also demonstrated that the function $\Delta_t(\omega)$ could be approximated by a delta function at times $t \ll \rho$. For longer times, the system would return to the original state with a Poincare or recurrence time of $t_{rec} \sim \rho$.

Although this model gave important qualitative understanding of the nature of the non-radiative process, the assumption of a constant matrix element V made it inappropriate for application to real molecular systems. This assumption may be justified for treatment of the purely electronic part of the matrix element. However, the vibrational terms will strongly depend on the final state vibrational distribution and thus the energy.

This was recognized quite early be Siebrand[4] who factored the matrix element as follows:

$$(71)\quad |\langle f|\tilde{H}'|i\rangle|^2 = |\langle \phi_f|\tilde{H}'|\phi_i\rangle|^2 \sum_{\rho} \pi_{K} |\langle \chi_f^K|\chi_i^K\rangle|^2$$

$$\equiv J^2 F .$$

where ϕ and χ are the electronic and vibrational wavefunctions, respectively. The rate equation became

$$(72)\quad k_{nr} = 2\pi J^2 F \rho$$

where the factor F represents an average Franck-Condon factor and ρ, an "effective" density of states.

Using this equation, Siebrand considered only relative rates for population of optical mode k according

to the relation

$$(73) \qquad \frac{k(m_k=0)}{k(m_k=1)} = \frac{\rho_o F(m_k=0)}{\rho_1 F(m_k=1)}$$

which eliminated the necessity of calculating an electronic matrix element. Eq. 73 was expanded in a series which summed over final state population of the optical mode and was simplified via Hermite polynomial recursion relations. Siebrand was thus able to get equations for non-totally symmetric optical modes and for totally symmetric modes. However, the equations were employed to predict the average population of the optical mode in the final state and not for relative rates.

Eq. 72 was also used by Burland and Robinson[5] to calculate the $^1A_{1g} \leftarrow {}^3B_{1u}$ transition rate in benzene. The electronic matrix element was calculated using a b_{2u} promoting mode of frequency 1330 cm^{-1} which coupled to a $^1B_{2u}$ state. The matrix element had the value $V = 0.16\ cm^{-1}$.

The density of states was obtained from a calculation by Schlag and was 4.4×10^{12} states/cm^{-1}. Since direct coupling occured only via the b_{2u} mode, the density of states was reduced by a factor of 16, the number of one dimensional representations for a molecule of D_{6h} symmetry.

The average Franck-Condon factor was formed by

averaging the values for each of 6 classes of vibrations in benzene. Thus,

$$F = \sum_i N_i F_i \; / \; \sum_i N_i$$

where N_i is the number of vibrations in class i. The theoretical result was $k_{nr} = 9.04 \times 10^{-5}$ sec^{-1} while the experimental result was $k_{nr} = 2.4 \times 10^{-2}$ sec^{-1}.

This large discrepancy was attributed to anharmonic effects. However, the main objection to density of states models is that there is a single, unique Franck-Condon factor for each final vibrational distribution. No amount of partitioning the vibrations into groups will get around the variations which occur within groups. Although these models give qualitative understanding, they are limited since both the average Franck-Condon factor and the effective density of states are ambiguously defined.

Time representation models

Density of states models in which the rate is calculated by the product of a level density and an average coupling strength have been almost completely replaced by models which transfer the calculation from the energy to the time representation. This is accomplished by a Laplace or Fourier transform of the equation

(74) $$k_{nr} = 2\pi \sum_f |V_{if}|^2 \int (E_i - E_f)$$

$$= 2\pi G(0)$$

where

$$G(E) = \sum_f |V_{if}|^2 \int (E_i - E_f - E) \ .$$

Most common is the Fourier transform which generally incorporates Kubo's generating function technique[6]. Using the integral representation of the delta function, the last equation can be written as

(75) $$G(E) = (2\pi)^{-1} \int_{-\infty}^{\infty} \exp(-iEt)\, Z(t)\, dt$$

where $Z(t)$ is the generating function. It is defined as the Fourier transform

(76) $$Z(t) = \int_{-\infty}^{\infty} G(E) \exp(iEt)\, dE \ .$$

The time integral of Eq. 75 is generally solved by means of the method of steepest descents[7,8,9].

This approach replaces the integrand of Eq. 75 with a Gaussian centered around a single, purely imaginary saddle point $t_o = -i\gamma$. The use of a single saddle point will be refered to as the first saddle point approximation (FSPA). Integration of the Gaussian leads to

(77) $$G(E) = Z(\gamma) \exp(-\gamma E) \left(\left(\langle h^2 \rangle - E^2 \right) 2\pi \right)^{-1/2}$$

where

$$Z(\gamma) = \sum_f |V_{if}|^2 \exp(\gamma \Delta E)$$

and

$$\langle h^2 \rangle = Z^{-1}(\gamma) \sum_f |V_{if}|^2 \Delta E^2 \exp(\gamma \Delta E)$$

which is the width of the Gaussian. The saddle point is determined via the equation

$$(78)\quad \langle h \rangle = \Delta E = Z^{-1}(\gamma) \sum_f |V_{if}|^2 \Delta E \exp(\gamma \Delta E).$$

Within this approximation, the rate is given by

$$(79)\quad k_{nr} = 2\pi Z(\gamma) \left(2\pi \langle h^2 \rangle \right)^{-1/2} .$$

If the vibronic modes are not mixed, the non-interacting oscillator approximation (NIO) may be used. In this case, the coupling matrix element assumes the form

$$(80)\quad |V_{if}|^2 = c_{if}^2 \prod_k |\langle \chi_i^k | \chi_f^k \rangle|^2$$

where k is the number of oscillators and C, the electronic matrix element. If C includes a promoting mode j, the product over k does not include j. The generating function then becomes a product of one oscillator generating functions $Z_k(\gamma)$,

$$(81)\quad Z(\gamma) = c_{if}^2 \prod_k Z_k(\gamma) \exp(-\Delta E \gamma) .$$

Solutions for harmonic potentials have been given in the literature[10, 11, 12].

The first theoretical analysis involved displaced, undistorted potential surfaces. Brailsford and Chang[13] assumed that all displacements ξ_a were small except for the mode of maximum frequency M, which was assumed to be the best accepting mode. The saddle point solution, which involved only mode M, predicted an

increase in the rate with increasing quanta in the optical mode, m_a. In addition, the saddle point t_o was shown to be independent of m_a in zero and first order. The neglect of higher order terms was criticized by Heller, Freed and Gelbart[10] (HFG) who believed that they were important.

In order to explicitly account for the optical mode, the HFG model factored out the optical mode Franck-Condon factor from all other modes. This gave the equation

$$k_{nr} \propto \sum_{n_a} |\langle m_a | n_a \rangle|^2 \; I(\Delta E_k^{n_a}) \tag{82}$$

where

$$I(\Delta E_k^{n_a}) = \int_{-\infty}^{\infty} \tilde{Z}_k(t) \prod_{j \neq k,a} Z_j(t) \exp(-i \Delta E^{n_a} t) \, dt$$

and a, k and j refer to optical, promoting and accepting modes, respectively. The generating functions were evaluated for displaced, distorted harmonic oscillators.

This model was applied to the calculation of non-radiative rates in benzene. Only ν_1 and ν_2 were assumed to undergo large displacements. Using a model of undistorted oscillators, the experimental results of Spears and Rice[14] were reproduced to within 20%. More important, however, was that the calculations showed that the contributions to the Franck-Condon factor by the optical mode were largest when the change in quantum number was small but still signif-

icant if greater than one. This was in variance with the assumption of Brailsford and Chang.

Calculations including displaced, distorted oscillators and two optical modes reproduced the experimental results within experimental error. The parameters found most important were the optical mode frequency changes and displacements. The energy gap was varied over a range of 2000 cm^{-1} and the predicted relative rates varied by less than 2%. Thus, the model showed insensitivity to the promoting mode frequency.

In a later work, HFG[15] expanded their equation to take account of any mode requiring special treatment. The effect of partitioning more and more modes out of the integral, however, is to reduce the effective energy gap. In addition, in the limit of small energy gaps, the saddle point approximation is known to break down.

Metz[12] has extended Kubo's method for arbitrary one dimensional oscillators which need not be harmonic and for arbitrary optical mode excitation. For displaced and distorted harmonic potentials, closed analytic expressions for $Z(\Upsilon)$, $\langle h \rangle$ and $\langle h^2 \rangle$ were derived. Thus, the model incorporates no prefactorization of Franck-Condon factors which could make the saddle point procedure invalid. A simple equation for the relative rates of harmonic optical

modes was derived which did not require explicit evaluation of Franck-Condon factors. The equation is given by

$$(83) \qquad \frac{k_{nr}(m)}{k_{nr}(0)} = \prod_{\mu} Z_{m\mu}(\gamma) / Z_{o\mu}(\gamma)$$

where $Z_{m\mu}(\gamma)$ is the one dimensional generating function for m quanta in mode μ . The saddle point was evaluated only once, the same approximation used by Lin[16] and Christie and Craig[17].

Calculations were made on the $T_1 \leftarrow S_1$ transition in benzene using two different parameter sets. The first set was characterized by weak coupling of the S_1-T_1 modes, the same coupling case as HFG. The results were virtually the same as those of HFG for relative rates. Absolute rates, however, were too small by about 6 orders of magnitude.

The second set was characterized by strong coupling, the same as employed by Christie and Craig[17]. In this case, the results could also duplicate the HFG values for relative rates. Thus, it was found that a very large manifold of saddle points and distortion parameters gave an equally good interpretation of relative rates. It was found that only the strong coupling case gave good agreement with absolute rates and the isotope effect.

The second type of time representation model

employs the Laplace transform. This method, which was first applied to density of states calculations[18], was applied to non-radiative rate calculations by Christie and Craig[17]. By use of harmonic recursion relations, the Laplace transform of Eq. 74 could be written in analytic form. The rate constant for the second vibronic level of ν_1 in benzene was calculated after fitting the experimental data with an attenuation parameter.

The model predicted an energy gap law which was also derived by Englman and Jortner[9] using a Fourier transform. It states that the rate of radiationless decay out of the vibrationless level of an electronic state to a lower electronic state decreases exponentially with increasing energy gap between the states. The model also predicted an increase in the rate with increasing quanta in the optical mode.

In an early paper Lin and Bersohn[7] derived an equation for the thermally equilibrated rate constant. Lin[16] later showed that a Laplace transform of this equation would give the single level rate constant. Within the FSPA he obtained solutions for the cases of displaced, undistorted and displaced, distorted potentials. The calculated rates reproduced HFG within 2%. Thus, Laplace and Fourier transform FSPA solutions can give similar rates. The Fourier solutions, however, assume a simpler form.

Higher approximations

The formulation of Eq. 69 requires that the initial and final states of the non-radiative transition be degenerate. Freed[19] has noted that it is more realistic to replace $\Delta_t(E)$ in Eq. 67 with a Lorentzian which incorporates γ, the natural linewidth of the state, instead of a delta function. Thus,

(84) $$\Delta_t(E) \rightarrow \Delta_\gamma(E) = \gamma\left(E^2 + (\gamma/2)^2\right)^{-1} .$$

In FSPA models, the results are independent of the exact form of the Δ function. Metz[20] has also noted that inclusion of the linewidths of the states is necessary to go beyond FSPA methods.

Nitzan and Jortner[21], assuming a constant width γ, wrote the expression for the integral in Eq. 75 as

(85) $$I = 2\,\mathrm{Re}\int_0^\infty \exp(-i\,\Delta E t - \gamma t)\; Z(t)\, dt .$$

Letting ω_N be an energy scaling factor such that ω_i/ω_N is an integer for all vibrational frequencies ω_i, Nitzan and Jortner note that Z(t) becomes periodic in $2\pi/\omega_N$. Using the procedures of Lax, the infinite integral could be transformed to a finite integral of the form

(86) $$I = (\pi\gamma)^{-1}\,\mathrm{Re}\int_0^{2\pi} dx\,\left(\exp(-ix\,\Delta E/\omega_N) Z(x/\omega_N)\right)$$

when $\Delta E/\omega_N$ is an integer. To develop a computational scheme γ in the last equation was replaced by ω_N.

This has the effect of increasing the energy region from which contributions to the integral come by a factor ω_N / γ. The final result is thus equivalent to setting $\gamma = 0$ in Eq. 85 and integrating to $2\pi/\omega_N$.

This scheme was used by Nitzan and Jortner to calculate the relative rates for the $T_1 \leftarrow S_1$ transition in benzene. The promoting mode was assumed to be an a_{2g} vibration. The calculation correctly predicted the gross features of the experimental observations. Due to approximations in the computational scheme detailed agreement was not very good. The results did show, however, that C-H and C-C displacements were important parameters in the calculation of the non-radiative rate.

This model was later used by Nitzan and Jortner[22] to calculate the rate of the $S_o \leftarrow T_1$ transition in benzene. Equations were derived which took account of frequency changes as well as displacements. The equation was solved by numerical integration. To test the procedure several different normalizing frequencies were used. The final results, however, showed a very poor correlation with experiment. It was concluded that the inclusion of frequency changes was crutial to the rate calculation.

An alternative approach for going beyond the FSPA method is to include more saddle points in the calculation. The additional saddle points have been

discussed by Fischer[8] and Metz[20] has noted that it is possible for them to contribute more to the time integral than the first, t_o. The first definite criteria for application of FSPA models was given by Medvedev, et al.[23] who also developed a method to properly account for all saddle points.

The Medvedev model begins with Eq. 67 and a lineshape function given by Eq. 84. The Fourier integral gives the rate equation

(87) $$k_{nr} = 2B\ \mathrm{Re} \int_0^\infty \exp(-i \Delta E t + \sum_M Z_M(t) - \gamma t)\ dt$$

where the constant B depends on the explicit form of the potential. In the case of distorted, undisplaced surfaces, the following equations apply:

(88) $$Z_M(t) = -1/2\ \ln(1 - A_M \exp(2i \omega_M t))$$

$$\beta_M = \omega_M^i / \omega_M^f$$

$$A_M = (\beta_M - 1)^2 \cdot (\beta_M + 1)^{-2}.$$

Within this model, the following saddle point equation was obtained:

(89) $$\Delta E = \sum_M \omega_M \frac{\exp(2i \omega_M (t + i n_M))}{1 + \exp(2i \omega_M (t + i n_M))}$$

where

$$n_M = (2 \omega_M)^{-1}\ \ln(1/A_M).$$

Retaining only those modes M with small m values and setting all A_M's equal, the following saddle points

were obtained:

(90) $$t_k = -i\gamma + \pi k/\langle \omega_M \rangle$$

$$\gamma = (1/2 \langle \omega_M \rangle) \ln(\Delta E/A_M(\Delta E + \sum_M \omega_M)) .$$

Analysis of the resulting rate equation showed that the FSPA was valid only on the condition that

(91) $$1/2 \sum_\mu \ln((1 - A_\mu \exp(2 \omega_\mu \gamma))^{-1}) \gg 1$$

which is fulfilled only in the case of large distortions. An analysis of a model based on displaced, non-distorted potentials showed that the FSPA also breaks down in the case of small displacements.

In the Medvedev model, the rate constant could be written in the form

(92) $$k_{nr} = k^o_{nr} P$$

where k^o_{nr} is the contribution from the first saddle point and P describes the effect of all others. The width of the vibronic levels of the non-radiative transition appear only in the factor P.

Numerical calculations were made for the $T_1 \leftarrow S_1$ transition of benzene. The non-radiative rate was found to be strongly dependent on γ, varying two orders of magnitude from γ = 0.1 to 10 cm^{-1}. The variation was linear except in regions where $\omega_\alpha / \Delta E$ was integer for optical mode α.

Calculations of k_{nr} as a function of Δ E showed

a general decrease in k_{nr} with increasing energy gap. However, resonances were superimposed on the curve. This structured behavior is generally absent from FSPA calculations and came from the contributions of the higher saddle points.

Another alternative for going beyond the FSPA approach has been developed by Metz[20]. The rate expression is written as

$$k_{nr} = 2\pi \sum_f |V_{if}|^2 \Delta_\gamma (\Delta E) . \tag{93}$$

The linewidth function assumes all final states to have the same width γ. In order to develop a computational scheme, all oscillator energies ω_j were reduced to integer multiples of a normalizing energy d such that

$$\omega_j = n_j d \tag{94}$$

where n_j is an integer. It is important to note that the quantity d is not a linewidth parameter.

Since all oscillator energies are integer, any combination of vibrational states yields a total energy E which is integer. It is thus possible to define

$$W_n = \sum_f |V_{if}|^2 \delta (E_{if} - nd) \tag{95}$$

where the delta function now represents a step function in n which assumes the values

$$\delta (E - nd) = 0 \quad \text{if } n \neq E/d$$

and $$\delta (E - nd) = d^{-1} \quad \text{if } n = E/d.$$

The rate constant is then given by

$$(96) \quad k_{nr} = 2\pi \sum_{n} W_n \, \Delta_{\gamma}(E_{if} - nd).$$

Rounding errors are negligable whenever $d \ll \gamma$.

Eq. 96 implies that the calculation of the non-radiative rate constant can be performed in direct analogy to methods used in band contour analysis. In a contour analysis, $|V_{if}|^2$ in Eq. 93 would represent the coupling of the ground and excited states via the dipole operator. The step function would round the transition energy ΔE such that $\Delta E/d=n$ where d is the box width and n, an index. Upon completion of the calculation, an equation similar to Eq. 96 would be used where the delta function would represent the bandwidth function of the excitation light.

Determination of W_n in Eq. 95 was achieved by an extention of the Stein-Rabinovitch application of the Bayer-Swinehart algorithm for density of states calculations[24]. Eq. 95 was initially applied by Christie and Craig[17] to the direct calculation of non-radiative rates. However, it is the Metz algorithm which made this technique practical for calculations. This algorithm is discussed in detail in Chapter XIII.

Model calculations for benzene ISC were made. At very large grains (d), the rate constant approached the value given by FSPA methods. As the grain was lowered, extreme fluctuations in W_n were observable.

For ISC to S_o, fluctuations were more than two orders of magnitude at d=20 cm^{-1} and over 5 orders of magnitude at d=2 cm^{-1}. A similar effect was seen for ISC to T_1. The strongest peaks were correlated with final states having the largest coupling strengths.

Optically excited modes which were weak acceptors generated W_n spectra shifted by the energy of the optical mode. Good accepting modes changed the entire structure of W_n.

The theoretical models have demonstrated that both the normal mode frequencies and displacements are important for the determination of the non-radiative rate constant. For large energy gaps, anharmonic effects are also important. Increasing the energy gap generally results in a decrease in the rate out of the vibrationless level. Increasing quanta in the optical modes generally increases the rate. However, structure in the vibrational terms can cause the change in rate to be non-linear in energy and/or quanta. In the next chapter, the effect of rotational selection on the rate constants will be discussed.

References to Chapter XI

1. M. Goldberger and K. Watson, Collision Theory, (Wiley, New York, 1964).
2. M. Bixon and J. Jortner, J. Chem. Phys., 48, 715 (1968).
3. B. I. Stepanov and V. P. Grobkovski, Theory of Luminescence, Iliffe (1968).
4. W. Siebrand, J. Chem. Phys., 54, 363 (1971).
5. D. M. Burland and G. W. Robinson, J. Chem. Phys., 51, 4548 (1969).
6. R. J. Kubo, Phys. Rev., 86, 929 (1952).
7. a) S. H. Lin and R. Bersohn, J. Chem. Phys., 48, 2732 (1968).
   b) S. H. Lin, J. Chem. Phys., 44, 3759 (1966).
8. S. F. Fischer, J. Chem. Phys., 53, 3195 (1970).
9. R. Englman and J. Jortner, Mol. Phys., 18, 145 (1970).
10. D. F. Heller, K. F. Freed and W. M. Gelbart, J. Chem. Phys., 56, 2309 (1972).
11. K. F. Freed and J. Jortner, J. Chem. Phys., 52, 6272 (1970).
12. F. Metz, Chem. Phys., 9, 121 (1975).
13. A. D. Brailsford and T. Y. Chang, J. Chem. Phys., 53, 3108 (1970).
14. K. Spears and S. A. Rice, J. Chem. Phys., 55, 5561 (1971).
15. D. F. Heller, K. F. Freed and W. M. Gelbart, Chem. Phys. Lett., 23, 56 (1973).
16. S. H. Lin, J. Chem. Phys., 58, 5760 (1973).
17. a) J. R. Christie and D. P. Craig, Mol. Phys., 23, 345 (1972).
    b) J. R. Christie and D. P. Craig, Mol. Phys., 23, 352 (1972).
18. P. C. Haarhoff, Mol. Phys., 7, 101 (1963).
19. K. F. Freed, J. Chem. Phys., 52, 1345 (1970).

20. F. Metz, Chem. Phys., 18, 385 (1976).
21. A. Nitzan and J. Jortner,
J. Chem. Phys., 55, 1355 (1971).
22. A. Nitzan and J. Jortner,
Theor. Chim. Acta, 30, 217 (1973).
23. E. S. Medvedev, V. I. Osherov and V. M. Pschenichnikov, Chem. Phys., preprint.
24. S. E. Stein and B. S. Rabinovitch,
J. Chem. Phys., 58, 2438 (1973).

Chapter XII

Rotational Dependence in Non-radiative Transitions

A characterization of the role of the rotational states in a non-radiative transition is more complicated than that of the vibrational states. In both ISC and IC, the vibrational states enter the rate expression through the Franck-Condon factor with the exception of the promoting mode. Thus, it has been possible to explain the vibrational effect on both of these processes within the same formalism[1] by choosing $\tilde{H}' = \tilde{H}_{so} + \tilde{T}_N$ where $\tilde{H}_{so}$ is the spin orbit operator and $\tilde{T}_N$ is the nuclear kinetic energy operator. However, the role of the rotational states depends to a greater degree on the exact nature of the coupled states and operator.

For an isolated molecule, total angular momentum must be conserved. No internal process can alter J, the total angular momentum quantum number or P, the projection of J on the symmetric top axis. The selection rules $\Delta J = 0$ and $\Delta P = 0$ are rigidly obeyed for ISC and IC. This can be shown quantum mechanically through the commutation relations

(96) $$\left[\tilde{J}^2 , \tilde{H}_{so} \right] = \left[\tilde{P} , \tilde{H}_{so} \right] = 0$$

and $$\left[\tilde{J}^2 , \tilde{T}_N \right] = \left[\tilde{P} , \tilde{T}_N \right] = 0 .$$

For the decay of an excited singlet, P is a good quantum number for IC but not for ISC. This gives rise to totally different selection rules for the rotational

transitions associated with these processes.

The angular momentum due only to molecular rotation is characterized by the quantum number N. The projection of N on the symmetric top axis is denoted by K. Both N and K are good quantum numbers for IC and ISC since they uniquely determine the rotational energy levels.

In large molecules, which may be presumed to be Hund's case b, the coupling of angular momenta is characterized by the relation

(98) $\tilde{N} = -\tilde{S} + \tilde{J}$

where $\tilde{S}$ is the spin angular momentum operator. Singlet states are characterized by S = 0. This immediately gives rise to the rotational selection rules for IC between two singlet states:

(99) $\Delta N = 0$ and $\Delta K = 0$.

For triplet states, the spin momentum is not zero. It is therefore necessary to solve the matrix elements explicitly.

The matrix element to be evaluated is of the form

$$\langle \Psi_T | \tilde{H}_{so} | \Psi_S \rangle .$$

It is not necessary to consider the effect of the promoting mode or $\tilde{T}_N$ at this stage since they enter in another matrix element which must maintain the selection rules of IC. Discussions of the $\tilde{H}_{so}$ matrix elements have been given by Hougen[2] and Brand[3].

In Hund's case b, the good quantum numbers are J, S, N and K. However, it is more convenient to start

with a basis in Hund's case a which has the good quantum numbers J, P, S and S^z. This will allow direct application of the selection rules $\Delta J = 0$ and $\Delta P = 0$ to the good quantum number of the basis set.

The functions $|J\ P\rangle$ need no further elaboration beyond the previously stated commutation relations. Thus, only the spin functions $|S\ S^z\rangle$ need to be characterized. For a system of two unpaired electrons a spin basis is given by the one electron spin eigenfunctions α_1, β_1, α_2 and β_2 where

(100) $\alpha = |1/2, 1/2\rangle$

and $\beta = |1/2, -1/2\rangle$.

The primary basis in these eigenfunctions is the set of product functions $\alpha_1\alpha_2$, $\alpha_1\beta_2$, $\beta_1\alpha_2$ and $\beta_1\beta_2$. This corresponds to a system diagonal in $\tilde{S}^2$ and $\tilde{S}^z$ for each electron. Via a Clebsch Gordon transformation a basis diagonal in $(\tilde{S}_1 + \tilde{S}_2)^2$ and $(\tilde{S}_1^z + \tilde{S}_2^z)$ can be obtained. The new eigenfunctions are

(101)
$$|00\rangle = 2^{-1/2}(\alpha_1\beta_2 - \alpha_2\beta_1)$$
$$|11\rangle = \alpha_1\alpha_2$$
$$|10\rangle = 2^{-1/2}(\alpha_1\beta_2 + \alpha_2\beta_1)$$
$$|1\text{-}1\rangle = \beta_1\beta_2.$$

In general, the initial spin-rotational wavefunctions in Hund's case a are given by $|J\ P\ S\ S^z\rangle$. The singlet wavefunctions will be the same in case a and b. It is thus necessary to transform only triplet case a wavefunctions to case b. The coupling is described by Eq. 98 and the transformation is again

Clebsch-Gordon. The expansion yields[4]

$$|S\ J\ N\ K\rangle = \sum_{S^z,P} (S\ -S^z\ J\ P\,|\,S\ J\ N\ K)\ |S\ -S^z\ J\ P\rangle$$

where the spin functions must be written in time reversed form. Application of the time reverse transformation and converting the Clebsch-Gordon coefficients to Wigner 3-J symbols gives the equation

(102) $$|S\ J\ N\ K\rangle = \sum_{S^z,P} (-1)^{J+P}\ (2N+1)^{1/2} \cdot \begin{pmatrix} J & N & S \\ P & -K & -S^z \end{pmatrix} |S\ S^z\ J\ P\rangle .$$

Substitution into the matrix element of $\tilde{H}_{so}$ and using the identities $J_T=N_S$, $P_T=K_S$ and $S_T=1$ gives

(103) $$\langle \Psi_s | \tilde{H}_{so} | \Psi_s \rangle = \sum_{S^z} (-1)^{N_S+K_S}\ (2N_T+1)^{1/2} \begin{pmatrix} N_S & N_T & 1 \\ K_S & -K_T & -S^z \end{pmatrix} \langle \phi_T \chi_T S_T | \tilde{H}_{so} | \phi_s \chi_s S_s \rangle$$

where $|S_S\rangle = |0\ 0\rangle$

and $|S_T\rangle = |1\ S^z\rangle$.

For direct spin-orbit coupling, the vibrational dependence can be factored out so that the matrix element is

(104) $$\langle \phi_T S_T | \tilde{H}_{so} | \phi_s S_s \rangle \langle \chi_T | \chi_s \rangle .$$

The operator $\tilde{H}_{so}$ will be approximated as a sum of one electron operators. Thus,

$$\tilde{H}_{so} = \sum_i \tilde{h}^i_{so}$$

and the one electron operator is given by

$$\tilde{h}^K_{so} = \lambda_K \tilde{\ell}_K \cdot \tilde{s}_K$$

where $\tilde{\ell}_k$ is the orbital and $\tilde{s}_k$ the spin angular momentum operator for the $k^{\underline{th}}$ electron. Calculations are simplified if an operator representation is chosen so that the operators transform under rotation of axes exactly like the angular momentum eigenfunctions. The irreducible tensor operators are thus given by

(105)
$$\begin{aligned}
\tilde{\ell}^0 &= \tilde{\ell}^z \\
\tilde{\ell}^{\pm 1} &= \mp 2^{-1/2}\left(\tilde{\ell}^x \pm i\tilde{\ell}^y\right) \\
\tilde{s}^0 &= \tilde{s}^z \\
\tilde{s}^{\pm 1} &= \mp 2^{-1/2}\left(\tilde{s}^x \pm i\tilde{s}^y\right).
\end{aligned}$$

The one electron spin-orbit operator assumes the form

$$\tilde{h}^k_{so} = \lambda_k \sum_{\alpha=\pm 1,0} (-1)^\alpha \tilde{\ell}^\alpha_k \cdot \tilde{s}^{-\alpha}_k .$$

The spin eigenfunctions were described in terms of two electrons. Within this approximation, there are only two terms which contribute to $\tilde{H}_{so}$. The full operator is given by

$$\begin{aligned}
\tilde{H}_{so} &= \tilde{h}^1_{so} + \tilde{h}^2_{so} \\
&= \lambda_1 \sum_{\alpha=\pm 1,0} (-1)^\alpha \tilde{\ell}^\alpha_1 \cdot \tilde{s}^{-\alpha}_1 \\
&\quad + \lambda_2 \sum_{\alpha=\pm 1,0} (-1)^\alpha \tilde{\ell}^\alpha_2 \cdot \tilde{s}^{-\alpha}_2 .
\end{aligned}$$

This may be rewritten as a sum of symmetric and anti-symmetric components to yield

(106)
$$\tilde{H}_{so} = \sum_{\alpha=\pm 1,0} \tilde{\ell}^\alpha_- \cdot \tilde{s}^\alpha_- + \sum_{\alpha=\pm 1,0} \tilde{\ell}^\alpha_+ \cdot \tilde{s}^\alpha_+$$

where

(107) $$\tilde{\ell}^{\alpha}_{\pm} = \tfrac{1}{2}\left(\lambda_1 \tilde{\ell}^{\alpha}_{1} \pm \lambda_2 \tilde{\ell}^{\alpha}_{2}\right)$$

and

(108) $$\tilde{S}^{\alpha}_{\pm} = \tfrac{1}{2}(-1)^{\alpha}\left(\tilde{S}_1^{-\alpha} \pm \tilde{S}_2^{-\alpha}\right).$$

For ISC, only the antisymmetric component will be important since the matrix element $\langle 1\alpha' | \tilde{S}^{\alpha}_{+} | 00\rangle$ is zero for any choice of α, α'.

The antisymmetric operator has the matrix elements

(109) $$\langle 1\alpha' | \tilde{S}^{\alpha}_{-} | 00\rangle = \delta_{\alpha,-\alpha'}.$$

The entire matrix element becomes

(110) $$\langle \Psi_T | \tilde{H}_{SO} | \Psi_S \rangle = \sum_{\alpha=\pm1,0} (-1)^{N_S + K_S} (2N_T+1)^{1/2} \cdot \begin{pmatrix} N_S & N_T & 1 \\ K_S & -K_T & \alpha \end{pmatrix} \langle \chi_T | \chi_S \rangle \langle \phi_T | \tilde{\ell}^{\alpha}_{-} | \phi_S \rangle.$$

which can be substituted into Eq. 93 to give

(111)

$$\begin{aligned} k_{nr} &= 2\pi \sum_{\{T\}} \sum_{\alpha} (2N_T+1) \begin{pmatrix} N_S & N_T & 1 \\ K_S & -K_T & \alpha \end{pmatrix}^2 \\ &\quad \cdot |\langle \chi_T | \chi_S \rangle|^2 \; |\langle \phi_T | \tilde{\ell}^{\alpha}_{-} | \phi_S \rangle|^2 \\ &\quad \cdot \Delta_{\alpha}(E_S - E_T) \\ &= 2\pi \sum_{\{T\}} \sum_{\alpha} (2N_T+1) \begin{pmatrix} N_S & N_T & 1 \\ K_S & -K_T & \alpha \end{pmatrix}^2 \\ &\quad \cdot |\langle \phi_T | \tilde{\ell}^{\alpha}_{-} | \phi_S \rangle|^2 \cdot F(E_S - E_T). \end{aligned}$$

This equation predicts rotational structure from two different mechanisms. The first is the obvious dynamic effect which comes from variation in the Wigner 3-J symbols. This may be especially effective when the electronic matrix elements are large for only particular values of α.

In the case of constant Franck-Condon factors, the rotational effect disappears due to the sum rule[4]

$$\sum_{N_T,K_T} (2 N_T + 1) \begin{pmatrix} N_S & N_T & 1 \\ K_S & -K_T & \alpha \end{pmatrix}^2 = 1 .$$

Thus, the rotational effect appears only if some of the final vibrational states have different coupling strengths.

From the Wigner 3-J symbols, the rotational selection rules for ISC can be obtained. They are

$\Delta N = \pm 1, 0$ and $\Delta K = \pm 1, 0$.

The $\Delta K = 0$ transitions are associated with population of the z spin component and $\Delta K = \pm 1$, with x and y.

The second mechanism for producing a change in the non-radiative rate constant as a function of rotational state selection is the effect of Energy Gap Branching. This comes from the fact that the energy delta function also contains the rotational energies of the initial and final states.

The full delta function is given by

$$\Delta_\gamma(E_S - E_T) \approx \Delta_\gamma \left[(E_S^e + E_S^v + E_S^r) - (E_T^e + E_T^v + E_T^r) \right] . \quad (112)$$

However, final rotational states $|N+1\ K\rangle$ and $|N-1\ K\rangle$ can be found by changing the vibrational energy of the final state, ΔE^v. In the following diagram, the arrows indicate the direction in which ΔE^v must be changed.

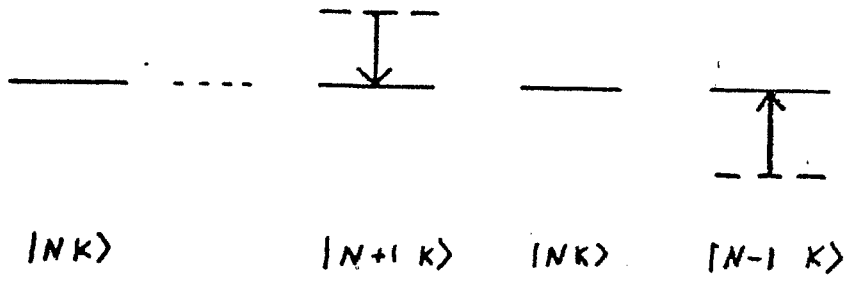

Thus, the vibrational energy must be decreased for higher rotational states and increased for lower rotational states. This is the meaning of Eq. 115.

In general, each rotational transition of a given N,K state is associated with a different set of final vibrational levels. Variations in the Franck-Condon factor for the different levels will be reflected in the non-radiative rate constant as a function of rotational state selection.

It is important to note that ΔE^r is not necessarily small. Such quantities are directly observable in high resolution optical spectra. They correspond to the transition energy offset from the rotational origin of an absorption band. It is not uncommon for ΔE^r in optical spectra to exceed 50-80 cm^{-1}. Shifts in this range can also be expected for ISC.

Although IC is restricted to $\Delta N = 0$ and $\Delta K = 0$ transitions, energy gap branching can also play an important role. To illustrate this, consider the equation for the energy of a prolate symmetric rotor. This is given by[5]

(116) $$E(N,K) = C\,(N(N+1)) + (A-C)\,K^2 .$$

The transition energy between $|N\,K\rangle$ and $|N'K'\rangle$ is given by

(117) $$\Delta E^r = E(N',K') - E(N,K).$$

For $N=N'$ and $K=K'$, one has

(118) $$\Delta E^r = \Delta C\, N(N+1) + (\Delta A - \Delta C)\, K^2 .$$

Thus, only when the inertial constants in the two states are equal, i.e. $\Delta A = \Delta C = 0$, do all rotational transitions in IC occur at the same energy. However, variation in ΔE^r for ISC is generally larger than for IC.

References to Chapter XII

1. W. Siebrand, Chem. Phys. Lett., 6, 192 (1970).
2. J. T. Hougen, Can. J. Phys., 42, 433 (1964).
3. C. G. Stevens and J. C. D. Brand, J. Chem. Phys., 58, 3324 (1973).
4. A. R. Edmonds, Angular Momentum in Quantum Mechanics, (Princeton Univ. Press, Princeton, N. J. , 1957).
5. H. C. Allen, Jr. and P. C. Cross, Molecular Vib-Rotors, (Wiley, New York, 1963).

Chapter XIII

Vibrational Coupling in ISC

Determination of the vibrational parameters

Model calculations as described in Chapter XI have shown that the ISC rate depends very strongly on the vibrational frequencies of the initial and final states, $\tilde{\omega}_\mu$ and ω_μ, as well as the reduced displacements of the totally symmetric modes, $\tilde{\Delta}_\mu$. The reduced displacements are defined as[1]

$$\tilde{\Delta}_\mu = \tilde{\omega}_\mu^{1/2} \left(Q_\mu^{S_1} - Q_\mu^{T_1} \right) \tag{119}$$

where Q_μ is given by

$$Q_\mu = \left(M_\mu / 2 \right)^{1/2} \Delta R_\mu \tag{120}$$

and ΔR_μ is the actual change in the equilibrium position of mode μ.

For most molecules, the triplet parameters are completely unknown and the excited singlet parameters are only partially known. This is also the case for naphthalene. Recent force field calculations on the S_1 state of benzene[2] indicate that it may soon be possible to have an entire set of good vibrational frequencies, at least for the excited singlet.

For determination of the S_1 and T_1 frequencies of naphthalene, a modified procedure introduced by Fischer[3] was used. The vibrations were first divided into 5 classes: C-H stretch, C-C in-plane, C-H bend, C-C out-of-plane and C-H out-of-plane. The frequency

changes of benzene were taken as typical for aromatic hydrocarbons and transferred to naphthalene. All unknown normal mode frequencies were uniformly varied until the average group frequency reached the preset value. The final results are given on Table V.

Normal mode displacements are restricted to totally symmetric modes of which there are nine in naphthalene. The displacements $\tilde{\Delta}_\mu(S_1-T_1)$ can be obtained from knowledge of the displacements $\tilde{\Delta}_\mu(S_o-S_1)$ and $\tilde{\Delta}_\mu(S_o-T_1)$. Fischer[4] has suggested the following relation:

$$(121)\quad \tilde{\Delta}^2_\mu(S_1-T_1) = \left[\tilde{\Delta}_\mu(S_1-S_o) - \Delta_\mu(T_1-S_o)\right]^2.$$

The coupling terms to the ground state can be obtained from the fluorescence and phosphorescence spectra. The relative emitted intensity is given by

$$(122)\quad \frac{I^\mu_{nm}}{I^\mu_{nK}} = \left(\frac{\nu_{nm}}{\nu_{nK}}\right)^4 \frac{|\langle n_\mu | m_\mu\rangle|^2}{|\langle n_\mu | K_\mu\rangle|^2}$$

where ν is the transition energy and the coupling parameter $\tilde{\Delta}_\mu$ is implicit in the Franck-Condon factor. Displacements $\tilde{\Delta}_\mu$ were determined by a least squares fit of all spectrally observed progressions of mode μ to Eq. 122. For the phosphorescence spectrum[5] only transitions $0 \rightarrow 1$ and $0 \rightarrow 0$ were observed. For the fluorescence spectra[6], other transitions were also observed.

The calculated frequencies and displacements were

Table V

Normal Mode Frequencies of Naphthalene, h_8

Mode	(S_o)	(S_1)	(T_1)
$1(a_g)$	3057	3112	3126
$2(a_g)$	3014	3069	3083
$3(a_g)$	1577	1435	1515
$4(a_g)$	1464	1390	1402
$5(a_g)$	1380	1147	1318
$6(a_g)$	1146	1140	1103
$7(a_g)$	1020	987	977
$8(a_g)$	760.7	702	698
$9(a_g)$	512	501	450
$1(a_u)$	1000	747	695
$2(a_u)$	875	622	570
$3(a_u)$	700	594	592
$4(a_u)$	400	294	292
$1(b_{1g})$	3025	3080	3094
$2(b_{1g})$	2980	3035	3049
$3(b_{1g})$	1629	1578	1567
$4(b_{1g})$	1445	1394	1383
$5(b_{1g})$	1244	1238	1201
$6(b_{1g})$	1168	1162	1125
$7(b_{1g})$	937.8	911	876
$8(b_{1g})$	506	438	444
$1(b_{1u})$	1014	865	709
$2(b_{1u})$	780	527	475

Table V (cont.)

$3(b_{1u})$	475	369	367
$4(b_{1u})$	176	166	68
$1(b_{2g})$	950	697	645
$2(b_{2g})$	727	474	422
$3(b_{2g})$	195	140	87
$1(b_{2u})$	3060	3115	3129
$2(b_{2u})$	3027	3082	3096
$3(b_{2u})$	1601	1550	1539
$4(b_{2u})$	1387	1336	1328
$5(b_{2u})$	1268	1262	1225
$6(b_{2u})$	1142	940	1099
$7(b_{2u})$	810	759	748
$8(b_{2u})$	355	355	293
$1(b_{3g})$	983	730	678
$2(b_{3g})$	880	627	575
$3(b_{3g})$	727	666	664
$4(b_{3g})$	468	362	360
$1(b_{3u})$	3086	3141	3155
$2(b_{3u})$	3029	3084	3098
$3(b_{3u})$	1508	1457	1446
$4(b_{3u})$	1375	1559	1313
$5(b_{3u})$	1214	1206	1171
$6(b_{3u})$	1144	1138	1101
$7(b_{3u})$	1010	959	948
$8(b_{3u})$	641	592	579

then used to regenerate the observed spectra. The calculated phosphorescence spectrum is shown on Fig. 53. This is directly comparable with the experimental spectrum of Stockburger[5]. The energy scale indicates the energy of the final vibrational mode of the transition. The final results for all displacements are given on Table VI.

Density of states

For models based on the density of states, the final state vibrational frequencies are sufficient for the calculation. The energy in vibrational degrees of freedom above the vibrationless or spectroscopic origin of a state is given by the formula

$$E = \sum_{\mu} m_{\mu} \omega_{\mu} \quad . \tag{123}$$

In general, many different sets of vibrational quantum numbers $\{m\}$ may generate a state with the same total energy, E. The density of states, $\rho(E)$, is defined as the number of vibrational " levels per unit of total vibrational energy."[7]

Several techniques have been developed to calculate $\rho(E)$. The first was simply a direct count.[8,9] The main drawback of this technique was that the computation of all permutations of vibrational quantum numbers became very time consuming at high energies.

The next technique was based on the fact that the vibrational partition function could be written as a

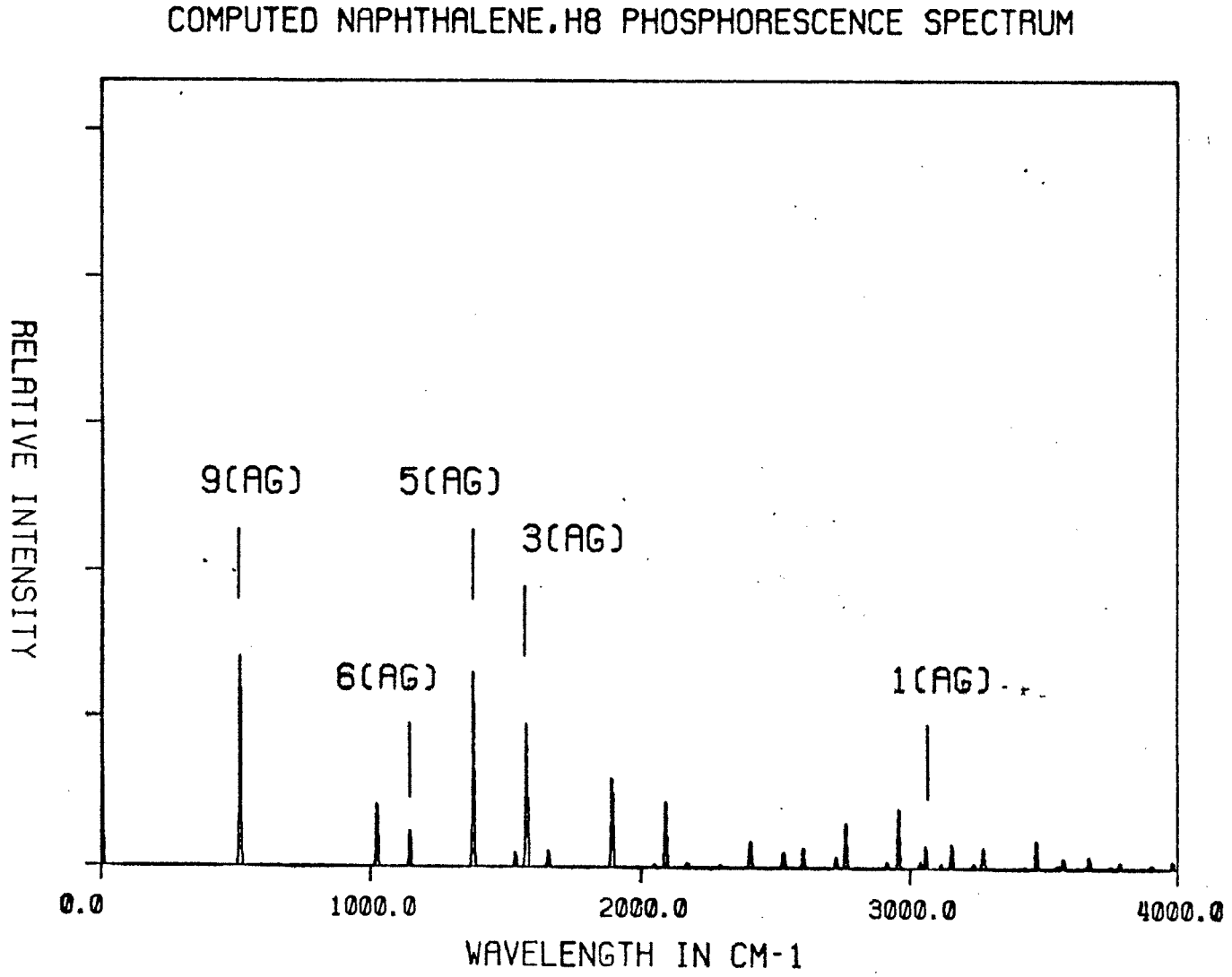
COMPUTED NAPHTHALENE.H8 PHOSPHORESCENCE SPECTRUM
RELATIVE INTENSITY
9(AG)
5(AG)
3(AG)
6(AG)
1(AG)
0.0
1000.0
2000.0
3000.0
4000.0
WAVELENGTH IN CM-1

Figure 53.

Laplace transform of the density of states. Thus,

$$(124) \quad Q_{vib}(s) = \int_0^\infty \rho(E) \exp(-sE) \, dE$$

The density of states can thus be represented as the inverse Laplace transform of the partition function. This yields

$$(125) \quad \rho(E) = \int_{-\infty}^{\infty} Q_{vib}(s) \exp(sE) \, ds \, .$$

The determination of the inversion integral via a series expansion was investigated by Haarhoff[7], Thiele[10] and Schlag[11].

The vibrational partition function for harmonic oscillators can be written in closed form as

$$(126) \quad Q_{vib}(s) = \prod_\mu (2 \sinh(\omega_\mu s/2))^{-1} \, .$$

Haarhoff first expanded this formula in a power series and then took the Laplace transform. The result is the well known Haarhoff formula:

$$(127) \quad \rho(E) = E^{3N-7} \, ((3N-7)! \prod_\mu (\omega_\mu))^{-1} \cdot (1 + \text{higher order terms }).$$

An alternative to the power series expansion has been the use of the method of steepest descents[12]. The saddle point s^* is obtained from the equation

$$(128) \quad \partial/\partial s (sE + \ln Q_{vib}(s)) \Big|_{s=s^*} = 0 \, .$$

The gaussian integral is then solved exactly to give the density of states. This method, like the series expansion, becomes accurate only in the limit of high energies.

The most powerful technique is a direct count method introduced by Stein and Rabinovitch[13]. Previous techniques generated all permutations of vibrational quantum numbers and sorted the final energies into a finite number of partitions as the last step. The Stein-Rabinovitch technique is based on a fast sorting algorithm from Bayer and Swinehart which pregrains the vibrational frequencies and uses iterative convolution instead of permutations to generate all combinations of quantum numbers.

The density of states is often defined as

$$\rho(E) = \sum_f \delta(E - E_f). \tag{129}$$

However, this formula is misleading since the definition is the number of states per unit vibrational energy. Any calculation will sort the final energies into finite intervals of width Δ. The total count within any interval is not, in general, the density of states since it is the number of states per unit Δ. The actual density of states is given by the count in an interval divided by the interval width Δ. A calculation which directly counts the states is thus related to the formula

$$\rho^{\Delta}(n\Delta \leq E < (n+1)\Delta) = \sum_f \delta^{\Delta}(n\Delta - E_f) \equiv \rho^{\Delta}(n) \tag{130}$$

where the delta function is a step function which assumes

the values

(131) $\int^{\Delta}(n\Delta - E_f) = 1 \quad$ if $\quad n \leq \frac{E_f}{\Delta} < n+1$

$\int^{\Delta}(n\Delta - E_f) = 0 \quad$ otherwise.

The true density of states is given by

(132) $\rho(E) = \rho^{\Delta}(n)\,\Delta^{-1}.$

Note that this insures that the equation

(133) $\int_0^E \rho(E')\,dE' = \sum_{i=0}^{n} \rho^{\Delta}(i)$

is independent of Δ .

In the Stein-Rabinovitch (SR) algorithm, all oscillator energies ω_μ are reduced to integers ϵ_μ such that $(\omega_\mu/\Delta) \leq \epsilon_\mu < (\omega_\mu/\Delta + 1)$.

The energy for the final state becomes

(134) $E_f = \sum_\mu m_\mu \epsilon_\mu \Delta$

which yields

(135) $\rho^{\Delta}(n) = \sum_\mu \sum_{\{m\}} \delta(n - m_\mu \epsilon_\mu).$

The addition of a single oscillator μ to a given density of states $\rho^{\Delta}_{\mu-1}(n)$ generates a new density of states $\rho^{\Delta}_{\mu}(n)$ via iteration of the equation

(136) $\rho^{\Delta}_{\mu}(n) = \sum_{m_\mu} \rho^{\Delta}_{\mu-1}(n - m_\mu \epsilon_\mu)$

from $n = \epsilon_{max}$ to ϵ_μ where ϵ_{max} is the maximum energy to be considered in the calculation.

For a single oscillator, there is only one level at n = 0 to be convoluted. Thus,

(137) $$\rho_0^{\Delta}(n) = \int(n)$$

and the single oscillator density of states function becomes $\rho_\mu^{\Delta}(n) = \int(n - m_\mu \epsilon_\mu)$.

Iteration of Eq. 136 for n = ϵ_{max} to ϵ_μ and for all modes μ = 1 to 3N-6 generates the total density of states as defined by Eq. 130. Metz[14] has noted that for a calculation employing this technique, the quantities $\rho_\mu^{\Delta}(n)$ and $\rho_{\mu-1}^{\Delta}(n)$ of Eq. 136 may use the same storage vector since counting from the top never destroys data which is later required. This is important if the levels are not harmonic and requires less core than the anharmonic algorithm of SR.

The SR algorithm for harmonic oscillators[13] is a variation of the previous technique and is based on the fact that harmonic oscillator energies come in equally spaced intervals. They obtained the result that the density of states is given by iteration of the equation

(138) $$\rho_\mu^{\Delta}(n) = \rho_{\mu-1}^{\Delta}(n) + \rho_\mu^{\Delta}(n - \epsilon_\mu)$$

from n = ϵ_μ to ϵ_{max} and for all modes μ = 1 to 3N-6. This algorithm thus eliminates the need to perform an extra sum over quantum numbers m_μ and can be very

efficiently programmed since ρ^{Δ}_{n} and ρ^{Δ}_{n-1} can occupy the same location in core.

Using the SR technique, the density of states for naphthalene, h_8 was calculated with the T_1 frequencies of Table V. The results in the vacinity of S_1 are shown on Fig. 54. The frequency scale gives the energy gap relative to the vibrationless origin of S_1. With 48 normal modes, a nearly exponential increase in $\rho(E)$ is observed at the gap of 10626 cm^{-1}. The scale is linear and the value at zero is ca. $3x10^{11}$ states/cm^{-1}. Density of states models would thus predict an increase in k_{nr} with the energy gap. This is in direct opposition to the energy gap law and the experimental observations.

Franck-Condon factors

For evaluation of the Franck-Condon (FC) factors, a model of non-interacting oscillators will be used. This assumes that there is no mode mixing. Thus, the entire FC factor can be written as a product of single oscillator FC factors. This is given by

(139) $$\prod_{n} |\langle n_n | m_n \rangle|^2.$$

More critical is the assumption that the normal modes are harmonic. It has been shown[3,4] that anharmonic effects can alter the rate constant for large energy gaps. However, for relatively small energy gaps such as T_1-S_1 ISC, these effects are expected to be much

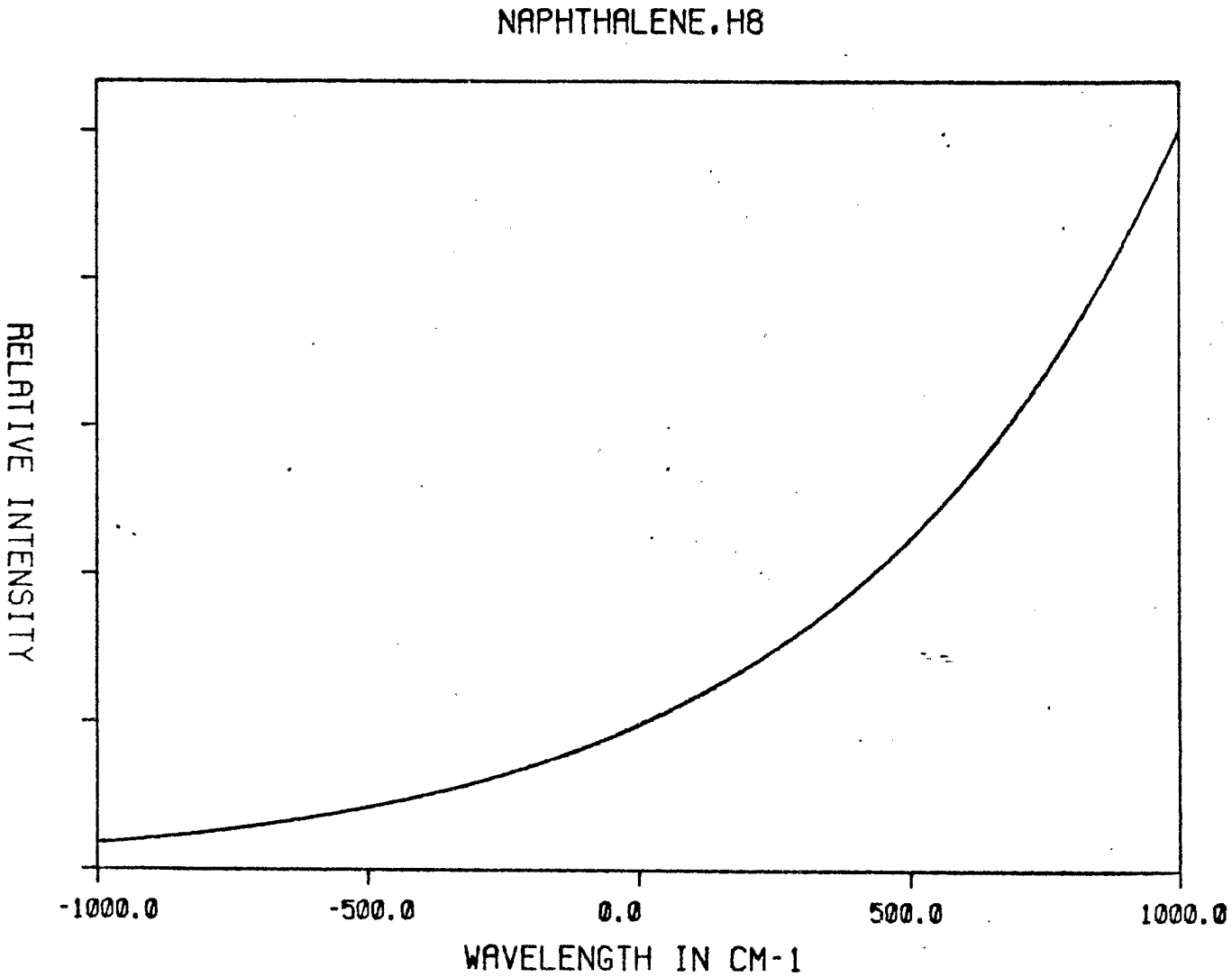

Figure 54. Density of triplet states relative to S_1.

smaller. Thus, they will not be treated.

One of the first analytic formulas for the FC factors of displaced, distorted one dimensional oscillators was given by Katriel[15]. Nitzan and Jortner have given expressions for displaced, identical surfaces[16] and for undistorted oscillators[17]. Other formulas have been given by Christie and Craig[18] and by Heller, Freed and Gelbart[19]. For the calculations presented here, the formula given by Metz[14] was chosen. The Metz algorithm is a very compact routine which uses harmonic oscillator recursion relations to rapidly compute FC factors $\langle n \mid m \rangle$ for all m, given the initial quantum number n.

Defining

$$\tilde{\Delta} = \tilde{\omega}^{1/2} (Q_1 - Q_2)$$

$$\beta = (\tilde{\omega} - \omega) / 2 (\tilde{\omega}\omega)^{1/2}$$

and

$$\alpha = (1 + \beta^2)^{1/2},$$

Metz has shown that the FC integrals are given by

$$(140)\quad \langle n|m\rangle = \left[m!\, n!\, \alpha^{-1} \exp\left(-\tilde{\Delta}^2 \frac{\alpha-\beta}{\alpha}\right) \right]^{1/2} \cdot \sum_{k=0}^{\min(n,m)} \left\{ R_{m-k}\left(-\frac{\beta}{\alpha}, -\frac{\tilde{\Delta}}{\alpha}\right) \cdot R_{n-k}\left(\frac{\beta}{\alpha}, \frac{\alpha-\beta}{\alpha}\tilde{\Delta}\right) \cdot \left(\frac{\alpha^{-k}}{k!}\right) \right\}$$

where $R_l(x,y)$ satisfies the recursion relation

$$R_l(x,y) = \left(2x\, R_{l-2}(x,y) + y\, R_{l-1}(x,y)\right) \cdot l^{-1}$$

with $R_0(x,y) = 1$ and $R_{-1}(x,y) = 0$.

The FC factor appears in the rate equation within the sum over isoenergetic levels. Considering only the

vibrational levels, the Franck-Condon weighted density of states (FCWDOS) can be defined by the equation

$$(141)\quad F(E) = \sum_{f} |\langle \chi_i | \chi_f \rangle|^2 \, \delta(E - E_f) = \prod_{\mu} \sum_{\{m\}} |\langle n_\mu | m_\mu \rangle|^2 \, \delta\left(E - \sum_{m_\mu} m_\mu \omega_\mu\right).$$

For a calculation, E and ω_μ are reduced to integers $n\Delta$ and ϵ_μ by a graining factor Δ as previously described. This yields the equation

$$(142)\quad F(n) = \prod_{\mu} \sum_{\{m\}} |\langle n_\mu | m_\mu \rangle|^2 \, \delta\left(n - \sum_{\mu} m_\mu \epsilon_\mu\right).$$

The true function F(E) is given by

$$(143)\quad F(E) = F(n)\,\Delta^{-1}$$

so that the relation

$$(144)\quad \int_0^E F(E')\,dE' = \sum_{i=0}^{n} F(i)$$

is independent of Δ .

Metz has shown that Eq. 142 may be written as the $3N-6^{\underline{th}}$ iteration of

$$(145)\quad F^{\mu}(n) = \sum_{m_\mu} F^{\mu-1}(n - m_\mu \epsilon_\mu) \, |\langle n_\mu | m_\mu \rangle|^2$$

from $n = \epsilon_{max}$ to ϵ_μ where $F^0(n) = \delta(n)$ and $F^i(n)$ is the $i^{\underline{th}}$ iteration. This algorithm may be programmed very efficiently since F^{μ} and $F^{\mu-1}$ are equivalent in terms of data storage.

Using the data of Table V, the FCWDOS spectrum of naphthalene was calculated. The first calculation used

a Gaussian of FWHM 25.0 cm^{-1}. This is shown on Fig. 55. The energy scale is the energy gap relative to the S_1 vibrationless level and the intensity scale is linear. In contrast to the density of states calculation, the FCWDOS shows a general decrease with increasing energy gap. This is in accordance with the energy gap law.

The second calculation used a Gaussian FWHM of 2.5 cm^{-1}. A saddle point calculation would yield a virtually straight line over the energy range shown on Figure 56 . The peaks correspond to vibrations which have large coupling strengths.

The structured behavior of the FCWDOS appears to be typical for all large molecules. Originally observed for benzene, structure also appears for glyoxal[20] and naphthalene.

The promoting mode

If spin-orbit coupling is not allowed in first order, it may be induced via vibronic coupling. This is a direct analog of vibronic intensity stealing in optical spectra. The electronic matrix element assumes the form

(146) $$\langle \phi_i | \tilde{H}_{so} | \phi_j \rangle \langle \phi_j | \partial/\partial Q_k | \phi_f \rangle$$

if ϕ_j is a triplet and the operators are reversed if it is a singlet. The promoting mode must make the term

$$\langle \phi_j | \partial/\partial Q_k | \phi_f \rangle$$

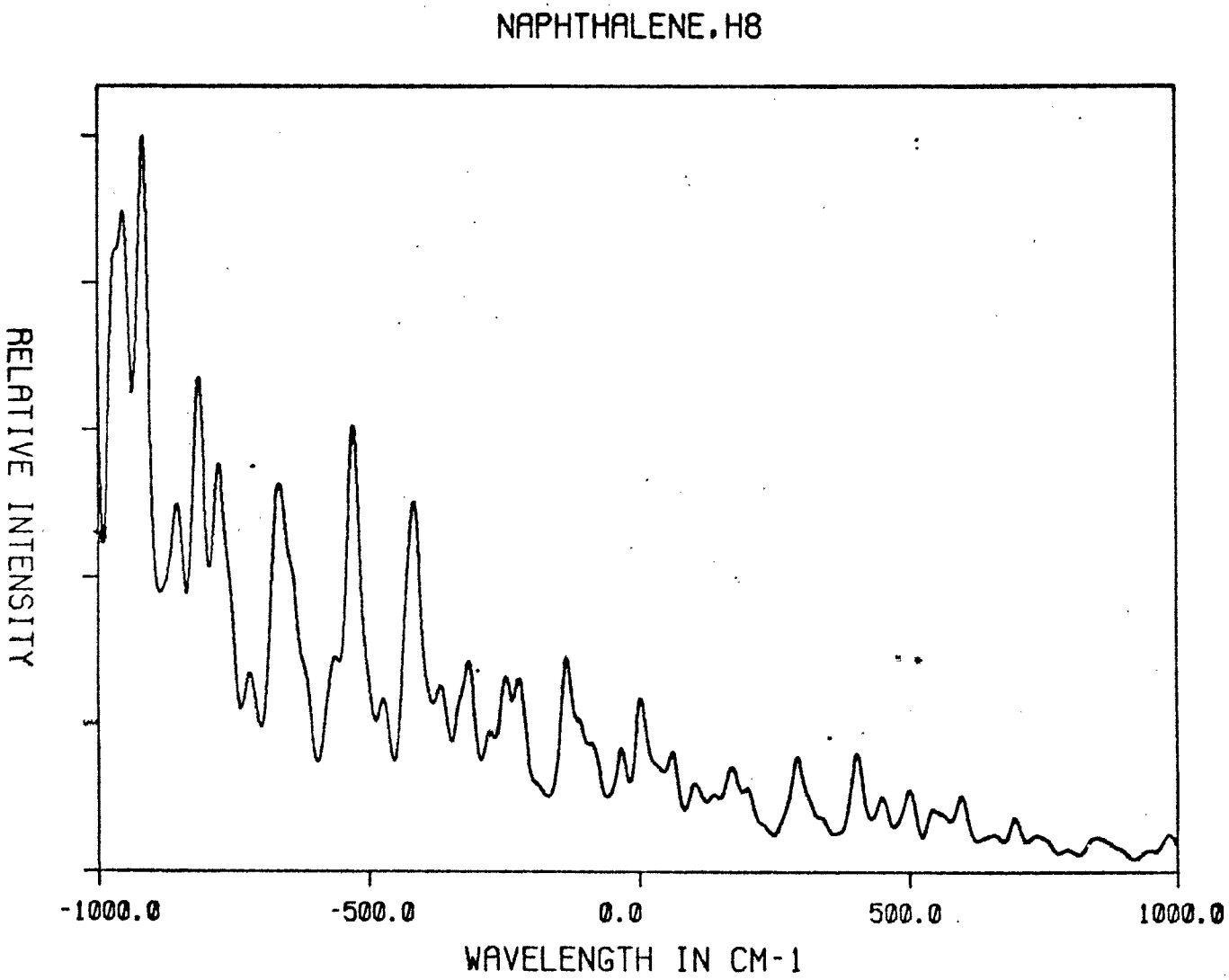

Figure 55. FCWDOS calculated with a final state linewidth of 25 cm^{-1}.

non-zero. Group theoretical methods generally allow a straightforward determination of the symmetry of the promoting mode, k. In large molecules, there are generally many modes of the same symmetry which means that there is not necessarily just one promoting mode.

In virtually all model calculations only one promoting mode has been assumed. The enhancement of the rate constant through optical excitation of a promoting mode can be predicted through an analysis of the vibronic overlap integrals of the form

$$\langle n_k | Q_k | m_k \rangle.$$

These integrals are non-zero only for a unity change in the vibrational quantum numbers. For identical oscillators, the following relations are expected to hold:

$$\langle 1 | Q_k | 0 \rangle = \langle 0 | Q_k | 1 \rangle$$

and

$$\langle 1 | Q_k | 2 \rangle = \sqrt{2} \langle 1 | Q_k | 0 \rangle.$$

Thus a total enhancement of 3 is expected upon population of a promoting mode. To date, no such dramatic changes in the non-radiative rate constants have been experimentally observed.

An analysis within the saddle point approximation[21] predicted that the enhancement should be 2.3 for a single promoting mode and 1.3 for multiple promoting modes. Thus, the enhancement could be on the same order as the other modes.

In the calculation of non-radiative rates in the next chapter, it is assumed that there is a single,

non-optical promoting mode. For naphthalene, it may have b_{2g} or b_{3g} symmetry as discussed in Chapter X. Since the primary effect of the promoting mode will be to alter the effective energy gap, the rate constant will be most sensitive to the energy of the mode. As a first approximation, the $2(b_{2g})$ mode was chosen as the promoting mode since its energy is approximately the average of all b_{2g} and b_{3g} modes. However, several calculations will be presented for which the energy of the $2(b_{2g})$ mode was altered in order to probe the sensitivity of the non-radiative rate to small changes in the energy gap.

References to Chapter XIII

1. F. Metz, Chem. Phys., 9, 121 (1975).
2. M. J. Robey and E. W. Schlag, The $^1B_{2u}$ Excited State of Benzene: Force Field and Normal Coordinates, preprint.
3. A. L. Stanford and S. F. Fischer, Chem. Phys., 1, 99 (1973).
4. S. F. Fischer, E. C. Lim and L. A. Stanford, J. Chem. Phys., 61, 582 (1974).
5. H. Gattermann and M. Stockburger, J. Chem. Phys., 63, 4541 (1975).
6. M. Stockburger, H. Gattermann and W. Klusmann, J. Chem. Phys., 63, 4519 (1975).
7. P. C. Haarhoff, Mol. Phys., 7, 101 (1963).
8. R. A. Marcus and O. K. Rice, J. Phys. Colloid Chem., 58, 894 (1951).
9. J. H. Current and B. S. Rabinovitch, J. Chem. Phys., 38, 783 (1963).
10. E. Thiele, J. Chem. Phys., 39, 3258 (1963).
11. E. W. Schlag and R. A. Sandsmark, J. Chem. Phys., 37, 168 (1962).
12. M. R. Hoare and T. W. Ruijrok, J. Chem. Phys., 52, 113 (1970).
13. S. E. Stein and B. S. Rabinovitch, J. Chem. Phys., 58, 2438 (1972).
14. F. Metz, Chem. Phys., 18, 385 (1976).
15. J. Katriel, J. Phys. B:Atom. Mol. Phys., 3, 1315 (1970).
16. A. Nitzan and J. Jortner, J. Chem. Phys., 56, 1355 (1971).
17. A. Nitzan and J. Jortner, J. Chem. Phys., 56, 2079 (1972).
18. J. R. Christie and D. P. Craig, Mol. Phys., 23, 345 (1972).

19. D. F. Heller, K. F. Freed and W. M. Gelbart, J. Chem. Phys., 56, 2309 (1972).
20. H. Kuettner, private communication.
21. F. Metz, private communication.

Chapter XIV

Numerical Results

Computational procedure

In Chapter VIII, it was shown that the properties of an ensemble, e.g. the quantum yield or radiative rate constant, must be calculated by a very specific averaging technique which uses the microscopic rate constants and populations as input parameters. In this chapter, calculations given by a solution of the Master Equation will be presented. The relative rate calculations are restricted to the rotational ensembles along the 0-0 and $8(b_{1g})^1_o$ absorption bands of naphthalene, h_8. As shown in Chapter VI, the absorption profiles of these two bands correspond to polarization in the long (type A band) and short (type B band) in-plane axes, respectively. The fact that both have low excess energies justifies the assumption that only T_1 can be the final electronic state of ISC.

Initial state populations were generated in a modified band contour program (see Chapter VI). For the origin, 14041 transitions were considered and for the $8(b_{1g})$, 21667. Along with the population, the excited state quantum numbers and rotational energies were stored. Relative populations were calculated using a Gaussian FWHM of 0.2 cm^{-1} which was very near the experimental value.

The microscopic non-radiative rate constants were calculated from Eq. 111. The electronic matrix elements corresponding to the three spin polarizations were treated as adjustable parameters and were varied as discussed below. The vibrational factors were taken directly from the Franck-Condon weighted density of states function F(E) as discussed in Chapter XIII. The rotational factors were calculated via a subroutine which gave all Wigner 3-J symbols. Symmetric rotor amplitudes were used.

The final state linewidth function was assumed to be a Gaussian of FWHM 2.5 cm^{-1}. Electronic, vibrational and rotational energies were used for calculation of the energy matching of initial and final states. Rotational energies of the triplet state were calculated seperately with inertial constants given by the average of those of S_1 and S_o.

The constant radiative rate constant was adjusted so that the final quantum yields were on the same order of magnitude as those observed. This was necessary because absolute rate constants were not calculated.

Master Equation solutions for the ensemble quantum yield, radiative rate constant, etc. as given in Chapter VIII used the parameters discussed above to generate an ensemble spectrum along the rotational absorption contour. In the figures below, the calculated

rotational contour is always plotted under the calculated ensemble spectrum.

ISC from the $8(b_{1g})^1_o$ band

Intersystems crossing along the rotational contour of the $8(b_{1g})^1_o$ band of naphthalene, h_8 will be considered first. Three different quantities will be discussed. Theoretically interesting is the average non-radiative rate constant of the rotational levels along the contour. This can be defined as

(146) $$k^a_{nr} = \left[\underset{\sim}{K}_{nr} \right] / N_o$$

This does not correspond to an observable since the ensemble non-radiative rate constant k^e_{nr} is defined by Eq. 38. The rate constant k^e_{nr} is equal to k^a_{nr} only in the limit of constant, zero quantum yield.

The second quantity is the ensemble radiative rate constant k^e_r. As discussed in Chapter VIII, for constant microscopic radiative rate constants the ensemble radiative rate constant is given by

(147) $$k^e_r = k^m_r \langle \underset{\sim}{\tau} \rangle^2 / \langle \underset{\sim}{\tau}^2 \rangle$$
$$= k^m_r L(\underset{\sim}{\tau}).$$

$L(\underset{\sim}{\tau})$ can be interpreted as a lifetime dispersion term. It assumes values from zero to one. If all lifetimes are equal, it is unity and k^e_r equals k^m_r. However, the condition that k^e_r be constant is given by $L(\underset{\sim}{\tau})$ being constant. Thus, the observation of

a constant k_r^e does not necessarily imply the equality of k_r^e and k_r^m. It is interesting to note that since $L(\underset{\sim}{\gamma})$ is always less than or equal to one, the measured radiative rate constant is a minimum limit to the true rate constant.

The third quantity to be considered is the ensemble quantum yield. This is defined by the equation

(148) $$\phi^e = [\underset{\sim}{\phi}] / N_o .$$

This corresponds to an observable and can be directly compared with the measured data.

The first set of calculations assumes that only the spin component along the molecular B axis is populated. The promoting mode energy was set at 422 cm^{-1}. Computed spectra for k_{nr}^a, k_r^e and ϕ^e are shown on Figs. 57, 58 and 59, respectively. k_{nr}^a exhibits strong variations with a maximum just to the blue of the red absorption peak. Much less structure is seen in k_r^e. Thus, the lifetime dispersion is nearly constant. However, the ϕ^e spectrum shows fluctuations of over 50%. This indicates that, although there is little change in the dispersion of lifetimes along the contour, the absolute value changes greatly. The trend of ϕ to increase from the red absorption peak to the blue is in qualitative agreement with experiment. However, the observed quantum yields increase more rapidly.

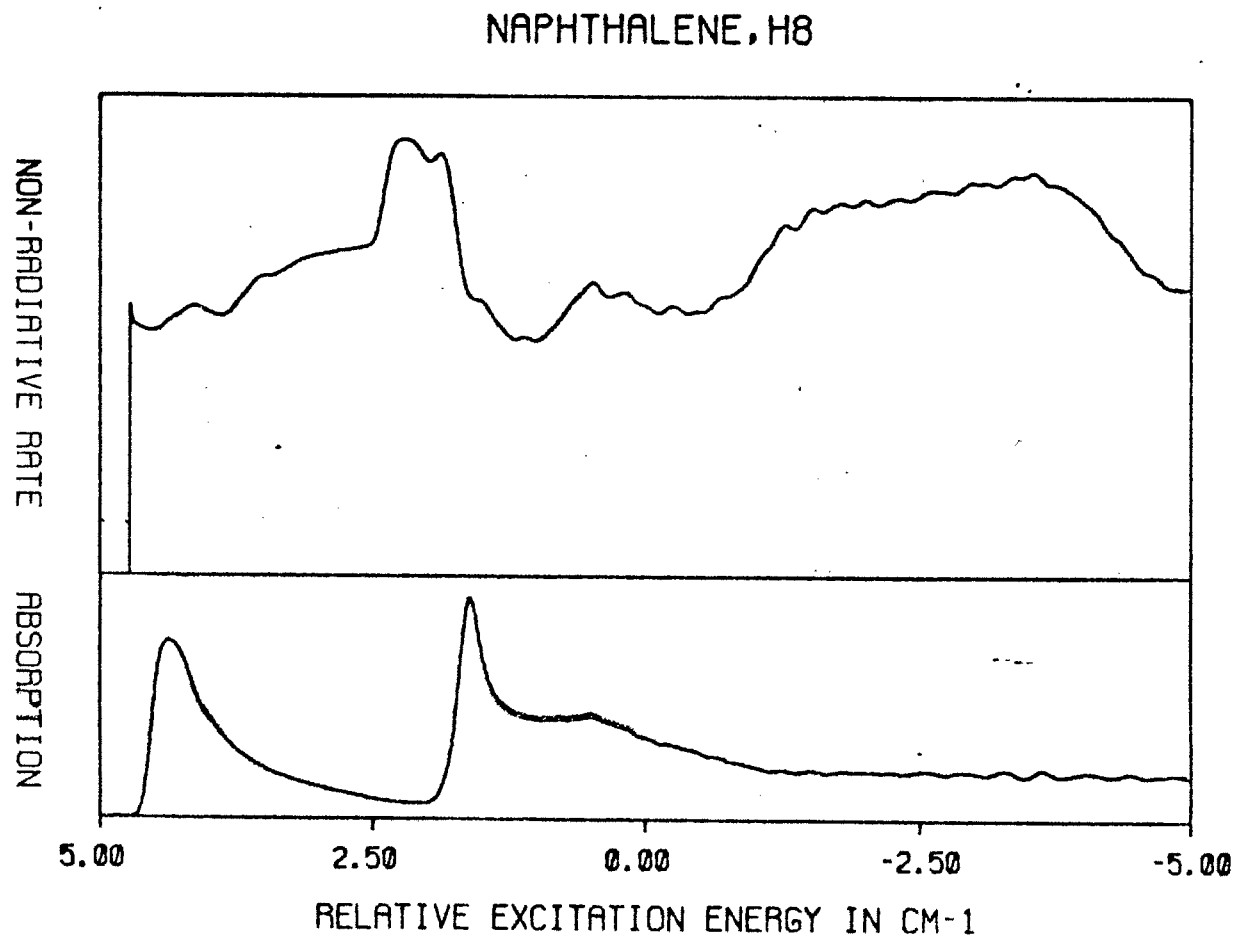

Figure 57. k_{nr}^{a} spectrum with B axis spin polarization.

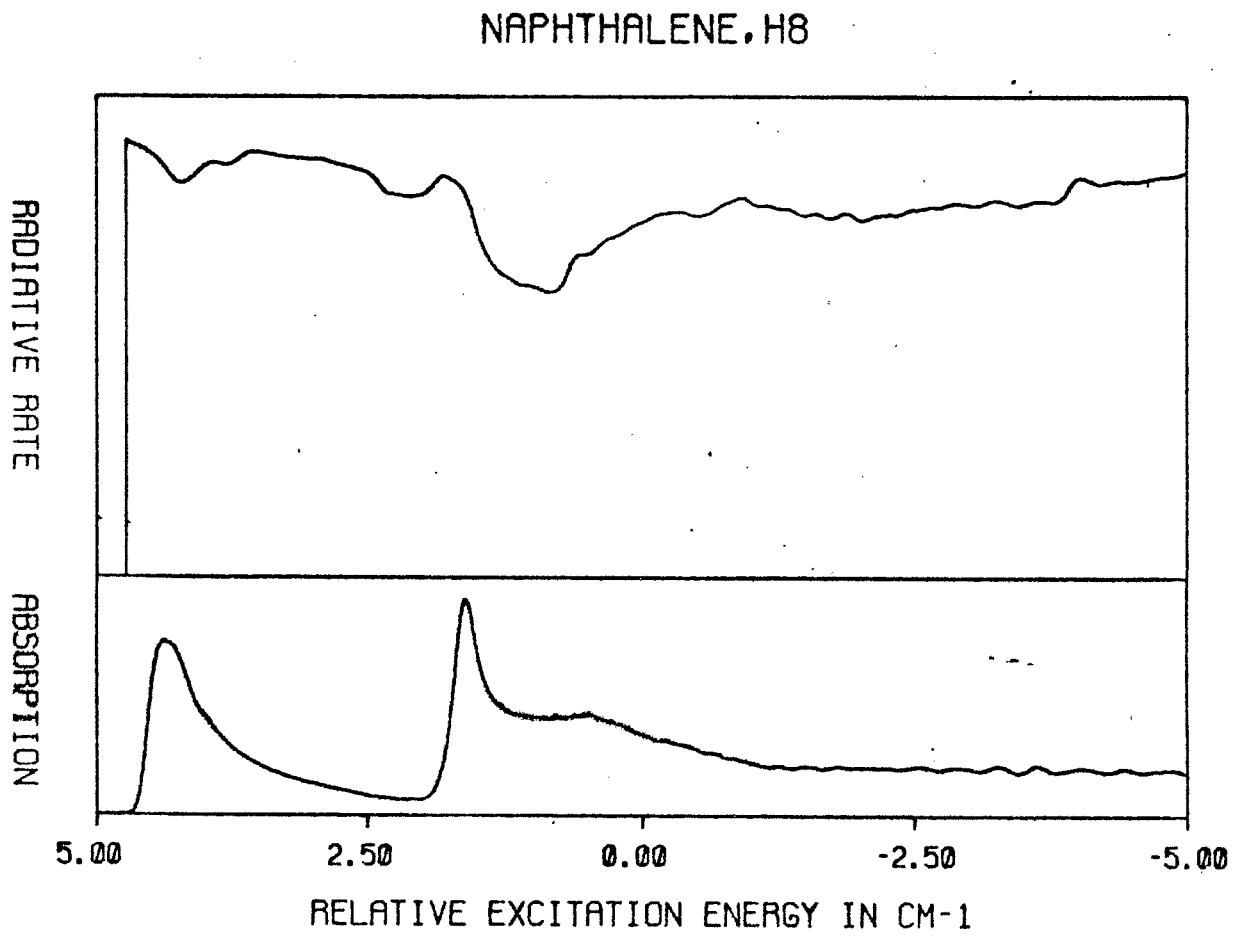

Figure 58. k_r^e spectrum with B axis spin polarization.

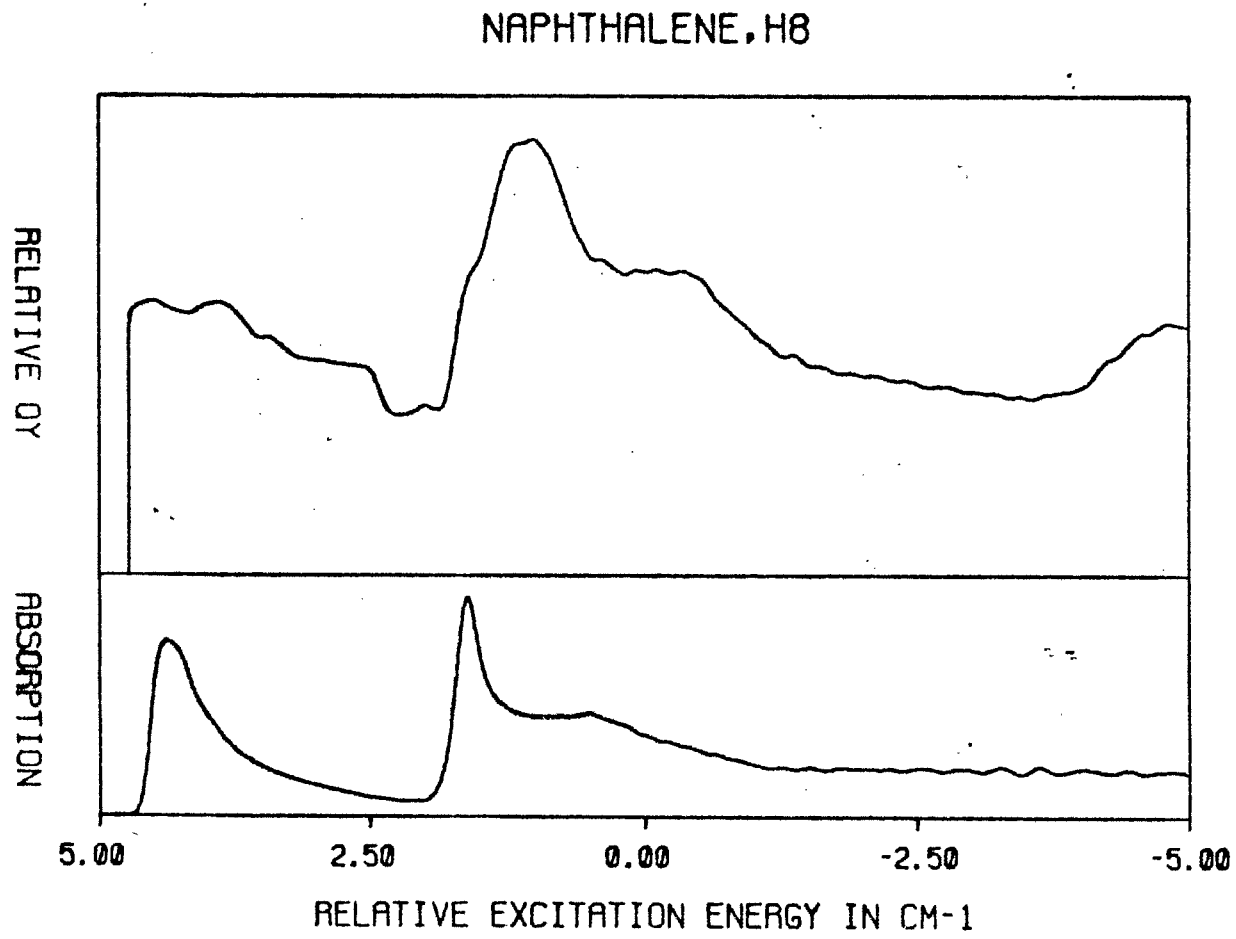

Figure 59. ϕ^{e} spectrum with B axis spin polarization.

The second set of calculations assumes that both in-plane spin components are equally populated. The calculated spectra are shown on Figs. 60, 61 and 62. The k^a_{nr} spectrum now shows a double peaked structure. Each peak occurs in the vacinity of an absorption peak. The k^e_r spectrum shows very little variation between the peaks, indicating a very constant lifetime dispersion in this energy region. The quantum yield spectrum does not correlate with experiment since the primary peak is to the red of the red absorption peak.

A third set of calculations assumed that only the A-axis spin component was populated. The calculated spectra are shown on Figs. 63, 64 and 65. The k^a_{nr} spectrum shows structure which is inverted relative to Fig. 57 (B-axis spin polarization). A peak is observed at the blue absorption maximum and a dip at the red. Radiative rate constants show maxima at the two absorption maxima. This corresponds with the experimental observations. The quantum yield spectrum shows a minimum at the blue absorption peak and thus does not correlate with experiment.

Although no set of calculations reproduced the experimental values, they allow several important conclusions to be drawn. First, rotational structure along an absorption contour is to be expected for the

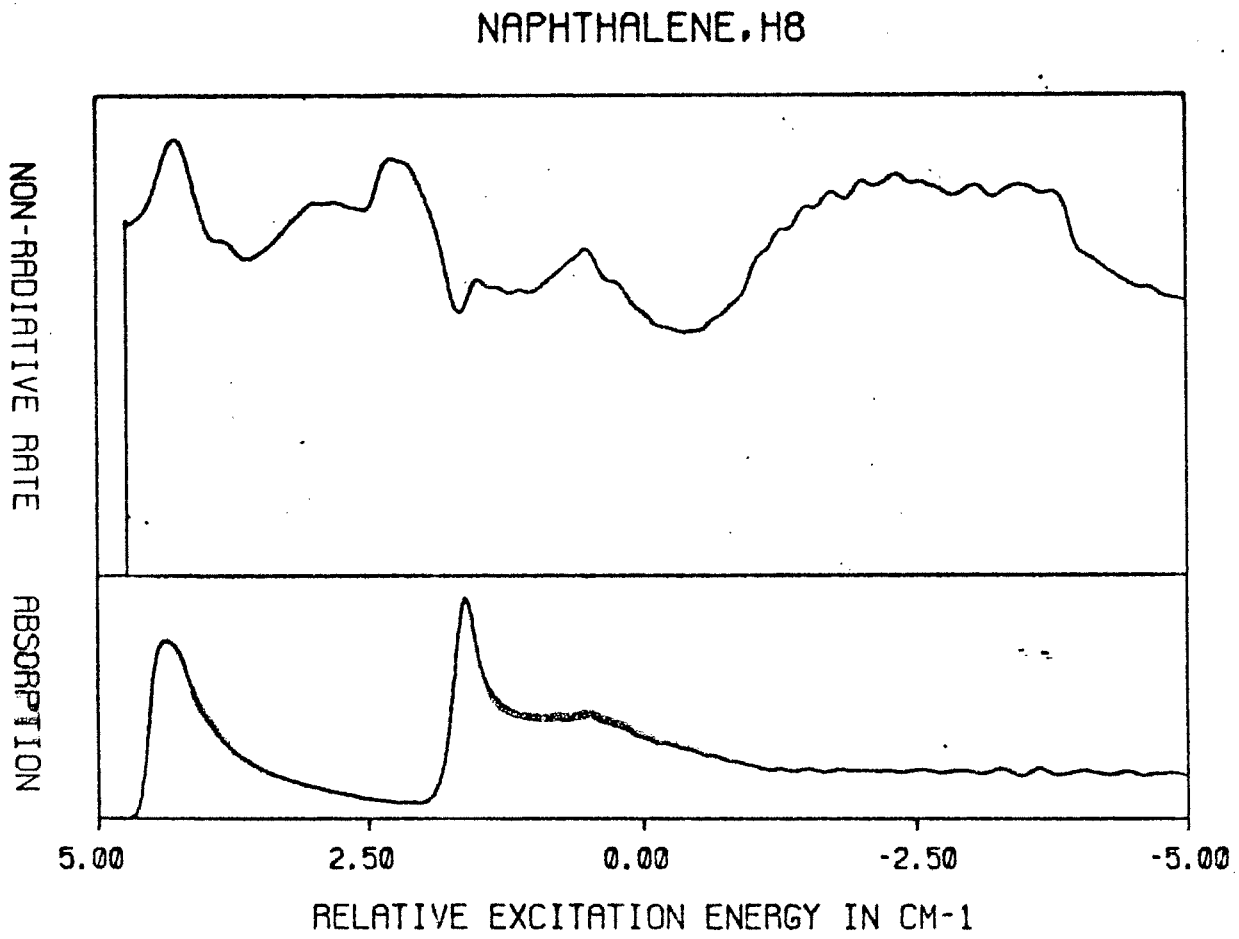

Figure 60. k_{nr}^{a} spectrum with in-plane spin polarization.

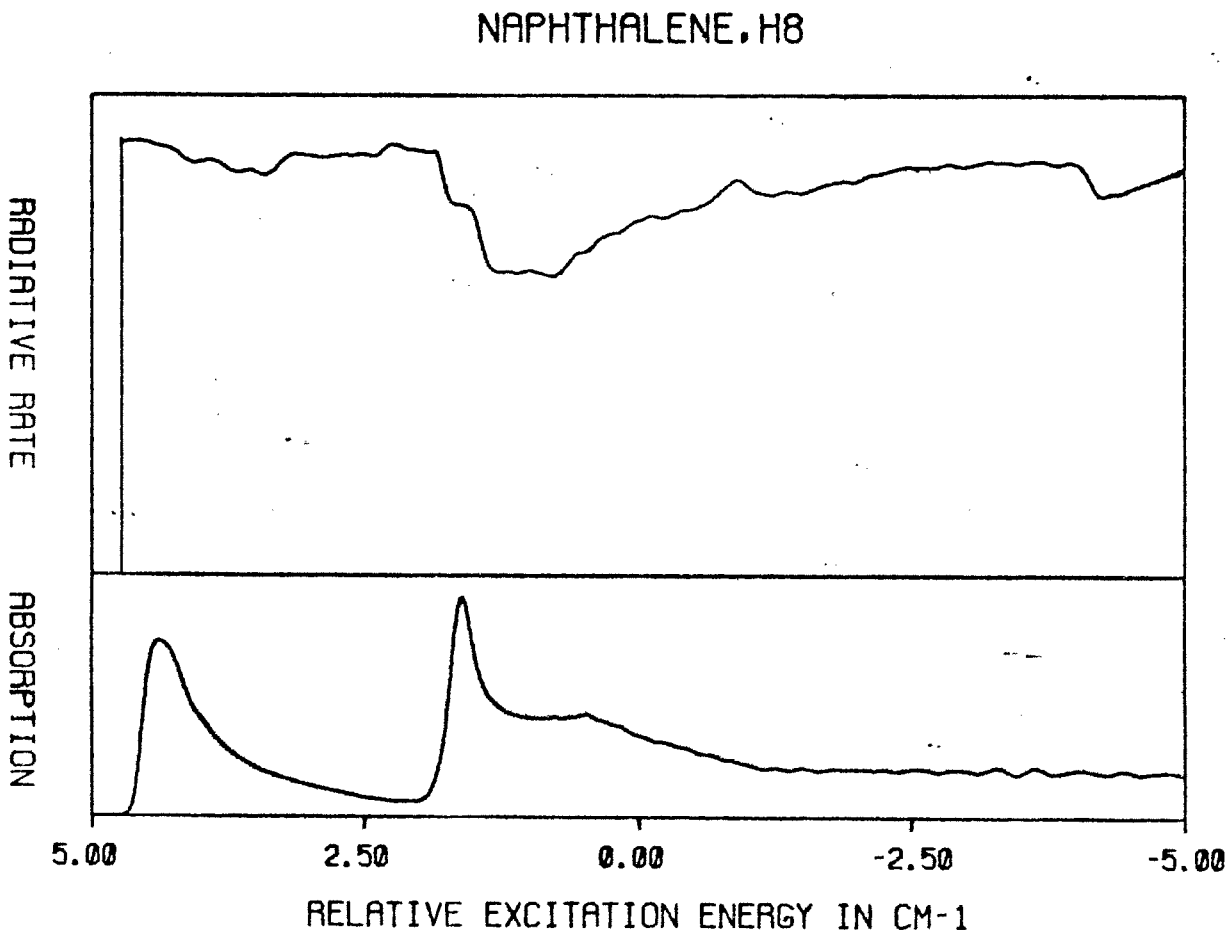

Figure 61. k_r^e spectrum with in-plane spin polarization.

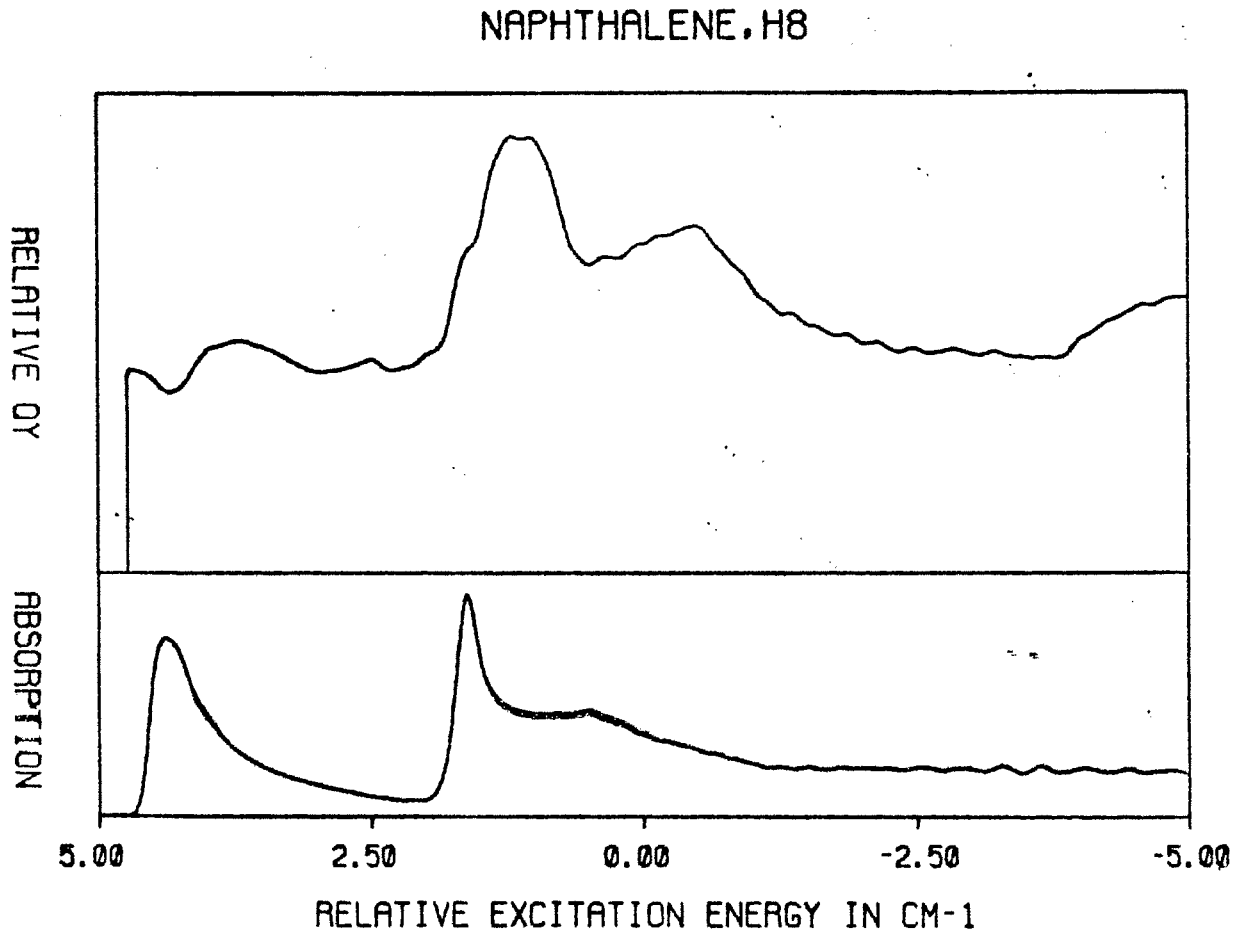

Figure 62. ϕ^{e} spectrum with in-plane spin polarization.

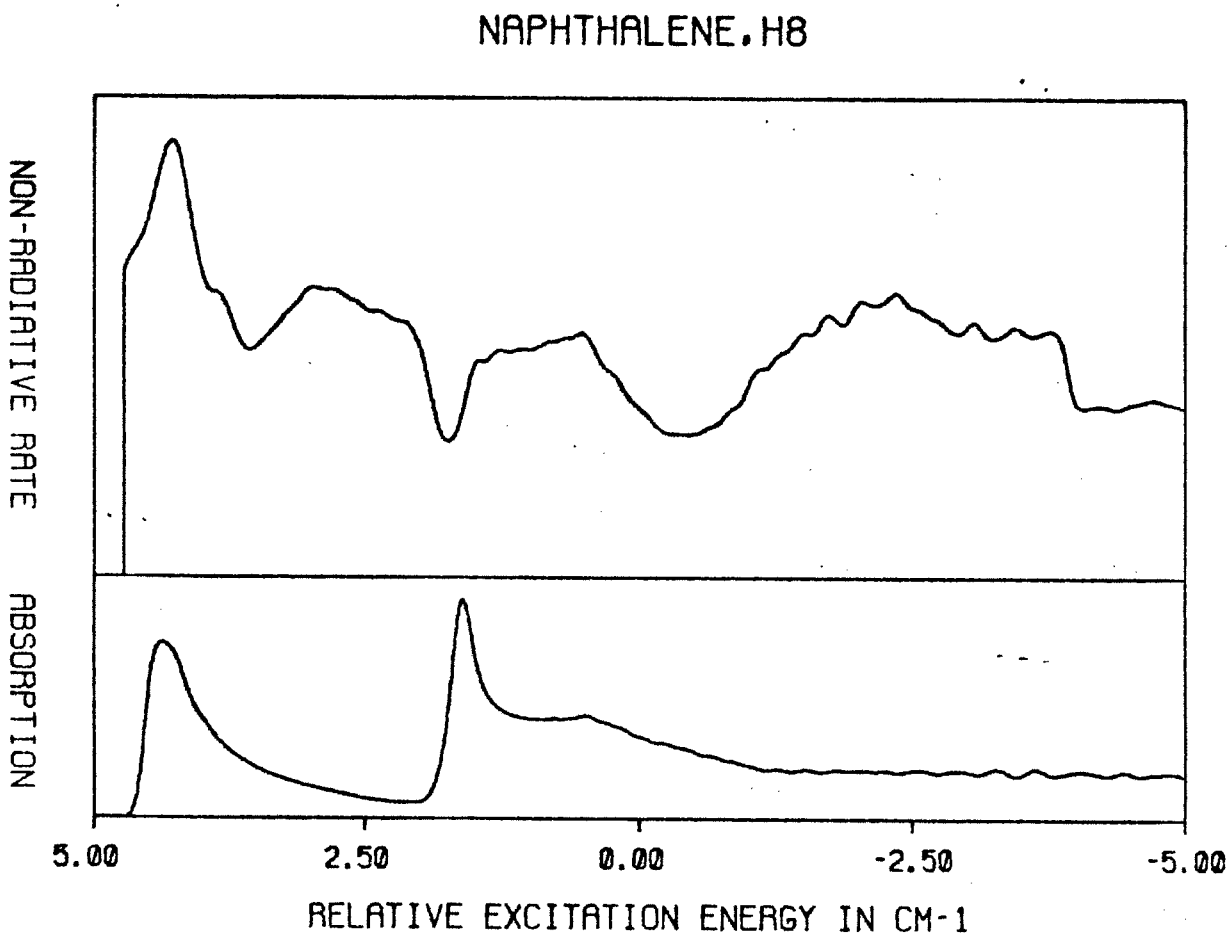

Figure 63. k_{nr}^{a} spectrum with A axis spin polarization.

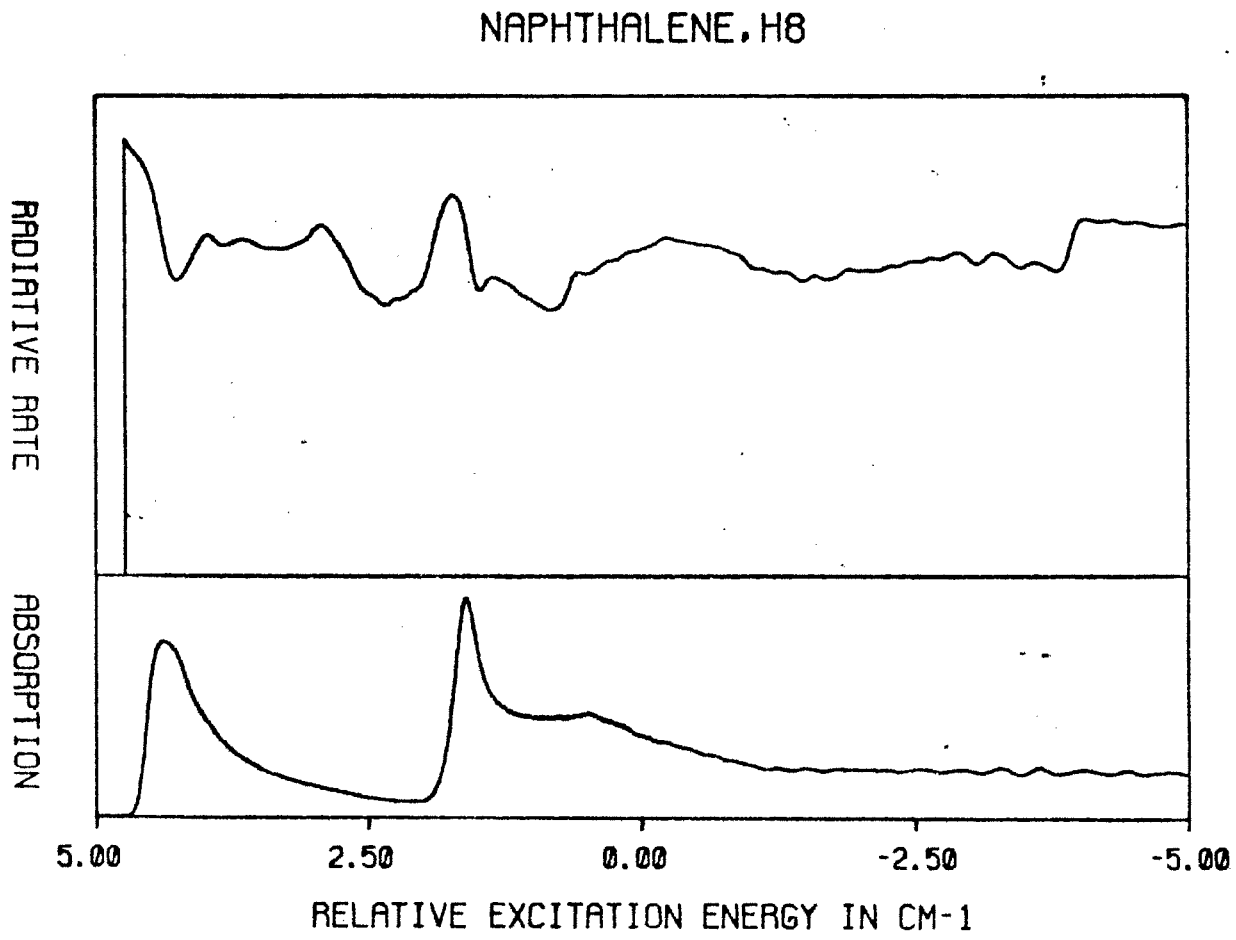

Figure 64. k_r^e spectrum with A axis spin polarization.

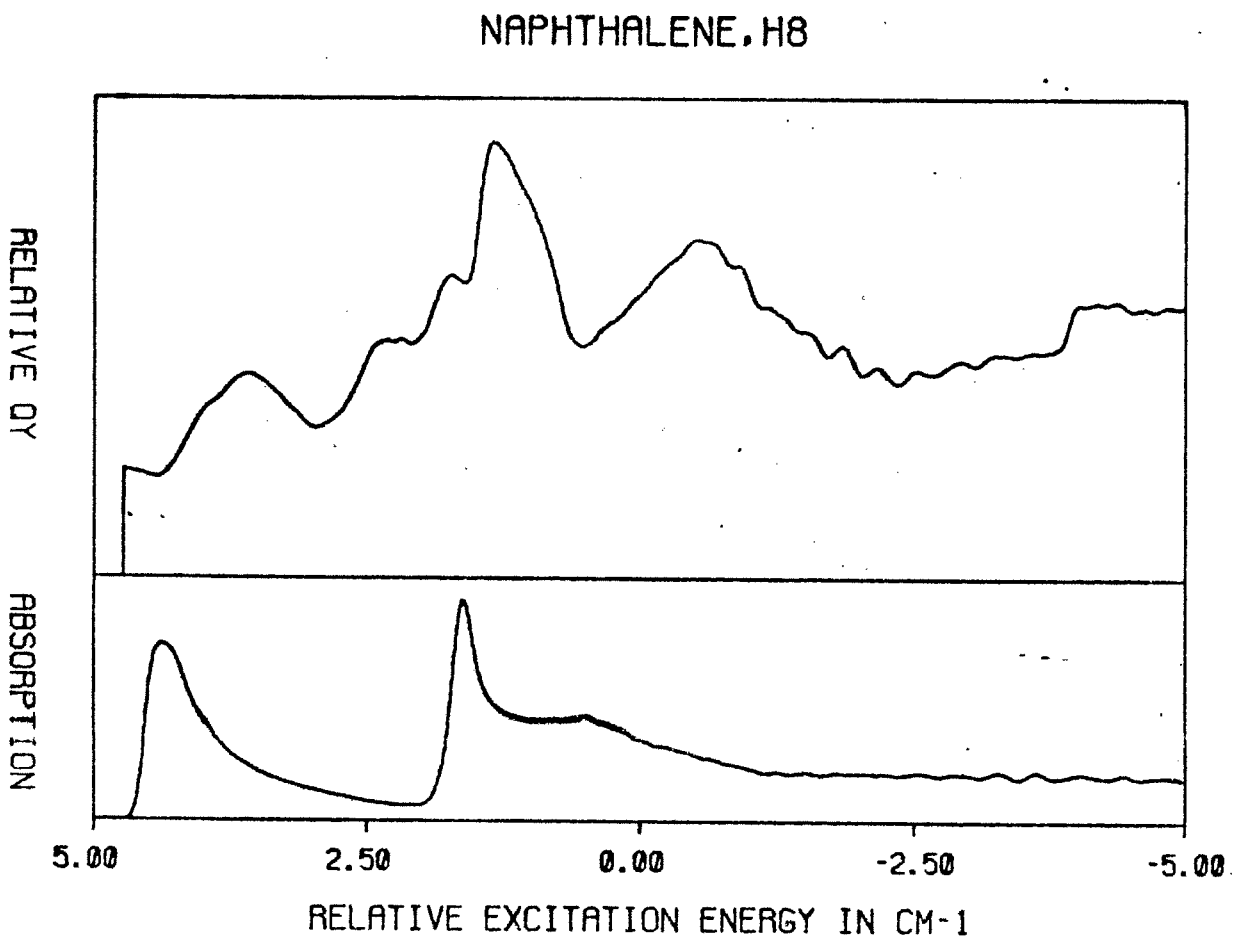

Figure 65. ϕ^e spectrum with A axis spin polarization.

non-radiative rate constants. This structure is not washed out by the excitation of many rotational levels. The structure also depends on which spin component is populated and thus the purely electronic matrix elements. The structure in the non-radiative rate constants generates structure in the quantum yields and causes variations in the ensemble radiative rate constant to appear.

It is interesting to consider the effects which give rise to structure in k_{nr}^{a}. The basic reason is the structure in the vibrational function F(E). Varying rotational energy differences select out different Franck-Condon factors. However, F(E) is also multiplied by a rotational term which includes the Wigner 3-J symbol. This rotational term is an additional weighting factor for the rate constant. For the following calculation, the rotational factor was set to unity for all allowed rotational transitions and zero otherwise. Repeating the calculation for spin polarization along the A axis generated Fig. 66. This is directly comparable with Fig. 63. It is important to note that the structure in k_{nr}^{a} is markedly different without rotational weighting.

A similar calculation was performed, this time with the normal rotational factors but with all vibrational terms set to unity. Thus, F(E)=1 for all E.

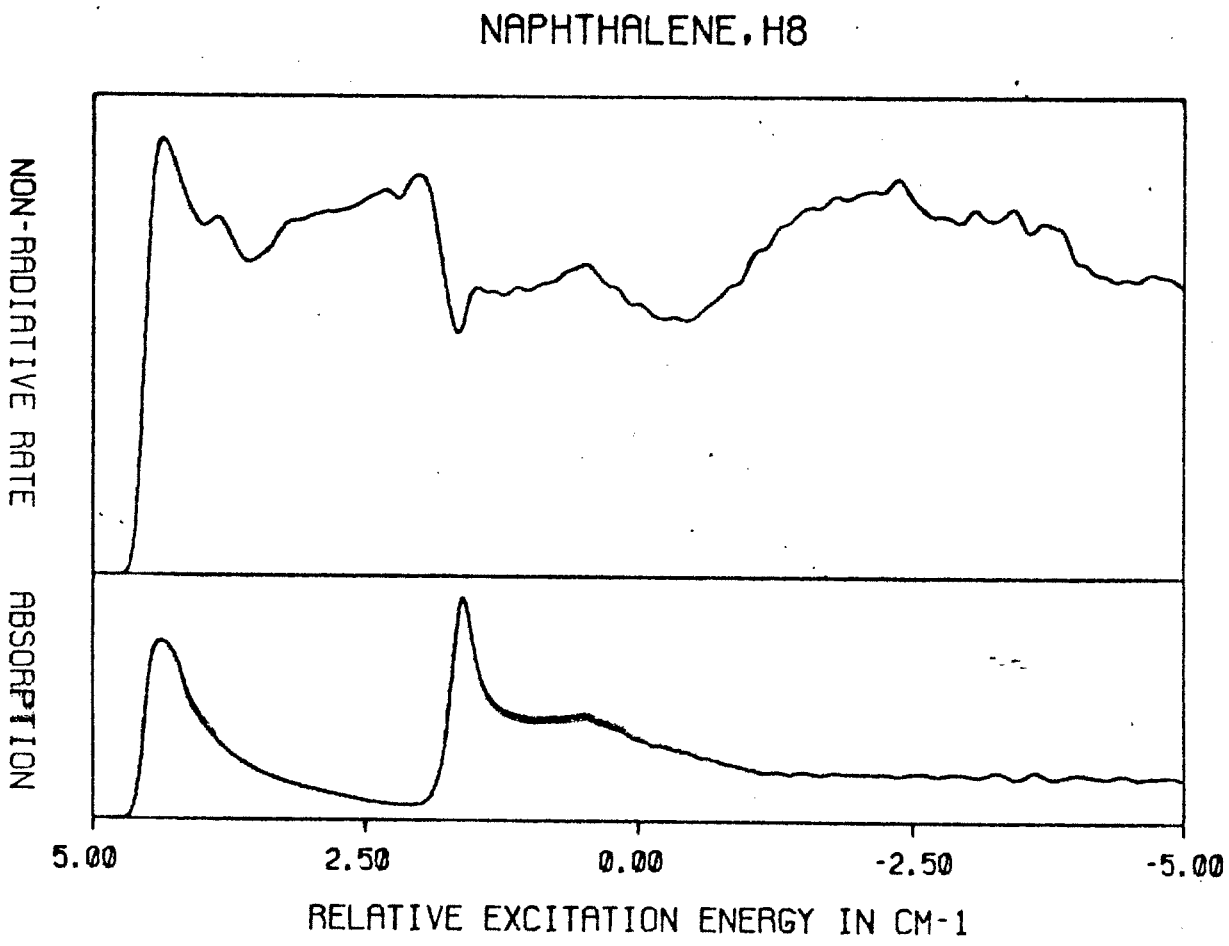

Figure 66. k_{nr}^{a} spectrum with A axis spin polarization and constant rotational factors.

The results of this calculation are shown of Fig. 67. The straight line indicates that without structure in F(E), no structure is observed in k^a_{nr}. This is the expected result due to the sum rule for the Wigner 3-J symbols.

In Figs. 57 to 67, the sum was taken over all final rotational states. This is necessary for a calculation of the rate constant. However, it is interesting to consider the structure due to the different rotational branches $\Delta N = \pm 1, 0$. The rotational branches each have different vibrational and rotational terms associated with them.

The next set of calculations considers the full vibrational and rotational dependence for spin polarization along the A axis. Components of k^a_{nr} due to $\Delta N = -1, 0$, and $+1$ are shown on Figs. 68, 69 and 70 respectively. The sum, of course, yields Fig. 63. The $\Delta N = -1$ spectrum shows large variations with a maximum between and minima at the two absorption peaks. This is entirely different from the $\Delta N = 0$ component which shows a strong peak only at the blue absorption peak. Different still is the $\Delta N = +1$ component which shows a minimum at the blue absorption peak and a maximum far to the red.

It is interesting to note that if the selection rules for ISC were $\Delta N = 0$ and $\Delta K = 0$, the final k^a_{nr}

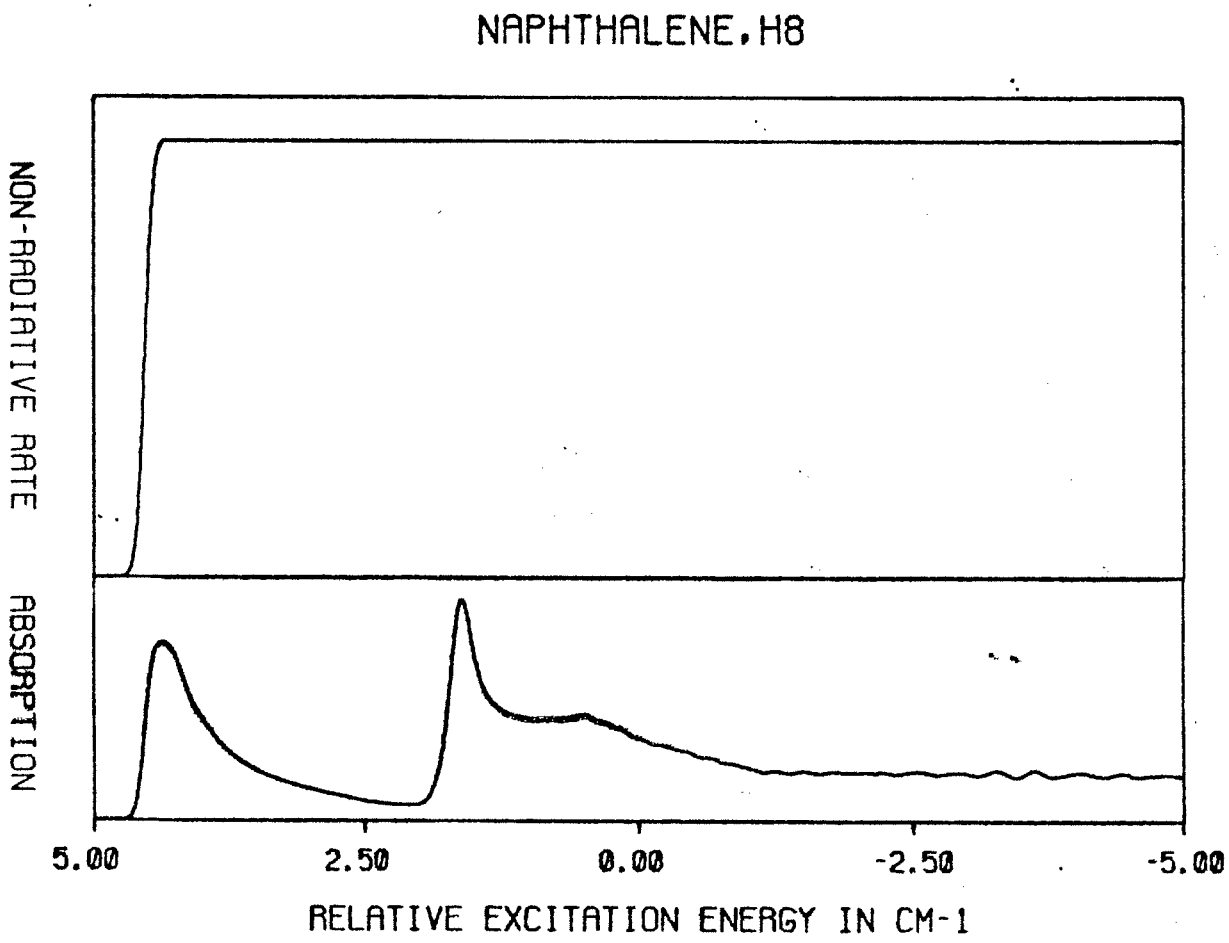

Figure 67. k_{nr}^{a} spectrum with A axis spin polarization and constant vibrational factors.

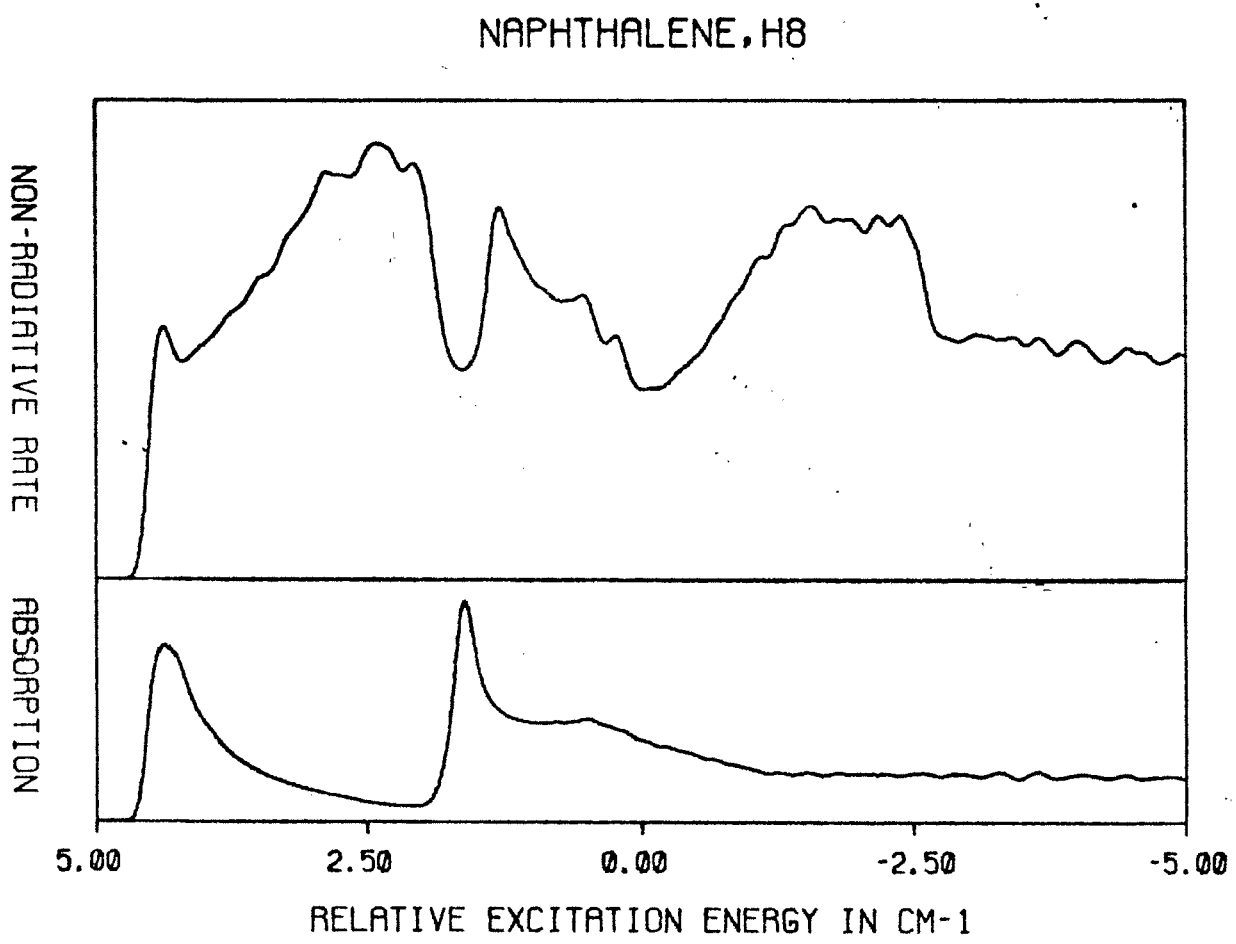

Figure 68. k_{nr}^{a} spectrum with A axis spin polarization (Δ N = -1).

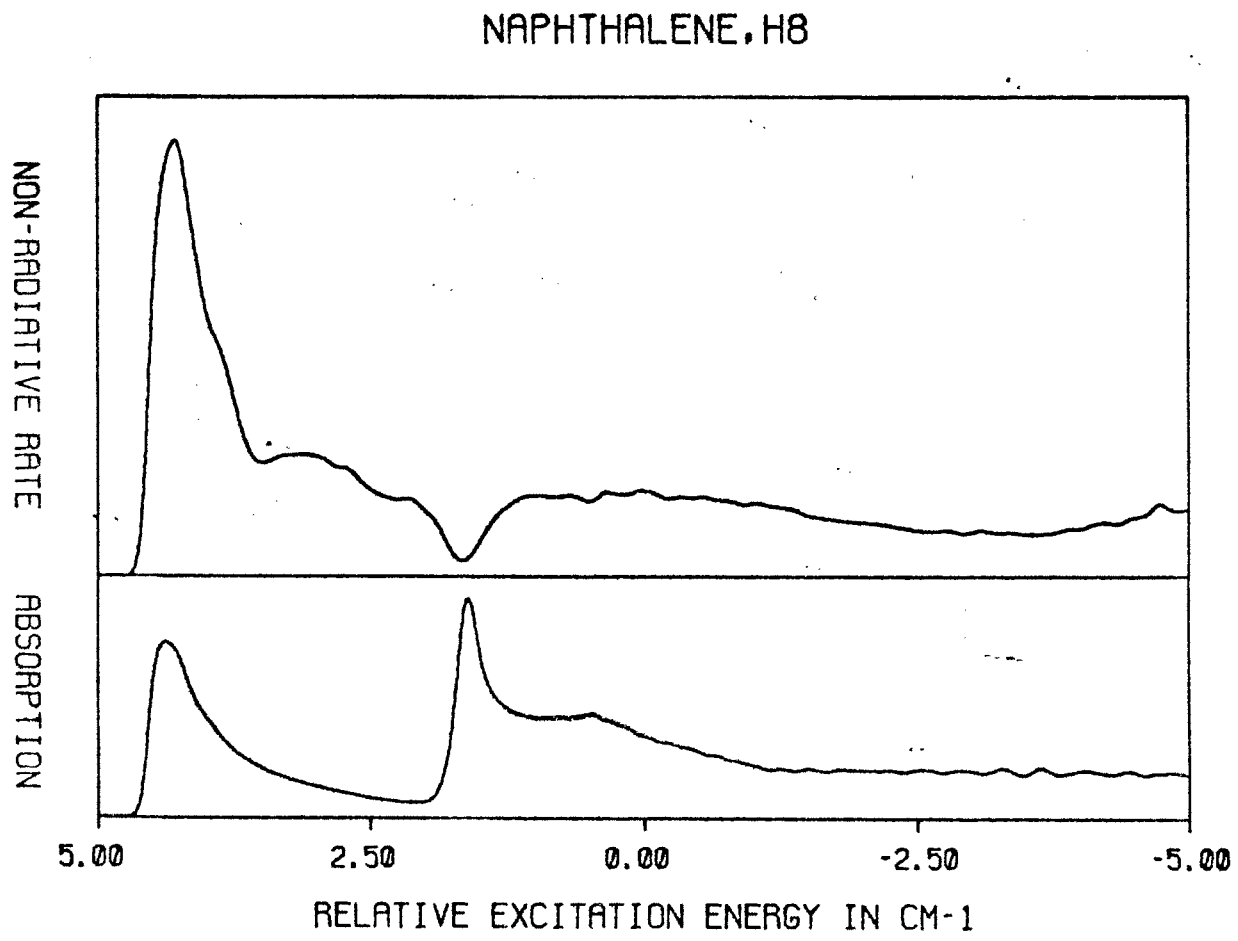

Figure 69. k_{nr}^{a} spectrum with A axis spin polarization ($\Delta N = 0$).

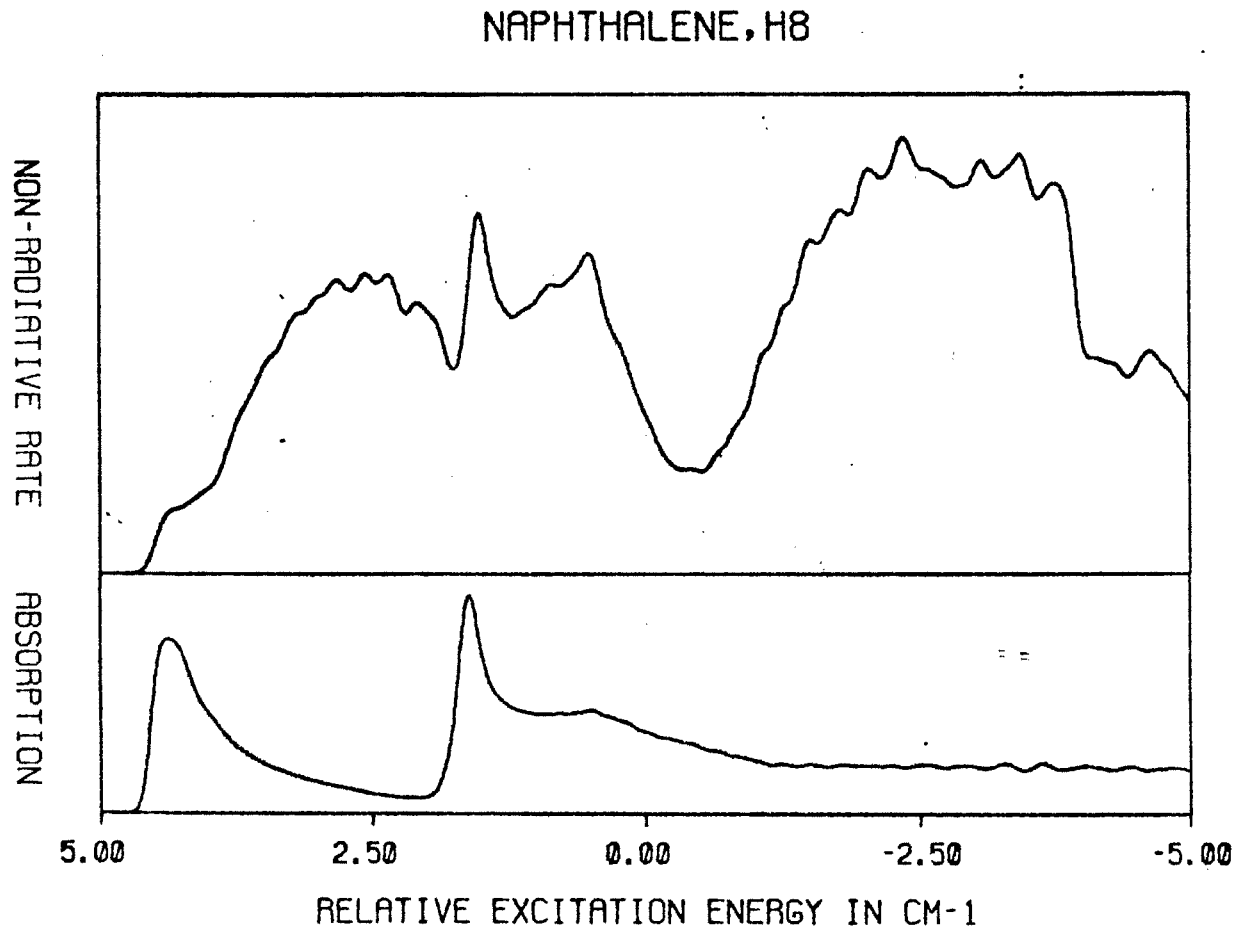

Figure 70. k_{nr}^{a} spectrum with A axis spin polarization (Δ N = +1).

spectrum would be that shown on Fig. 69. This spectrum has a worse correlation with experiment than that given by the sum of the components.

In the next set of calculations, only the vibrational contributions to the rate were considered. The rotational factors were unity for allowed transitions and zero otherwise. Rotational transitions for $\Delta N = -1$, 0 and +1 are shown on Figs. 71, 72 and 73, respectively. The sum of these curves yields Fig. 66. In each case, the neglect of rotational factors gives a different k_{nr}^{a} spectrum than that calculated with rotational terms. Fig. 72, which is for $\Delta N = 0$ and $\Delta K = 0$, shows structure which is completely inverted relative to the experimentally observed values.

However, it is interesting to note that Fig. 72 is a calculation based on the assumption that the only effect of the rotational states is to alter the effective energy gap. This is considered to be the case for IC. Thus, Fig. 72 gives the predicted k_{nr}^{a} spectrum for a final singlet at the energy of T_1.

The final set of calculations for the $8(b_{1g})_{o}^{1}$ band used normal rotational factors and set F(E) to unity. Spectra for $\Delta N = -1$, 0 and +1 are shown on Figs. 74, 75 and 76, respectively. The sum of these three curves is unity as shown on Fig. 67. However, the $\Delta N = \pm 1$ spectra show minima and the $\Delta N = 0$ spectrum shows a

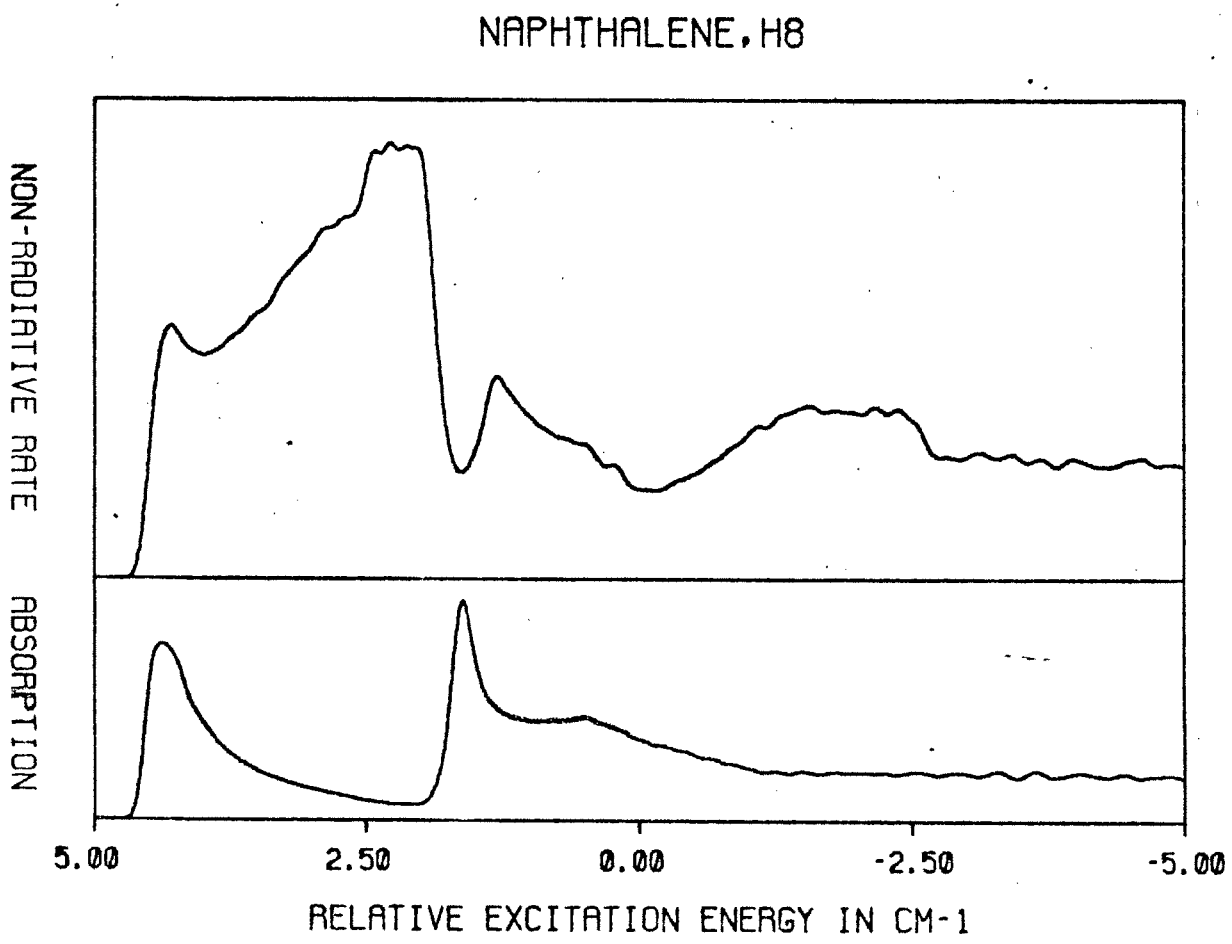

Figure 71. k_{nr}^{a} spectrum with constant rotational factors ($\Delta N = -1$).

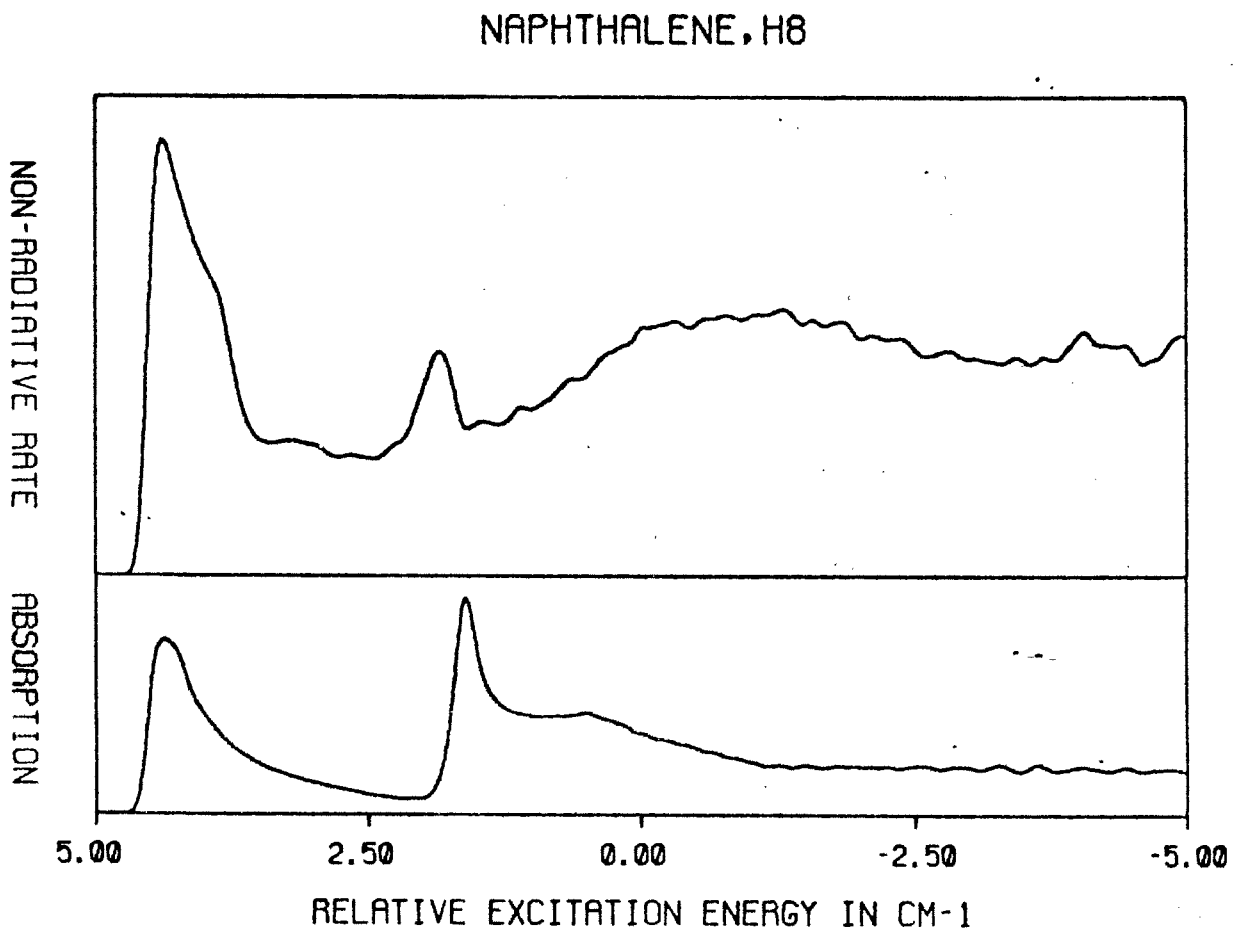

Figure 72. k_{nr}^{a} spectrum with constant rotational factors ($\Delta N = 0$).

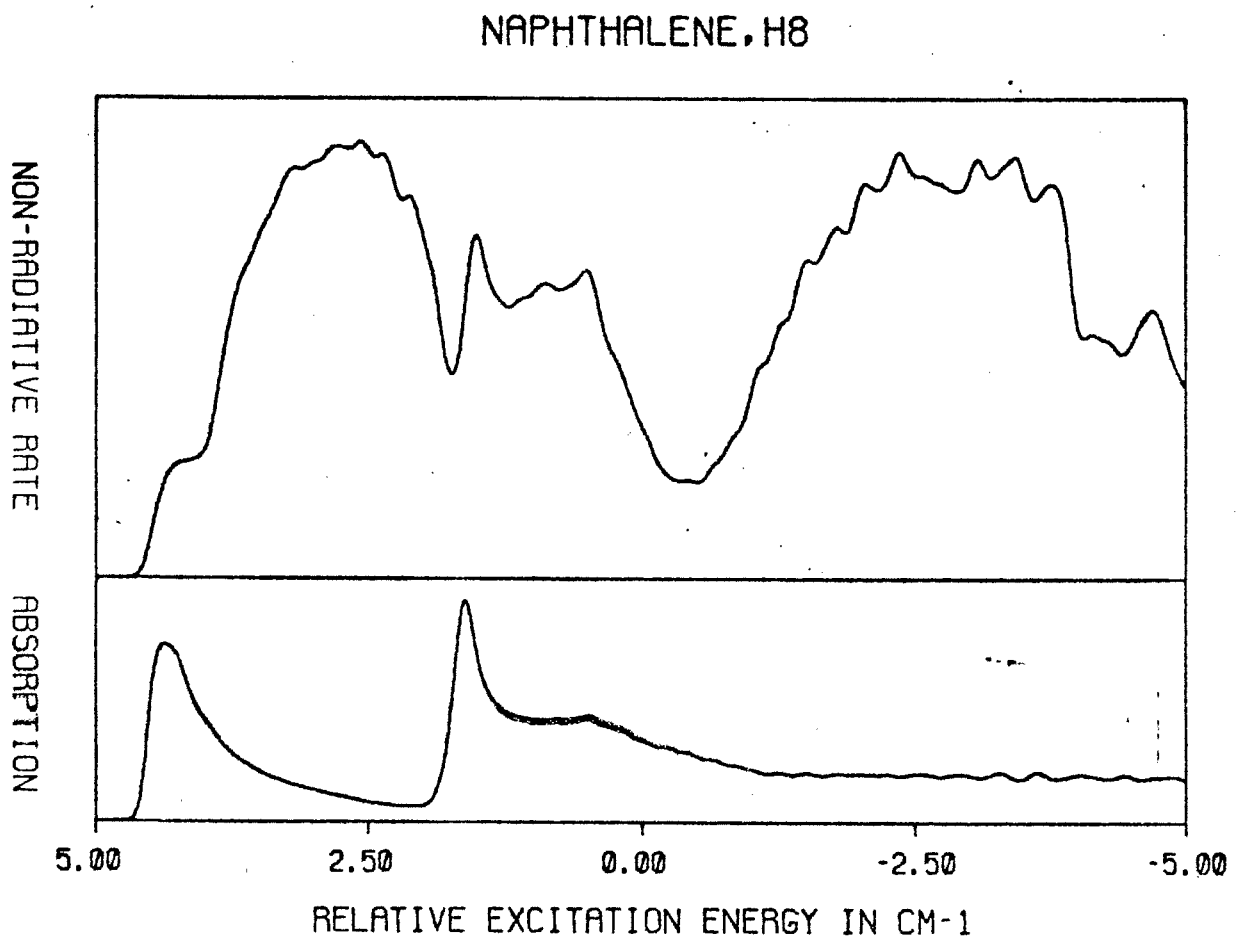

Figure 73. k_{nr}^{a} spectrum with constant rotational factors ($\Delta N = +1$).

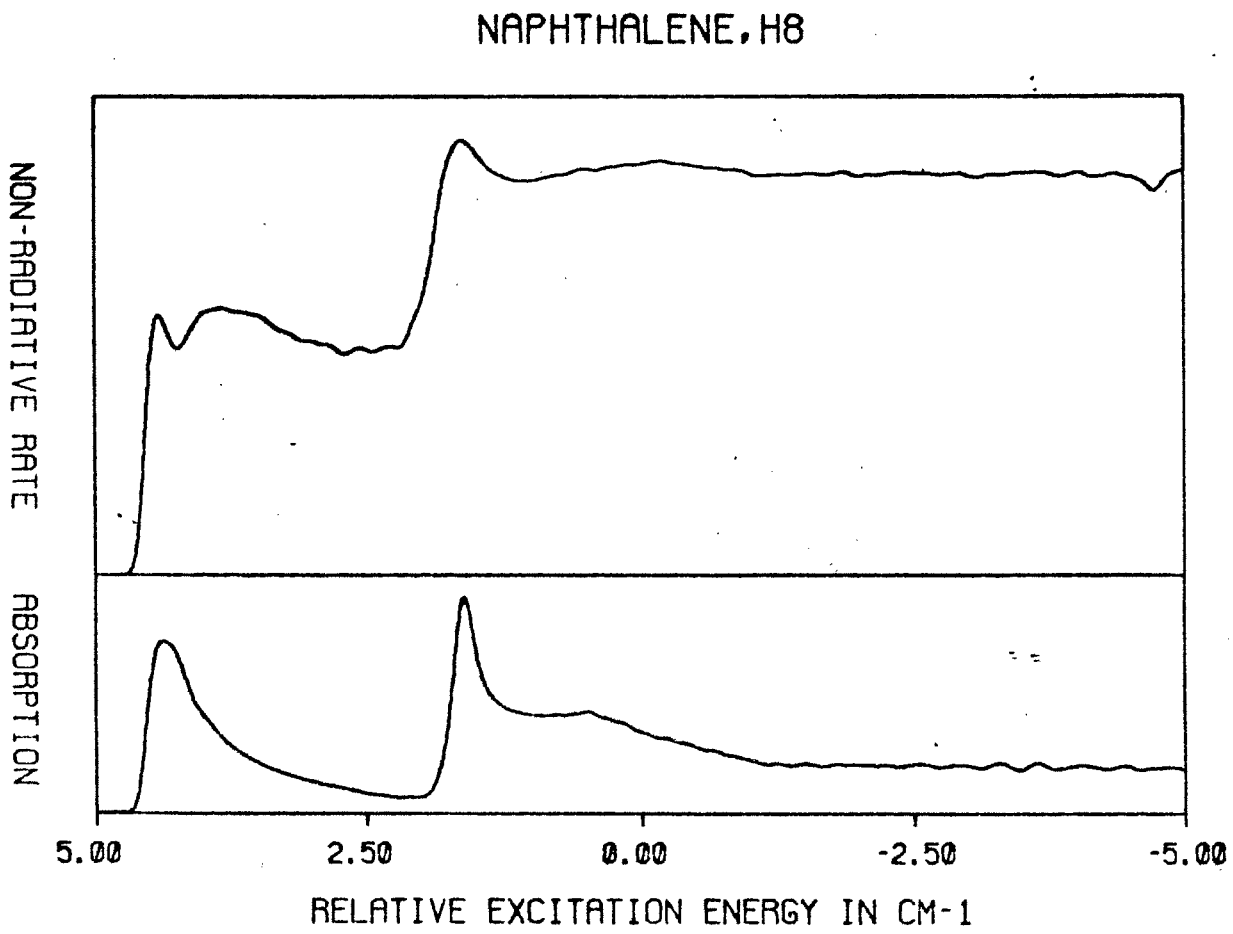

Figure 74. k_{nr}^{a} spectrum with constant vibrational factors ($\Delta N = -1$).

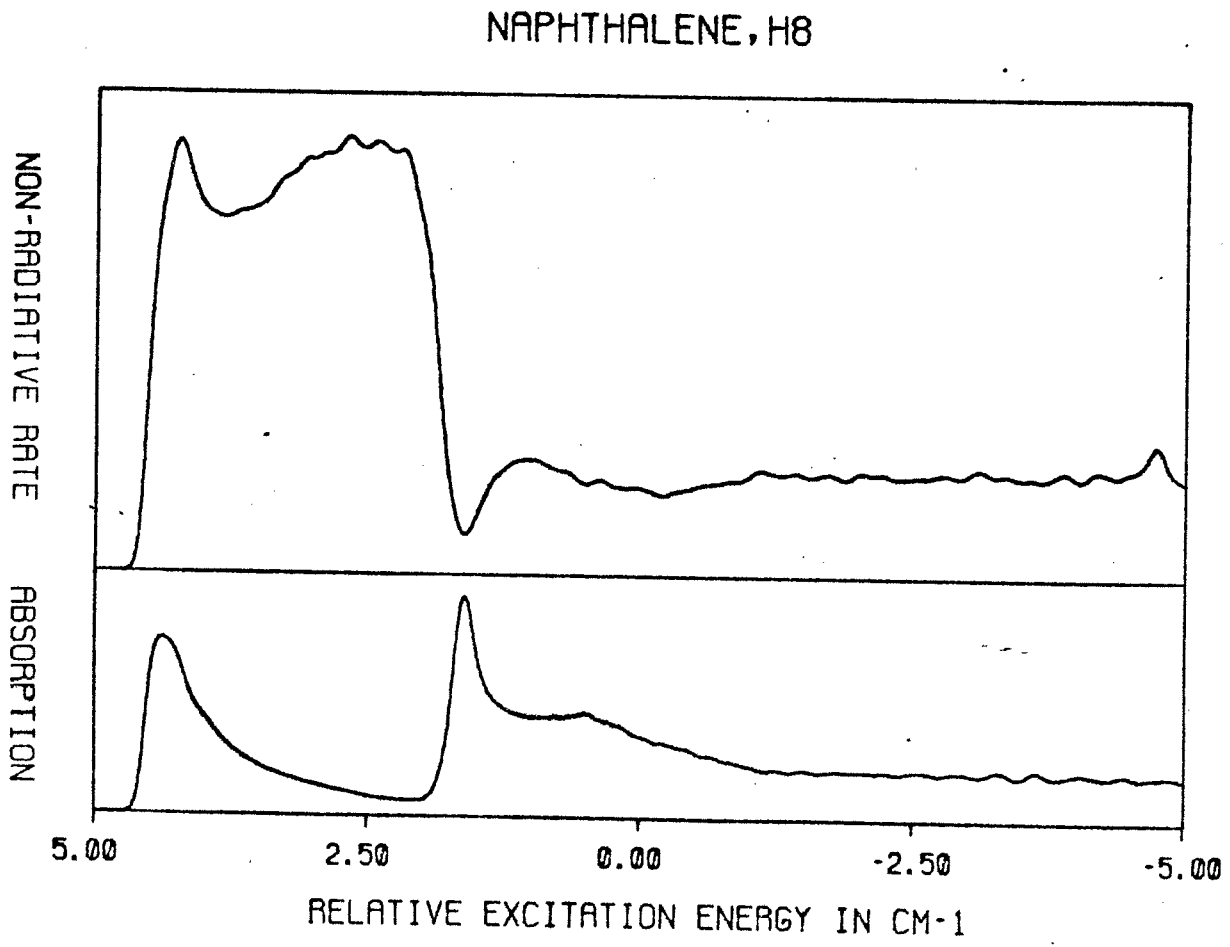

Figure 75. k_{nr}^{a} spectrum with constant vibrational factors (Δ N = 0).

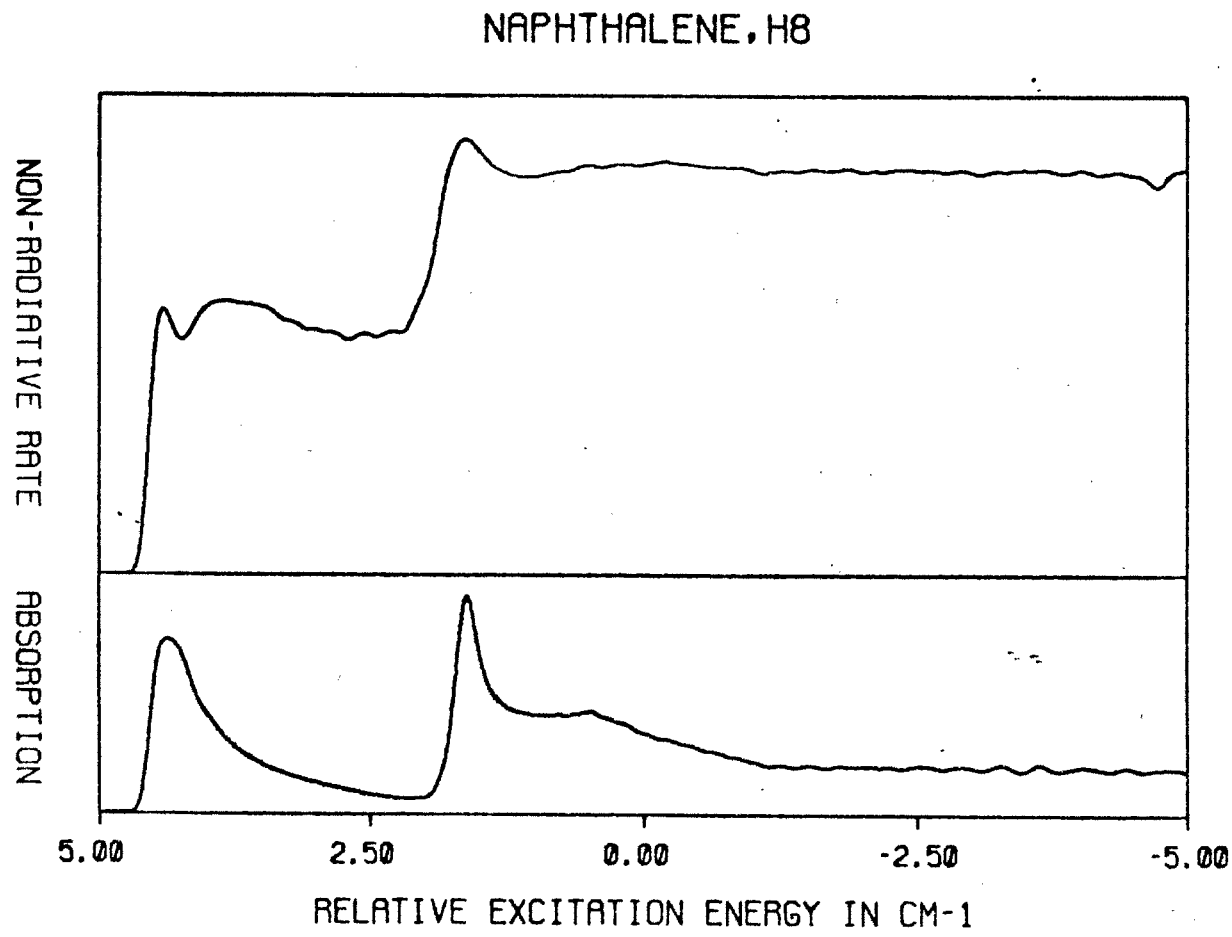

Figure 76. k_{nr}^{a} spectrum with constant vibrational factors (Δ N = +1).

maximum in the region between the two absorption maxima. Thus, even though the effect of all rotational transitions is constant for constant F(E), this is not the case for various ΔN components.

ISC from the 0-0 band

Intersystems crossing from the 0-0 band of naphthalene differs in two primary respects from that from the $8(b_{1g})^1_o$. First, the contour is type A which changes the structure of the excited state rotational distribution. Second, the final vibrational levels are different due to the change in excess energy.

As in the previous section, the quantities k^a_{nr}, k^e_r and ϕ^e were calculated. The calculations summed over all final states and used the full vibrational and rotational terms. Only spin polarization along the A and/or B axes were considered. In these calculations, the effect of the energy of the promoting mode was probed. The function F(E) is shifted up or down the energy scale by the energy of the promoting mode in the final state. The excited ensemble thus views an entirely different set of final vibrational states with correspondingly different coupling strengths.

The first two sets of calculations used the same promoting mode as that of the $8(b_{1g})^1_o$ calculation. It was a $2(b_{2g})$ mode with a frequency of 422 cm^{-1}.

The first set of calculations considered spin polarization along the B axis. Spectra of k_{nr}^{a}, k_{r}^{e} and ϕ^{e} along the rotational contour of the origin are shown on Figs. 77, 78 and 79, respectively. The k_{nr}^{a} spectrum shows moderate structure. The radiative rate spectrum shows a peak around the absorption maximum. This corresponds with the experimental observations. The quantum yield spectrum, however, is quite flat around the absorption peak and corresponds poorly with experiment.

The next set of calculations corresponds to spin polarization along the A axis. The calculated spectra are shown on Figs. 80, 81 and 82. The k_{nr}^{a} spectrum decreases almost monotonically from the blue to the red over a range of about 5 cm^{-1}. The radiative rate constant peaks at the absorption maximum but the quantum yield shows an almost monotonic increase from the blue to the red.

The set of calculations showing the best correlation with experiment assumed a B axis spin polarization and a promoting mode frequency of 522 cm^{-1}. The spectra of k_{nr}^{a}, k_{r}^{e} and ϕ^{e} are shown on Figs. 83, 84 and 85, respectively. The k_{nr}^{a} spectrum shows a local dip around the absorption maximum. The radiative rate constant decreases slowly from the blue to the red and the quantum yield peaks around the absorption maximum.

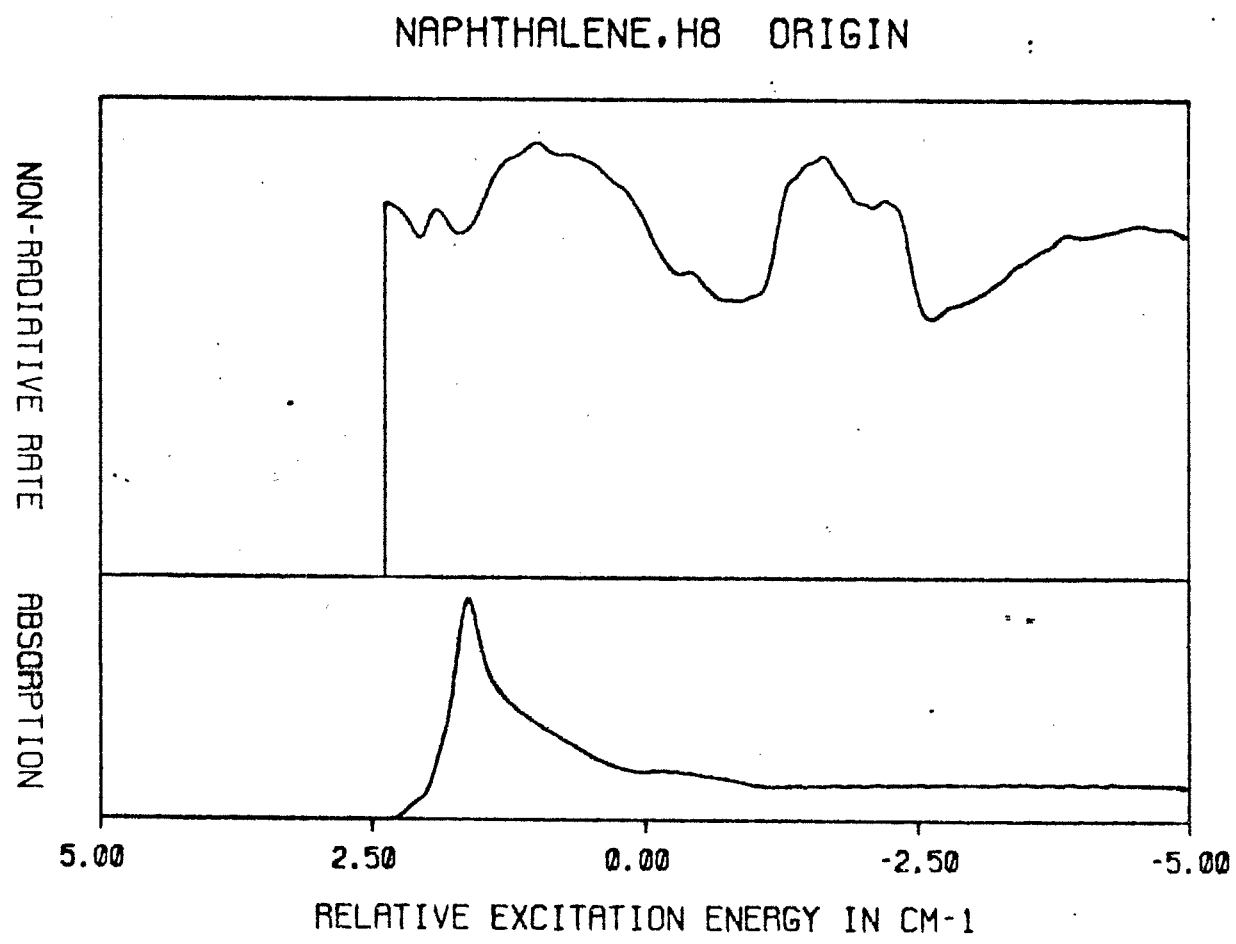

Figure 77. k_{nr}^{a} spectrum with B axis spin polarization and ω_p = 422.

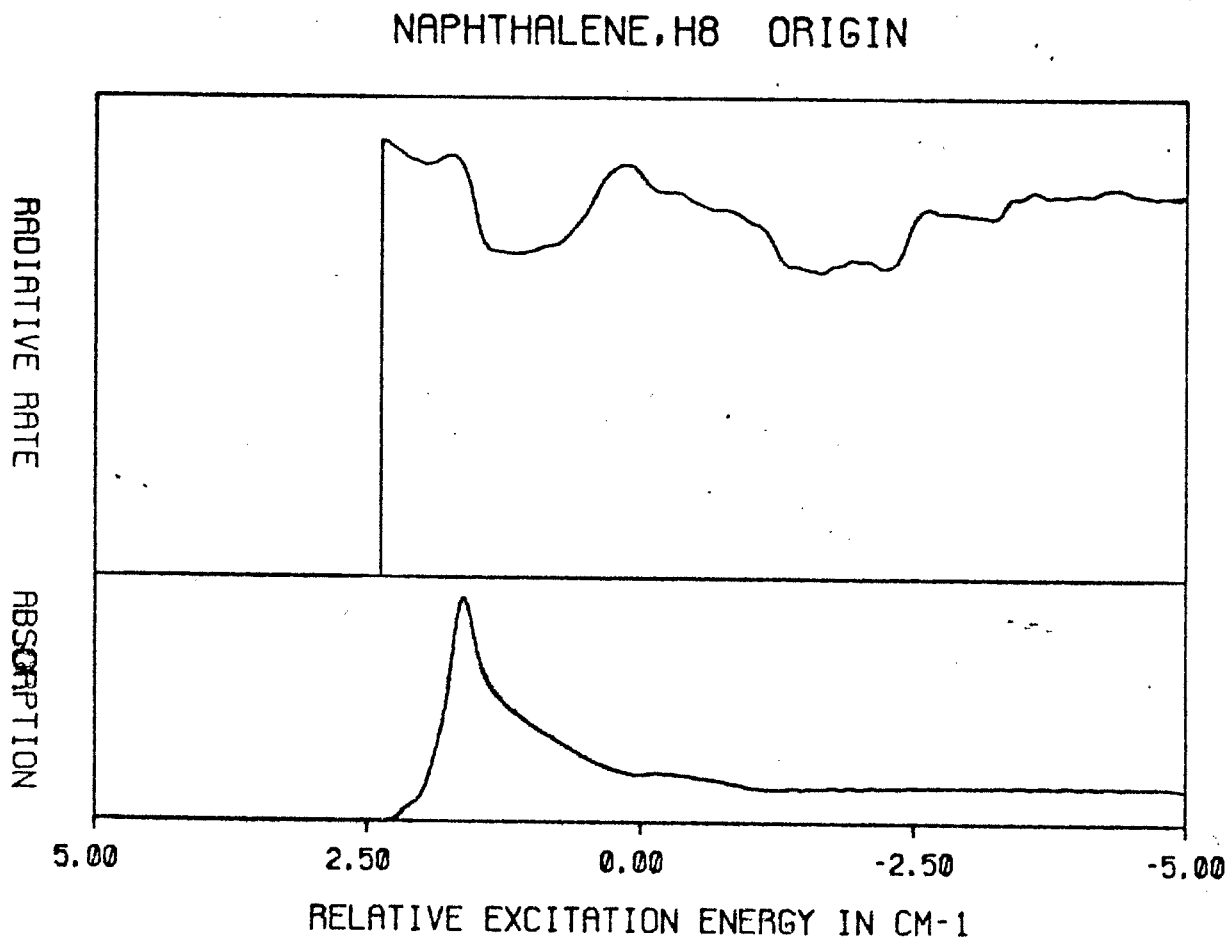

Figure 78. k_r^e spectrum with B axis spin polarization and $\omega_p = 422.$

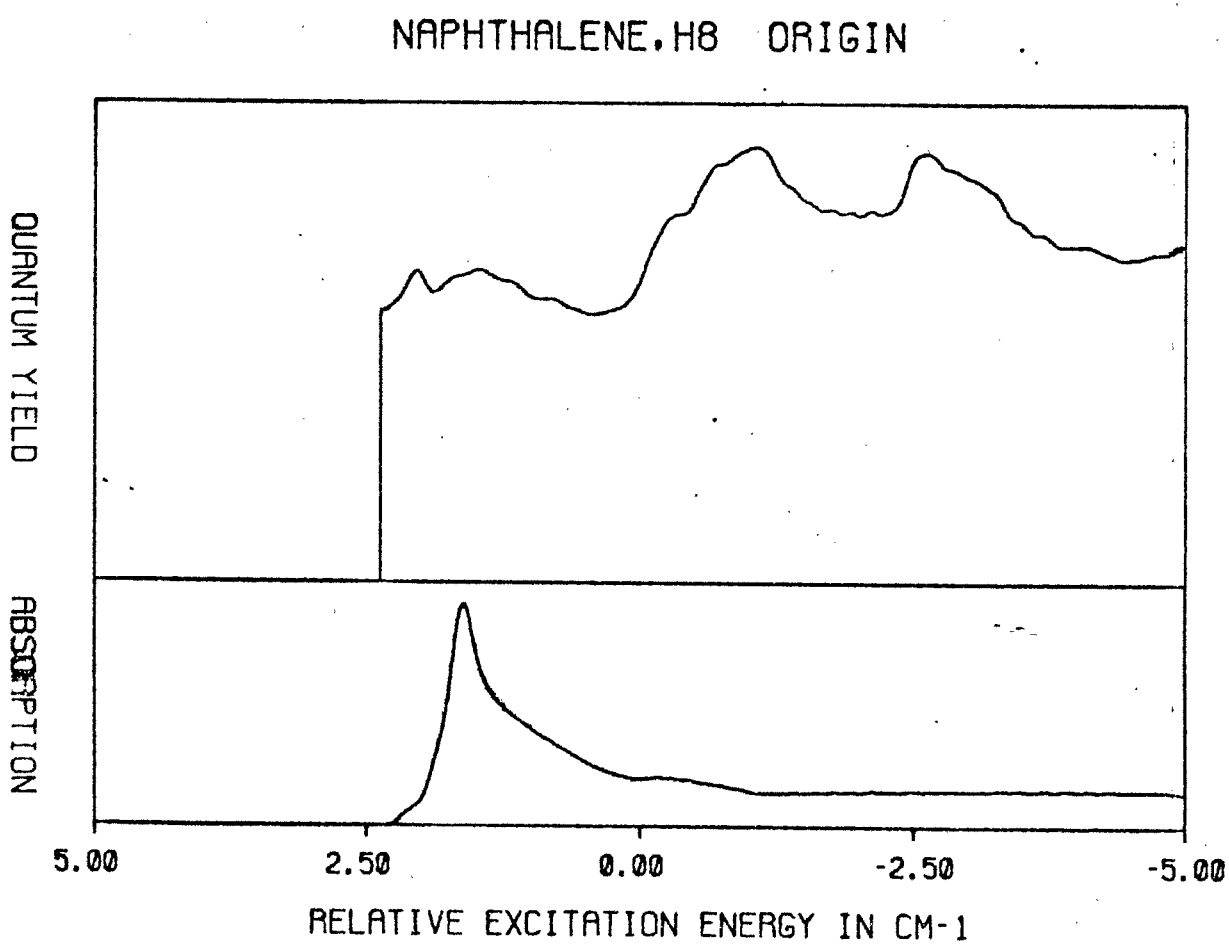

Figure 79. ϕ^e spectrum with B axis spin polarization and $\omega_p = 442$.

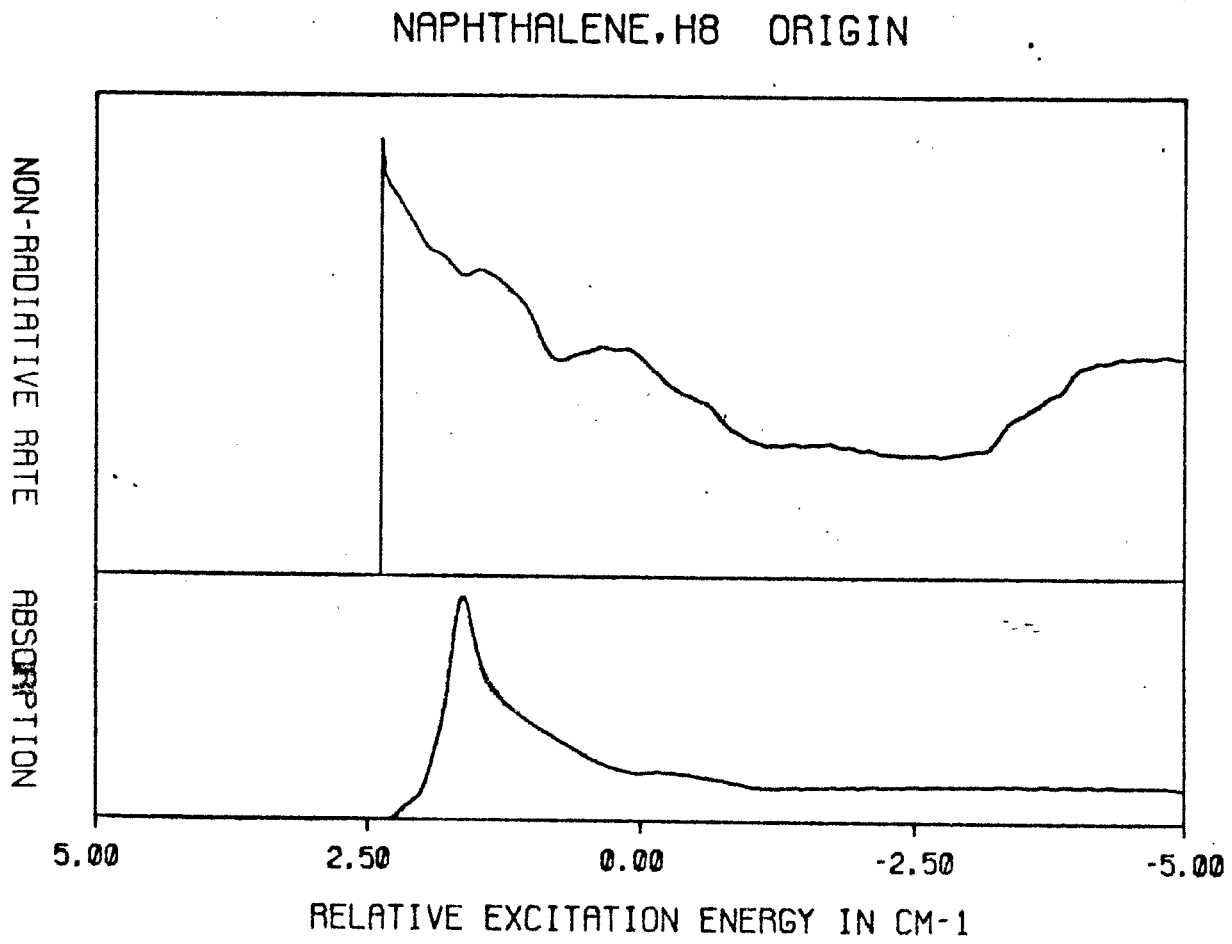

Figure 80. k_{nr}^{a} spectrum with A axis spin polarization.

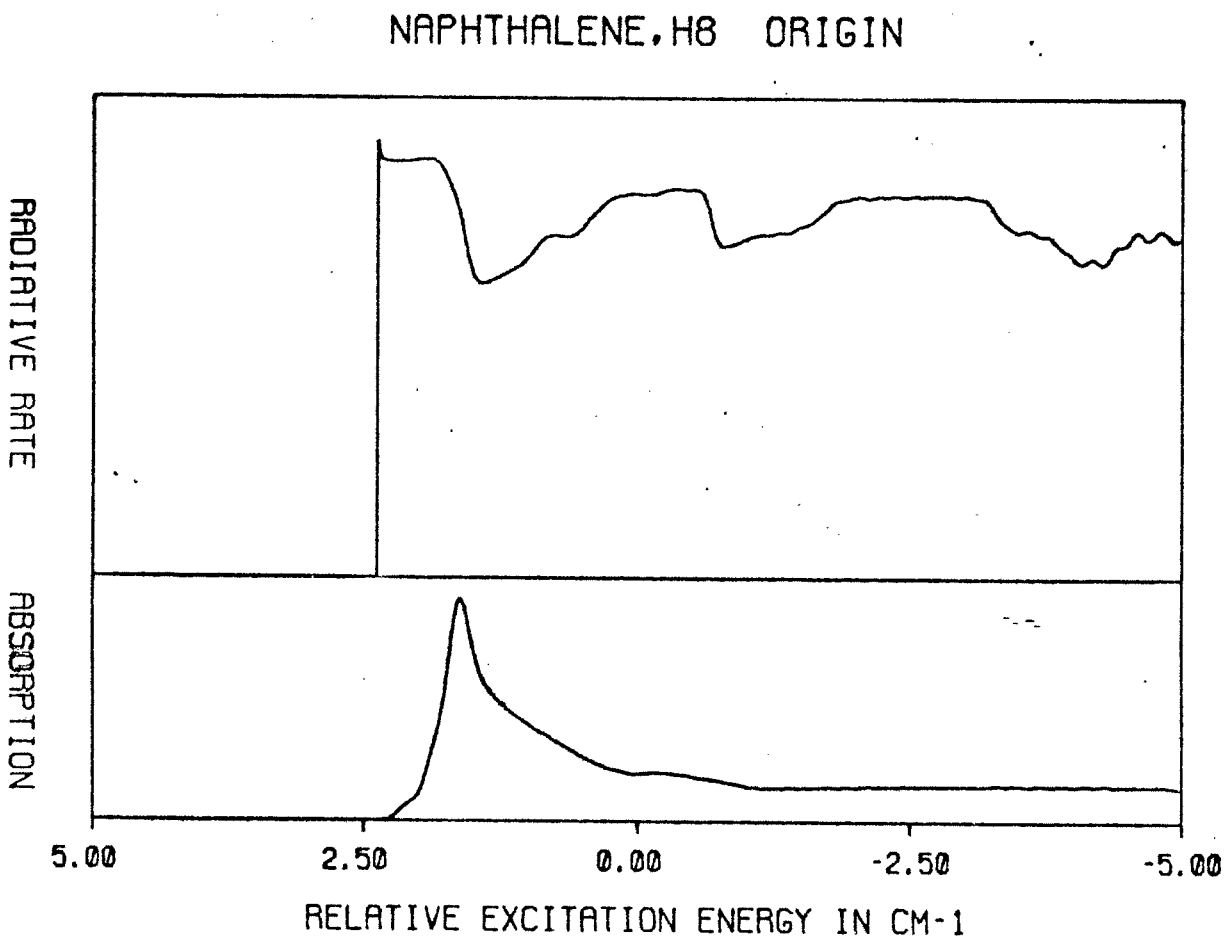

Figure 81. k_r^e spectrum with A axis spin polarization.

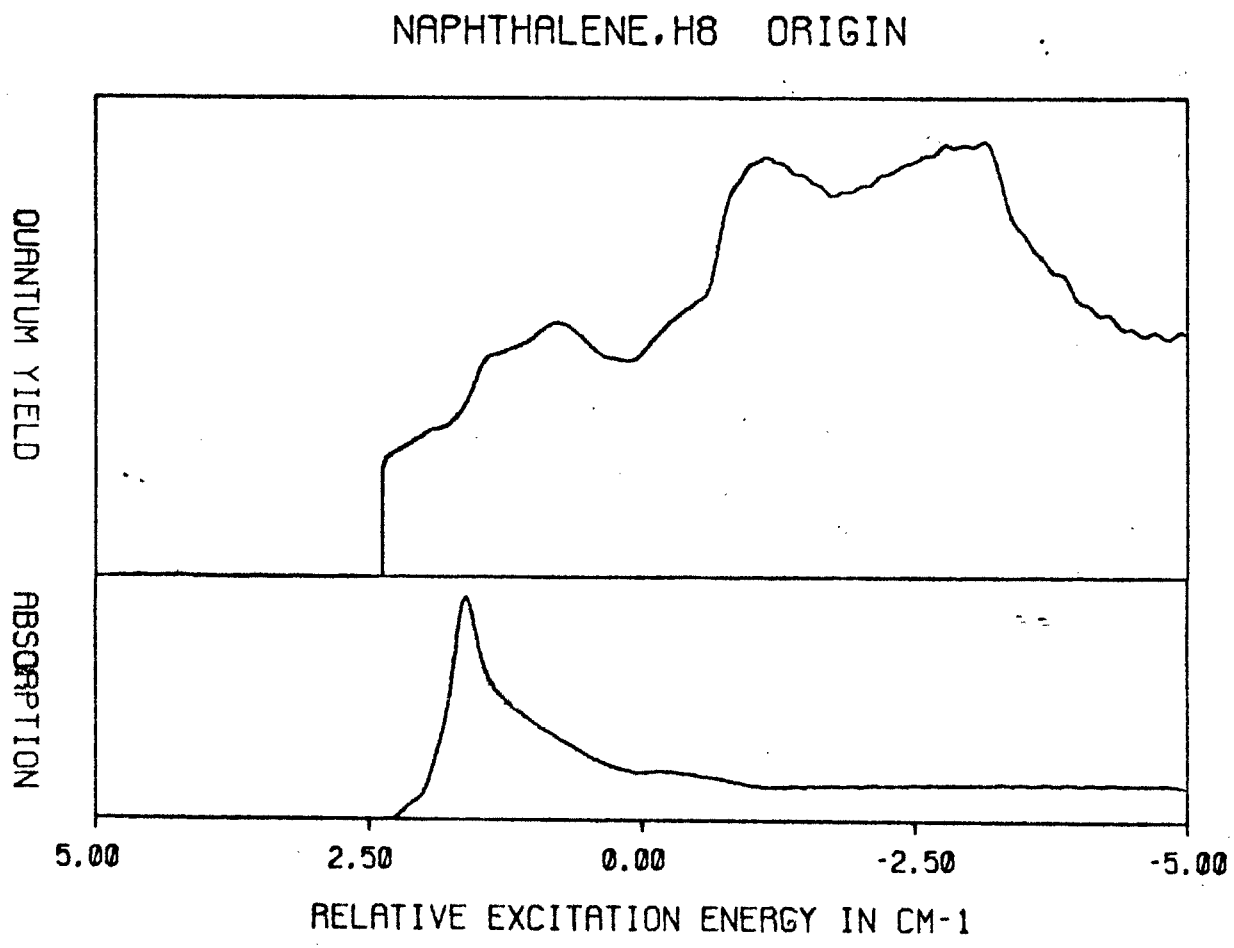

Figure 82. ϕ^e spectrum with A axis spin polarization.

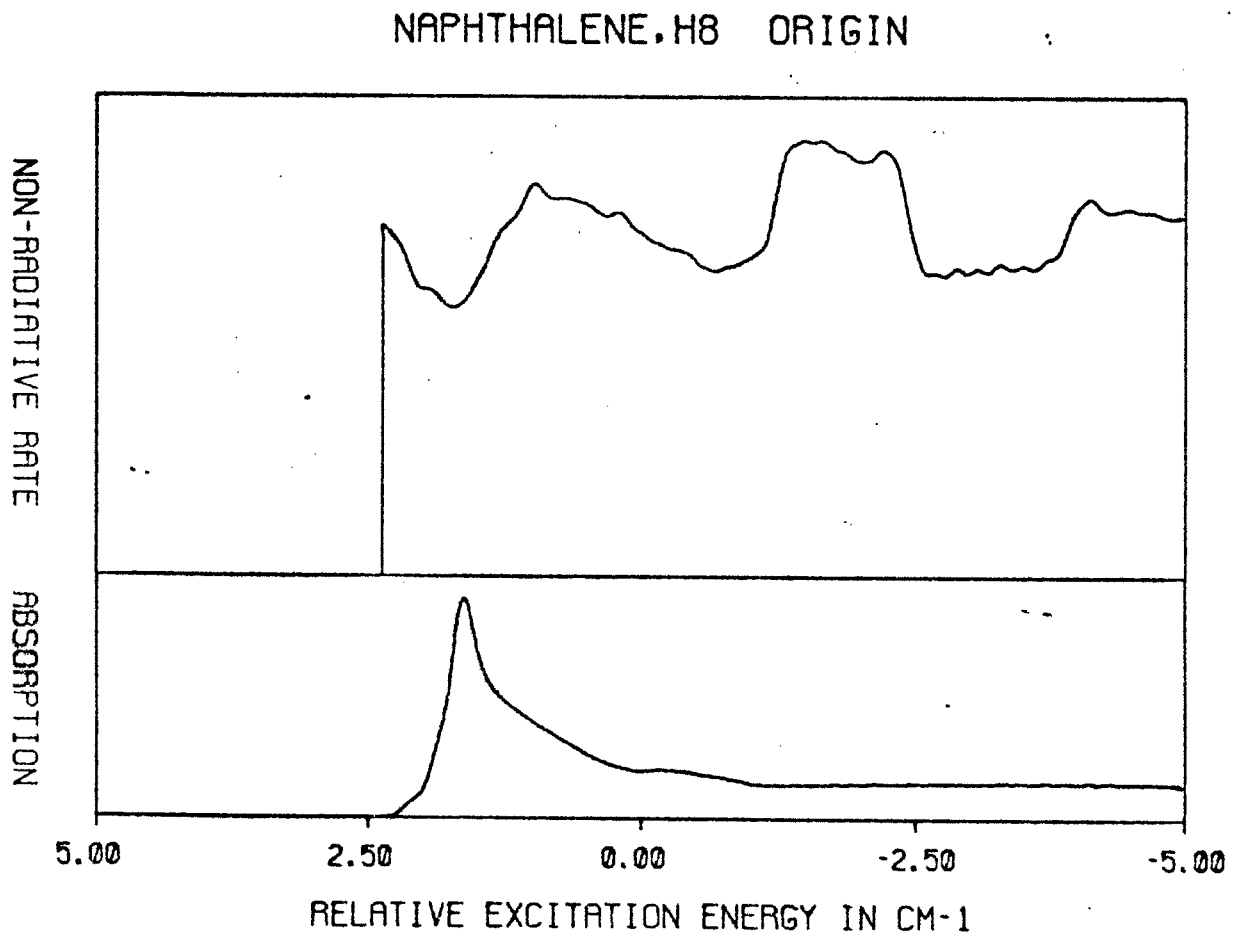

Figure 83. k_{nr}^{a} spectrum with B axis spin polarization and $\omega_p = 522\ cm^{-1}$.

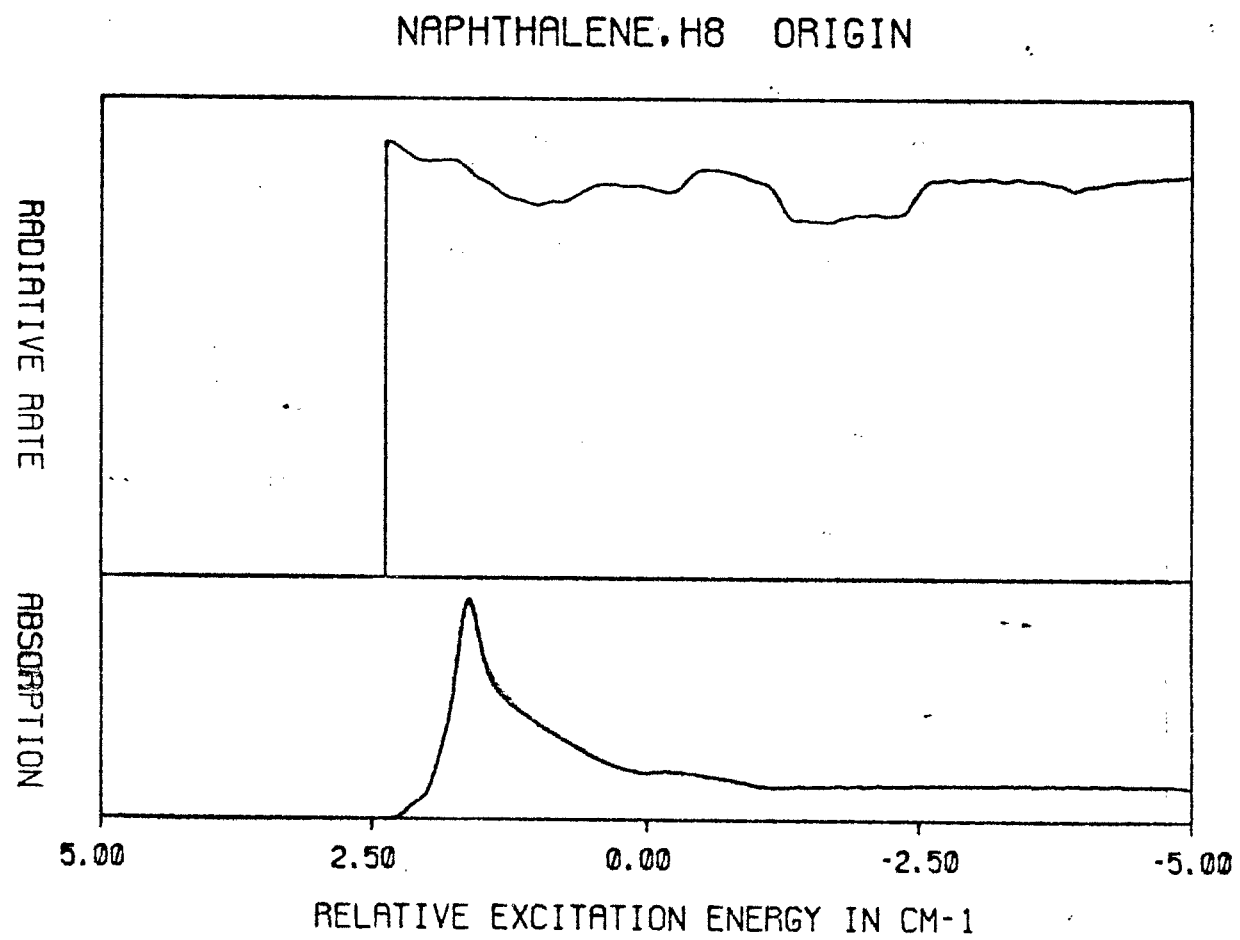

Figure 84. k_r^e spectrum with B axis spin polarization and ω_p = 522 cm^{-1}.

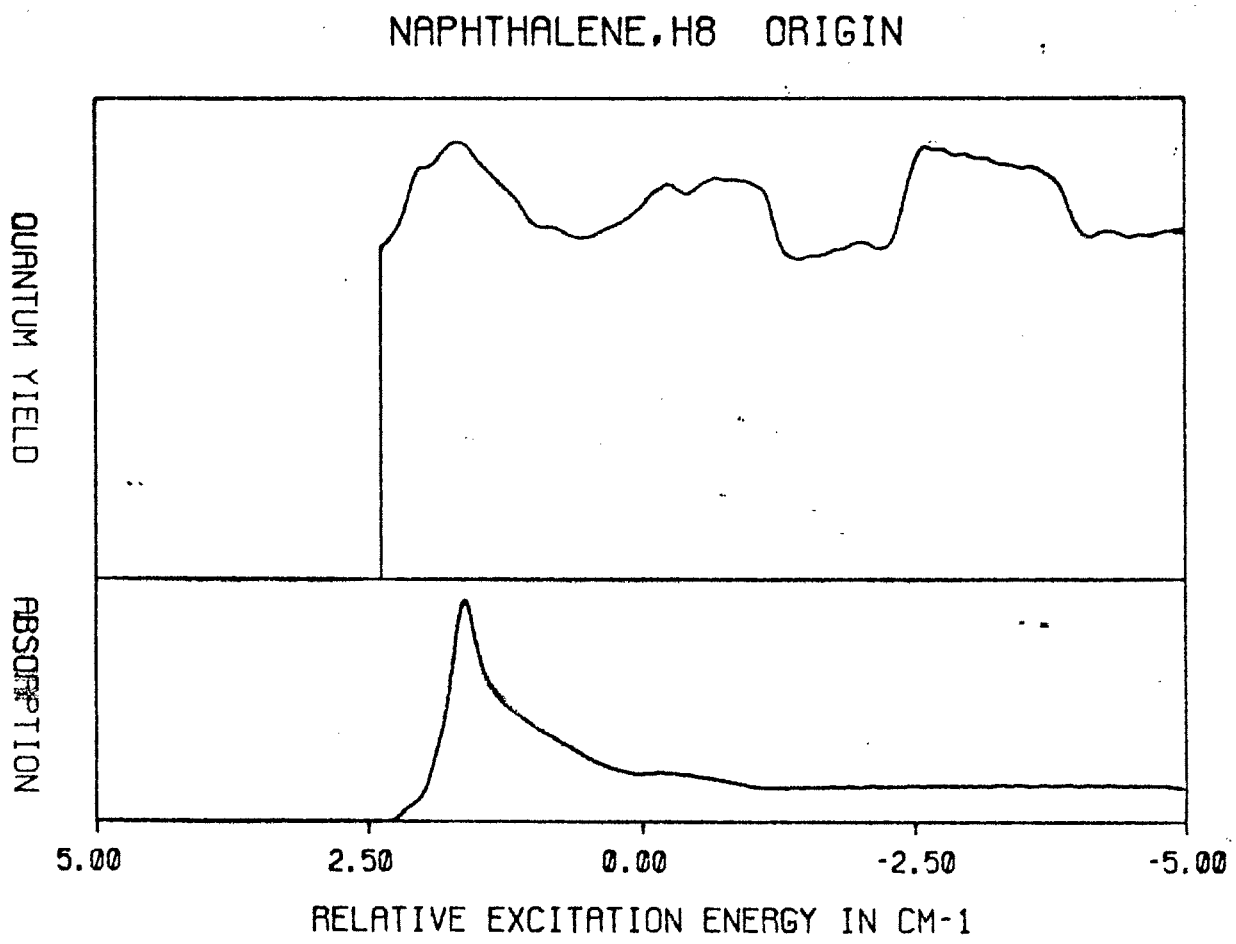

Figure 85. ϕ^e spectrum with B axis spin polarization and $\omega_p = 522\ cm^{-1}$.

The set of calculations showing the worst correlation with experiment assumed a B axis spin polarization and a promoting mode frequency of 622 cm^{-1}. The calculated spectra are shown on Figs. 86, 87 and 88. In all spectra, virtually no structure is observed. This calculation demonstrates that, in spite of a strongly fluctuating vibrational function F(E), it is still possible to excite regions which show a constant average lifetime and lifetime dispersion. Thus, the experimental observation of no structure does not necessarily imply that there is no structure on the microscopic level.

The last set of calculations assumed A axis spin polarization and a promoting mode frequency of 722 cm^{-1}. Spectra of k_{nr}^{a}, k_{r}^{e} and ϕ^{e} are shown on Figs. 89, 90 and 91, respectively. The average non-radiative rate constant shows a maximum at the rotational origin. A lack of structure in k_{r}^{e} indicates that lifetime dispersion is constant. The quantum yield spectrum peaks near the absorption maximum and correlates quite well with the experimental observations.

These calculations show that the promoting mode energy is a very important parameter in non-radiative rate calculations. Variation of only a few hundreds of wavenumbers completely changes the observed structure along the rotational contour.

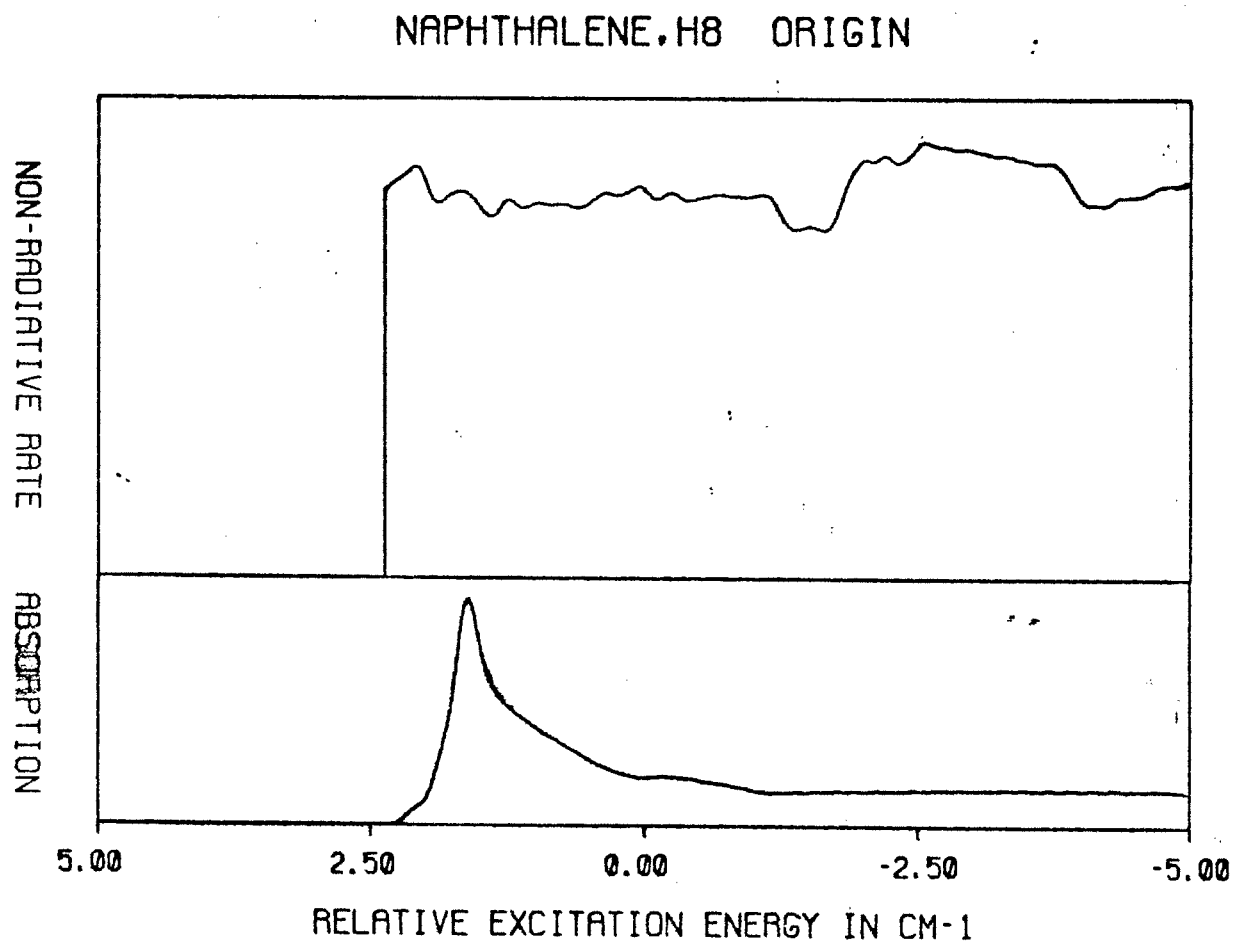

Figure 86. k_{nr}^{a} spectrum with ω_p = 622 cm^{-1}.

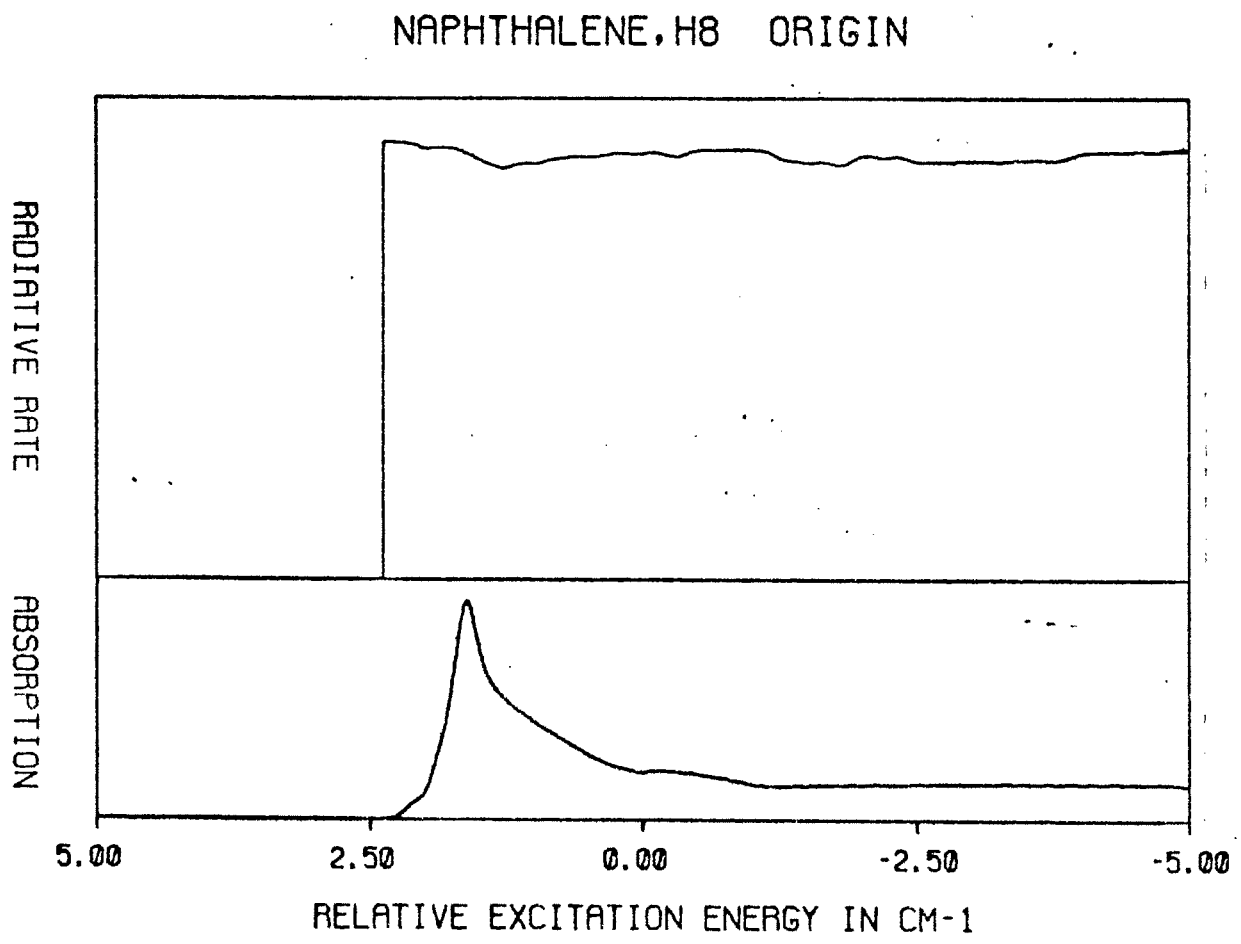

Figure 87. k_r^e spectrum with $\omega_p = 622\ cm^{-1}$.

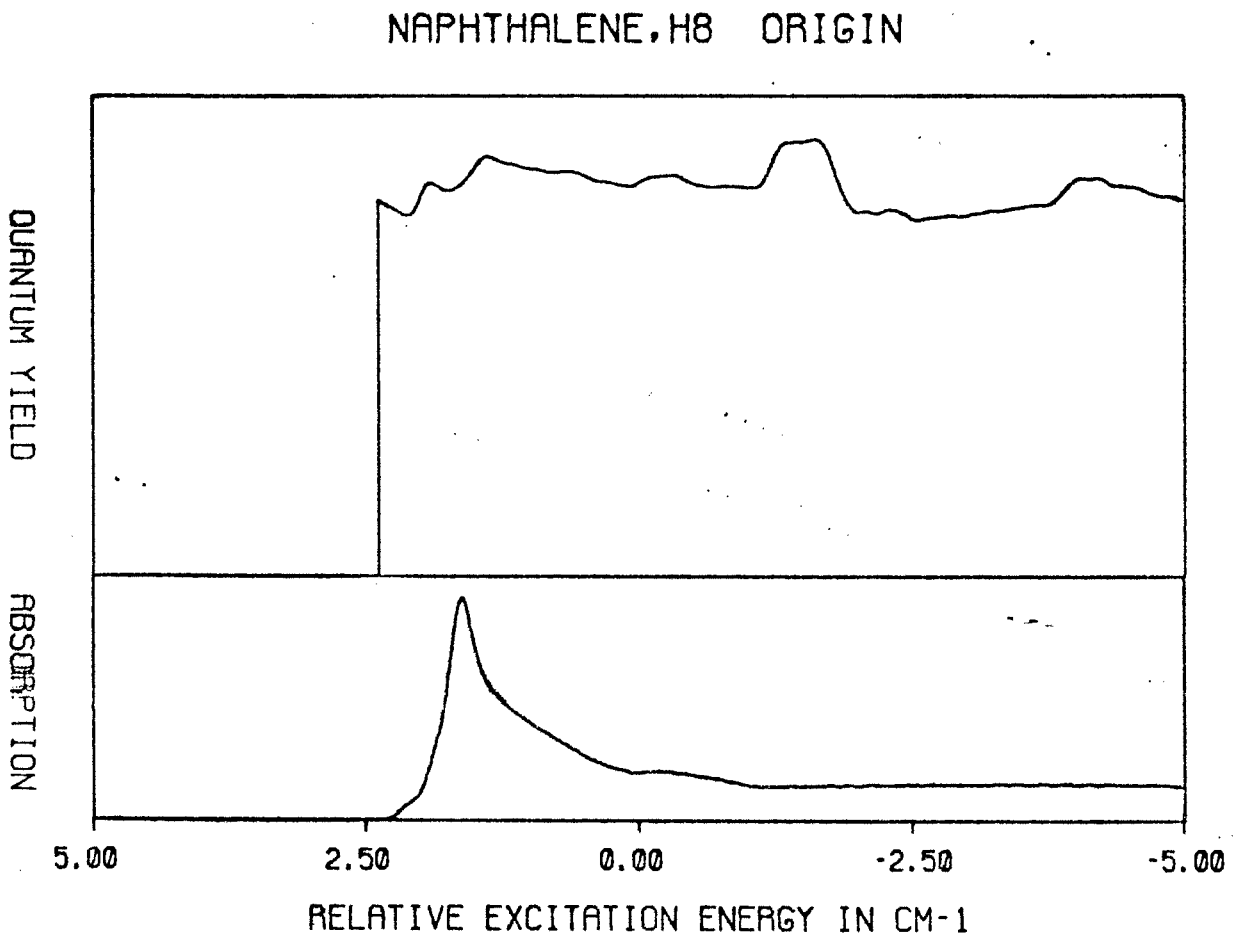

Figure 88. ϕ^{e} spectrum with ω_{p} = 622 cm^{-1}.

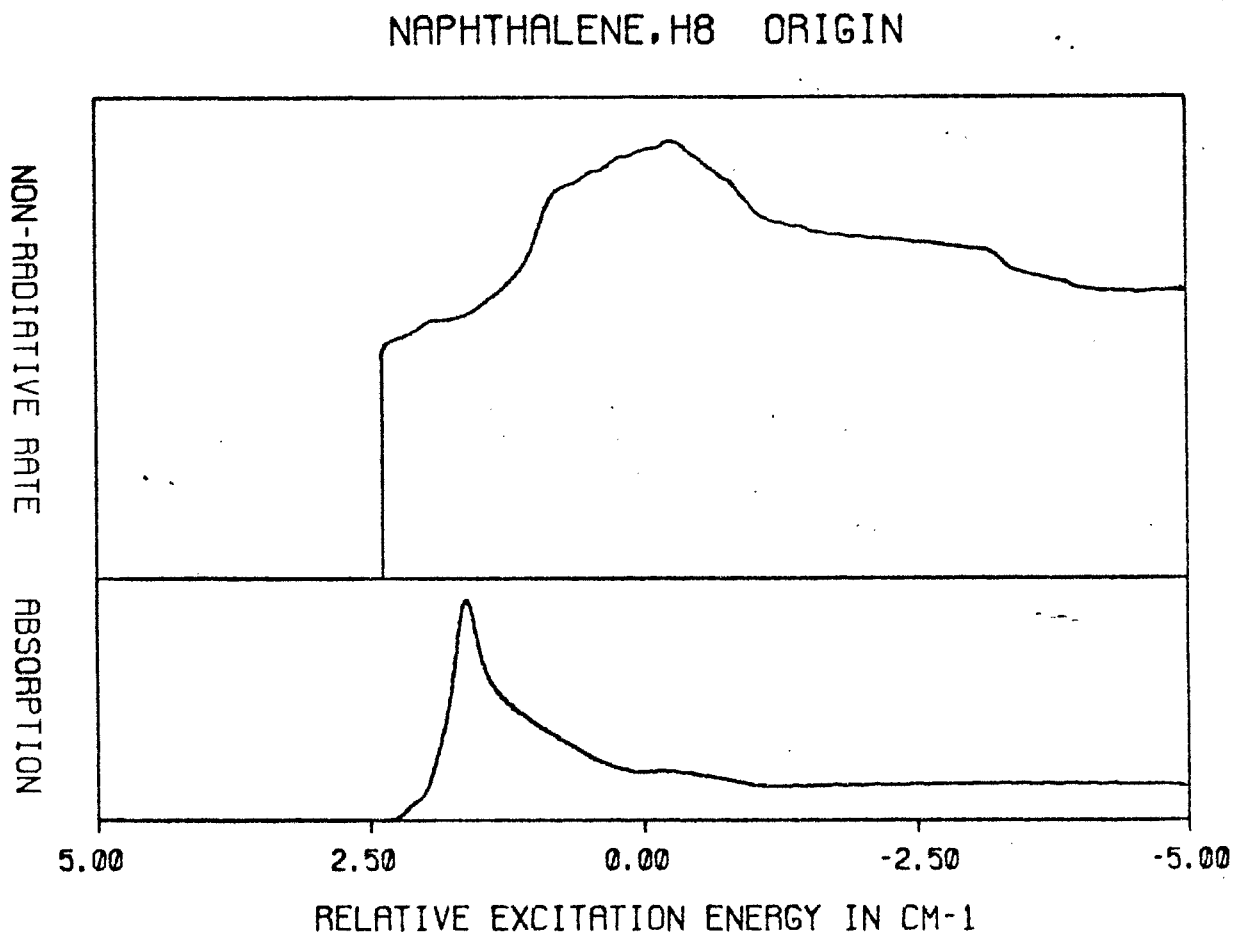

Figure 89. k_{nr}^{a} spectrum with A axis spin polarization and ω_p = 722 cm^{-1}.

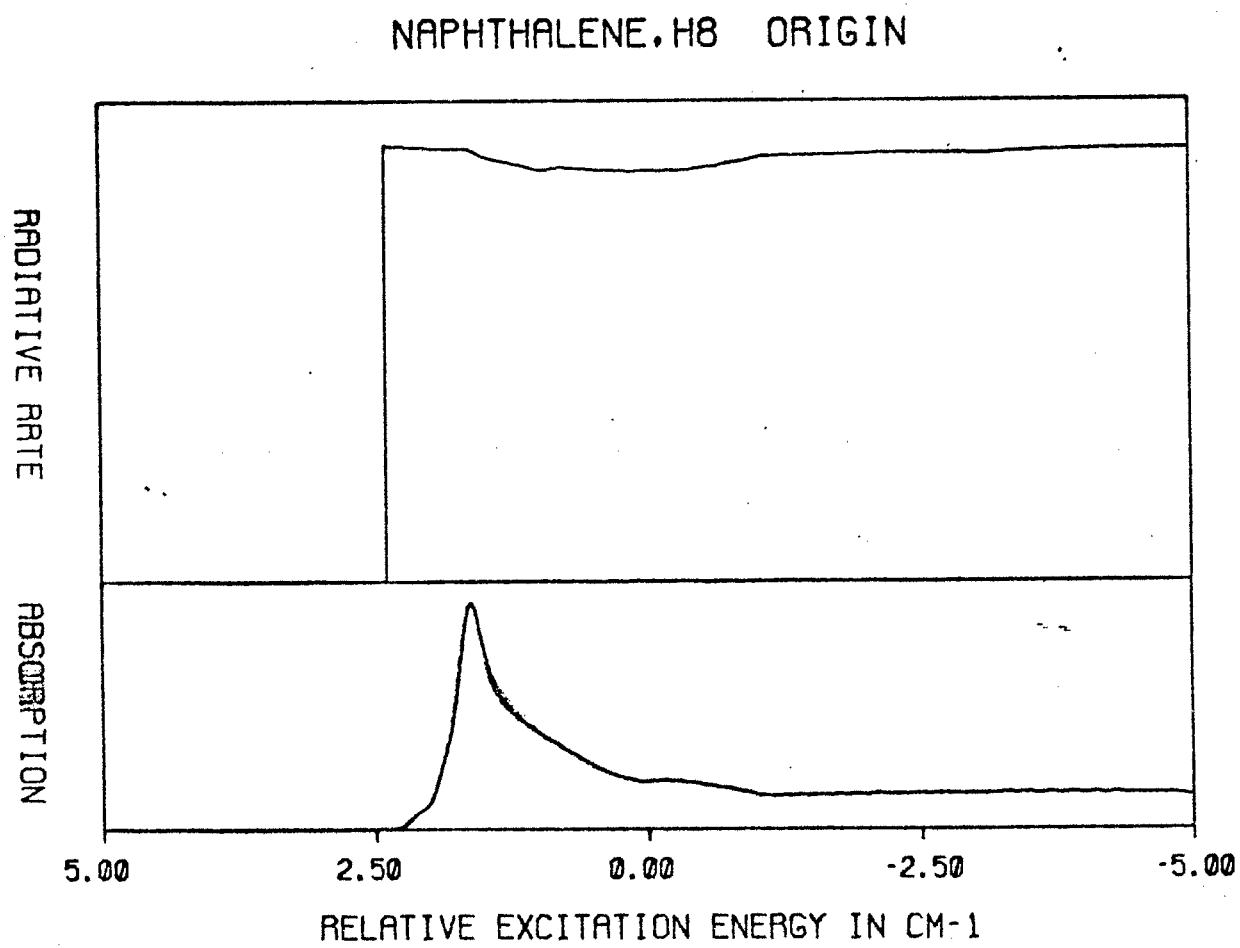

Figure 90. k_r^e spectrum with A axis spin polarization and ω_p = 722 cm^{-1}.

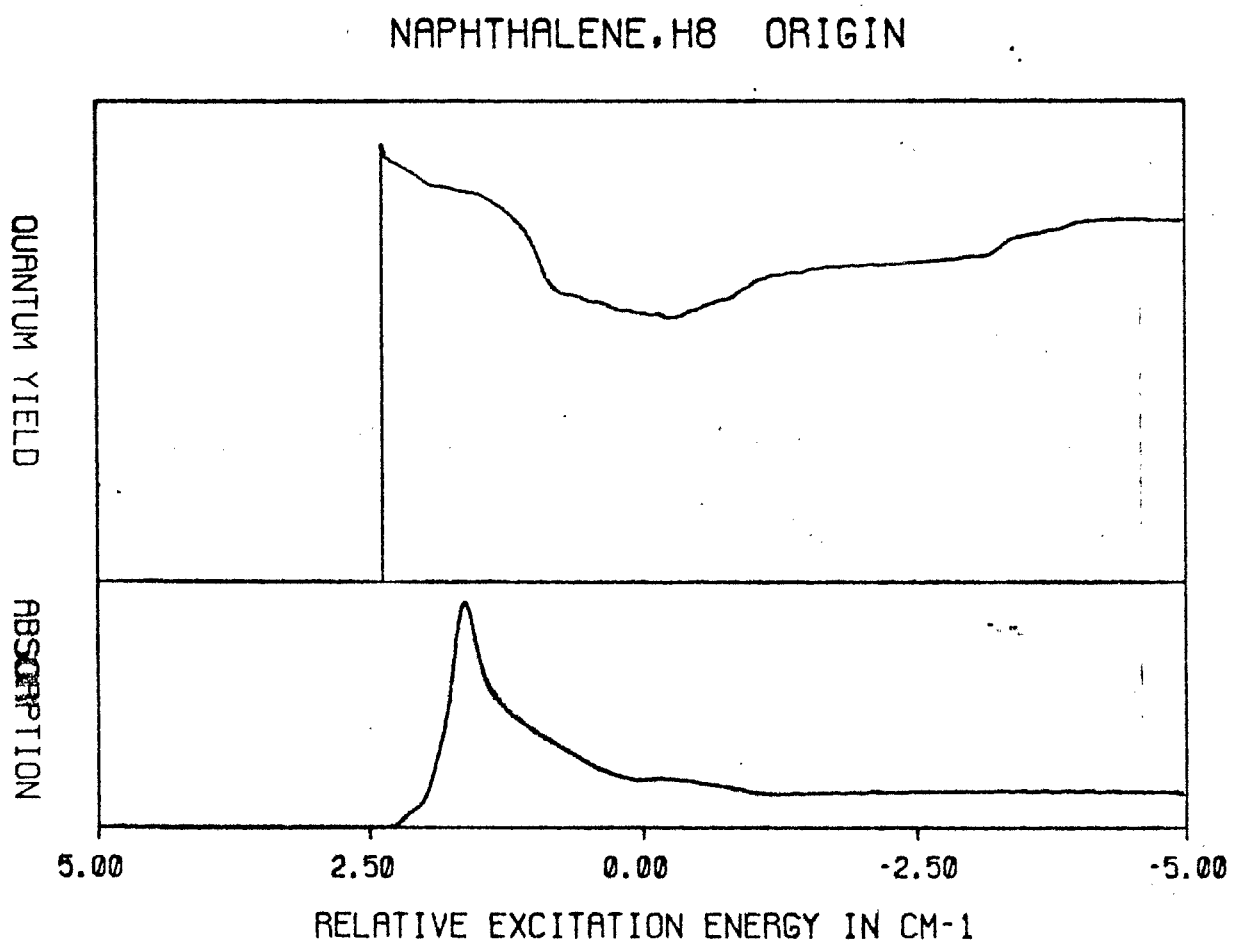

Figure 91. ϕ^{e} spectrum with A axis spin polarization and ω_{p} = 722 cm^{-1}.

For any given promoting mode energy, the spin polarization in the final state also introduces large changes in the calculated non-radiative rate constant. This comes primarily from the change in the rotational selection rules from H_{so}^{z} which allows only $\Delta K = 0$ to $H_{so}^{x,y}$ which allow only $\Delta K = \pm 1$. The change in selection rules affects not only the rotational factor but also the vibrational factor through energy gap branching.

Chapter XV

Conclusion

The experimental measurement of lifetimes and quantum yields along the rotational contours of several vibrational bands of naphthalene, h_8 revealed that the excited state decay processes are dependent on rotational state selection. To a very good approximation, the radiative rate constant can be considered independent of rotational excitation for a given vibrational level. Thus, the observation of structure in quantum yields and other observables must be related to the non-radiative rate constants.

A theoretical description of the decay of the ro-vibronic levels was based on several factors. First, the excitation of many levels required the solution of a Master Equation to describe the decay of the ensemble after pulsed excitation. The input parameters required by the final solutions were the microscopic populations and rate constants. Excited state populations were calculated by techniques similar to those used in band contour analysis.

The derivation of a model of non-radiative decay which included the effects of rotational selection showed that the rate constant expression for ISC derived in earlier models must be modified by the inclusion of a rotational factor similar to the dir-

ection cosines of optical spectroscopy. In addition, rotational energies must be included in the energy matching condition for initial and final states. Calculations showed that both of these were critical additions to the rate constant expression.

Model calculations employing the full Master Equation solution for two quite different vibronic origins lead to several important conclusions. First, even upon excitation of many ro-vibronic levels, the ensemble observables can vary strongly as a function of excitation energy. The fluctuations are smoothed out only in the limit of broadband excitation but do not average out to the value given by the neglect of rotational factors.

The structure in ISC depends strongly upon the electronic spin-orbit matrix elements. This comes from the ΔK selection rules implicit in them. Variation of the promoting mode energy completely changes the structure along a rotational contour. This is in sharp contrast to saddle point methods for which the promoting mode energy is not a critical parameter.

The experimental and numerical results reported here support the view that there is a strong rotational dependence in non-radiative processes. This puts non-radiative processes on par with radiative processes.

Both depend upon the nature of the states which are coupled by an interaction operator and all states of the molecule - electronic, vibrational, rotational and spin - play an important role in the transitions.